Surface evaporation and water vapor transport in the convective boundary layer

Chiel C. van Heerwaarden

Thesis committee

Thesis supervisor

Prof. dr. A.A.M. Holtslag

Professor of Meteorology
Wageningen University

Thesis co-supervisor

Dr. J. Vilà-Guerau de Arellano

Associate professor, Meteorology and Air Quality Group
Wageningen University

Other members

Prof. dr. F. Porté-Agel, EPFL, Lausanne, Switzerland
Prof. dr. H.J.J. Jonker, TU Delft
Prof. dr. ir. B.J.J.M. van den Hurk, KNMI, De Bilt / Utrecht University
Prof. dr. ir. R. Uijlenhoet, Wageningen University

This research was conducted under the auspices of the SENSE Research School

Surface evaporation and water vapor transport in the convective boundary layer

Chiel C. van Heerwaarden

Thesis
submitted in fulfilment of the requirements for the degree of doctor
at Wageningen University
by the authority of the Rector Magnificus
Prof. dr. M.J. Kropff,
in the presence of the
Thesis Committee appointed by the Academic Board
to be defended in public
on Wednesday 8 June 2011
at 4 p.m. in the Aula.

Chiel C. van Heerwaarden
Surface evaporation and water vapor transport in the
convective boundary layer,
158 pages.

Thesis, Wageningen University, Wageningen, NL (2011)
With references, with summaries in Dutch and English

ISBN 978-90-8585-913-0

Printed by Universal Press, Veenendaal, NL

Contents

1 Introduction

1.1 Motivation

This thesis deals with surface evaporation and transport of water vapor in the lowest part of the atmosphere. More specifically, it describes how turbulence in the lowest part of the atmosphere influences how much water and heat is taken up from the land surface, and how, in turn, these fluxes feed back on the state of the atmosphere. Before introducing the topic in detail, I would like to explain why this topic is worth studying.

Water that evaporates from the land or sea surface, either through direct evaporation or through transpiration by vegetation, is the only provider of moisture for the atmosphere. The atmosphere contains water in all three phases: water vapor determines the relative humidity of the air and the liquid and solid phases occur in the form of clouds and precipitation. In other words, atmospheric moisture determines to a large extent how we experience the weather—it is evaporation that explains whether the air feels humid or dry, whether there is sunshine or shade and whether it rains or not.

The previous examples show that the role of evaporation in the weather and climate system is evident. Evaporation has a large impact on the temperature close to the land surface, simply because energy that is not used for evaporating water is mostly used to heat the atmosphere and the land surface. If we need to predict rainfall, we have to know how much water evaporates. For the assessment of the impact of global warming on water resources, it is necessary to understand how global warming influences evaporation and whether this dampens or enhances the effects of global warming by altering the temperature, cloudiness and precipitation.

Water that enters the atmosphere is also inherently connected to food production. To be able to optimize food production and to minimize water use, we need to understand every aspect of water exchange between the land surface and the atmosphere. Furthermore, the understanding of the role of water in ecosystems requires full knowledge on how, when

and why plants exchange water with the environment and which path the evaporated water follows to eventually return to the land surface through precipitation.

In addition to highlighting the importance of evaporation, these examples emphasize that surface evaporation directly influences the atmosphere and that the land surface and the atmosphere are in fact a closely coupled system.

The study of evaporation and transpiration—evapotranspiration—belongs to the fields of hydrology and biology. By investigating the impact of the amount of soil moisture, the soil type, the type and stage of vegetation and the near-surface atmospheric conditions on evapotranspiration a great amount of knowledge has been acquired. In turn, the study of the atmosphere close to the surface—the atmospheric boundary layer—is mostly associated with meteorology. The research in this field is generally focused on understanding atmospheric turbulence under a wide range of conditions. The research presented in this thesis aims at combining and integrating knowledge and methods from both disciplines to improve the understanding of water exchange between the land surface and the atmospheric boundary layer and of water vapor transport in this boundary layer.

1.2 Evaporation and transport of water vapor

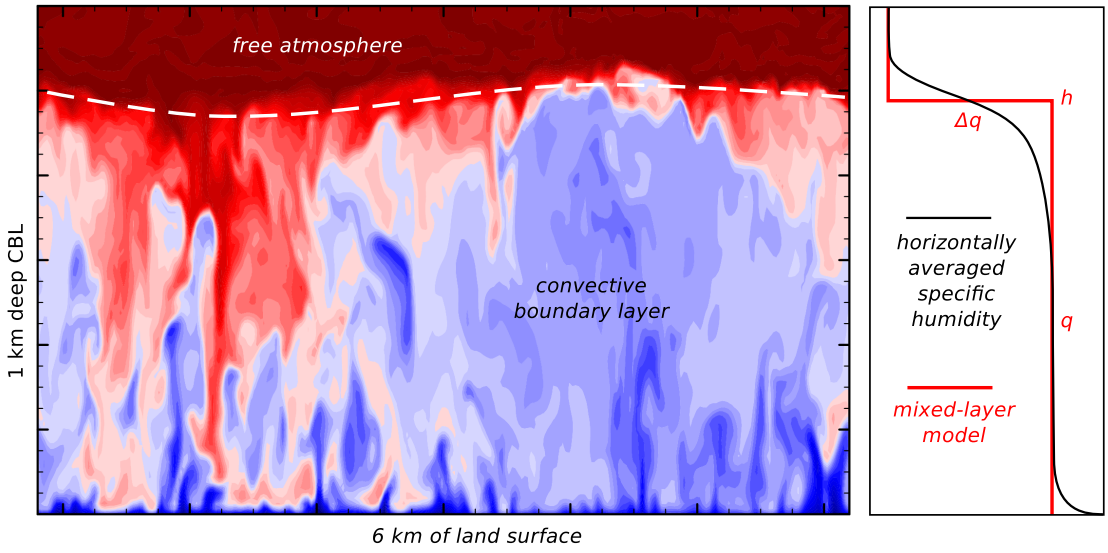

Figure 1.1: Left panel: vertical cross section of a convective boundary layer showing the distribution of specific humidity, created using a Large Eddy Simulation model. Right panel: horizontally averaged profile of specific humidity based on the cross section in the left panel (black line) with an overlay of the mixed-layer model representation of that profile (red line). In the mixed-layer model, q is the specific humidity, h is the boundary layer height and Δq is the jump in specific humidity between the free atmosphere and the CBL.

Figure 1.1 illustrates the essence of the physics that are studied in this thesis and the tools which are used. The left panel contains a cross section of moisture in the lowest kilometer of the atmosphere in typical afternoon conditions of a sunny day in a midlatitude summer. The layer that defines this lowest kilometer is called the atmospheric boundary layer, as it connects the atmosphere to its bottom boundary: the land surface. Due to the adjustment of the

atmospheric flow to the surface, the atmospheric boundary layer is generally turbulent. Under daytime conditions, the sun heats the land surface and heat and moisture are released into the atmosphere, thereby generating convective turbulence. Therefore, such an atmospheric boundary layer is called a *convective boundary layer* (CBL).

Convection is organized in rising thermals, visible as the blue plumes in Figure 1.1 (left panel). These plumes are warmer and moister and therefore less dense than their surroundings, which explains their rising motions. In a time period in the order of ten minutes such a plume reaches the top of the turbulent layer, where it meets the stably stratified and relatively dry *free atmosphere*. There, the turbulent plumes cannot rise further upwards, because their density is no longer less than that of their surrounding. Therefore, the plumes sink back into the atmosphere, but not without mixing a part of this dry and stable air into the CBL. This process, which is called *entrainment*, can be clearly seen in Figure 1.1, where the red colors, representing the relatively dry free atmospheric air, enter from the top into the turbulent layer. An interesting feature shown in the figure, is that the dry air from the free atmosphere is able to reach the land surface.

That brings us to the next aspect of this thesis: *surface evaporation* and *land-atmosphere interactions*. As explained in the previous section, the dynamics of the CBL are driven by the heating of the land surface by solar radiation. A small part of the radiative energy that is available at the land surface enters the soil or is used for the photosynthesis of plants. The major part of the energy, however, is directly available to reenter the atmosphere, either as a temperature flux (sensible heat flux) or as a moisture flux (latent heat flux). How the available energy is distributed over these two fluxes strongly depends on the properties of the near-surface atmosphere. To summarize: the heating and moistening of the atmosphere are driven by the surface fluxes, but the surface fluxes also respond strongly to the atmospheric conditions. Therefore, we can state that the land and the atmosphere interact.

Both the dynamics of the CBL and the processes at the land surface have been studied intensively and both can be modeled in detail. State-of-the art weather and climate models contain both land surface and convective boundary layer parameterizations, thus their interactions are taken into account in such models. Nevertheless, we have only limited knowledge on their behavior as an integrated system. In particular, the influence of the entrainment of dry and warm air from the free atmosphere into the CBL is poorly understood.

Under daytime conditions, the atmospheric boundary layer is very efficient in vertically mixing the air. Therefore, by averaging the specific humidity profile in the horizontal, we retrieve a vertical profile of specific humidity that is approximately constant with height in the CBL (see right panel in Figure 1.1). In addition, the horizontal averaging of potential temperature and momentum also yields vertical profiles that are nearly constant with height. Note that specific humidity, potential temperature and momentum are so-called conserved variables. Conserved variables are variables that remain constant under vertical displacement as long as there are no sources and sinks acting on them, which makes them very convenient as variables for usage in models.

The profile of a conserved variable that is constant with height can be described with a minimal set of properties. Figure 1.1 (right panel) shows that it only takes three: the value in the CBL (q in the figure), the CBL height (h) and the difference between the free atmospheric and the CBL value of the variable (Δq). This conceptualization forms the basis of

a simple, but accurate CBL model: the *mixed-layer model*, which has an important role in this thesis. Combined with a land surface model and a simple description of radiation, this model allows for a fast and efficient way to study interactions between surface evaporation and CBL dynamics under a wide range of conditions.

The mixed-layer model assumes that the atmosphere is homogeneous in the horizontal direction. This, however, is not the case if the land surface properties vary in space. If, for instance, the soil moisture content or the land use type is heterogeneous, the input of moisture and heat into the CBL varies in space as well. The water transport dynamics in the CBL can be strongly altered by heterogeneous forcings. Under such conditions, modeling the interactions between surface evaporation and water transport in the CBL requires a more complex type of model than the mixed-layer model. This brings us back to the left panel of Figure 1.1. Here, we can clearly recognize the structures of the the plumes that are being generated by convection. This implies that turbulence is at least partly resolved. The type of model that produced the data used in the figure, and that forms the second important tool in this thesis, is a *large-eddy simulation model* (LES). Such a model resolves the large turbulent motions and parameterizes small ones in a three dimensional domain. Since we can resolve the largest motions, thus not rely on parameterizations, we can simulate heterogeneously forced boundary layers of which the surface properties vary in space.

Despite its ability to simulate water transport dynamics over heterogeneous land surfaces, there is also a downside to LES, compared to the mixed-layer model: the modeling of land-atmosphere interactions in turbulence-resolving models is not straightforward. The common models to describe the interactions, are validated for spatial and temporal scales that are so large, that the turbulent fluctuations in wind, temperature and moisture are averaged out. This is clearly not the case in a grid cell adjacent to the land surface in a LES model (see left panel of Figure 1.1), but well-established alternative methods are lacking.

The previous paragraphs define the two main objectives of this thesis. The first is understanding the interactions between the land surface and the convective boundary layer from an integrated perspective. Here, the focus is on the impact of entrainment processes on the surface energy balance, thus how processes that are on the order of one kilometer away from the land surface directly influence what happens at the surface. The second objective is understanding land-atmosphere interactions over heterogeneous terrain. This objective is twofold. First, the goal is understanding water transport over a heterogeneous land surface, without taking into account land-atmosphere interactions. Second, to be able to model land-atmosphere interactions over heterogeneous terrain, I investigate to which extent the land surface models that are currently used in weather and climate models can be used in LES models, by evaluating their assumptions. Section 1.4 contains a full overview of the research connected to the objectives, but before describing them, the place of this research within existing literature will be given.

1.3 Brief overview of past research

1.3.1 The coupled land surface-CBL system

The first to highlight the importance of the link between surface evaporation and the CBL were Priestley and Taylor (1972). They showed that the evaporation over a wet surface approaches an equilibrium that is a function of the temperature of the atmosphere. They, however, did

not discuss in detail the underlying physical mechanisms. The pioneers in studying the convective boundary layer and the land surface as an interactive system and to include the effects of entrainment, were De Bruin (1983) and McNaughton and Spriggs (1986). Their studies provided a solid proof that the daily cycle of evaporation is strongly connected to the convective boundary layer dynamics, although McNaughton and Spriggs (1986) emphasized that there is not necessarily a connection between a correctly resolved surface energy balance and correctly predicted CBL height. One of the first papers to quantify the importance of feedbacks between the land surface and the atmosphere that are related to evaporation were Jacobs and De Bruin (1992). They showed that the sensitivity of evaporation to wind speed and surface roughness is much less in coupled models than in offline evaporation models. This finding had an important implication as it emphasized the errors that can be made in studies on evaporation if the feedbacks with the boundary layer are not taken into account. Hereafter, a set of theoretical papers have been released (Brubaker and Entekhabi, 1995, 1996; Raupach, 2000, 2001; Margulis and Entekhabi, 2001; Ek and Holtslag, 2004), that provide mathematical frameworks of the integrated land-atmosphere system that extend on the work of Jacobs and De Bruin (1992), by providing methods to quantify some of the feedbacks between the land surface and the CBL. At the same time the concept of the coupling between the land surface and the atmospheric boundary-layer gained interest among the climate modeling community. One of their key findings was that especially for the monsoon influenced regions in the world, such as the Great Plains (USA), West-Africa and India, the precipitation is largely influenced by the local evaporation (Koster et al., 2004). Nevertheless, the exact physical mechanisms behind this coupling and the role of the CBL herein are only partially understood (Trenberth et al., 2007; Seneviratne et al., 2010). In this thesis, the aim is on extending the mathematical frameworks in such a way that they become easier applicable for interpreting measurement data and model results.

1.3.2 Modeling land-atmosphere interactions over heterogeneous terrain using LES

Modeling of heterogeneous terrain and land-atmosphere interactions in LES studies only recently gained interest among the LES modeling community as computers became strong enough to study longer simulations and larger domains. Land surface heterogeneity can be split in thermal heterogeneity, where the fluxes of heat and moisture vary in space, and in mechanical heterogeneity, where the roughness lengths vary in space. The first study investigating the impact of thermal land surface heterogeneity in LES was done by Hechtel et al. (1990). Avissar and Schmidt (1998) provided an extensive overview of the impact of heterogenous heating on the CBL. Although the conclusions of these studies confirmed the importance of heterogeneity, the computer power at that time did not allow for sufficient resolution to draw definitive conclusions. Later, many studies of heterogeneously heated and moistened convective boundary layers using higher resolution have been carried out (e.g. Albertson and Parlange, 1999; Letzel and Raasch, 2003; Huang and Margulis, 2009). An important, evaporation related finding that arose from these studies is the limited impact of heterogeneity on the horizontally averaged temperature and humidity profiles profiles in a cloud-free CBL. However, these studies did not take into account the impact of heterogeneity on cloud formation, nor the impact of an interactive land surface on their results. Studies into

heterogeneous roughness show that mechanical heterogeneity can increase the area-averaged mixing, but also that the treatment of heterogeneous roughness is not straightforward and that this requires advanced parameterizations for the smallest and modeled scales of the turbulence (e.g. Albertson and Parlange, 1999; Porté-Agel et al., 2000; Bou-Zeid et al., 2005, 2007).

The first LES study to include a land surface model was Patton et al. (2005), who studied the effect of idealized heterogeneous soil moisture on land-atmosphere interactions and turbulence in the CBL. Later on, the study to land surface interactions in LES was extended to more realistic land surfaces by Huang and Margulis (2009). What the studies of Patton et al. (2005) and Huang and Margulis (2009) have in common is that they introduce an existing land surface model into their LES model. Nevertheless, none of these studies has done a thorough evaluation on the validity of the assumptions behind the land surface models.

1.4 Outline of this thesis

To increase the conceptual understanding of the coupled land-atmosphere system and the role of entrainment, I make use of the coupled mixed-layer model, that accurately describes the most essential physics of the CBL, the land surface and the soil. This model, which has been developed throughout this PhD research, is described in Chapter 2. As the model is very fast, it allows for a quick exploration of a large parameter space. This helped me in making the first step: understanding the role of feedbacks that exist between the land surface, the CBL and the free atmosphere and the equilibria that are associated with these feedbacks. This work is presented in Chapter 4. As this research provided insight in these feedbacks, but did not provide a way to actually quantify them, the research has been extended by creating a method that allows for a quantification of all forcings and feedbacks that control the daily cycle of evapotranspiration (see Chapter 5). This method has been applied to interpret data from Cabauw, The Netherlands and Niamey, Niger. To show that the framework can help in interpreting data and model results, it has been applied to contribute to the discussion on the evaporation paradox in Chapter 6. In brief, this paradox is about the unexpected decreasing trends in measurements of pan evaporation in the second half of 20th century, where an accelerated hydrologic cycle was expected because of global warming.

To meet the second objective of this thesis, which is related to the understanding of land-atmosphere interactions over heterogeneous terrain, the Dutch Large-Eddy Simulation model (DALES) has been used (see Chapter 3 for a description). Before moving to land surface modeling in LES, I first explore in Chapter 7 a typical case of a convective boundary layer over a land surface with heterogeneous surface evaporation and temperature fluxes. To build upon previous studies, the focus is here on how heterogeneity modifies the turbulent transport from the land surface towards the top of the boundary layer and how this influences entrainment and potential cloud formation. Subsequently, the focus is shifted to the land surface again. I have coupled a land surface model to DALES and investigate in Chapter 8, whether the assumptions enclosed in the land surface model, which are particularly related to the vegetation heat capacity and the turbulent fields over the vegetation, are violated in LES and how sensitive the model results are to this violation.

In Chapter 9, the most important findings of this thesis are summarized and an outline is given on the implications of this thesis to future research on the topic.

2

Description of the coupled mixed-layer model

2.1 Introduction

This section contains the full description of the coupled model that has been used for the studies in Chapters 4, 5 and 6. The model has been developed throughout my PhD. In Figure 2.1 a conceptual overview of the model and its most relevant variables is presented. The full version contains a convective boundary-layer model, a surface model, a soil model and a simple radiation model, but the model containing all features has only been used in Chapter 6. The full description is written down here, and it is indicated in the text below how the models in the three studies differ from each other.

2.2 Convective boundary-layer model

The atmospheric model describes the dynamics of the convective boundary layer and therefore the model can only be used in convective conditions, where a mixed layer is present. The most basic part of the model, which originates from the work of Lilly (1968) and Tennekes (1973), describes the time evolution of the bulk temperature, and humidity of the mixed-layer, the jump between the mixed-layer and free atmosphere values and the height of the boundary layer. This forms the following set of five prognostic equations.

The boundary layer growth is described by:

$$w_e = A_{\theta_v} \frac{\frac{H}{\rho c_p} + \theta \left(\frac{R_v}{R_d} - 1 \right) \frac{LE}{\rho L_v}}{\Delta \theta_v} \tag{2.1}$$

$$\frac{dh}{dt} = w_e + w_s \tag{2.2}$$

with w_e as the entrainment velocity, A_{θ_v} as the ratio between the entrainment virtual heat flux

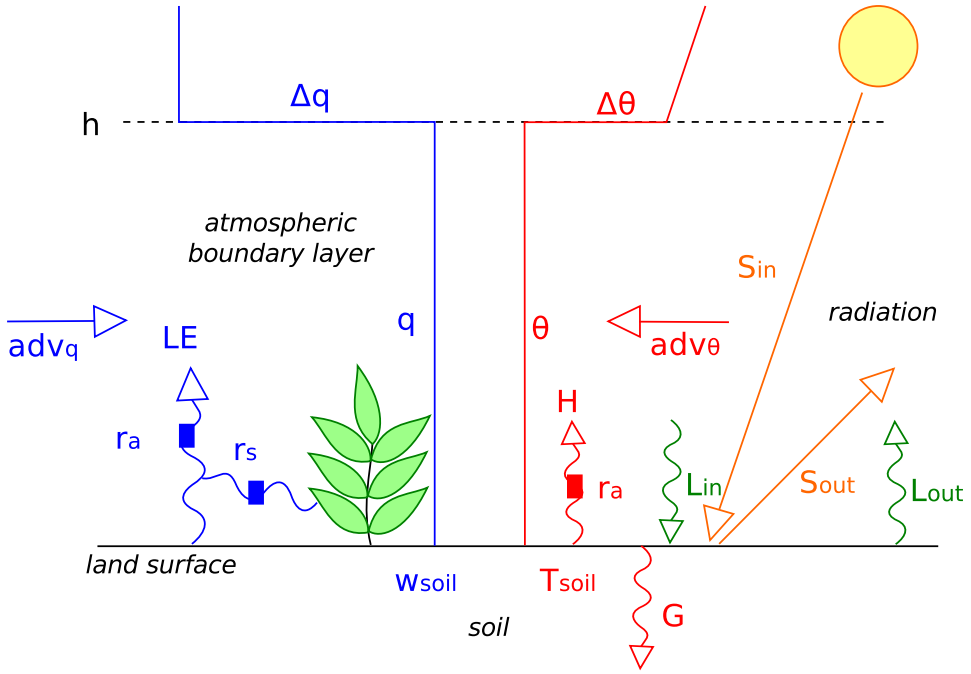

Figure 2.1: The four components of the coupled mixed-layer model and their most relevant variables.

and the surface virtual heat flux, ρ as the density of air, c_p as the heat capacity of air at constant pressure, R_v as the gas constant of moist air, R_d as the gas constant of dry air and w_s as the large-scale vertical motion. H is the sensible heat flux, LE is the latent heat flux and L_v is the latent heat of vaporization.

The evolution of the temperature related variables is described by:

$$\frac{d\theta}{dt} = \frac{1}{h}\left(\frac{H}{\rho c_p} + w_e \Delta\theta\right) + adv_\theta \tag{2.3}$$

$$\frac{d\Delta\theta}{dt} = \gamma_\theta w_e - \frac{d\theta}{dt} \tag{2.4}$$

where θ is the potential temperature of the mixed layer, $\Delta\theta$ the jump between the mixed layer and the free atmosphere, γ_θ the lapse rate of potential temperature and adv_θ the large-scale advection of potential temperature.

The same two equations for moisture are:

$$\frac{dq}{dt} = \frac{1}{h}\left(\frac{LE}{\rho L_v} + w_e \Delta q\right) + adv_q \tag{2.5}$$

$$\frac{d\Delta q}{dt} = \gamma_q w_e - \frac{dq}{dt} \tag{2.6}$$

with q as the specific humidity of the mixed layer and Δq as the jump between the mixed layer and the free atmosphere, γ_q as the lapse rate of specific humidity and adv_q as the large-scale advection of specific humidity.

This simple, but accurate model forms the atmospheric part of the model used in Chapter 4. Similar expressions can be used for the two horizontal components of the wind speed. These equations also contain the Coriolis force that takes into account the rotation of the earth and a large scale pressure gradient, where the pressure gradient is converted to geostrophic

wind using the geostrophic equilibrium. This yields another four similar equations:

$$\frac{du}{dt} = \frac{1}{h}\left(\overline{u'w'} + w_e\Delta u\right) - f_c\Delta v + adv_u \tag{2.7}$$

$$\frac{dv}{dt} = \frac{1}{h}\left(\overline{v'w'} + w_e\Delta v\right) + f_c\Delta u + adv_v \tag{2.8}$$

$$\frac{d\Delta u}{dt} = \gamma_u w_e - \frac{du}{dt} \tag{2.9}$$

$$\frac{d\Delta v}{dt} = \gamma_v w_e - \frac{dv}{dt} \tag{2.10}$$

where u and v are the zonal and meridional wind speeds, Δu and Δv are the jumps of these two variables, γ_u and γ_v are the lapse rates and f_c is the Coriolis parameter. The free atmospheric wind velocities are assumed to be equal to the geostrophic wind at their height. Note that in Chapter 5 we treat the wind as the total wind, rather than two individual components.

2.3 Surface model

2.3.1 The surface energy balance

The basis of the surface model is the surface energy balance that relates the net radiation Q_* to the surface heat fluxes:

$$Q_* - G = H + LE \tag{2.11}$$

where G is the ground heat flux, H is the sensible heat flux and LE is the latent heat flux.

The sensible and latent heat flux, which together form the available energy to the atmosphere, can be parameterized as:

$$H = \frac{\rho c_p}{r_a}\left(\theta_s - \theta\right) \tag{2.12}$$

$$LE = \frac{\rho L_v}{r_a + r_s}\left(q_{sat}\left(T_s\right) - q\right) \tag{2.13}$$

where r_a is the aerodynamic resistance, r_s is the surface resistance, θ_s and θ are the potential temperatures of the surface and the mixed-layer respectively, $q_{sat}\left(T_s\right)$ is the saturated specific humidity inside the canopy and q is the mixed-layer specific humidity.

Both equations 2.12 and 2.13 contain surface temperature. The combination of these two expressions with the surface energy balance (equation 2.11) allows for the elimination of the surface temperature, when the $q_{sat}(T)$ term is linearized. This yields the well-known Penman-Monteith equation (Monteith, 1965):

$$LE = \frac{\frac{dq_{sat}}{dT}\left(R_n - G\right) + \frac{\rho c_p}{r_a}\left(q_{sat}\left(T\right) - q\right)}{\frac{dq_{sat}}{dT} + \frac{c_p}{L_v}\left(1 + \frac{r_s}{r_a}\right)}, \tag{2.14}$$

where $\frac{dq_{sat}}{dT}$, which is the slope of the saturated specific humidity curve with respect to temperature, and q_{sat} are evaluated using the atmospheric mixed-layer temperature at the top of the atmospheric surface layer defined as $z_{sl} = 0.1\,h$.

The set of equations until here is the model that is used in Chapter 4, where simple approximations are made for the term $Q_* - G$. The remainder of this chapter describes the full surface and radiation model used in Chapters 5 and 6.

2.3.2 Resistances

Aerodynamic resistance

The aerodynamic resistance that appears in equations 2.12 and 2.13 is inversely related to the efficiency of the atmosphere to exchange momentum and heat with the surface, which is the intensity of the turbulence.

The expression that defines r_a is:

$$r_a = \frac{1}{C_H U} \tag{2.15}$$

where C_H is the drag coefficient for heat and U is the mixed-layer wind speed. Here, the dependency with the turbulence can be seen—more wind results in more turbulence. Also the drag coefficient contains information about the turbulence, as the drag coefficient increases with surface layer instability to take into account the enhanced mixing caused by convection. The drag coefficient is calculated following:

$$C_H = \frac{\kappa^2}{\left[\ln\left(\frac{z_{sl}}{z_{0m}}\right) - \Psi_M\left(\frac{z_{sl}}{L}\right) + \Psi_M\left(\frac{z_{0m}}{L}\right)\right]\left[\ln\left(\frac{z_{sl}}{z_{0h}}\right) - \Psi_H\left(\frac{z_{sl}}{L}\right) + \Psi_H\left(\frac{z_{0h}}{L}\right)\right]} \tag{2.16}$$

where κ is the von Kármán constant, z_{0m} and z_{0h} are the roughness lengths for momentum and heat, z_{sl} is the depth of the atmospheric surface layer of 0.1 h, L is the Monin-Obukhov length and Ψ_M and Ψ_H are the integrated stability functions for momentum and heat taken from Beljaars (1991). To find the values of L that are required in this function, we solve the following implicit function using a Newton-Raphson iteration method:

$$Ri_B = \frac{g}{\theta_v}\frac{z_{sl}\left(\theta_v - \theta_{vs}\right)}{U^2} = \frac{z_{sl}}{L}\frac{\left[\ln\left(\frac{z_{sl}}{z_{0h}}\right) - \Psi_H\left(\frac{z_{sl}}{L}\right) + \Psi_H\left(\frac{z_{0h}}{L}\right)\right]}{\left[\ln\left(\frac{z_{sl}}{z_{0m}}\right) - \Psi_M\left(\frac{z_{sl}}{L}\right) + \Psi_M\left(\frac{z_{0m}}{L}\right)\right]^2} \tag{2.17}$$

where Ri_B is the bulk Richardson number and θ_{vs} and θ_v are the virtual potential temperatures of the surface and the mixed-layer atmosphere respectively.

Surface resistances

The model used in Chapters 5 and 6 takes into account both evaporation and transpiration. Both components are calculated using equation 2.13, but each with their own resistance. Both resistances r_{veg} and r_{soil} are modeled following the method of Jarvis (1976) and employed similarly as in the ECMWF IFS. The vegetation resistance is based on the following equation that takes into account four correction functions of which the first three originate from the ECMWF IFS documentation and the fourth from Noilhan and Planton (1989).

$$r_{veg} = \frac{r_{s,min}}{LAI} f_1\left(S_{in}\right) f_2\left(w_{soil2}\right) f_3\left(VPD\right) f_4\left(T\right) \tag{2.18}$$

with $r_{s,min}$ as the minimum surface resistance, LAI as the leaf area index of the vegetated fraction, f_1 as a correction function depending on incoming short wave radiation S_{in}, f_2 as a function depending on soil moisture w, f_3 as a function depending on vapor pressure deficit (VPD) and f_4 as a function depending on temperature T. These functions are defined as:

$$\frac{1}{f_1(S_{in})} = \min\left(1, \frac{0.004S_{in} + 0.05}{0.81\,(0.004S_{in} + 1)}\right) \tag{2.19}$$

$$\frac{1}{f_2(w)} = \frac{w - w_{wilt}}{w_{fc} - w_{wilt}} \tag{2.20}$$

$$\frac{1}{f_3(VPD)} = \exp\left(g_D VPD\right) \tag{2.21}$$

$$\frac{1}{f_4(T)} = 1.0 - 0.0016(298.0 - T)^2, \tag{2.22}$$

where w_{wilt} is the volumetric soil moisture at wilting point, w_{fc} is the volumetric soil moisture at field capacity and g_D is a correction factor for vapor pressure deficit that only plays a role in high vegetation.

The soil resistance does not contain LAI and is only dependent on the amount of soil moisture in the layer that has direct contact with the atmosphere.

$$r_{soil} = r_{s,min}\ f_2\left(w_{soil1}\right), \tag{2.23}$$

where f_2 is calculated following equation 2.20.

2.3.3 Three component evapotranspiration calculation

The total evapotranspiration consists of three separate components. There is the transpiration from vegetation, soil evaporation and direct evaporation from liquid water, either from interception or dew water. The latter can only take place from the vegetated part of the land surface and is therefore a fraction of the vegetated part of the land surface. The total evaporation is:

$$LE_{tot} = c_{veg}(1 - c_{liq})LE_{veg} + c_{veg}c_{liq}LE_{liq} + (1 - c_{veg})LE_{soil}, \tag{2.24}$$

where LE_{tot} is the evapotranspiration, LE_{veg} the transpiration from vegetation, LE_{soil} the evaporation from the soil and LE_{liq} evaporation of liquid water. The fractions that are used are c_{veg} which is the fraction of the total area that is covered by vegetation and c_{liq}, which is the fraction of the vegetated are that contains liquid water. Since c_{liq} is not constant in time, it is modeled following:

$$c_{liq} = \frac{W_l}{LAI\ W_{max}} \tag{2.25}$$

where W_{max} is the representative depth of a water layer that can lay on one leaf and W_l the actual water depth. The time evolution of W_l is governed by the following equation:

$$\frac{dW_l}{dt} = \frac{LE_{liq}}{\rho_w L_v} \tag{2.26}$$

where ρ_w is the density of water.

2.4 Force-restore soil model

The soil model attached to the other model components is a force-restore soil model that is based on the model formulation of Noilhan and Planton (1989). The soil temperature formulation has been replaced by that of Duynkerke (1991), because this formulation yields more accurate ground heat fluxes for vegetated land surfaces.

The soil is modeled using two layers: a thin upper layer that has a daily cycle and a deeper layer that is constant during one day. For the soil temperature in the thin layer this gives the following equation, where the first term is the force term and the second the restore term:

$$\frac{dT_{soil1}}{dt} = C_T G - \frac{2\pi}{\tau}(T_{soil1} - T_{soil2}), \tag{2.27}$$

where C_T is the surface soil/vegetation heat capacity, G the soil heat flux already introduced in the SEB and τ the time constant of one day. The soil heat flux is calculated using

$$G = \Lambda\,(T_s - T_{soil1}) \tag{2.28}$$

where Λ is the thermal conductivity of the skin layer. The heat capacity C_T is calculated following Clapp and Hornberger (1978) using:

$$C_T = C_{T,sat}\left(\frac{w_{sat}}{w_2}\right)^{b/2log10} \tag{2.29}$$

where $C_{T,sat}$ is the soil heat capacity at saturation and b an empirical constant that originates from data fitting.

We similarly solve the evolution of the volumetric water content W, using:

$$\frac{dw_1}{dt} = -\frac{C_1}{\rho_w d_1}\frac{LE_{soil}}{L_v} - \frac{C_2}{\tau}\left(w_2 - w_{2,eq}\right) \tag{2.30}$$

where w_1 and w_2 are the volumetric water content of the first two layers, C_1 and C_2 are two coefficients related to the Clapp and Hornberger parameterization (Clapp and Hornberger, 1978), that are calculated using:

$$C_1 = C_{1,sat}\left(\frac{w_{sat}}{w_2}\right)^{b/2+1} \tag{2.31}$$

$$C_2 = C_{2,ref}\frac{w_2}{w_{sat} - w_2} \tag{2.32}$$

where $C_{1,sat}$ and $C_{2,ref}$ are constants taken from Clapp and Hornberger (1978). The water content in equilibrium $w_{g,eq}$ is:

$$w_{g,eq} = w_2 - w_{sat}a\left(\frac{w_2}{w_{sat}}\right)^p\left(1 - \frac{w_2}{w_{sat}}\right)^{8p} \tag{2.33}$$

with a and p as two more fitted constants from Clapp and Hornberger (1978).

2.5 Radiation model

The surface energy balance as described in Equation 2.11 makes use of the net radiation Q_*. This variable is defined as the sum of the four radiation components:

$$Q_* = S_{in} - S_{out} + L_{in} - L_{out} \tag{2.34}$$

where S_{in} and S_{out} are the incoming and outgoing components of the short wave radation, and L_{in} and L_{out} the incoming and outgoing component of the long wave radiation.

The incoming short wave radiation S_{in} is calculated by:

$$S_{in} \;=\; S_o \; T_r \; sin\,(\Psi) \tag{2.35}$$

where S_o is the constant solar irradiance at the top of the atmosphere, taken at 1368 W m^{-2}, T_r the net sky transmissivity, that takes into account the influence of radiative path length and atmospheric absorption and scattering using:

$$T_r = 0.6 + 0.2sin\,(\Psi) \tag{2.36}$$

Through Ψ, both expressions depend on geographical location, day of the year and time of the day. Ψ is calculated using:

$$sin(\Psi) = sin(\phi)sin(\delta_s) - cos(\phi)cos(\delta_s)cos\left(2\pi\frac{t_{UTC}}{t_d} + \lambda_e\right) \tag{2.37}$$

where t_{UTC} is the universal time (UTC) and t_d is the diurnal period of 24 hours. The latitude ϕ (positive north of Equator) and longitude λ_e (positive east of Greenwich) define the geographic location. Variable δ_s is the solar declination, which is a function of the day number:

$$\delta_s = \Phi_r cos\left(2\pi\frac{d - d_r}{d_y}\right) \tag{2.38}$$

where Φ_r is the tilt of the earth's axis relative to the elliptic, equal to 0.409 rad. The Julian day is represented by d and d_r is 173. The number of days in a year d_y is taken as 365.

The outgoing shortwave radiation depends on the surface albedo:

$$S_{out} = \alpha S_{in} \tag{2.39}$$

where α is the surface albedo.

The outgoing long wave radiation is calculated using the the Stefan-Boltzmann Law:

$$L_{out} = \epsilon_s \sigma_{SB} T_s^4 \tag{2.40}$$

where ϵ_s is the surface emissivity taken equal to 1. σ_{SB} is the Stefan-Boltzmann constant equal to 5.67.10^{-8} W m^{-2} K^{-4}.

The incoming long wave radiation is computed using the same expression, but here the temperature at the top of the surface layer T_{sl} is used. This temperature is acquired by converting the potential temperature of the mixed-layer θ to absolute temperature using the

height of surface layer top, which we define as 10 % of the boundary-layer height h. This gives expression:

$$L_{in} = \epsilon_a \sigma_{SB} T_{sl}^4 \tag{2.41}$$

where the atmospheric emissivity ϵ_a is 0.8.

3 Description of DALES

3.1 Introduction

DALES is rooted in the LES code of Nieuwstadt and Brost (1986). Cuijpers and Duynkerke (1993) first used DALES for moist convection, and provided a general description of an older version of DALES. Large parts of the code have been changed ever since and contributions of many people over a number of years have resulted in the current version 3.2 of DALES. Currently, DALES is maintained by researchers from Delft University, the Royal Netherlands Meteorological Institute (KNMI), Wageningen University and the Max Planck Institute for Meteorology.

This chapter only describes the parts of DALES that are used for this thesis. Therefore, it contains sections of Heus et al. (2010) and it includes an extended description of the land surface model.

3.2 Prognostic variables

The prognostic variables of DALES are the three velocity components u_i ($i = 1, 2, 3$), the liquid water potential temperature θ_l, the total water specific humidity q_t, the rain water specific humidity q_r, the rain droplet number concentration N_r, and up to 100 passive or reactive scalars. The subfilter-scale turbulence kinetic energy (SFS-TKE, e) is an additional prognostic variable, and is being used in the parameterization of the sub-filter scale dynamics. To decrease simulation time, only calculations of u_i, e, and θ_l are compulsory; all the additional scalars need not to be calculated when these variables are not used.

Given that ice is not currently implemented in the model, the total water specific humidity is defined as the sum of the water vapor specific humidity q_v and the cloud liquid water

This chapter is a modified version of Heus et al. (2010) of which the author of this thesis is the second author.

specific humidity q_c:

$$q_t = q_v + q_c. \tag{3.1}$$

Note that this definition of q_t does not include the rain water specific humidity q_r. Any conversion between rain water on one hand, and cloud water or water vapor on the other hand, will therefore enter the equations for q_t and for θ_l as an addition source term. We use the close approximation explained by Emanuel (1994):

$$\theta_l \approx \theta - \frac{L}{c_{pd}\Pi} q_c, \tag{3.2}$$

with θ being the potential temperature (related to the absolute temperature T following $T = \theta\Pi$), L=2.5×10^6 J kg^{-1} the latent heat of vaporization, c_{pd}=1004 J kg^{-1} K^{-1} the heat capacity of dry air, and Π being the Exner function:

$$\Pi = \left(\frac{p}{p_0}\right)^{\frac{R_d}{c_{pd}}}, \tag{3.3}$$

in which R_d=287.0 J kg^{-1} K^{-1} is the gas constant for dry air and p_0=10^5 Pa is a reference pressure.

In the absence of precipitation and other explicit sources, θ_l and q_t are conserved variables. The liquid water virtual potential temperature θ_v is in good approximation defined as (Emanuel, 1994):

$$\theta_v \approx \left(\theta_l + \frac{L}{c_{pd}\Pi} q_c\right)\left(1 - \left(1 - \frac{R_v}{R_d}\right) q_t - \frac{R_v}{R_d} q_c\right), \tag{3.4}$$

with R_v=461.5 J kg^{-1} K^{-1} being the gas constant for water vapor. The most important thermodynamical constants that are used throughout this paper are summarized in Table 3.1.

Table 3.1: The main thermodynamical constants used throughout this paper.

R_v	Gas constant for water vapor	461.5 J kg^{-1} K^{-1}
R_d	Gas constant for dry air	287.0 J kg^{-1} K^{-1}
L	Latent heat release for vaporization	2.5×10^6 J kg^{-1}
c_{pd}	Heat capacity for dry air	1004 J kg^{-1} K^{-1}

DALES is discretized on an Arakawa C-grid (see Fig. 3.1). The pressure, the SFS-TKE, and the scalars are defined at grid cell center, the three velocity components are defined at the West side, the South side, and the bottom side of the grid cell, respectively.

Hereafter, quantities that are averaged over the LES filter width are denoted with a tilde $\widetilde{\cdot}$, time averages with a overbar $\overline{\cdot}$, and averages over the two horizontal directions of the domain with angular brackets $\langle\cdot\rangle$ (slab average). The prognosed scalars can often be treated in an identical manner as the generic scalar field $\varphi \in \{\theta_l, q_t, q_r, N_r, s_n\}$. Primes denote the subfilter-scale fluctuations with respect to the filtered value. Double primes indicate local deviations from the horizontal slab average. To remain consistent with notational conventions used in literature and also in the source code of DALES, some symbols can have different meaning

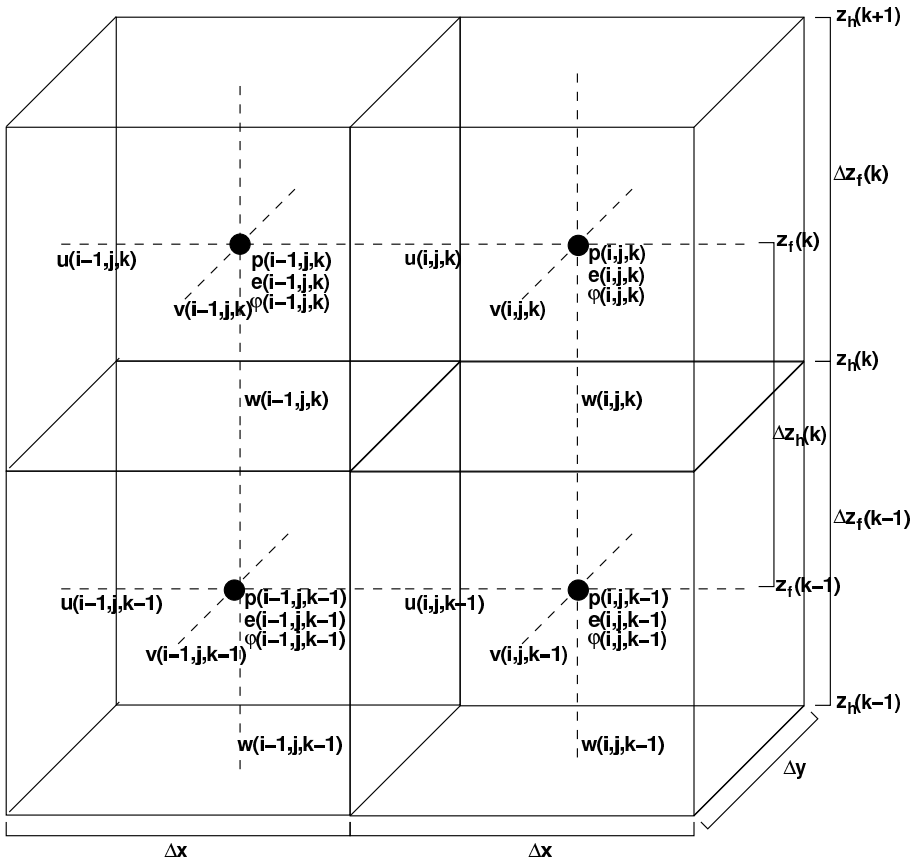

Figure 3.1: The Arakawa C-grid as used in DALES. Pressure, SFS-TKE and the scalars are defined at cell-center, the 3 velocity components at the face of the cell. The level of cell center is called the full level (denoted with an "f"); the level where w is located is called the half level (an "h"). The (variable) vertical grid spacing Δz is defined centered around the belonging level. The grid spacing in the horizontal directions (Δx and Δy) are constant over the entire domain.

between different subsections. In such cases, the immediate context should always make it clear what each symbol stands for in a particular section. Vertical velocities and fluxes are in general positive when directed upward; only the radiative and sedimentation fluxes are positive when pointing downward, following conventions.

In the following sections, different components of the code are described one by one. Sections 3.3–3.8 describe the physical and numerical components that are necessary to conduct an experiment with DALES.

3.3 The governing equations

DALES assumes the Boussinesq approximation, with the reference state θ_0, ρ_0, p_0 equal to the surface values of liquid water potential temperature, density and pressure, respectively. For an extended treatment see for example Wyngaard (2004).

Within the Boussinesq approximation the equations of motion, after application of the LES

filter, are given by

$$\frac{\partial \widetilde{u_i}}{\partial x_i} = 0, \tag{3.5}$$

$$\frac{\partial \widetilde{u_i}}{\partial t} = -\frac{\partial \widetilde{u_i}\widetilde{u_j}}{\partial x_j} - \frac{\partial \pi}{\partial x_i} + \frac{g}{\theta_0}\widetilde{\theta_v}\delta_{i3} + \mathcal{F}_i - \frac{\partial \tau_{ij}}{\partial x_j}, \tag{3.6}$$

$$\frac{\partial \widetilde{\varphi}}{\partial t} = -\frac{\partial \widetilde{u_j}\widetilde{\varphi}}{\partial x_j} - \frac{\partial R_{u_j,\varphi}}{\partial x_j} + \mathcal{S}_\varphi, \tag{3.7}$$

where the tildes denote the filtered mean variables. Molecular transport terms have been neglected. The z-direction (x_3) is taken to be normal to the surface, $\pi = \frac{\widetilde{p}}{\rho_0} + \frac{2}{3}e$ is the modified pressure, δ_{ij} the Kronecker delta, and $\mathcal{F}_i$ represents other forcings, including large scale forcings and the Coriolis acceleration

$$\mathcal{F}_i^{\text{cor}} = -2\epsilon_{ijk}\Omega_j\widetilde{u_k}, \tag{3.8}$$

where Ω is the Earth's angular velocity. Source terms for scalar φ are denoted by $\mathcal{S}_\varphi$, and may include of microphysical ($\mathcal{S}^{\text{mcr}}$), radiative ($\mathcal{S}^{\text{rad}}$), chemical ($\mathcal{S}^{\text{chem}}$), large-scale ($\mathcal{S}^{\text{ls}}$), and relaxation ($\mathcal{S}^{\text{rel}}$) terms. The subfilter-scale (SFS), or residual, scalar fluxes are denoted by $R_{u_j,\varphi} \equiv \widetilde{u_j\varphi} - \widetilde{u_j}\widetilde{\varphi}$, i.e., the contribution to the resolved motion from all scales below the LES filter width. The deviatoric part of the subgrid momentum flux is:

$$\tau_{ij} \equiv \widetilde{u_i u_j} - \widetilde{u_i}\widetilde{u_j} - \frac{2}{3}e, \tag{3.9}$$

A schematic overview of how the different processes affect the different variables is given in Fig. 3.2.

3.4 Subfilter-scale model

In DALES, the SFS fluxes are modeled through an eddy diffusivity as:

$$R_{u_j,\varphi} = -K_h\frac{\partial \widetilde{\varphi}}{\partial x_j}, \tag{3.10}$$

and

$$\tau_{ij} = -K_m\left(\frac{\partial \widetilde{u_i}}{\partial x_j} + \frac{\partial \widetilde{u_j}}{\partial x_i}\right), \tag{3.11}$$

where $e = \frac{1}{2}(\widetilde{u_i u_i} - \widetilde{u_i}\widetilde{u_i})$ is the subfilter-scale turbulence kinetic energy (SFS-TKE) and K_m and K_h are the eddy viscosity/diffusivity coefficients. In DALES, these eddy diffusivity coefficients are modeled as a function of the SFS-TKE e (Deardorff, 1973).

Following Deardorff (1980), the prognostic equation for e is adopted in the form:

$$\frac{\partial e}{\partial t} = -\frac{\partial \widetilde{u_j}e}{\partial x_j} - \tau_{ij}\frac{\partial \widetilde{u_i}}{\partial x_j} + \frac{g}{\theta_0}R_{w,\theta_v} - \frac{\partial R_{u_j,e}}{\partial x_j} - \frac{1}{\rho_0}\frac{\partial R_{u_j,\pi}}{\partial x_j} - \varepsilon, \tag{3.12}$$

with ε the SFS-TKE dissipation rate. The first right-hand-side term is solved, and the second

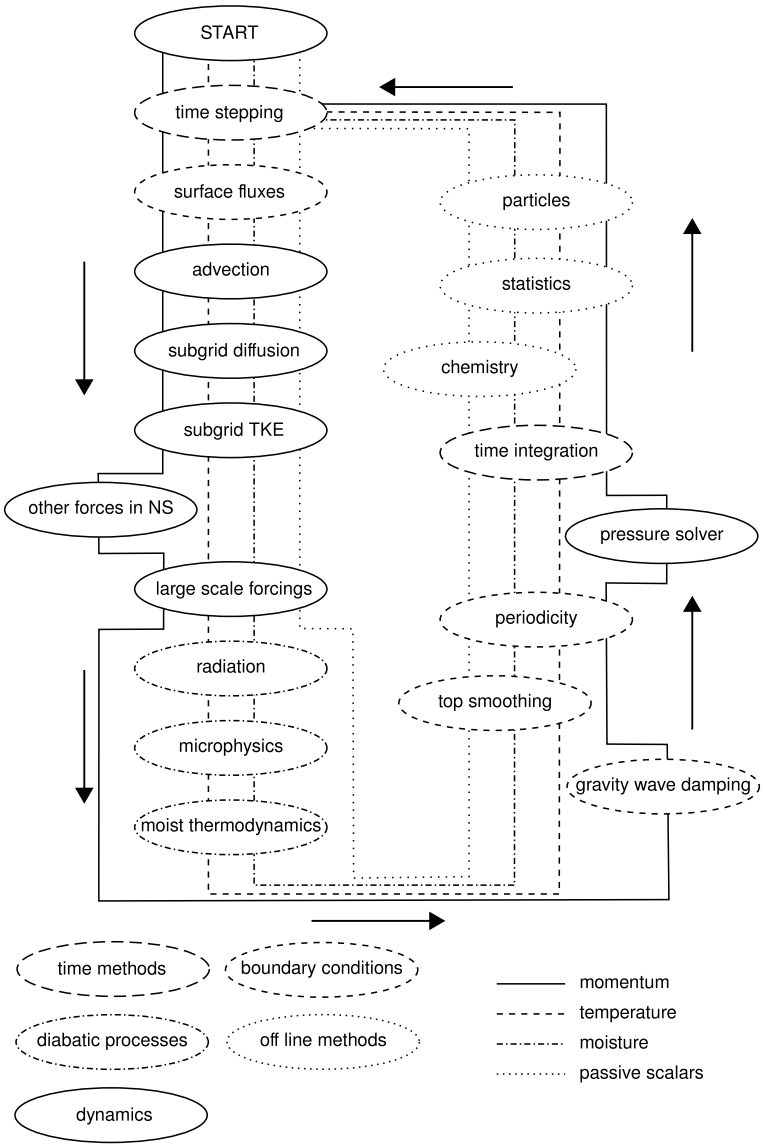

Figure 3.2: Flowchart of DALES.

term (the production of SFS-TKE by shear) can be calculated with Eq. (3.11). The other right-hand-side terms need to be parameterized to close the equation. Following Deardorff (1980), we express the third term, the SFS-TKE production due to buoyancy, as:

$$\frac{g}{\theta_0} R_{w,\theta_\mathrm{v}} = \frac{g}{\theta_0} \left(A\, R_{w,\theta_\mathrm{l}} + B R_{w,q_\mathrm{t}} \right), \tag{3.13}$$

with coefficients A and B in case of a dry boundary layer:

$$\left.\begin{aligned} A &= A_\mathrm{d} = 1 + \tfrac{R_\mathrm{v}}{R_\mathrm{d}} \widetilde{q_\mathrm{t}} \\ B &= B_\mathrm{d} = \left(\tfrac{R_\mathrm{v}}{R_\mathrm{d}} - 1 \right) \theta_0 \end{aligned}\right\} \text{ if } q_\mathrm{c} = 0, \tag{3.14}$$

The fourth and fifth term in Eq. (3.12) are together parameterized as

$$-\frac{\partial}{\partial x_j} \left(R_{u_j,e} + \frac{1}{\rho_0} R_{u_j,p} \right) = \frac{\partial}{\partial x_j} \left(2 K_\mathrm{m} \frac{\partial e}{\partial x_j} \right). \tag{3.15}$$

Table 3.2: An overview of the parameters used in the SFS scheme of DALES. Not all parameters are independent.

α	c_f	$c_{\varepsilon,1}$	$c_{\varepsilon,2}$	c_m	$c_{\mathrm{h},1}$	$c_{\mathrm{h},2}$	c_N
1.5	2.5	0.19	0.51	0.12	1	2	0.76

To model the dissipation rate ε, we again follow Deardorff (1980):

$$K_\mathrm{m} = c_\mathrm{m} \lambda e^{1/2}, \tag{3.16}$$

$$\text{with } c_m = \frac{c_\mathrm{f}}{2\pi}\left(\frac{3}{2}\alpha\right)^{-3/2}, \tag{3.17}$$

with $\alpha = 1.5$ the Kolmogorov constant and $c_\mathrm{f}\lambda$ the filter width.

The eddy diffusivity for heat and scalars is modeled similarly as K_h=$c_\mathrm{h}\lambda e^{1/2}$, and for the dissipation ε we write:

$$\varepsilon = \frac{c_\varepsilon}{\lambda} e^{3/2}. \tag{3.18}$$

Still following Deardorff (1980), the SFS parameters are depending on the stability of the flow:

$$\lambda = \min\left(\Delta, c_N \frac{e^{1/2}}{N}\right), \tag{3.19}$$

$$c_\mathrm{h} = \left(c_{\mathrm{h},1} + c_{\mathrm{h},2}\frac{\lambda}{\Delta}\right) c_\mathrm{m}, \tag{3.20}$$

$$c_\varepsilon = c_{\varepsilon,1} + c_{\varepsilon,2}\frac{\lambda}{\Delta}, \tag{3.21}$$

with N=$\left[\frac{g}{\theta_0}\frac{\partial\widetilde{\theta_\mathrm{v}}}{\partial z}\right]^2$ denoting the Brunt-Väisälä frequency, and c_N=0.76. Now all parameters of the subfilter-scale parameterization of DALES are defined and are summarized in Table 3.2.

Substituting the closure relations and parameters into Eq. (3.12) gives the following prognostic equation for $e^{1/2}$, which is implemented in DALES:

$$\begin{aligned}\frac{\partial e^{1/2}}{\partial t} &= -\widetilde{u_j}\frac{\partial e^{1/2}}{\partial x_j} + \frac{1}{2e^{1/2}}\left[K_\mathrm{m}\left(\frac{\partial\widetilde{u_j}}{\partial x_i} + \frac{\partial\widetilde{u_i}}{\partial x_j}\right)\frac{\partial\widetilde{u_i}}{\partial x_j} - K_\mathrm{h}\frac{g}{\theta_0}\frac{\partial(A\widetilde{\theta_\mathrm{l}} + B\widetilde{q_\mathrm{t}})}{\partial z}\right] \\ &\quad + \frac{\partial}{\partial x_j}\left(2K_\mathrm{m}\frac{\partial e^{1/2}}{\partial x_j}\right) - \frac{c_\varepsilon e}{2\lambda},\end{aligned} \tag{3.22}$$

which closes the system.

3.5 Boundary conditions: the surface model

3.5.1 Theory

DALES requires a model to parameterize the turbulent drag and the exchange of scalars between the surface and the atmosphere, because it has a no-slip boundary at the bottom,

but does not resolve the flow up to the surface-roughness scale. The surface fluxes enter the domain at subfilter-scale, since by definition the resolved fluctuations in the vertical velocity at the surface are equal to zero. In the remainder of this section we define an arbitrary surface flux of variable ϕ as $F_{s,\phi} = \widetilde{w\phi} - \widetilde{w}\widetilde{\phi}$.

We followed the common way of parameterizing turbulent fluxes in atmospheric models by applying the transfer laws of Louis (1979). In DALES we assume that the first model level is in the atmospheric surface layer. We apply Monin-Obukhov similarity theory for the computation of the spatially averaged fluxes $\left\langle F_{s,\phi} \right\rangle$ and gradients at the bottom boundary of the model.

The procedure for determining the bottom boundary conditions starts with the evaluation of the Obukhov length. This value is approximated using a Newton-Raphson method for solving the implicit equation that relates the bulk Richardson number to the Obukhov length (see Eq. (3.23)).

$$Ri_B = \frac{z_1}{L} \frac{\left[\ln\left(\frac{z_1}{z_{0h}}\right) - \Psi_{\mathrm{H}}\left(\frac{z_1}{L}\right) + \Psi_{\mathrm{H}}\left(\frac{z_{0h}}{L}\right)\right]}{\left[\ln\left(\frac{z_1}{z_{0m}}\right) - \Psi_{\mathrm{M}}\left(\frac{z_1}{L}\right) + \Psi_{\mathrm{M}}\left(\frac{z_{0m}}{L}\right)\right]^2}, \tag{3.23}$$

with

$$Ri_B = \frac{g}{\theta_0} \frac{z_1 \left(\left\langle \widetilde{\theta_{v1}} \right\rangle - \left\langle \widetilde{\theta_{v0}} \right\rangle\right)}{\langle U_1 \rangle^2}, \tag{3.24}$$

and

$$L = -\frac{u_{*0}^3}{\kappa \frac{g}{\langle \theta_{v0} \rangle} \left\langle F_{s,\theta_v} \right\rangle}, \tag{3.25}$$

where Ri_B is the averaged bulk Richardson number of the layer between the surface and the first full level z_1, L is the Obukhov length, z_{0m} and z_{0h} are the roughness lengths for momentum and heat, Ψ_H and Ψ_M are the integrated stability functions as provided by Beljaars (1991), $\left\langle \widetilde{\theta_{v0}} \right\rangle$ is the spatially averaged filtered surface virtual potential temperature, $\left\langle \widetilde{\theta_{v1}} \right\rangle$ is the spatially averaged filtered virtual potential temperature at the first model level, $\langle U_1 \rangle$ is the magnitude of the horizontal wind vector at the first model level, defined as $\langle U_1 \rangle = \sqrt{\langle \widetilde{u_1} \rangle^2 + \langle \widetilde{v_1} \rangle^2}$, κ is the Von Karman constant and $\left\langle \widetilde{w'\theta'_{v0}} \right\rangle$ is the horizontally averaged surface virtual temperature flux.

Subsequently, the calculated Obukhov length is used in the computation of the slab averaged friction velocity u_{*0} and scalar scales $\varphi_{*0} = -\frac{\langle F_{s,\phi} \rangle}{u_{*0}}$, based on the scaling arguments of Businger et al. (1971); Yaglom (1977).

Now, we can calculate the drag coefficients C_{M} and C_φ:

$$C_{\mathrm{M}} = \frac{u_{*0}^2}{\langle U_1 \rangle^2}, \tag{3.26}$$

$$C_\varphi = \frac{u_{*0}\varphi_{*0}}{\langle U_1 \rangle \langle \widetilde{\varphi_1} - \varphi_0 \rangle}. \tag{3.27}$$

Although all locations in the horizontal use the same drag coefficient, we calculate local fluxes and gradients that average to the values computed in our evaluation of the Obukhov length. The subfilter-scale momentum fluxes are calculated by decomposing u_{*0}^2 along the two

components of the horizontal wind vector (Eq. 3.28,3.29), whereas Eq. (3.30) gives the scalar flux. This results in

$$F_{s,u} = -C_{\mathrm{M}} \langle U_1 \rangle \widetilde{u_1}, \tag{3.28}$$

$$F_{s,v} = -C_{\mathrm{M}} \langle U_1 \rangle \widetilde{v_1}, \tag{3.29}$$

$$F_{s,\varphi} = -C_{\varphi} \langle U_1 \rangle (\widetilde{\varphi_1} - \varphi_0). \tag{3.30}$$

For land surfaces where moisture is not freely available, such as a vegetated land surface or a bare soil, an additional step has to be made before the similarity relation as in Eq. (3.30) can be applied to the specific humidity. Here, we define the aerodynamic resistance r_{a} as $\left(C_{\varphi} \langle U_1 \rangle\right)^{-1}$ and introduce the surface resistance r_{s} that takes into account the limited water supply at the land surface. The value for r_s is either prescribed or calculated using the Jarvis-Stewart model, similar as in the coupled mixed-layer model (see Eq. (2.18-2.22)). A correct surface value can be computed:

$$\langle q_0 \rangle = \frac{r_{\mathrm{a}}}{r_{\mathrm{a}} + r_{\mathrm{s}}} \langle q_s(T_0) \rangle + \frac{r_{\mathrm{s}}}{r_{\mathrm{a}} + r_{\mathrm{s}}} \langle \widetilde{q_1} \rangle. \tag{3.31}$$

Note that the drag coefficients and resistances are based on slab averaged values, to assure that the spatially averaged fluxes and gradients are consistent with Monin-Obukhov similarity theory. In DALES there is also the option available to work with locally computed values. We are aware that this method overpredicts gradients at the first model level (Bou-Zeid et al., 2005). We, however, use this method for exploratory experiments over heterogeneous land surfaces, because here a universal surface model formulation is still lacking (Bou-Zeid et al., 2005).

3.5.2 Overview of surface boundary options in DALES

DALES has four options to provide the surface momentum and scalar fluxes and surface scalar values to the model, with different degrees of complexity.

1. *Parameterized surface scalar and momentum fluxes, parameterized surfaces values*. Here, a Land Surface Model (LSM, see Sect. 3.5.3) calculates the surface temperature and the stomatal resistance which enters in the evaporation equation based on the vegetation type that is assigned to the grid cell. The variables u_{*0}, L and φ_{*0} are determined iteratively to get the drag coefficients. This is the method that represents a fully interactive land surface. Combined with the radiation model, this options allows for the simulation of full diurnal cycles, in which both the surface fluxes and the surface temperature are free variables.

2. *Parameterized surface scalar and momentum fluxes, prescribed scalar values at the surface*. In this option u_{*0}, L and φ_{*0} are solved iteratively to get the drag coefficients. The surface momentum and scalar fluxes are computed using the prescribed scalar values at the surface and the acquired drag coefficients. This option is commonly used as the surface boundary condition for simulations of marine boundary-layers. It is also applied in the simulation of stable boundary layers. For simulations over land, a fixed surface resistance r_{s} can be prescribed.

3. *Prescribed surface scalar fluxes, prescribed* u_{*0}. In this option no iterations are necessary and the scalar surface values φ_0 are calculated diagnostically. This is an option that is used in idealized simulations in which the surface drag is preferred to be controlled, thereby neglecting that u_{*0} is an internal parameter of the flow.

4. *Prescribed surface scalar fluxes, parameterized* u_{*0}. Here u_{*0} and L are calculated iteratively, whereas φ_* is diagnostically calculated as a function of the prescribed scalar fluxes and the calculated u_{*0}. This is the most commonly used option for simulation of daytime convection over land.

Prescribed fluxes or surface values may depend on time; linear interpolation is then performed between the given "anchor" points.

In addition to the previous description which assumed homogeneous surfaces, DALES is also able to simulate heterogeneously forced ABLs. Under such conditions, only the prescribed scalar fluxes boundary conditions are available. Scalar fluxes are defined per grid cell, whereas the momentum flux is dynamically computed. Under these conditions, local values of u_{*0}, L and φ_{*0} are used.

3.5.3 Land surface model

DALES has the option to use a land surface model (LSM). The LSM has two components, namely a solver for the surface energy balance and a four layer soil scheme which calculates the soil temperature profile for each grid cell. The following surface energy balance equation is solved:

$$\begin{aligned} C_{\mathrm{sk}}\frac{dT_0}{dt} &= Q_* - \rho c_p F_{s,\theta_l} - \rho L_{\mathrm{v}} F_{s,q_t} - G, \\ &= Q_* + \frac{\rho c_p}{r_a}\left(\widetilde{\theta_1} - \theta_0\right) + \frac{\rho L_{\mathrm{v}}}{r_a + r_s}\left(\widetilde{q_1} - q_{sat}\left(T_0\right)\right) - \Lambda\left(T_0 - T_{\mathrm{soil1}}\right) \end{aligned} \tag{3.32}$$

in which C_{sk} is the heat capacity per unit of area of the skin layer (see Duynkerke, 1999), T_0 is the surface temperature, θ_0 is the surface potential temperature, Q_* is the net radiation and G is the ground heat flux. G is calculated following the method of Duynkerke (1999), where Λ is a bulk conductivity for the stagnant air in the skin layer depending on the type of surface, and T_{soil1} is the temperature of the top soil layer. In cases where the heat capacity of the surface is chosen to be zero, an implicit equation is acquired in which the surface temperature can be solved by iteration using a Newton-Raphson method or directly by linearizing the $q_{sat}\left(T_0\right)$ term in time.

The soil consists of four layers in which the heat transport is modeled using a simple diffusion equation in which both the conductivity and the heat capacity are functions of the properties of the soil material and of the soil moisture content:

$$\left(\rho C\right)_{soil}\frac{\partial T_{soil}}{\partial t} = \frac{\partial}{\partial z}\left(\lambda_T \frac{\partial T_{soil}}{\partial z}\right), \tag{3.33}$$

in which $\left(\rho C\right)_{soil}$ is the volumetric heat capacity of the soil and λ_T the soil heat conductivity.

At the top, the soil model uses a flux boundary condition, where the ground heat flux

G defines the amount of energy that enters the soil. At the bottom boundary, the deep soil temperature is fixed. The conductivity λ_T is a function of the water content of the soil and can be acquired by:

$$\lambda_T = K_e \left(\lambda_{T,sat} - \lambda_{T,dry}\right) + \lambda_{T,dry} \tag{3.34}$$

where $\lambda_{T,sat}$ and $\lambda_{T,dry}$ are the soil conductivities in fully saturated and dry soil. Both $\lambda_{T,sat}$ and K_e, the Kersten number, are a function of the actual volumetric water content W and the saturated volumetric water content W_{sat} of the soil:

$$K_e = log_{10}\left[max\left(0.1, \frac{W}{W_{sat}}\right)\right] + 1 \tag{3.35}$$

$$\lambda_{T,sat} = \lambda_{T,sm}^{1-W_{sat}} \lambda_{T,w}^{W_{sat}} \tag{3.36}$$

where $\lambda_{T,sm}$ and $\lambda_{T,w}$ are the conductivities of respectivily the soil matrix and water.

The volumetric water content W is modeled based on a similar concept as the soil temperature using Richards' equation:

$$\frac{\partial W}{\partial t} = \frac{\partial}{\partial z}\left(\lambda_W \frac{\partial W}{\partial z} - \gamma_W\right) + S_W, \tag{3.37}$$

where λ_W is the soil diffusivity, γ_W the hydraulic conductivity and S_W the sink that is related to evaporation. The first two variables are modeled following Clapp and Hornberger (1978):

$$\gamma_W = \gamma_{W,sat}\left(\frac{W}{W_{sat}}\right)^{2b+3} \tag{3.38}$$

$$\lambda_W = \frac{b\gamma_{W,sat}\left(-\psi_{sat}\right)}{W_{sat}}\left(\frac{W}{W_{sat}}\right)^{b+2}. \tag{3.39}$$

$$\tag{3.40}$$

where b is a non-dimensional exponent depending on the soil type, $\gamma_{W,sat}$ and ψ_{sat} are the values of the hydraulic conductivity and matrix potential at saturation. Both λ_W and γ_W cannot decrease below their values at wilting point.

3.6 Boundary conditions: the sides and top

In comparison with the boundary conditions at the bottom boundary, the boundary conditions at the top and the sides of the domain are relatively straightforward. In the horizontal directions, periodic boundary conditions are applied for all fields. At the top of the domain, we take:

$$\frac{\partial \widetilde{u}}{\partial z} = \frac{\partial \widetilde{v}}{\partial z} = 0; \widetilde{w} = 0; \frac{\partial \widetilde{\varphi}}{\partial z} = \text{ constant in time.} \tag{3.41}$$

Fluctuations of velocity and scalars at the top of the domain (for instance due to gravity waves) are damped out by a sponge layer through additional forcing/source terms (added to

the right-hand-side of the transport equations):

$$\mathcal{F}_i^{\mathrm{sp}}(z) = \frac{1}{t^{\mathrm{sp}}}\left(\langle\widetilde{u_i}\rangle - \widetilde{u_i}\right), \tag{3.42}$$

$$\mathcal{S}_\varphi^{\mathrm{sp}}(z) = \frac{1}{t^{\mathrm{sp}}}\left(\langle\varphi\rangle - \widetilde{\varphi}\right), \tag{3.43}$$

with t^{sp} a relaxation time scale that goes from t_0^{sp}=1/(2.75×10^{-3}) s≈6 min at the top of the domain to infinity at the bottom of the sponge layer, which is by default a quarter of the number of levels, with a minimum of 15 levels.

3.7 Pressure solver

To solve for the modified pressure π, the divergence $\frac{\partial}{\partial x_i}$ of Eq. 3.6 is taken. Subsequently, the continuity equation (Eq. 3.5) is applied (both divergence and continuity equation are applied in their discrete form). As a result, the left hand side of the equation is equal to zero. Rearranging the terms leads to a Poisson equation for the modified pressure:

$$\frac{\partial^2\pi}{\partial x_i^2} = \frac{\partial}{\partial x_i}\left(-\frac{\partial\widetilde{u_i}\widetilde{u_j}}{\partial x_j} + \frac{g}{\theta_0}\widetilde{\theta_{\mathrm{v}}}\delta_{i3} + \mathcal{F}_i - \frac{\partial\tau_{ij}}{\partial x_j}\right). \tag{3.44}$$

Since computations are performed in a domain that is periodic in both horizontal directions, the Poisson equation is solved by applying a Fast Fourier Transform in the lateral directions followed by solving a tri-diagonal linear system in the z-direction using Gaussian elimination. In the latter, the pressure gradients at the upper and lower boundary are set to zero. An inverse Fast Fourier Transform in both lateral directions is applied to the result of the Gaussian elimination to obtain the modified pressure.

3.8 Numerical scheme

A Cartesian grid is used, with optional grid stretching in the z-direction. For clarity, an equidistant grid is assumed in the discussion of the advection scheme. The grid is staggered in space as an Arakawa C-grid; the pressure, the SFS-TKE and the scalars are defined at $\vec{x}+\frac{1}{2}(\Delta x, \Delta y, \Delta z)$, the $\widetilde{u}$ is defined at $\vec{x}+\frac{1}{2}(0, \Delta y, \Delta z)$, and similar for $\widetilde{v}$ and $\widetilde{w}$. The level of cell center is called the full level (denoted with an "f"); the level where w is located is called the half level (an "h"). The (variable) vertical grid spacing Δz is defined centered around the belonging level (see Fig. 3.1). The grid spacing in the horizontal directions (Δx and Δy) is constant over the entire domain.

To be able to use multiple computational processes, thus decreasing the wall clock time of experiments, DALES 3.2 has been parallelized by dividing the domain in separate stripes in the y-direction. Tests show that this method is computationally efficient as long as the amount of processes is smaller than a quarter of the number of grid points in the y-direction.

Time integration is performed by a third order Runge-Kutta scheme following Wicker and Skamarock (2002). With $f(\phi^n)$ the right-hand side of the appropriate equation of Eqs. (3.6)–(3.7)

for variable ϕ=$\{\widetilde{u}, \widetilde{v}, \widetilde{w}, e^{1/2}, \widetilde{\varphi}\}$, ϕ^{n+1} at t+Δt is calculated in three steps:

$$\begin{aligned} \phi^{*} &= \phi^{n} + \frac{\Delta t}{3} f(\phi^{n}), \\ \phi^{**} &= \phi^{n} + \frac{\Delta t}{2} f(\phi^{*}), \\ \phi^{n+1} &= \phi^{n} + \Delta t f(\phi^{**}), \end{aligned} \tag{3.45}$$

with the asterisks denoting intermediate time steps. The size of the time step Δt is determined adaptively, and is limited by both the Courant-Friedrichs-Lewy criterion (CFL)

$$\text{CFL} = \max\left(\left|\frac{\widetilde{u}_i \Delta t}{\Delta x_i}\right|\right), \tag{3.46}$$

and the diffusion number d (see Wesseling, 1996).

$$d = \max\left(\sum_{i=1}^{3} \frac{K_{\text{m}} \Delta t}{\Delta x_i^2}\right). \tag{3.47}$$

The numerical stability and accuracy depends on the spatial scheme that is used. Furthermore, additional terms, such as chemical or microphysical source, may require more stringent time stepping. Therefore, the limiting CFL and d numbers can be manually adjusted to further optimize the timestep. By default CFL and d are set well below the stability levels known from the literature of the respective combinations of spatial and temporal integration scheme (see Wicker and Skamarock, 2002).

Depending on the desired properties (like high accuracy or monotonicity), several advection schemes are available. With advection in the x-direction discretized as

$$\frac{\partial \widetilde{u}_i \phi_i}{\partial x} = \frac{F_{i+\frac{1}{2}} - F_{i-\frac{1}{2}}}{\Delta x}, \tag{3.48}$$

with $F_{i-\frac{1}{2}}$ the convective flux of variable ϕ through the $i-\frac{1}{2}$ plane; the $i-\frac{1}{2}$ plane is the plane through the location of velocity $\widetilde{u}_i(i)$, perpendicular on the direction of velocity $\widetilde{u}_i(i)$. Since we are using a staggered grid, the velocity is available at $i-\frac{1}{2}$ without interpolation (see Fig. 3.1). Second order central differencing can be used for variables where neither very high accuracy nor strict monotonicity is necessary:

$$F^{\text{2nd}}_{i-\frac{1}{2}} = \widetilde{u}_{i-\frac{1}{2}} \frac{\phi_i + \phi_{i-1}}{2}, \tag{3.49}$$

and similar for $F^{\text{2nd}}_{i-\frac{1}{2}}$. A higher-order accuracy in the calculation of the advection is reached with a sixth-order central differencing scheme (see Wicker and Skamarock, 2002):

$$F^{\text{6th}}_{i-\frac{1}{2}} = \frac{\widetilde{u}_{i-\frac{1}{2}}}{60}\left[37(\phi_i + \phi_{i-1}) - 8(\phi_{i+1} + \phi_{i-2}) + (\phi_{i+2} + \phi_{i-3})\right]. \tag{3.50}$$

Starting with this sixth-order scheme, a nearly monotonous fifth-order scheme can be con-

structed by adding a dissipative term to $F^{6\text{th}}_{i-\frac{1}{2}}$,

$$F^{5\text{th}}_{i-\frac{1}{2}} = F^{6\text{th}}_{i-\frac{1}{2}} - \left|\frac{\widetilde{u}_{i-\frac{1}{2}}}{60}\right| \Big[10(\phi_i - \phi_{i-1}) - 5(\phi_{i+1} - \phi_{i-2}) + (\phi_{i+2} - \phi_{i-3})\Big]. \tag{3.51}$$

For advection of scalars that need to be strictly monotonous (for example chemically reacting species) the κ scheme (Hundsdorfer et al., 1995) has been implemented:

$$F^{\kappa}_{i-\frac{1}{2}} = \widetilde{u}_{i-\frac{1}{2}} \left[\phi_{i-1} + \frac{1}{2}\kappa_{i-\frac{1}{2}} \left(\phi_{i-1} - \phi_{i-2}\right)\right], \tag{3.52}$$

in case $\widetilde{u}>0$. Following Hundsdorfer et al. (1995), $\kappa_{i-1/2}$ serves as a switch between third-order upwind advection in case of small upwind gradients of ϕ, and a first-order upwind scheme in case of stronger gradients. This makes the scheme monotonous, but also more dissipative, effectively taking over the role of the SFS-scheme in regions of strong gradients.

3.9 Other forcings and sources

Large-scale forcings and sources, such as the mean geostrophic wind $\vec{u_g}$, the large-scale subsidence w_s, and the horizontal advective scalar transport can be added and may depend on height and time.

4

Interactions between dry-air entrainment, surface evaporation and convective boundary layer development

The influence of dry-air entrainment on surface heat fluxes and the convective boundary layer (CBL) properties is studied for vegetated land surfaces, using a mixed-layer CBL model coupled to the Penman-Monteith equation under a wide range of conditions. In order to address the complex behaviour of the system, the feedback mechanisms involved were put into a mathematical framework. Simple expressions for the evaporative fraction and the Priestley-Taylor parameter were derived, based on the concept of equilibrium evaporation. Dry-air entrainment enhances the surface evaporation under all conditions, but the sensitivity of the evaporation rate to the moisture content of the free troposphere falls as temperature rises. Due to the evaporation enhancement, shallower CBLs develop beneath dry atmospheres. In all cases, dry-air entrainment reduces the relative humidity at the land surface and the top of the CBL. However, because of dry-air entrainment induced land-atmosphere feedback mechanisms, relative humidity at the top of the CBL responds nonlinearly to temperature rise; it decreases as temperature rises beneath a moist free troposphere, whereas it increases beneath a dry free troposphere. Finally, it was found that in certain conditions the evolution of the surface fluxes, relative humidity and CBL height can be as sensitive to the free tropospheric moisture conditions as to the land surface properties. Therefore, studies of the land surface and of convective clouds, have to take into account the influence of dry-air entrainment through land-atmosphere feedback mechanisms.

4.1 Introduction

The convective boundary layer (CBL) over land is closely coupled to the land surface and the free troposphere (e.g. De Bruin, 1983; Jacobs and De Bruin, 1992; Betts, 2004). Its evolution throughout the day largely depends on the partitioning of the available energy into latent

This chapter is published as van Heerwaarden et al. (2009).

and sensible heat fluxes at the land surface. The latent heat flux moistens the CBL, while the sensible heat flux provides the energy that induces CBL growth and the entrainment of free tropospheric air into the CBL. Due to the coupled nature of the land-atmosphere system, the CBL feeds back to the partitioning of the surface heat fluxes by modifying the atmospheric demand for water. In other words, the CBL regulates how intensely the atmosphere can extract water from the land surface.

In this system, in which the land surface, the CBL and the free troposphere interact, surface energy partitioning evolves towards a state that is known as equilibrium evaporation (Priestley and Taylor, 1972), when the evaporative fraction ($EF = LE/(H + LE)$, in which H is the sensible and LE the latent heat flux) reaches a steady state, because the atmospheric demand for water has become constant (Raupach, 1991, 2000). In this state the extra water capacity of the CBL that is induced by heating is exactly compensated for by an increase in the atmospheric moisture content. In the absense of large scale advection, two processes determine CBL moisture content: evaporation at the land surface and entrainment of dry-air at the interface of the CBL and the free troposphere.

In this paper we focus on the complex role of dry-air entrainment in the CBL evolution over vegetated land surfaces. The first effect of dry-air entrainment is simple, namely, a reduction in the specific humidity of the CBL. Subsequently, a set of feedback mechanisms is triggered, leading to complex interactions between the land surface and the atmosphere. The latent heat flux increases beneath a drier atmosphere, but this immediately implies a reduction of the sensible heat flux that results in reduced CBL growth and therefore less dry-air entrainment.

Due to these feedback mechanisms, it is not clear whether dry-air entrainment can systematically enhance the equilibrium evaporation. The first indirect indication that it might do so, originated from the work of Priestley and Taylor (1972). Their analysis of daily evaporation rates over wet surfaces showed that the EF was approximately 1.26 times the value of the equilibrium EF, but they based their equilibrium expression on a CBL of constant height, being unaware of the effects of entrainment. Priestley and Taylor (1972) therefore did not relate the increase of EF to dry-air entrainment. The first to link the two, were De Bruin (1983) and McNaughton and Spriggs (1986), who were able to reproduce the EF enhancement by including dry-air entrainment into a conceptual model that coupled the land surface to the CBL. Later, Culf (1994) and Betts (1994) derived an analytical expression for equilibrium evaporation including entrainment. By applying typical values for CBL properties in their expression, they showed that the increase in the EF by entrainment corresponds to the findings of Priestley and Taylor (1972). Also Eichinger et al. (1996) highlight the potential important role of entrainment. Although equilibrium evaporation over wet surfaces is enhanced by dry-air entrainment, none of the papers discussed whether any enhancement occurs over dry surfaces characterised by low soil moisture. Raupach (2000) has raised some doubts about the use of equilibrium evaporation in dry conditions, suggesting that under these conditions convergence to equilibrium evaporation cannot be achieved on a semi-diurnal time scale. This is because the characteristic time-scale of the system largely increases under dry conditions, due to the large surface resistance and deep CBLs.

In this study, we systematically investigate the influence of dry-air entrainment on the partitioning of the surface heat fluxes and their propagation into the properties of the CBL through the land surface feedbacks for a large and complete range of atmospheric and land

surface conditions. Our methodology is based on a coupled land-atmosphere model similar to that of McNaughton and Spriggs (1986), consisting of a slab model for the CBL (Tennekes, 1981) and the Penman-Monteith equation (Monteith, 1965) to solve the surface energy balance. This methodology has proven to be an adequate tool for dealing with the essential dynamics of a growing CBL coupled to the land surface (e.g. De Bruin, 1983; McNaughton and Spriggs, 1986; Raupach, 2000, 2001; Freedman et al., 2001).

The first aim of this paper is to quantify the role of dry-air entrainment on the partitioning of surface heat fluxes. First, we explain in Section 4.2 the physical feedback mechanisms in the CBL that direct the system towards equilibrium evaporation. We derive a new and simple expression of equilibrium evaporation based on the slab equations of the CBL and we validate this expression against the coupled model. In Section 4.3 we introduce the model and the experiments that we perform. Next, in Section 4.4.1, we perform an analysis on the sensitivity of the equilibrium EF to the moisture conditions in the free troposphere and evaluate the use of the concept of equilibrium evaporation for both wet and dry surfaces.

Our second aim is to study how strongly dry-air entrainment feeds back to the CBL structure. In order to demonstrate the feedback mechanisms involved, we first explore in Section 4.4.3 the semi-diurnal evolution of the CBL in a typical case for which we perturb the state of the free tropospheric moisture. Subsequently, in Section 4.4.4, we perform multiple series of numerical experiments to analyse the sensitivity of the surface fluxes, the CBL height and the relative humidity at the land surface and the CBL top to a range of free tropospheric conditions. We chose to analyse these variables on the basis of their importance for studies concerning air quality, the water balance and cloud formation. Finally, in Section 4.4.4 we simulate an ensemble of model runs for a range of free tropospheric moisture and land surface conditions in order to study the relevance of the free troposphere vis-à-vis the land surface conditions in the determination of EF and the CBL properties. By doing so, we show that the influence of the free tropospheric moisture on the partitioning of the surface heat fluxes and the CBL evolution has generally been underestimated by many modelling studies that regard land surface conditions and atmospheric stability as the dominant factors in the evolution of surface heat fluxes and the state of the CBL (e.g. De Bruin, 1983; Santanello et al., 2007; Trier et al., 2008).

4.2 Equilibrium evaporation beneath a growing CBL

4.2.1 Relevance of the concept

In this study we use the concept of equilibrium evaporation to improve our understanding of the effects of dry-air entrainment on evaporation. This concept allows us to relate the surface processes to all the processes that occur in the CBL and to understand their connected behaviour. We learned from previous studies (McNaughton and Spriggs, 1986; Culf, 1994; Betts, 1994; Raupach, 2000, 2001) that the CBL drives the surface fluxes towards a state in which the atmospheric demand for water becomes constant. If we wish to describe the partitioning of the surface fluxes in this state and whether it can be achieved, we need to understand and quantify the feedback mechanisms that drive the process of regulation.

4.2.2 Feedback mechanisms in the coupled land-atmosphere system

Here, we discuss the mechanisms that regulate the heat exchange between the land surface and the CBL. Since there is a set of negative feedback mechanisms that regulates evaporation, there is only one stable equilibrium for the evaporation rate. Figure 4.1 is a diagram of the negative feedback mechanisms and the relationships among the variables involved in them. In short, they are:

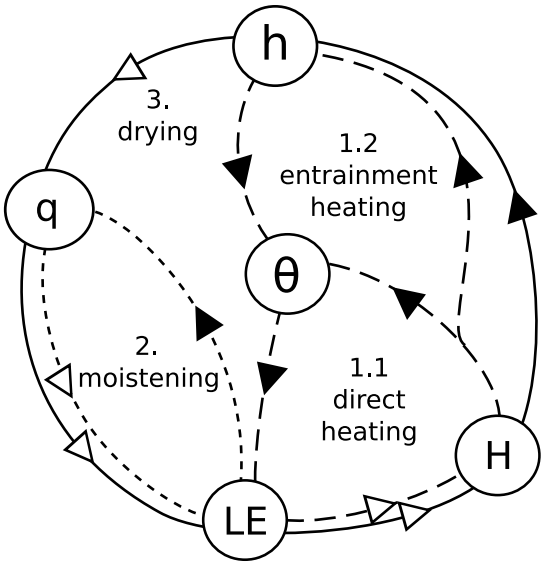

Figure 4.1: Feedbacks in the coupled land-atmosphere system. Closed arrows represent positive relationships, open arrows negative relationships. Each of the three feedbacks has a distinct line style. LE is the latent heat flux, H is the sensible heat flux, θ is the bulk potential temperature of the CBL, q is the bulk specific humidity of the CBL and h is the CBL height.

- Feedback 1 is the *heating* feedback (dashed line). This mechanism enhances evaporation when the atmosphere warms up. The excess available energy that is not used for evaporation (*LE*) is released as sensible heat *H*. This flux directly increases the CBL potential temperature θ (feedback 1.1) and through entrainment of heat at the top of the CBL h (feedback 1.2). In consequence, the atmospheric demand for water rises. *LE* is therefore enhanced, while *H* falls.

- Feedback 2 is the *moistening* feedback (dotted line). This mechanism reduces evaporation when the atmosphere becomes more humid. The diagram shows that evaporation *LE* leads to a higher specific humidity q. Consequently, the gradient of specific humidity between the land surface and the CBL decreases and *LE* is reduced.

- Feedback 3 is the *drying* feedback (solid line) that enhances evaporation when the CBL becomes drier. This feedback is similar to the heating feedback, driven by the sensible heat flux *H*, which triggers CBL growth (increasing h) through the entrainment process. As the CBL grows, dry free tropospheric air is entrained into the boundary layer and the specific humidity of the CBL q therefore decreases. This results in an increase of *LE* and a fall in *H*. Usually this feedback is negative as a decrease in *LE* is opposed, but in the rare event that the free tropospheric air contains more moisture than the CBL, the feedback can become positive.

Later in this study, we make extensive use of the diagram to explain the behaviour of the coupled land-atmosphere system under various conditions.

4.2.3 Feedbacks in a mathematical framework

In this section we put the concept of equilibrium evaporation into a mathematical framework that enables us to quantify the importance of entrainment. In equilibrium, the CBL's demand for water ($q_{sat} - q$) is constant and therefore air from the CBL that is adiabatically transported to the land surface must fulfill the following condition (Culf, 1994):

$$\left.\frac{dq_{sat}}{dT}\right|_T \frac{dT}{dt} - \frac{dq}{dt} = 0 \tag{4.1}$$

in which $\frac{dq_{sat}}{dT}$ is the slope of the saturated specific humidity evaluated at the air temperature, T is the air temperature and q is the specific humidity. McNaughton and Spriggs (1986) pointed out that this state is a quasi-equilibrium as it depends on temperature. However, the use of this equilibrium was validated by Raupach (2000), who showed that the rate of change of temperature with time is slow compared to the characteristic time scales of the feedbacks under wet to moderately dry conditions.

By assuming that the temperature T equals the potential temperature θ at the land surface, Raupach (2000) showed that the above relationship can be rewritten in a form that is valid at all heights within the CBL by deriving the so-called potential saturation deficit $q_{sat}(\theta) - q$ in time. This yields an equation containing only conserved variables:

$$\left.\frac{dq_{sat}}{dT}\right|_\theta \frac{d\theta}{dt} - \frac{dq}{dt} = 0 \tag{4.2}$$

in which $\frac{dq_{sat}}{dT}$ is the slope of the saturated specific humidity evaluated at the potential temperature and θ is the potential temperature. Hereafter, each instance of $\frac{dq_{sat}}{dT}$ is evaluated at θ.

In our study we limit ourselves to a cloudless CBL, which implies that we can substitute the temperature and moisture tendencies in the previous equation, by those proposed by the mixed-layer theory for the CBL (Tennekes, 1973, 1981) resulting in the following equation under equilibrium conditions:

$$\begin{aligned} \left.\frac{dq_{sat}}{dT}\right|_\theta \frac{1}{h}\left\{\overline{w'\theta'}_s + w_e\Delta\theta\right\} \\ -\frac{1}{h}\left\{\overline{w'q'}_s + w_e\Delta q\right\} \quad &= \quad 0 \end{aligned} \tag{4.3}$$

where $\overline{w'\theta'}_s$ and $\overline{w'q'}_s$ are the kinematic surface fluxes of potential temperature and specific humidity. Furthermore, h is the CBL height and $\Delta\theta$ and Δq are the jumps of potential temperature and specific humidity at the interface of the CBL and the free troposphere, defined as the free tropospheric value minus the CBL value. The entrainment velocity w_e is parametrised as:

$$w_e = A_{\theta_v}\frac{\overline{w'\theta'_{v_s}}}{\Delta\theta_v} \tag{4.4}$$

in which $\overline{w'\theta'_{vs}}$ is the virtual potential temperature flux at the land surface, A_{θ_v} is the ratio between the virtual potential temperature fluxes in the entrainment zone and at the land surface and $\Delta\theta_v$ is the jump of virtual potential temperature at the interface of the CBL and the free troposphere.

Rewriting the kinematic fluxes in terms of heat fluxes ($H = \rho c_p \overline{w'\theta'}_s$, $LE = \rho L_v \overline{w'q'}_s$) results in the following equation:

$$\overbrace{\frac{dq_{sat}}{dT}\frac{H}{\rho c_p h}}^{\text{heating}} + \overbrace{\frac{dq_{sat}}{dT}A_{\theta_v}\frac{\Delta\theta}{\Delta\theta_v}\left\{\frac{H}{\rho c_p h} + \theta\left(\frac{R_v}{R_d}-1\right)\frac{LE}{\rho L_v h}\right\}}^{\text{entrainment heating}} \tag{4.5}$$

$$-\overbrace{\frac{LE}{\rho L_v h}}^{\text{moistening}} - \overbrace{A_{\theta_v}\frac{\Delta q}{\Delta\theta_v}\left\{\frac{H}{\rho c_p h} + \theta\left(\frac{R_v}{R_d}-1\right)\frac{LE}{\rho L_v h}\right\}}^{\text{drying}} = 0$$

where H and LE are the surface sensible and latent heat flux, ρ the air density, c_p is the heat capacity of dry air, L_v the heat of vaporisation of water and R_v and R_d the gas constants of moist and dry air respectively.

In the equation we can identify the processes explained in Figure 4.1. The first term describes the direct heating of feedback 1.1, whereas heat entrainment (feedback 1.2) is expressed by term 2. Notice that the entrainment of heat is parametrised as a fixed fraction of the virtual heat flux at the surface, thus both H and LE enter in this term. The third term is the moistening of the CBL through evaporation (feedback 2) and the final term describes the effect of dry-air entrainment on q through feedback 3.

Since equation 4.5 describes a linear relation between H and LE, it can be rewritten in terms of the evaporative fraction. This yields an expression for EF in equilibrium evaporation in which all of the feedback mechanisms are contained:

$$EF_{eq} = \frac{LE}{H+LE} = \tag{4.6}$$

$$\frac{\frac{dq_{sat}}{dT} + \frac{dq_{sat}}{dT}A_{\theta_v}\frac{\Delta\theta}{\Delta\theta_v} - A_{\theta_v}\frac{\Delta q}{\Delta\theta_v}}{\frac{dq_{sat}}{dT} + \frac{dq_{sat}}{dT}c_0 A_{\theta_v}\frac{\Delta\theta}{\Delta\theta_v} - c_0 A_{\theta_v}\frac{\Delta q}{\Delta\theta_v} + \frac{c_p}{L_v}}$$

$$c_0 = \left(1 - \frac{c_p}{L_v}\theta_{ref}\left(\frac{R_v}{R_d}-1\right)\right) = 0.93. \tag{4.7}$$

As the daily variation of temperature is small compared to its absolute value, we use a reference value of 290 K for θ_{ref} in the equilibrium expression. We can thus simplify our equation by defining the constant c_0. In Section 4.4.4, we calculate the value of the equilibrium EF for a wide range of parameters and discuss the contribution of the feedbacks in detail.

In the introduction we mentioned that Culf (1994) also derived an expression for the equilibrium evaporation beneath a growing CBL. He followed a more general approach than we did, as the only assumption he made was parameterising the entrainment virtual heat flux as a fixed ratio of the surface flux. He derived his equilibrium expressions from the Bowen ratios at the land surface and the top of the CBL. However, by including the mixed-layer equations, our expression shows explicitly the contribution of each individual feedback to the

equilibrium. We are aware that our mixed-layer approach, in contrast to that of Culf (1994), is less accurate in situations in which the inversion in the free troposphere is very weak, because in these conditions entrainment is underestimated if the interface between the CBL and the free troposphere is considered as being sharp (Sullivan et al., 1998). Nevertheless, vanZanten et al. (1999) and Pino et al. (2006) showed that for a large range of conditions, our CBL model is accurate.

4.2.4 Physical expression of the Priestley-Taylor parameter

In the introduction we wrote that Priestley and Taylor (1972) were the first to find a systematic enhancement of the evaporative fraction compared to the equilibrium evaporative fraction over a non-growing CBL (EF_o). Priestley and Taylor (1972) included this enhancement in their widely used expression by including a parameter α. Its value was fitted according to their dataset of evaporation rates over wet surfaces:

$$EF_{PT} = \alpha EF_o = \alpha \frac{\frac{dq_{sat}}{dT}}{\frac{dq_{sat}}{dT} + \frac{c_p}{L_v}}. \tag{4.8}$$

Since we derived a physical expression for the EF beneath a growing CBL, the ratio of equations 4.6 and 4.8 is a physical expression for the Priestley-Taylor parameter α:

$$\alpha = \frac{EF_{eq}}{EF_o} = \frac{\frac{dq_{sat}}{dT} + \frac{dq_{sat}}{dT} A_{\theta_v} \frac{\Delta\theta}{\Delta\theta_v} - A_{\theta_v} \frac{\Delta q}{\Delta\theta_v}}{\frac{dq_{sat}}{dT} + \frac{dq_{sat}}{dT} c_0 A_{\theta_v} \frac{\Delta\theta}{\Delta\theta_v} - c_0 A_{\theta_v} \frac{\Delta q}{\Delta\theta_v} + \frac{c_p}{L_v}} \frac{\frac{dq_{sat}}{dT} + \frac{c_p}{L_v}}{\frac{dq_{sat}}{dT}}. \tag{4.9}$$

Note, that if we put A_{θ_v} to zero in equation 4.6, the equilibrium simplifies to the one used in equation 4.8 and α becomes equal to one. In Section 4.4.4 we evaluate the value of α alongside the derived expressions for the equilibrium EF, in order to illustrate that α is a variable rather than a fixed parameter of the system.

4.3 Coupled mixed-layer model

4.3.1 Model description

We use a conceptual model to validate our derived expressions for equilibrium evaporation (equation 4.6) and the Priestley-Taylor parameter (equation 4.9) and for exploring the effects of dry-air entrainment on the properties of the CBL. It consists of a mixed-layer model (Tennekes, 1981) that solves the CBL properties (CBL model hereafter) and the Penman-Monteith equation (Monteith, 1965) to solve the surface heat fluxes. As our model is essentially similar that of McNaughton and Spriggs (1986), we only briefly discuss the assumptions that are incorporated in these equations and deviations from their model. For a full description, see McNaughton and Spriggs (1986).

Before describing the model assumptions, we would like to stress that this model describes the evolution of evaporation and the convergence to equilibrium evaporation during a single day. The absence of night time processes and balancing radiative cooling requires that this model is initialized with early-morning temperature and moisture profiles each day it is run.

The surface model

At the surface we apply the Penman-Monteith equation to calculate the latent heat flux and the other terms of the surface energy balance. Our calculations incorporate the following assumptions:

- The net radiation Q_* is prescribed to the model and is the only source of energy. This implies that we do not take into account the radiative feedback of a warming surface. Raupach (2001) showed that this feedback needs to be taken into account when we explore the limits of the possible solutions, but in a coupled convective case, this feedback can be neglected.
- The ground heat flux G is assumed to be 10% of the net radiation Q_*, which has been validated over grass by De Bruin and Holtslag (1982).
- The aerodynamic resistance r_a in the Penman-Monteith equation is taken to be a constant with a value of 50 s^{-1} m, as this value is relatively constant for convective cases over grassland. In order to relate it to the mixed-layer model, the surface layer top is assumed to be at 10% of the CBL height. By fixing r_a we neglect surface layer feedbacks, but Jacobs and De Bruin (1992) showed that these do not change the qualitative behaviour of the system and are of minor importance compared to the feedbacks between the land surface and the CBL.
- The Penman-Monteith equation implicitly assumes that the land surface has no heat capacity. The surface temperature is therefore a result rather than a forcing of the surface heat fluxes.
- As net radiation is specified and the ground heat flux is parameterized, the latent, but also the sensible heat flux directly follows from the Penman-Monteith equation.
- The stomatal resistance r_s is constant during diurnal cycles in this study. We consider a land surface covered with grass for which the resistance is largely a function of soil moisture.

CBL model

In the model we parameterise the CBL by means of a mixed-layer model. In brief, this model consists of five prognostic equations resolving the CBL height and the mixed-layer value and the interface jump of the potential temperature θ and the specific humidity q. The mixed-layer model assumes the following:

- The CBL is considered to be well-mixed. This implies that both the potential temperature and specific humidity are in quasi-steady state and that their respective flux profiles are therefore linear.

- The interface between the CBL and the free troposphere is sharp. Therefore, the entrainment zone has an infinitesimal thickness.
- Full prognostic equations for the jumps of potential temperature and specific humidity at the CBL-free troposphere interface are solved. We do not assume the product of the CBL height and the jump of virtual potential temperature at the CBL-free troposphere interface to be constant, as McNaughton and Spriggs (1986) did.
- The ratio between the virtual potential temperature flux at the CBL-free troposphere interface and the flux at the land surface A_{θ_v} is fixed at 0.2, while the entrainment fluxes of other quantities are parameterised as functions of the entrainment velocity and the jump between the CBL and the free troposphere of the variable. Since the exact value of A_{θ_v} is uncertain (Conzemius and Fedorovich, 2006), we show the sensitivity of the results to the value of this variable in Section 4.4.4.

4.3.2 Numerical experiments

Here, we describe the different model experiments that we perform and their relationships to the research questions. Before discussing the specific experiments, we point out that our model consists of a large set of parameters and initial and boundary conditions. Since in most of the experiments these are identical, we summarise them in Appendix A. In this section we discuss only the specific characteristics of each experiment.

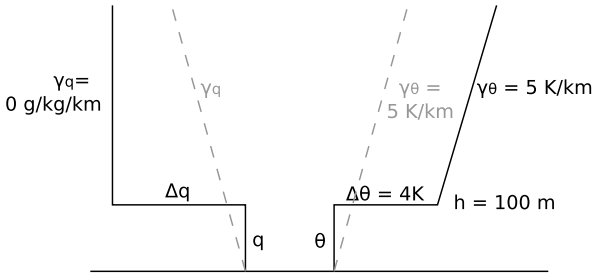

Figure 4.2: Sketch of initial profiles of specific humidity q and potential temperature θ for idealized cases (grey) and realistic cases (black). Variables θ, q, γ_q and Δq are subjected to a sensitivity analysis during the experiments.

In the first experiment, we evaluate our derived equilibrium EF (see equation 4.6) against the actual time varying EF as calculated in an idealized situation in order to determine if, and on which time scale, equilibrium can be achieved. This situation is initialized from an initial profile that consists only of a constant lapse rate (see Figure 4.2) and is forced with a constant net radiation Q_* of 400 W m^{-2}.

Table 4.1: Initial mixed-layer potential temperature θ_o and the lapse rate of specific humidity γ_q for the idealized cases.

run	θ_0 [K]	γ_q [g kg^{-1} km^{-1}]
const1	285	0
const2	285	-3
const3	285	-6

Table 4.1 shows the specifications of the three runs. The integration time is 120 h. We vary the lapse rate of specific humidity, which has a large influence on Δq, in order to perform a sensitivity analysis on the variables that determine the equilibrium EF (see equation 4.6).

From these idealized cases, we proceed to simulations characterized by a semi-diurnal sinusoidal evolution of the net radiation Q_* (from 6 to 18 LT, having a maximum of 400 W m^{-1} at 12 LT) and realistic initial profiles. These profiles are inspired by typical early summer conditions for Cabauw (The Netherlands) shown using the black lines in Figure 4.2. Although all our model runs are based on real data inspired values, we explicitly chose in this study not to do data analysis as this would have limited the possibilities for addressing the effects of dry-air entrainment in a very general way. In the second experiment (see Table 4.2) we

Table 4.2: Initial jump of specific humidity at the interface Δq_0, the stomatal resistance of the vegetation r_s and the atmospheric resistance r_a as used in the realistic experiments.

run	Δq_0 [g kg^{-1}]	r_s [s m^{-1}]	r_a [s m^{-1}]
wet1	0	0	50
wet2	-2.5	0	50
wet3	-5	0	50
dry1	0	100	50
dry2	-2.5	100	50
dry3	-5	100	50
wet1ra5	0	0	5
wet2ra5	-2.5	0	5
wet3ra5	-5	0	5

analyse the convergence of EF to equilibrium on a semi-diurnal time scale. Here, we perform our analyses on both wet (r_s = 0 s m^{-1}) and dry (r_s = 100 s m^{-1}) surfaces. The latter merits some attention as Raupach (2001) showed that over dry surfaces the semi-diurnal time scale is too short to achieve equilibrium. In these experiments we chose to fix the initial potential temperature at 285 K and to vary the initial Δq_0 and the surface resistance r_s. Notice that the first six runs have realistic values for the aerodynamic resistance r_a and that three additional runs with a very small value of 5 s m^{-1} for r_a are included, in order to enable us to discuss the relevance of r_a to the convergence of the EF to equilibrium.

Following our analysis of the equilibrium EF on a semi-diurnal time scale, we continue by illustrating the effect of land-atmosphere coupling for cases *dry*1, *dry*2 and *dry*3 from the previous experiment. In a comparison of the temporal evolution of the three cases, we explore the effect of dry-air entrainment on the surface heat fluxes, on the CBL height and the potential temperature and the specific humidity of the CBL.

Table 4.3: Initial mixed-layer potential temperature θ_0, initial jump of specific humidity at the interface Δq_0, stomatal resistance of the vegetation r_s and entrainment coefficient A_{θ_v} for series of runs performed.

series	Δq_0 [g kg^{-1}]	θ_0 [K]	r_s [s m^{-1}]	A_{θ_v}
seriesrs0	-4 - 0	275 - 295	0	0.2
seriesrs50	-4 - 0	275 - 295	50	0.2
seriesrs100	-4 - 0	275 - 295	100	0.2
seriesA_{θ_v}	-4 - 0	280	50	0.05 - 0.6
seriesT290	-4 - 0	290	0 - 400	0.2

In the final experiment, we perform an extensive sensitivity analysis that consists of series of model runs (see Table 4.3), in order to address the question under which atmospheric and land surface conditions dry-air entrainment is relevant to the surface fluxes and CBL development. In each series a sensitivity analysis is performed on two initial or boundary conditions. For each condition a range of 16 values is selected and the model is run for all combinations. All experiments start at 6 LT and last until 13 LT. The model results at 13 LT are stored and used for the analyses. First, we investigate the sensitivity of dry air entrainment to initial temperature over a well-watered soil (*seriesrs*50), a wet soil (*seriesrs*0) and a dry soil (*seriesrs*100) and complete this analysis by evaluating the sensitivity of the results to the value of the entrainment coefficient ($seriesA_{\theta_v}$). For the analysis, we create contour plots of the EF, CBL height and relative humidity at the land surface and the CBL top at 13 LT. Second, in *seriesT*290 we evaluated the importance of the free tropospheric moisture conditions against the land surface properties by varying the initial specific humidity jump (Δq) and the stomatal resistance (r_s).

4.4 Results

4.4.1 Idealised validation of derived equilibrium EF

In the first experiment, we look at whether our coupled land-atmosphere system converges to the previously defined equilibrium expression for the evaporative fraction (equation 4.6). The experiment consists of a set of model runs (see Table 4.1), the results of which are shown in Figure 4.3.

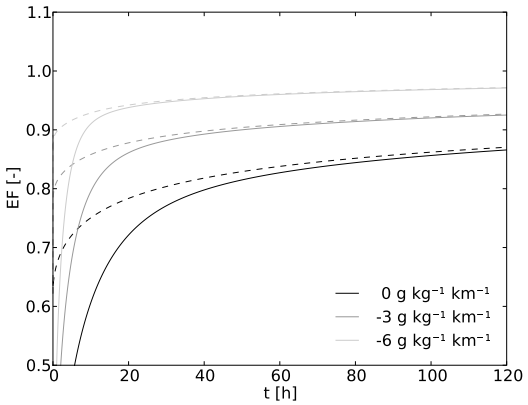

Figure 4.3: Evaporative fraction (solid line) and equilibrium EF (dashed line, calculated from model data using equation 4.6) as a function of time in cases const1, const2 and const3 (see Table 4.1).

The figure validates our derived equilibrium expression by showing that the three cases with constant forcings converge to equilibrium. If we define equilibrium as the state in which the EF is within 2% of the equilibrium EF then *const1* reaches equilibrium after 45 h at an EF of 0.81, *const2* after 19 h with EF = 0.86 and *const3*, which has the largest dry-air entrainment, after 10 h at an EF of 0.91. In addition to confirming the convergence of the system to equilibrium, the results also reveal information about the magnitude and the characteristic time scale of the convergence to equilibrium. Dry-air entrainment enhances the equilibrium EF, but at

the same time it tends to greatly decrease the characteristic time scale of the system, as was shown by Raupach (2000). The enhancement is explained by equation 4.6, as a larger negative value for Δq results in a larger value for the equilibrium EF, because dry air supports larger evaporation rates. The more rapid convergence to equilibrium can be attributed to an increase of the efficiency of the drying feedback (see Figure 4.1). When the free troposphere is dry, an increase in CBL height results in a larger reduction in q in the CBL by the entrainment of dry free tropospheric air, compared to conditions with a moist free troposphere. In Section 4.4.3 we discuss this feedback mechanism in more detail.

4.4.2 Validation of equilibrium EF on a semi-diurnal time scale

This experiment evaluates the applicability of equilibrium evaporation on a semi-diurnal time scale, as shown in Figure 4.4. The cases with a diurnal cycle of net radiation (left-hand panel)

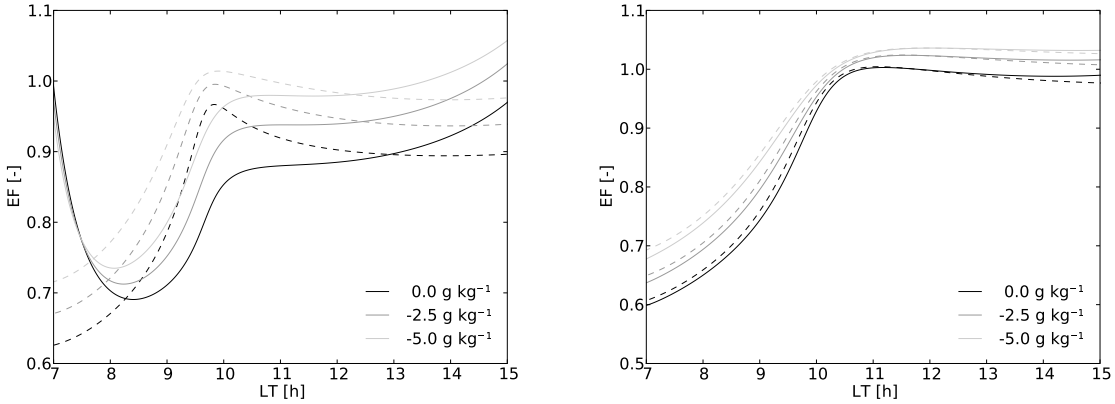

Figure 4.4: Evaporative fraction (solid) and equilibrium EF (dashed line, calculated using equation 4.6) as a function of time in cases wet1, wet2 and wet3 in the left panel. Time evolution of EF and equilibrium EF of wet1ra5, wet2ra5 and wet3ra5 in the right panel (see Table 4.2)

show that between 12 and 14 LT the EF approximates equilibrium evaporation. As in the idealised cases, entrainment enhances the EF throughout the whole day. At 13 LT the values of the EF of cases *wet1*, *wet2* and *wet3* are 0.89, 0.95 and 0.99 respectively, while the equilibria for the same cases are 0.89, 0.94 and 0.98. In contrast to the cases with constant surface forcings, the convergence to equilibrium is less evident.

Although the EF follows the equilibrium with a time lag close to one hour, there is never convergence, because the forcings change more rapidly than the adjustment time of the equilibrium EF. In other words, the characteristic time scale of the feedbacks is too long, because the atmospheric resistance r_a is fixed at 50 s m^{-1} under our conditions. If we set the resistance to a very low value (see right-hand panel of Figure 4.4) of 5 s m^{-1}, allowing the atmosphere to take up water very quickly, we drastically reduce the characteristic time scale of the feedbacks. Under these conditions convergence for this case is clearly visible from the figure, thereby proving that during the day the systems still tend to converge to equilibrium. In this special limiting case, the EF reaches values larger than 1. Despite the slightly negative sensible heat flux in such situations, the virtual potential flux is still positive due to the large moisture flux. Therefore, convection is maintained and our model is still valid.

In spite of the fact that under the conditions of our numerical experiments convergence is

not achieved during the day, the equilibrium EF is still an appropriate indicator of the effect of dry-air entrainment. The enhancement of the equilibrium EF from *wet*1 to *wet*3 corresponds well to the enhancement found in the actual EF for those cases. In Figure 4.5 we plotted the semi-diurnal evolution of EF for the cases with a dry soil (r_s = 100 s m^{-1}).

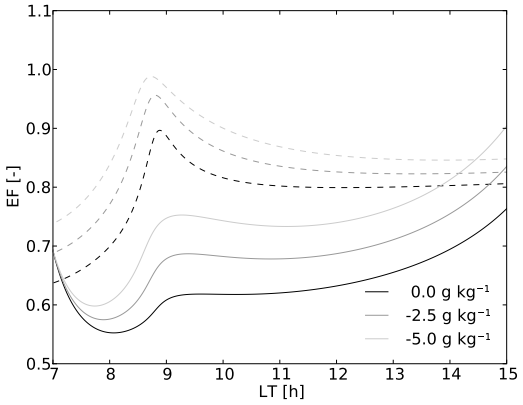

Figure 4.5: Evaporative fraction (solid line) and equilibrium EF (dashed line, calculated from model data using equation 4.6) as a function of time in cases dry1, dry2 and dry3 (see Table 4.2).

The importance of dry-air entrainment is very pronounced in the EF, even though its values are now far from equilibrium. For instance, case *dry*1 has an EF of 0.66 at 13 LT and *dry*3 of 0.76, which is the same enhancement of 0.10 by dry air entrainment as is found in the wet cases discussed above. Our results thus extend the findings of De Bruin (1983) to dry surfaces. Here, we found enhancements of evaporation by dry-air entrainment over dry soils that equal the enhancements over wet soils. We would stress that even over dry soils, the increase in the equilibrium EF is a good indicator of the increase in the actual EF. For this reason, the change in the evaporation induced by a modification in the free tropospheric properties can be estimated by using the simple expression for equilibrium (equation 4.6).

4.4.3 Dry-air entrainment and land-atmosphere coupling

The results of the previous experiments showed us that dry-air entrainment clearly enhances surface evaporation. In this section we further analyse the consequences of the enhancement for the CBL properties. We select case *dry1*, *dry2* and *dry3* to serve as example cases to determine the effect of all the feedbacks, before discussing the general and less specific approach of our final experiment.

Figure 4.6 shows the temporal evolution of the CBL variables that are involved in the feedback loops (Figure 4.1). It is obvious that evaporation is enhanced by dry-air entrainment (top left-hand panel). For instance, at 12 LT *dry1* has a *LE* of 228 W m^{-2} and *dry3*, with the largest dry-air entrainment, has 268 W m^{-2}. This is a moderate increase of 40 W m^{-2}, but with significant implications for other variables. The effects of dry-air entrainment are most profound when the CBL grows most rapidly, between 8.5 and 10 LT. During this period large amounts of dry air enter the CBL, as is made evident by the rapid drop in specific humidity (bottom left panel). The reduction is particularly large in *dry3*, where q drops to 2.4 g kg^{-1} at 12 LT, compared to 6.3 g kg^{-1} for *dry1*. In this case, the stronger drying feedback (see Figure 4.1) enhances evaporation moderately, but induces a strong relative reduction in the sensible

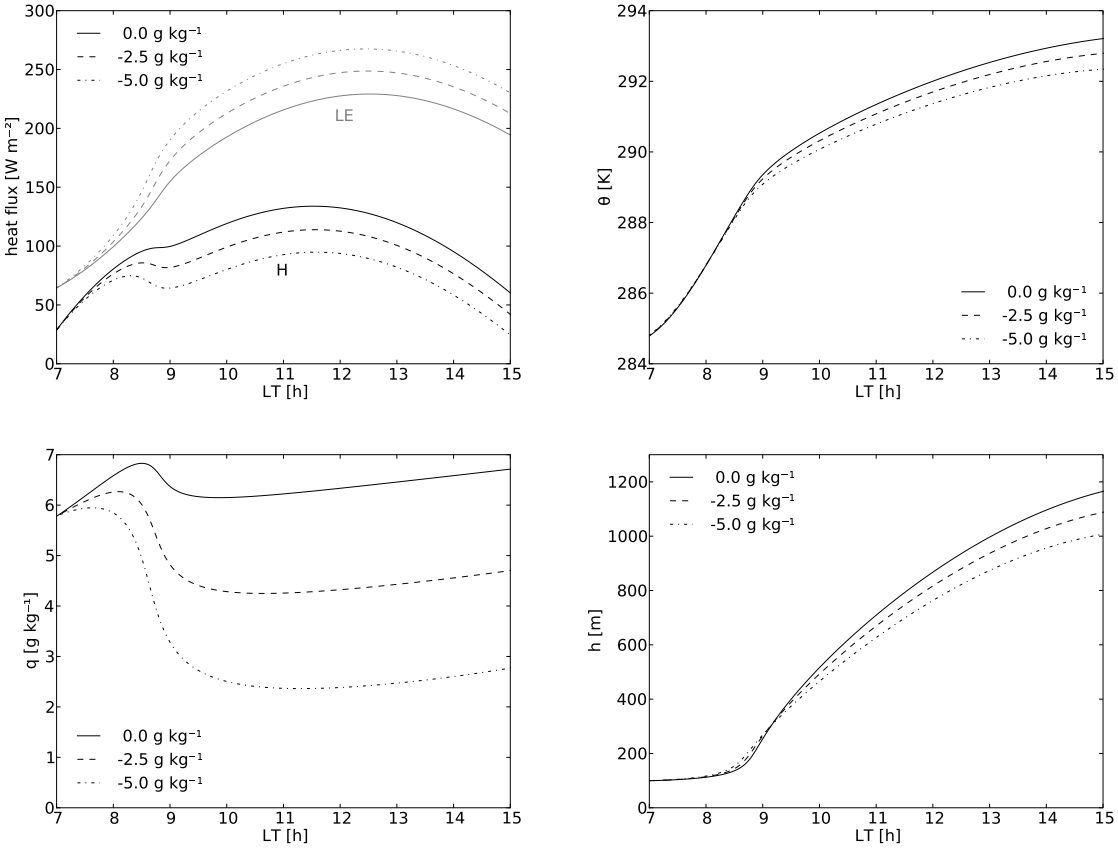

Figure 4.6: Time series of surface heat fluxes and CBL variables in cases dry1, dry2 and dry3 (see Table 4.2). The upper panel shows the surface heat fluxes (left) and the CBL potential temperature (right) and the lower panel shows the specific humidity of the CBL (left) and the CBL height (right).

heat flux. At 12 LT the sensible heat flux has fallen by 29% (from 132 to 94 W m^{-2}). As CBL growth is driven by H, the modification of the surface fluxes by dry-air entrainment is evident in the time evolution of this variable. Dry-air entrainment reduces the CBL height at 15 LT from 1165 m to 1007 m. This has significant effects on the RH at the top of the CBL and thus on cloud formation, which we discuss in our analyses of the final experiment.

In spite of the large entrainment-induced changes in CBL height and specific humidity, the temperature is less sensitive to dry-air entrainment, although the surface sensible heat flux has fallen significantly. The reason for this is that the largest heating occurs while the CBL is hardly growing (between 7 and 10 LT) and at that time the three cases still have nearly identical CBL properties. In addition, the contribution of heat entrainment to the total temperature tendency is relatively small compared to the contribution of dry-air entrainment to the tendency of specific humidity. Nevertheless, the dry-air entrainment-induced temperature change is 0.9 K at 15 LT.

4.4.4 The impacts of dry-air entrainment on surface heat fluxes and CBL development under a wide range of conditions

To summarise the results so far, we found that dry-air entrainment significantly enhances the equilibrium evaporation. This in turn influences the development of the CBL and the

possible occurence of clouds. In the following experiment we evaluate the effects of dry-air entrainment in a large parameter space to investigate its sensitivity to the atmospheric and land surface conditions.

The influence on evaporation and near-surface RH

We start the experiment by investigating the role played by atmospheric conditions. For this purpose, we perform *seriesrs*50 in which we vary the initial values for the potential temperature and the jump of specific humidity between the CBL and the free troposphere. These variables are selected, because they determine the value of the equilibrium EF (see equation 4.6) and the relative contribution of each of the feedback mechanisms involved (see Figure 4.1). The left-hand panel of Figure 4.7 shows the values of the EF and the Priestley-Taylor parameter at 13 LT as a function of these variables.

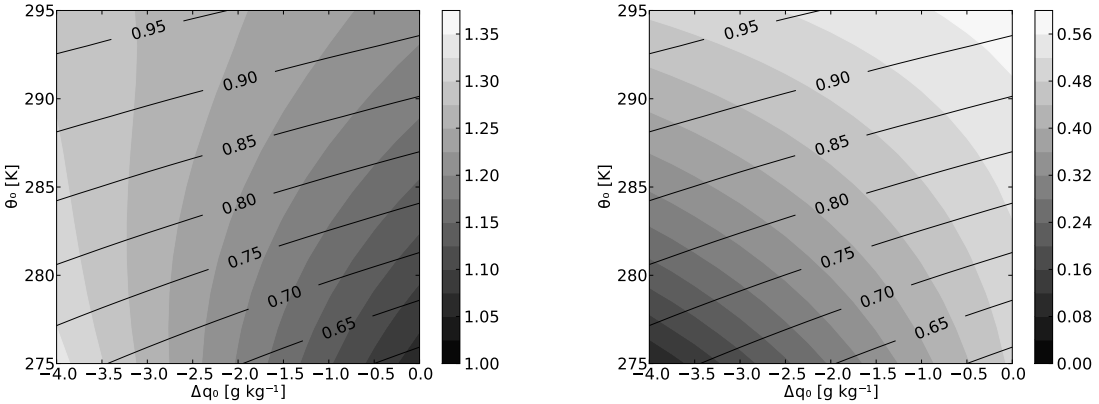

Figure 4.7: In the left-hand panel evaporative fraction (contour lines) and the Priestley-Taylor parameter α (shades) at 13 LT as a function of the initial specific humidity jump Δq_0 and the initial potential temperature θ_0. In the right-hand panel relative humidity at the land surface (shades) and the evaporative fraction (contour lines). Both figures are based on the results of seriesrs50.

It is clear that the EF at 13 LT is larger if the free troposphere is drier, regardless of the initial potential temperatures. For instance, at an initial temperature of 275 K the EF is 0.53 for an initial Δq_0 = 0.0 g kg^{-1}, while it rises to 0.70 at Δq_0 = -4.0 g kg^{-1}. Furthermore, the EF increases with increasing temperature for all Δq_0. Although initial potential temperature and initial specific humidity are both unambiguously correlated with the EF, we find that the sensitivity of EF to the initial Δq_0 becomes less at higher temperatures. Equation 4.6 explains that the equilibrium evaporation increases with temperature, due to the exponential character of the saturated specific humidity curve. The EF therefore increases at higher temperatures. The drying feedback therefore has less influence, because of the lower availability of energy for the sensible heat flux. This explains the lower sensitivity of EF for Δq_0.

The values of the Priestley-Taylor parameter α (see Figure 4.7) also show a dependence on the initial Δq. Dry-air entrainment enhances the α-value, but at high temperatures the sensitivity is low. For a wide range of conditions, we model values for α close to the 1.26 that Priestley and Taylor (1972) found for well-watered surfaces. Since dry-air entrainment is the only possible reason for enhanced evaporation in our model, we attribute the larger than unity value of α to this phenomenon.

The right-panel of Figure 4.7 shows the relative humidity (RH) at the land surface for the same range of initial conditions as the left-hand panel. The EF is contoured in black as a reference. Like the EF, the RH is also sensitive to the initial Δq at low temperatures and is less sensitive at high temperatures. We find a poor correlation between evaporation and relative humidity at the land surface, which has also been observed by Juang et al. (2007) and Siqueira et al. (2009). This is because the increase in evaporation achieved through the drying feedback has an opposite influence on RH compared to the heating feedback. For instance, if we move in the figure to larger values of EF parallel to the initial temperature axis, we find a rise of RH because of the increase in EF due to higher temperatures. However, if we enhance evaporation through an increase of dry-air entrainment, the figure shows a decrease of the RH, because of the drier air. There is therefore a range of combinations of initial potential temperatures and specific humidities that produce the same value for EF at 13 LT, but significantly different values for RH.

We repeated the whole analysis in this section also for wet surfaces in *seriesrs*0 and for dry surfaces in *seriesrs*100 (not shown). Here, nearly similar behaviour was found as in *seriesrs*50, except that the EF and RH have higher values under all the initial conditions in *seriesrs*0 and lower values in *seriesrs*100. This is due to the fact that the land surface can meet the atmospheric demand for water more rapidly when the surface is wet and slower when the surface is dry.

The influence on the conditions at the CBL top

So far, we have found that dry-air entrainment under all conditions influences the surface heat fluxes. Since these effects are to a large extent a function of temperature, the modification of the CBL properties by entrainment must also be temperature dependent. Figure 4.8 shows the influence of dry-air entrainment on CBL height and RH at the top of the CBL for *seriesrs50* at 13 LT.

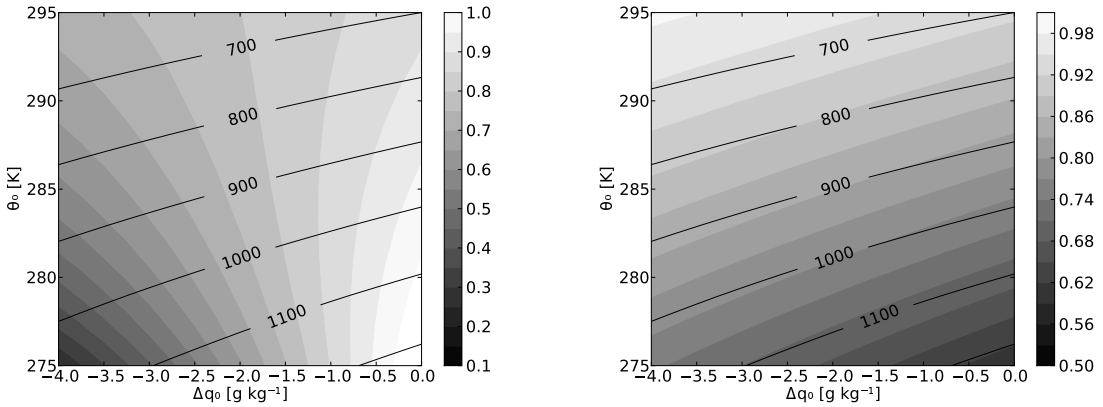

Figure 4.8: In the left-hand panel relative humidity at the CBL top (shades) and the CBL height (contour lines) at 13 LT as a function of the initial specific humidity jump Δq_0 and the initial potential temperature θ_0. In the right-hand panel evaporative fraction (shades) and the CBL height (contour lines) at 13 LT. Both figures are based on the results of seriesrs50.

In the left-hand panel, the CBL height decreases as the initial Δq_0 becomes more negative. This is explained by the fact that dry-air entrainment enhances the equilibrium EF (see previous section). For this reason, the LE increases and the subsequent reduction in the sensible heat

flux results in a lower CBL. For instance, at 280 K the height of the CBL for an Δq_0 of 0.0 g kg^{-1} is 1100 m, while in a dry atmosphere (Δq_0 of -4.0 g kg^{-1}) the CBL height is only 950 m. Moreover, as temperature increases, the CBL height displays straightforward behaviour. Under all free tropospheric moisture conditions an increase of 1 K results in a CBL that is about 22 m less deep.

In spite of the simple relationship between the CBL height and the initial conditions, the relative humidity at the CBL top (RHtop) is nonlinear. The RHtop decreases if Δq_0 becomes more negative for all initial temperatures. In addition, the sensitivity of the RHtop to Δq_0 is much larger at low temperatures than at high temperatures, due to the importance of the drying feedback under these conditions. We already have discussed this in detail in the previous section.

However, the response of the RH at the CBL top to initial temperature changes is complex. If the free troposphere is moist, the RHtop falls as temperature rises. At a Δq_0 of -0.5 g kg^{-1} the RHtop drops from 0.95 to 0.87 in the temperature range from 275 to 295 K. However, under conditions of a dry free troposphere, for instance at Δq_0 = -3.0 g kg^{-1}, the RHtop increases from 0.45 to 0.76 over the same temperature range. To explain the difference between these two situations, it is important to define the role of the different competing processes in the determination of RH. The evolution of RHtop is the result of competition between RH-enhancing processes, such as surface evaporation and absolute temperature decrease by CBL growth, with RH-reducing processes, such as dry-air entrainment and CBL heating (Ek and Mahrt, 1994; Ek and Holtslag, 2004). Our feedback diagram (Figure 4.1) may help us to understand the effects of rising temperature. An increase in temperature enhances evaporation through the heating feedback. Energy is thus shifted towards the latent heat flux, thereby decreasing the sensible heat flux. In consequence, there is less CBL growth and less free tropospheric air is therefore entrained into the CBL. In the case of a dry free troposphere this produces an increase of the relative humidity, because the increase in RHtop due to less dry-air entrainment is the most essential process. However, beneath a moist free troposphere the drying effect of entrainment is not important. The increase of absolute temperature at the top of the CBL as a consequence of the decrease in boundary layer height, thus results in a lowered relative humidity.

The right-hand panel of Figure 4.7 shows the evaporative fraction, but this time combined with the CBL height. We have already discussed the behaviour of the two quantities, but it is important to note that the two are highly correlated. The EF determines which fraction of the energy is available for the sensible heat flux, which is the driving force of boundary layer growth. Therefore, cases that share the same EF should have approximately the same CBL height. If we analyze the figure carefuly, we find that the EF is more sensitive to initial Δq_0 than the CBL height. This is because all cases initially have the same CBL height and the same EF despite their different initial Δq_0 value. During the period of fast CBL growth, differences between the cases start to develop (see also the development of h and q in Figure 4.6). The CBL height is the integrated result of the sensible heat fluxes during the whole period until 13 LT, while the EF corresponds to the actual surface fluxes at that time. Therefore, the evolution of CBL height is less sensitive than EF moving over the initial Δq_0 axis because the integrated heat fluxes between the cases are less different than the actual heat fluxes at 13 LT.

So far, the results have shown a large impact of dry air entrainment on the surface fluxes

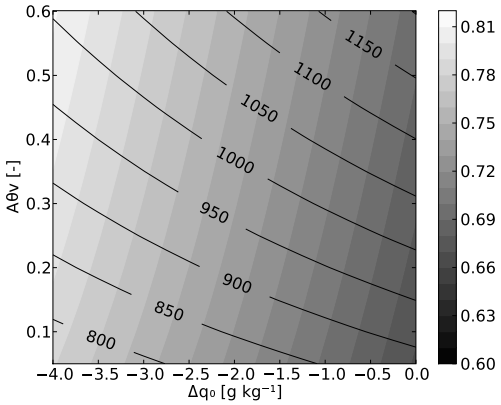

Figure 4.9: Evaporative fraction (shades) and the CBL height (contour lines) at 13 LT as a function of the initial specific humidity jump Δq_0 and the entrainment parameter A_{θ_v}. The figure is based on the results of seriesA_{θ_v}.

and the CBL height. In our model the entrainment of virtual potential temperature, the driving force for CBL growth, is parameterized by equation 4.4. Therefore, the value of A_{θ_v} has, according to equation 4.6, a significant impact on the equilibruim evaporation. In Figure 4.9 we evaluate therefore the sensitivity of the EF and the CBL height to the initial specific humidity and the entrainment parameter A_{θ_v}. The figure shows that larger values for A_{θ_v}, thus more entrainment, lead to higher boundary layers in all conditions. Doubling A_{θ_v} from 0.2 to 0.4 results in a CBL that is approximately 100 m higher. However, the effects on the EF are only marginal, since a doubling of A_{θ_v} results here in enhancements of only approximately 0.01 in all conditions. This implies that despite the larger CBL growth, an increase in A_{θ_v} leads to only little enhancement of the drying feedback. The reason is that during the rapid growth phase of the CBL, the specific humidity quickly drops (see Figure 4.6), thereby approaching the free tropospheric value. In such conditions, a larger A_{θ_v} does increase the CBL growth, but not the dry air entrainment since Δq has a very small value. Therefore, the influence of dry air entrainment on the surface heat fluxes is much more dependent on the initial Δq than on the entrainment parameter A_{θ_v}.

It is interesting and relevant to link the implications of our model results to convective cloud formation. In the case of constant land surface conditions, a reduction of the free tropospheric moisture results in a decrease of the RHtop and cloud formation therefore reduces or initiates later in the day. An increase in early morning temperature can result in more cloud formation in a dry free atmosphere or to less cloud formation in a moist situation. Our study provides a framework for the analyis of case studies such as that of Vilà-Guerau de Arellano (2007).

Importance of land surface properties versus free troposphere conditions

Previous studies (e.g. De Bruin, 1983; Santanello et al., 2007; Trier et al., 2008) have treated the land surface as the fundamental determinator of the partitioning of the surface heat fluxes. In order to compare the relative importance of land surface to free tropospheric moisture conditions, we perform *seriesT290*, a series of trials with a range of surface resistances and initial specific humidity jumps.

The left-hand panel of Figure 4.10 shows relative humidity and EF as functions of the

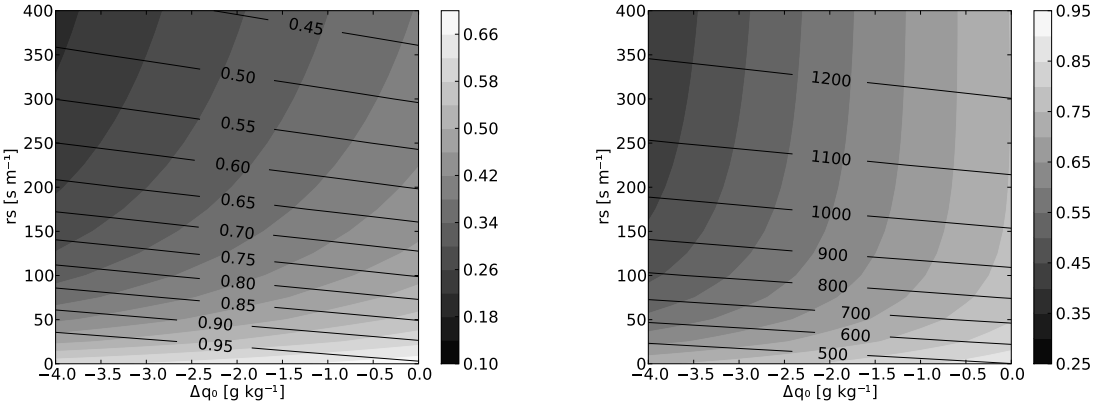

Figure 4.10: In the left-hand panel relative humidity at the land surface (shades) and the EF (contour lines) at 13 LT as a function of the initial specific humidity jump Δq_0 and the surface resistance r_s. In the right-hand panel relative humidity at the CBL top (shades) and the CBL height (contour lines). Both figures are based on the results of seriesT290.

initial specific humidity (Δq_0) and of the land surface resistance r_s, which for grassland can be regarded as a measure of the water availability of the soil. The figure shows that over all surface resistances, dry-air entrainment produces an increase in EF and a fall in RH, as we have already explained in the discussion of Figure 4.7. This figure also shows that an increase in the surface resistance r_s results in a decrease of EF and RH. However, the reduction in EF is not the effect of a reduction in equilibrium evaporation, but rather of an increase in the characteristic time scale of the coupled system under dry conditions. Figure 4.4 and 4.5 show that in all cases the equilibrium EF is low in the early morning due to the low temperature and the relatively high specific humidity in the CBL (see Figure 4.6). Subsequently, after sunrise the forcings rapidly increase the equilibrium EF. However, in the dry cases (large r_s) in the upper part of Figure 4.10, the system adapts only slowly to a larger equilibrium EF, as we learned from Figure 4.5. The EF therefore remains low, due to the characteristic long time scale of the coupled system under dry conditions (Raupach, 2000, 2001). In consequence, the CBL heats and grows rapidly, resulting in a low RH. The figure also shows that the sensitivity of the RH to dry-air entrainment rises if r_s increases. This is because, in spite of the overall low strength of the feedbacks, the drying feedback still increases in line with the sensible heat flux. At high resistances we have a large sensible heat flux, with the result that the dry-air entrainment reduces the RH more than under conditions with a low sensible heat flux.

We show the CBL height and the RH at the top of the CBL in the right panel of Figure 4.10. The CBL height responds as expected to changes in r_s as a greater resistance and thus more sensible heat results in a higher CBL. The response of CBL height to changes in Δq_0 has already been discussed in Figure 4.7. We also find that the RH at the top of the CBL decreases for larger negative values of Δq_0. The decrease of RHtop as well as the reduced sensitivity of that variable for large values of r_s can be explained using similar arguments as for the RH findings in the left-hand panel of Figure 4.10. The figure also shows that if we move along the r_s-axis in the direction of larger r_s we find a rapid decrease in RH at low values of r_s. When we move towards large r_s values, the RHtop continues to decrease, but the sensitivity vanishes at high resistances, especially if the free troposphere is moist. Eventually, RHtop becomes constant

even while the CBL height continues to increase with r_s. The left-hand panel shows us that EF also decreases in line with r_s. If the CBL continues to be enhanced for an increasing r_s, thereby increasing the RHtop, then other processes must exactly compensate this effect here. Figure 4.6 showed that q becomes constant in the afternoon: to maintain the same RHtop, therefore, the absolute temperature at the CBL top must remain constant. To achieve this, the cooling of the absolute temperature at the CBL top by boundary layer growth is compensated for by warming induced through the surface and the entrainment heat flux.

Our results indicate that, as De Bruin (1983) concluded, r_s is the most sensitive parameter in the determination of surface evaporation. Nevertheless, a decrease in free tropospheric moisture by 4 g kg^{-1}, which can happen in the time scale of hours (see Vilà-Guerau de Arellano (2007)), results in an increase in evaporation of 5 to 10%, depending on temperature. It should also be emphasised that land-atmosphere feedbacks make cloud formation insensitive to land-surface properties over very dry surfaces (large r_s). Under such conditions, free tropospheric specific humidity is the key variable.

4.5 Conclusions

This study addressed the effects of dry-air entrainment on the surface evaporation and the development of the convective boundary layer (CBL), through associated feedbacks mechanisms. We used a simple mixed-layer model coupled to the land surface with the Penman-Monteith equation to reproduce the essential physics of the coupled land-atmosphere system.

First, we studied the physical properties of the feedbacks in the coupled land-atmosphere system. This produced a framework that enables us to separate the effects of dry-air entrainment from the other feedbacks in the system. Using this framework, we derived simple equilibrium expressions for the evaporative fraction (EF) and the Priestley-Taylor parameter α and showed that the expressions are valid. However, only over wet surfaces the evaporation is able to approach equilibrium on a semi-diurnal time scale. Nevertheless, over dry land surfaces the expression is still a good indicator of the enhancement of surface evaporation by dry-air entrainment.

Second, we studied the impact of dry-air entrainment on the evolution of the surface fluxes and atmospheric properties throughout the day for a wide range of atmospheric conditions. The most important finding of this study is that dry-air entrainment enhances surface evaporation significantly under all conditions, but to different degrees. More specifically, dry-air entrainment has more influence on the surface heat fluxes at low potential temperatures (275 - 280 K) than at higher potential temperatures (290 - 295 K). This is because under cooler conditions the feedback in which dry-air entrainment is contained is the most dominant one. The analysis shows that dry-air entrainment is the process which creates a poor correlation between relative humidity and evaporation at the surface.

By modifying the surface heat fluxes, dry-air entrainment has a major effect on CBL height and relative humidity at the top of the CBL. An increase in evaporation by dry-air entrainment results in a relatively large reduction of the sensible heat flux, as the latent heat flux is normally larger than the sensible heat flux over vegetated surfaces. As this is the driving force of CBL growth, dry-air entrainment potentially reduces the CBL height by hundreds of meters compared to a situation in which the free troposphere contains more moisture. The choice of

the value of the entrainment parameter A_{θ_v} has only little impact on the surface fluxes, despite its strong influence on the growth of the CBL, because the dry air entrainment is limited by the moisture difference between the CBL and the free troposphere, rather than by the rate of CBL growth.

The interactions of dry-air entrainment and surface fluxes lead to nonlinear responses of the relative humidity at the CBL top (RHtop). The value of this variable falls if there is more dry-air entrainment. However, the response of RHtop to an rise in initial temperature is nonlinear. A rise in temperature results in a larger EF and thus in a reduced surface sensible heat flux and less CBL growth. In situations characterized by a dry free troposphere, less CBL growth results especially in less drying by entrainment, thus RHtop rises. However, if the free troposphere is moist, then the increase of absolute temperature induced by less CBL growth is stronger than the reduced drying, thus RHtop falls.

Third and last, we compared the relative importance of free tropospheric moisture conditions with land surface properties vis-à-vis the values of surface fluxes and CBL properties. The surface resistance, which is related to vegetation and soil moisture, is found to be the most sensitive parameter in the determination of the surface fluxes and the CBL height. However, the free tropospheric moisture content still has a significant effect on the surface fluxes. Regarding the relative humidity at the CBL top, the effects of free tropospheric moisture conditions are more important than the effects of land surface conditions.

Our results thus contain an important message for modellers. To reproduce realistic surface fluxes and CBL properties it is essential not only to have correct land surface properties and temperature profiles, but it is also fundamental to have accurate moisture profiles and to represent dry-air entrainment properly. For studies regarding cloud formation, it is essential to understand that dry-air entrainment determines whether a rise in temperature enhances or surpresses cloud formation. If the free troposphere is dry, a temperature rise enhances the possibility of cloud formation, while it reduces this possibility if the free troposphere is moist.

To conclude, our study can serve as a framework for modellers to quickly understand how sensitive their model results are to dry air entrainment. We recommended to check first whether dry air entrainment has a significant impact by calculating the Priestley-Taylor parameter α from equation 4.9. This calculation requires vertical profiles of temperature and moisture, either from measurements or from model results. If α exceeds unity, then dry air entrainment is fundamental in the determination of the surface fluxes. In that case, our contour plots serve as an indication of how changes in the surface characteristics or the atmospheric moisture structure influence the surface heat fluxes, the relative humidity and the CBL height. Since our contour plots do not cover all situations because we prescribed in all simulations the same cycle of net radiation and we fixed either the surface resistance or the initial temperature, we are aiming on extending this work into a more flexible framework in a future paper. In this future research we will incorporate less idealized vertical profiles of temperature and moisture, more detailed radiation, clouds and additional external forcings such as advection and subsidence.

Appendix A: overview of model parameters

This section contains an overview of all constants, initial and boundary conditions used in our coupled model (see table 4.4).

Table 4.4: Model constants, initial conditions and boundary conditions of coupled model runs. Deviations from this setup are described in the text. Variables subjected to a sensitivity analysis are indicated with SA in the table.

parameter	value	units	description
constants			
L_v	2.45e6	[J kg^{-1}]	heat of vaporization
c_p	1005	[J kg^{-1} K^{-1}]	specific heat of dry air
g	9.81	[m s^{-2}]	gravity acceleration
R_d	287.05	[J kg^{-1} K^{-1}]	gas constant for dry air
R_v	461.5	[J kg^{-1} K^{-1}]	gas constant for moist air
A_{θ_v}	SA	[-]	entrainment/surface ratio buoyancy flux
boundary conditions			
r_s	SA	[s m^{-1}]	stomatal resistance
r_a	50	[s m^{-1}]	aerodynamic resistance
Q_{*max}	400	[W m^{-2}]	maximum net radiation
f_G	0.1	[-]	ratio ground heat flux / net radiation
P_0	101300	[Pa]	surface pressure
γ_θ	0.005	[K m^{-1}]	free atmosphere potential temperature lapse rate
γ_q	0.0	[kg kg^{-1} m^{-1}]	free atmosphere specific humidity lapse rate
initial conditions			
h_0	100	[m]	initial ABL height
θ_0	SA	[K]	initial mixed-layer potential temperature
$\Delta\theta_0$	4.0	[K]	initial potential temperature jump at h
q_0	$0.7 = q_{sat}(\theta_0)$	[kg kg^{-1}]	initial mixed-layer specific humidity
Δq_0	SA	[kg kg^{-1}]	initial specific humidity jump at h
θ_{s0}	$= \theta_0$	[K]	surface potential temperature

5

Understanding the daily cycle of evapotranspiration: a method to quantify the influence of forcings and feedbacks

A method to analyze the daily cycle of evapotranspiration over land is presented. It quantifies the influence of external forcings, such as radiation and advection, and of internal feedbacks induced by boundary-layer, surface-layer and land surface processes on evapotranspiration. It consists of a budget equation for evapotranspiration that is derived by combining a time derivative of the Penman-Monteith equation with a mixed-layer model for the convective boundary-layer. Measurements and model results of days in two contrasting locations are analyzed using the method: mid-latitudes (Cabauw, The Netherlands) and semi-arid (Niamey, Niger). The analysis shows that the time evolution of evapotranspiration is a complex interplay of forcings and feedbacks. Although evapotranspiration is initiated by radiation, it is significantly regulated by the atmospheric boundary-layer and the land surface throughout the day. Boundary-layer feedbacks enhance in both cases the evapotranspiration up to 20 W m^{-2} h^{-1}. However, in the case of Niamey this is offset by the land surface feedbacks, since the soil drying reaches -30 W m^{-2} h^{-1}. Remarkably, surface-layer feedbacks are of negligible importance in a fully coupled system.Analysis of the boundary-layer feedbacks hints at the existence of two regimes in this feedback depending on atmospheric temperature, with a gradual transition region in between the two. In the low-temperature regime specific humidity variations induced by evapotranspiration and dry-air entrainment have a strong impact on the evapotranspiration. In the high-temperature regime the impact of humidity variations is less pronounced and the effects of boundary-layer feedbacks are mostly determined by temperature variations.

5.1 Introduction

The exchange of water between the land surface and the atmosphere is an essential component of the hydrologic cycle. Previous studies have shown that this exchange, evapotranspiration,

This chapter is published as van Heerwaarden et al. (2010a).

is closely coupled to the atmosphere (e.g. Jacobs and De Bruin, 1992; Betts et al., 1996; Koster et al., 2004). To be able to make credible predictions about the water balance of the earth in future climates, it is therefore fundamental to understand the driving mechanisms behind evapotranspiration and the link between the land surface and the atmospheric boundary-layer (ABL).

Evapotranspiration and land-atmosphere interactions have been the subject of many studies. These studies cover a large spectrum of spatial and temporal scales and range from conceptual studies to realistic 3D modeling. Relevant examples of large-scale studies using complex models are Betts et al. (1996), who discussed the memory of soil moisture and its impact on precipitation over a longer period, or Koster et al. (2004) who used an ensemble of GCMs to investigate the response of precipitation to soil moisture change by locating the regions with the strongest land-atmosphere coupling.

Then there are studies discussing land-atmosphere coupling on a local scale. Studies as De Bruin (1983) and McNaughton and Spriggs (1986) were the first to study the land surface, ABL and free atmosphere as a coupled system. Their finding that the ABL dynamics have an important influence on the surface evaporation formed the basis for more advanced studies. These are, for instance, Brubaker and Entekhabi (1995, 1996) and Margulis and Entekhabi (2001), who made mathematical frameworks to quantify feedbacks in the coupled land-atmosphere system. Furthermore, Ek and Holtslag (2004) quantified the link between soil moisture, surface evapotranspiration and boundary-layer clouds. Recent studies discussing evapotranspiration from an atmospheric perspective are Santanello et al. (2007), who analyzed the existence of evaporation regimes as a function of soil moisture and atmospheric stability and Raupach (2000); van Heerwaarden et al. (2009), who investigated the impact of atmospheric temperature and moisture on surface exchange and the regulation of the surface energy balance by feedbacks.

What most of these studies have in common is that they investigate the response of the integrated set of all feedbacks mechanisms to variations in the properties of either the land surface or the atmosphere. To our knowledge, only the studies of Brubaker and Entekhabi (1996) and Margulis and Entekhabi (2001) have provided methods to quantify the influence of individual forcings and feedbacks in the coupled land-atmosphere system on evapotranspiration. Our study focuses on evapotranspiration on the diurnal time scale and is therefore complementary to the work of Brubaker and Entekhabi (1996). Their study aims at understanding the longer time scales involved in the heat and moisture budget, which can for instance be seen in their assumption of constant ABL height. In turn, we are mostly interested in time scales of one day and shorter and focus particularly on the dynamics of the ABL. The study of Margulis and Entekhabi (2001) covers a theoretical overview of the feedback pathways that exist in the land-atmosphere system on a diurnal time scale using an example based on the FIFE data (Sellers et al., 1992) and shows in a conceptual way how studying evapotranspiration using offline models can be misleading.

In this paper, we describe a method for quantifying forcings and feedbacks during daytime convective conditions and apply it to two real data cases. In comparison to Margulis and Entekhabi (2001) our method is designed to quantify forcings and feedbacks directly from measurement or model data and is therefore complementary to their method.

The evapotranspiration is dependent on both the properties of the atmospheric boundary-

layer and the land surface. The temperature and humidity of the atmosphere control the maximum amount of water that the atmosphere can take up, which is the potential evapotranspiration. The land surface properties, such as the vegetation characteristics and the soil texture and its moisture content, determine the supply of water, thus to which degree the evapotranspiration rate reaches the potential. In the coupled land-atmosphere system, all variables are connected through a set of feedback mechanisms (Brubaker and Entekhabi, 1995; van Heerwaarden et al., 2009). For instance, an increase in soil moisture results in a larger evapotranspiration rate, which in turn has a positive effect on the atmospheric moisture content and a negative effect on the temperature as less energy is available for the sensible heat flux. In Section 5.2.1 we give a comprehensive description of the coupled land-atmosphere system, in which we define what we consider the forcings and the feedbacks that act on surface evapotranspiration.

The Penman-Monteith equation (Monteith, 1965) provides a way to quantify surface evapotranspiration taking into account the capacity of the atmosphere to take up water, as well as the ability of the land surface to provide it. For this reason, it is the most widely used parameterization for evapotranspiration in atmospheric and hydrologic models. In this paper we show that by differentiating the Penman-Monteith equation with respect to time, we obtain a budget equation for evapotranspiration. This can be rewritten in a form that provides separate terms for all forcings and feedbacks that act on the evapotranspiration if it is combined with the mixed-layer equations (Lilly, 1968; Tennekes, 1973) that describe the most essential dynamics of the daytime ABL. In Section 5.2.2 we explain this budget equation in detail.

Then, we demonstrate how our method can be used to analyze data to be able to identify the driving forces behind the daily cycle of evapotranspiration. Here, we use data of two contrasting locations. The two selected cases are 25 September 2003 at Cabauw, The Netherlands (Casso-Torralba et al., 2008) and 22 June 2006 at Niamey, Niger, measured during the AMMA campaign (Redelsperger et al., 2006). The first case is a typical mid-latitudes case, where evapotranspiration is energy-limited. This case is characterized by relatively cold temperatures, a moist and fully grass-covered land surface and only little advection. The second case corresponds to semi-arid conditions, where evapotranspiration is limited by the amount of available water. This case is a hot pre-monsoon day over a sparsely vegetated savanna, subjected to strong heat and moisture advection in the morning and a fast drying land surface throughout the day.

We reproduce the two days using a coupled land-atmosphere model. First, in Section 5.3 we discuss the model and the modeling experiment in detail and describe the data we use for the model evaluation. Second, in Section 5.4.1 we evaluate the model output against observations. In the subsequent analysis in Section 5.4.2 we apply our budget equation to the model result and do a thorough evaluation of all the terms in the budget equation. Per location we demonstrate how our method can be used to find out the importance of the forcings compared to the feedbacks in determining to which extent the evaporation is locally regulated. In this analysis, we compare the forcings, boundary-layer and land surface feedbacks in detail.

5.2 Evapotranspiration analysis framework

5.2.1 Overview of the coupled land-atmosphere system

In this section we explain the elements of the coupled land-atmosphere system that are relevant for the daily evolution of evapotranspiration. Figure 5.1 shows all the variables that are contained in this system and which will later appear in the budget equation that we present in Section 5.2.2.

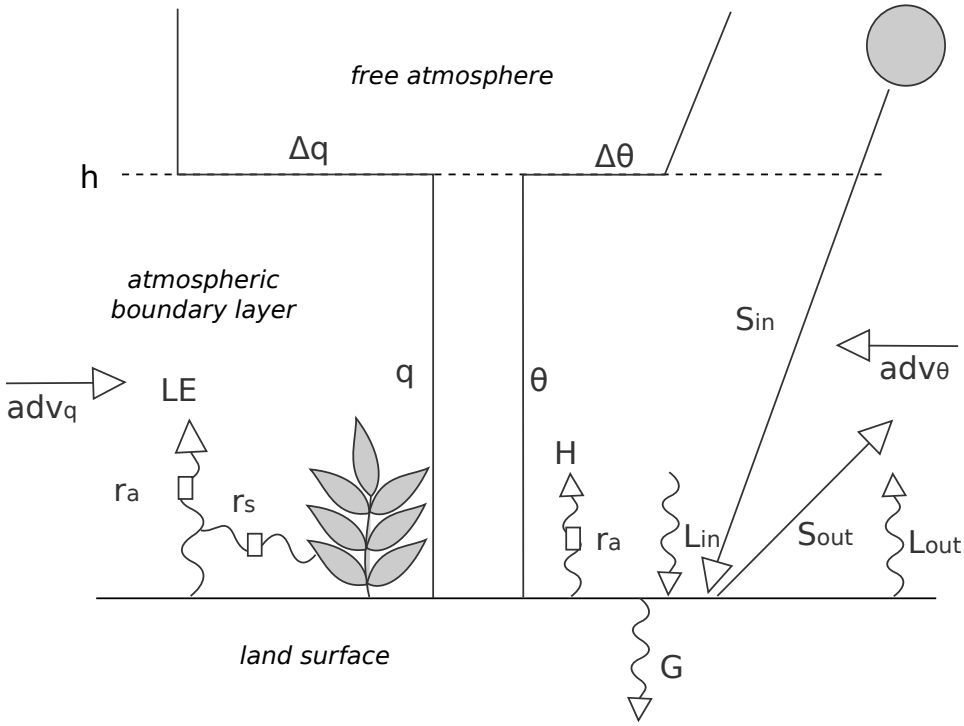

Figure 5.1: Overview of the coupled land-atmosphere system and the relevant variables in the daily evolution of evapotranspiration.

The system essentially consists of three components. First, there is the land surface, which provides water and heat to the atmosphere through the surface evapotranspiration LE and the sensible heat flux H. The energy that is available for these two processes is the net radiation Q_*, which is the sum of incoming S_{in} and outgoing S_{out} short wave radiation and incoming L_{in} and outgoing L_{out} long wave radiation, minus the energy that enters the soil through the ground heat flux G. Land surface properties, such as the vegetation type and cover or soil moisture, are accounted for through the surface resistance r_s, whereas the turbulent characteristics of the near-surface atmosphere, which determine how efficient water is taken up, are accounted for through the aerodynamic resistance r_a.

Second, there is the convective atmospheric boundary-layer (ABL) that has a well-mixed profile for potential temperature θ and specific humidity q. In this layer, the moisture that enters the ABL through the surface heat fluxes and the entrainment heat fluxes is vertically mixed by the convection. Large-scale temperature adv_θ and moisture adv_q advection act on the thermodynamic state of the ABL, which subsequently feeds back on the surface evapotranspiration.

Third and last, there is the free atmosphere. Its potential temperature and specific humid-

ity minus the values in the ABL define the jumps of potential temperature $\Delta\theta$ and specific humidity Δq. These jumps are strongly related to the vertical profiles of temperature and humidity in the free troposphere (see Equations 5.11 and 5.12). The first determines to a large extent the ABL growth, thus the evolution of the ABL height h, whereas the latter determines the amount of dry air that can be entrained during growth of the ABL.

In this study, we strictly separate forcings and feedbacks. As forcings we consider all processes that influence surface evapotranspiration, but which are not or only very weakly influenced by the state of the coupled land-atmosphere system on the time scale of one day. Therefore, these processes do not respond to the surface evapotranspiration, thus we assume them to be external forcings. As feedbacks on surface evapotranspiration, we consider the processes that react on the surface evapotranspiration and that, because of this reaction, have an influence on the evapotranspiration itself. Because these processes locally regulate the evapotranspiration, we call them feedbacks. In the next section we discuss the complete set of forcings and feedbacks in the system.

5.2.2 Budget equation for surface evapotranspiration

Now, we introduce the mathematical expression that describes the time evolution of evapotranspiration LE as a function of all forcings and feedbacks in the coupled land-atmosphere system sketched in Figure 5.1. This equation is acquired by combining a time derivative of the Penman-Monteith equation with the mixed-layer equations for the ABL (see Appendix A for a full derivation). Equation 5.1 shows the tendency of evapotranspiration ordered in forcings and feedbacks.

$$
\begin{aligned}
\frac{dLE}{dt} &= \overbrace{c_0 \frac{dq_{sat}}{dT}\left\{(1-\alpha)\frac{dS_{in}}{dt} + \frac{dL_{in}}{dt}\right\}}^{\text{surface radiation forcings}} \\
&+ \overbrace{c_0\left(H\frac{d^2q_{sat}}{dT^2} + \frac{\rho c_p}{r_a}\frac{dq_{sat}}{dT}\right)\left\{adv_\theta\right\} - c_0\frac{\rho c_p}{r_a}\left\{adv_q\right\}}^{\text{boundary-layer forcings}} \\
&+ \overbrace{c_0\left(H\frac{d^2q_{sat}}{dT^2} + \frac{\rho c_p}{r_a}\frac{dq_{sat}}{dT}\right)\left\{\frac{H}{\rho c_p h} + \frac{w_e\Delta\theta}{h}\right\} - c_0\frac{\rho c_p}{r_a}\left\{\frac{LE}{\rho L_v h} + \frac{w_e\Delta q}{h}\right\}}^{\text{boundary-layer feedbacks}} \\
&- \overbrace{c_0\left(\frac{\rho c_p}{r_a^2}(q_{sat}-q) - LE\frac{c_p}{L_v}\frac{r_s}{{r_a}^2}\right)\frac{dr_a}{dt}}^{\text{surface-layer feedback}} \\
&- \overbrace{c_0\frac{dq_{sat}}{dT}\frac{dL_{out}}{dt} - c_0\frac{dq_{sat}}{dT}\frac{dG}{dt} - c_0 LE\frac{c_p}{L_v}\frac{1}{r_a}\frac{dr_s}{dt}}^{\text{land surface feedbacks}}
\end{aligned}
\tag{5.1}
$$

$$
c_0 = \frac{1}{\frac{dq_{sat}}{dT} + \frac{c_p}{L_v}\left(1 + \frac{r_s}{r_a}\right)} \tag{5.2}
$$

with $\frac{dq_{sat}}{dT}$ as change of saturated specific humidity with respect to temperature, c_p as the heat capacity of air at constant pressure, L_v the latent heat of vaporization, ρ the density of the atmosphere, w_e the entrainment velocity and α the albedo of the land surface.

Each of the terms on the right hand side shows the contribution of a separate process to the time evolution of evapotranspiration. The terms can be interpreted as a sensitivity of evapotranspiration to a change in a variable ($\frac{\partial LE}{\partial var}$) multiplied with the tendency of that specific variable ($\frac{dvar}{dt}$), although in the case of potential temperature and specific humidity, the tendency has been replaced by the mixed-layer equations (see Appendix A). The five lines, in which the terms are ordered in their respective category, represent the following:

1. *Surface radiation forcings*. This forcing represents the effects of variations in the incoming radiation. The first term represents the net shortwave radiation, since the outgoing shortwave is defined as the albedo α multiplied with S_{in}, whereas the second term represents the incoming long wave radiation. Both are considered as external forcings. The net shortwave radiation represents the incoming solar energy, and since we do not take into account clouds here, it is therefore independent of the properties of the coupled land-atmosphere system. Although the incoming long wave radiation is function of the atmospheric temperature, it is rather insensitive to fluctuations in the ABL temperature on the time scale of one day, and is therefore assumed to be an external forcing. Both terms are positively related to the evapotranspiration tendency, for the reason that more available energy allows for more evapotranspiration.

2. *Boundary-layer forcings*. This forcing represents the large-scale processes that influence either the potential temperature or the specific humidity of the mixed-layer. In this study, where we do not consider clouds or radiation divergence in the atmosphere, this is only the large-scale advection. The first term describes the potential temperature advection. The second term represents the consequences of large-scale moisture advection. The boundary-layer forcings and feedbacks, shown in the next paragraph, enhance evapotranspiration if they warm or dry the ABL and reduce evapotranspiration if they cool or moisten the ABL.

3. *Boundary-layer feedbacks*. The first term of this forcing represents the effects of the surface (first term in bracket) and entrainment (second term in bracket) sensible heat flux on the potential temperature. The second term of this forcing describes the impact of evapotranspiration (first term in bracket) and dry-air entrainment (second term in bracket) on the specific humidity.

4. *Surface-layer feedbacks*. This term represents the impact of changes in the atmospheric resistance. If the atmosphere becomes more unstable or if the surface wind speed increases, then the atmospheric resistance decreases and evapotranspiration rises.

5. *Land surface feedbacks*. This last term shows the effects of the three processes of which the land surface feedbacks consist. The first term represents the outgoing long wave radiation, which is a function of the surface temperature. The second term describes the ground heat flux, which is the part of the incoming radiation that enters the ground

and is therefore not available for evapotranspiration. The third term accounts for variations in the surface resistance, which are induced by the response of the vegetation to changes in radiation or soil moisture or by the drying of the soil in the case of bare soil evaporation. An increase in outgoing long wave radiation results in a reduction of the evapotranspiration, because it reduces the net radiation. Similarly, a rise in the ground heat flux results in a decrease of evapotranspiration, as this reduces the available net radiation. An increase in surface resistance results in a fall in evapotranspiration as the land surface is less efficient in making water available for evapotranspiration.

5.3 Methods

5.3.1 Model

Here, we define the experiment to which we apply our framework. We use an extended version of the simple coupled land-atmosphere model which is described in van Heerwaarden et al. (2009). This model is inspired on the early studies of De Bruin (1983) and McNaughton and Spriggs (1986) and has proven to be successful in reproducing the essential land-atmosphere feedbacks accurately. The atmospheric part of the model is described in Appendix A by equations 5.7 to 5.12, and is based on Lilly (1968) and Tennekes (1973). We have extended these models by including a simple radiation model, dynamical models for the aerodynamic and surface resistance and a soil model.

In the simple radiation model the incoming short wave radiation is a function of the time, day, latitude and longitude and the incoming long wave radiation a function of the mixed-layer temperature.

To calculate the atmospheric resistance we include stability corrections based on Monin-Obukhov similarity theory, using the integrated flux-gradient relationship as proposed by Paulson (1970). For this, we evaluate the gradient at the top of the surface-layer, assuming that this height is at 0.1 of the boundary-layer height that is calculated by the atmospheric model.

To mathematically describe the land surface and to be able to model partially vegetated surfaces, we have introduced a force-restore soil model. The surface energy balance and temperature equations are based on Duynkerke (1991), whereas the soil moisture equations are based on Noilhan and Planton (1989). We chose the soil temperature description of Duynkerke (1991) over that of Noilhan and Planton (1989) since this formulation yields more accurate ground heat fluxes for nearly fully vegetated surfaces as in Cabauw. Since, in contrast to van Heerwaarden et al. (2009), we have added a soil model, the ground heat flux is resolved and therefore no longer a fixed fraction of the net radiation.

The evapotranspiration calculated by the model is a sum of three components: transpiration from vegetation, evaporation from bare soil and evaporation from wet foliage. A bulk surface resistance r_s is diagnosed from this sum and used in our budget equation for evapotranspiration. The computation of the transpiration from vegetation requires a canopy resistance, which we compute using the Jarvis-Stewart model (Jarvis, 1976) (see Appendix B for a full description). We added a parametrization to take into account the impact of interception water and dew formation on evapotranspiration (Viterbo and Beljaars, 1995).

5.3.2 Numerical experiments

Cabauw, The Netherlands: 25 September 2003

For our first case, we have selected measurements from Cabauw, The Netherlands, observed during 25 September 2003 (Casso-Torralba et al., 2008). This was a cloudless day with negligible horizontal advection for heat and moisture. The early morning profile was characterized by a large and moist residual layer, which had a very strong inversion on top of it above which the atmosphere was relatively dry. In Appendix C we have included a list of all model parameters, initial conditions and boundary conditions for this study.

To evaluate our model results, we use tower measurements of temperature and dew point temperature taken at 140 m to calculate the mixed-layer temperature θ and the mixed-layer specific humidity q. In addition, we compare surface measurements of incoming and outgoing short and long wave radiation with the radiation balance calculated by the model. Furthermore, we evaluate the calculated surface sensible H and latent LE heat flux against 10-min eddy correlation data, measured at 3 m above the land surface. The calculated atmospheric boundary-layer height h is evaluated against low-mode wind profiler measurements.

Niamey, Niger: 22 June 2006

For the second case, we have selected 22 June 2006 measured during the AMMA campaign (Redelsperger et al., 2006). This was a nearly cloudless day in the early stage of the monsoon. Deep convection with heavy rainfall occurred during the previous night, which provided water to the soil. A large part of this water was already removed via run-off, drainage or evaporation during the night. There is a large diurnal cycle of temperature combined with a strong drying of the soil throughout the day. In addition, both the moisture and the temperature balance are significantly affected by advection of relatively moist and cold air, which ceases in the afternoon.

To validate the model, we use surface measurements of the ARM mobile facility (Miller and Slingo, 2007) that measured the surface energy and radiation balance at the location. The mixed-layer potential temperature θ and specific humidity q are validated by comparing them to four radiosoundings taken at intervals of three hours. From these radiosoundings, the boundary-layer height h is constructed by picking the lowest height at which the virtual potential temperature at that specific height is 0.25 K higher than the mean from the land surface to that height. The mixed-layer potential temperature and humidity are acquired by averaging the radiosounding from the land surface to the boundary-layer height. The turbulent fluxes of temperature and moisture that represent the sensible H and latent LE heat flux are compared with eddy correlation measurements taken at the airport of Niamey, where the vegetated part of the land surface is covered with grass. Initial soil temperatures are close to those measured at the nearby station of Wankama. Large scale advection tendencies are estimated from the ECMWF re-analysis data for the AMMA observational campaign.

5.4 Results

5.4.1 Model validation

Cabauw, The Netherlands

We start our analysis by verifying the capability of the model to reproduce the measurements of the selected case of 25 September 2003. First, we compare the measured and modeled radiation balance, which confirms a close match between the model and the observations (not shown). Second, we validate the model against the measured potential temperature, specific humidity, boundary-layer height and surface heat fluxes (see Figure 5.2). Here, we

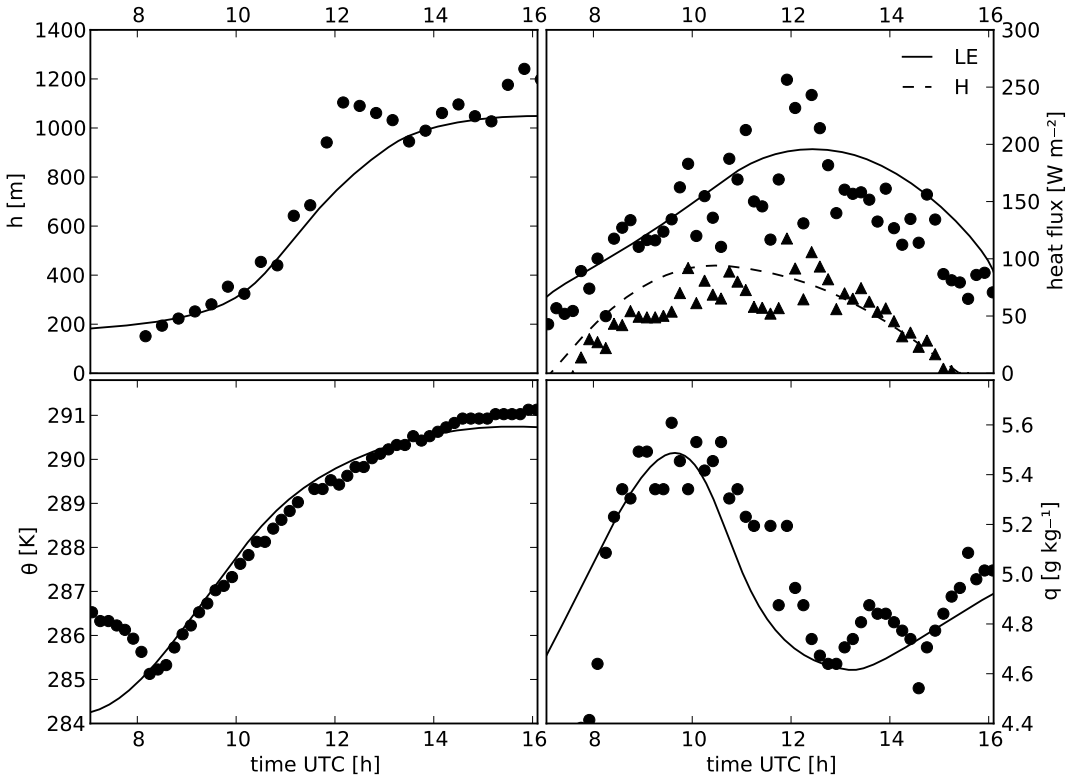

Figure 5.2: Time evolution of boundary-layer height (top left panel), surface heat fluxes (top right panel), potential temperature of the mixed-layer (bottom left panel) and specific humidity of the mixed-layer (bottom right panel) for the Cabauw case. Model is represented by continuous lines, observations by symbols.

find a satisfactory agreement between the measured and modeled boundary-layer height, potential temperature and specific humidity, which is a confirmation that our conceptual model captures the most relevant dynamics of the coupled land-atmosphere system. The data of the boundary-layer height shows significant fluctuations in the afternoon, which could be related to the measurement error in this data which could reach 40 per cent (Steeneveld et al., 2007). Nevertheless, the fact that our model reproduces the time evolution of the specific humidity well is an indication that the complex interplay of surface and entrainment fluxes is correctly represented by the model. Note that between 7h30 and 8h10 UTC the modeled potential temperature and specific humidity deviate strongly from the measurements. In the early morning phase, the ABL is not yet well-mixed, whereas within our model setup, we

assume it to be. This causes a deviation from the observations that quickly disappears after 8 h UTC, when the ABL becomes well-mixed.

The modeled surface heat fluxes show larger differences with the observed data than the temperature and humidity, although they approximately capture the values and tendencies. Since closing the surface energy balance is notoriously difficult using eddy covariance data (Brotzge and Crawford, 2003) and the tower has a different footprint than the surface flux measurements, we assume that the correct reproduction of the boundary-layer properties confirms that we model the appropriate fluxes.

Niamey, Niger

Also for the second case, the model compares well with the measurements. There is a close match between the measured and modeled radiation at the surface, which confirms that we prescribe the right available energy to the model (not shown). In addition, the modeled surface heat fluxes and the height, temperature and humidity of the mixed-layer match well with the observations (see Figure 5.3).

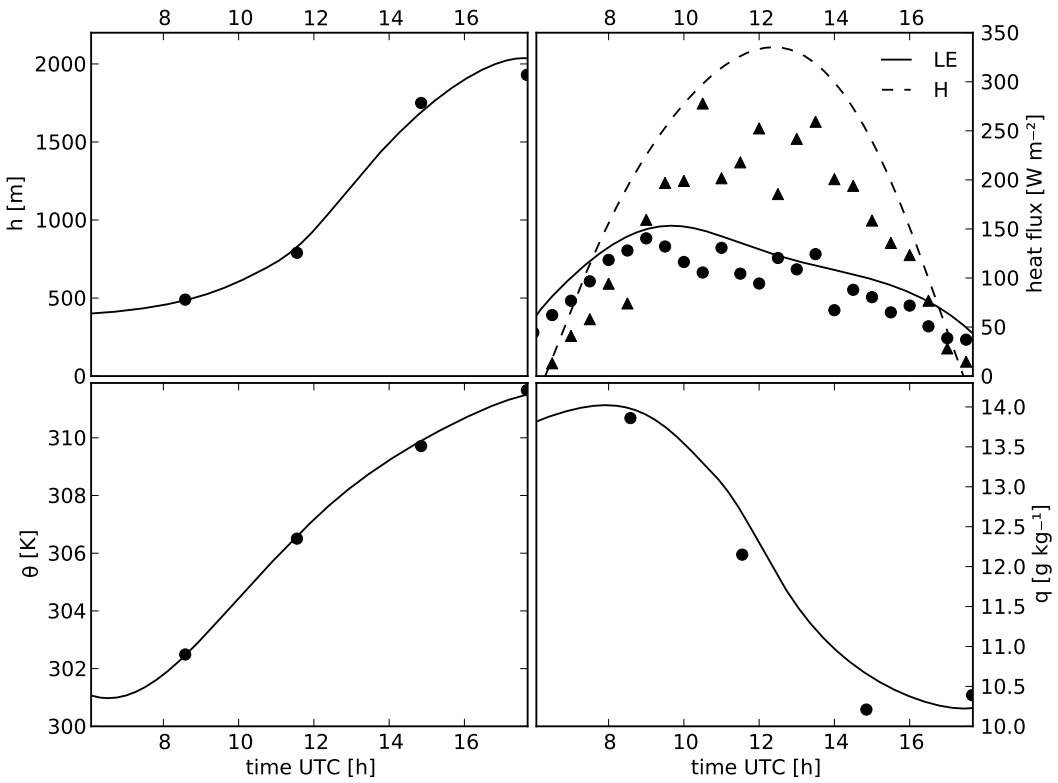

Figure 5.3: Time evolution of boundary-layer height (top left panel), surface heat fluxes (top right panel), potential temperature of the mixed-layer (bottom left panel) and specific humidity of the mixed-layer (bottom right panel) for Niamey. Model is represented by continuous lines, observations by symbols.

This is confirmed by a comparison of the mixed-layer profiles with radiosoundings taken at 3-hour intervals during this day, shown in Figure 5.4. The figure proves the quality of the mixed-layer model in convective conditions. The potential temperature and the specific humidity are described well over the whole mixed-layer depth by a single value. Only in the profile of 17h40 UTC, a limited gradient is observed in the top of the mixed-layer for both

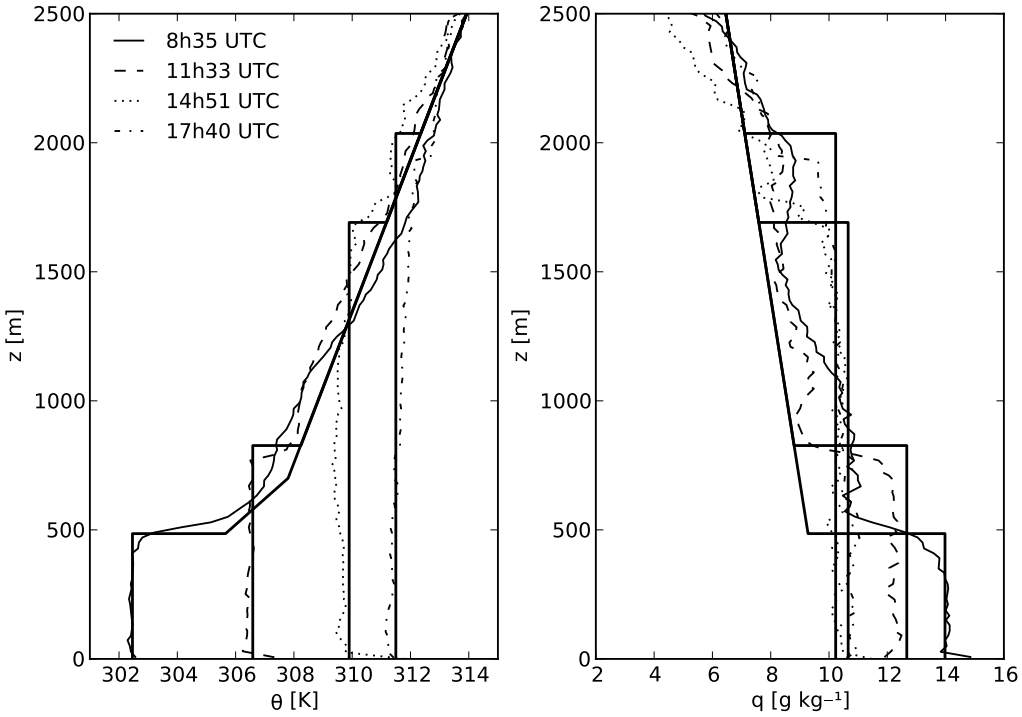

Figure 5.4: Comparison between radiosoundings (thin line) and model results (thick line) for potential temperature (left panel) and specific humidity (right panel) at Niamey.

temperature and moisture. At this time the virtual heat flux at the surface is barely positive anymore (see Figure 5.3) and the mixing is therefore less intense.

The surface evapotranspiration measurements show a good match with the modeled evapotranspiration, but the modeled values are slightly higher than the observations. Since the curve describing the modeled evapotranspiration follows the complex tendency of the observations well, we can assume that both the processes at the land surface and in the atmosphere are adequately reproduced by the model. The fact that a large part of the rain water already left the system during the night, explains the fast decline of the evapotranspiration during the day, as the reservoir is quickly depleted. The sensible heat flux is, similar to the evapotranspiration, larger in the model results than in the observations. Under the conditions of Niamey, a non-closure of the surface energy balance up to 20 percent of the net radiation is very common (Ramier et al., 2009). In our case, this would indicate a loss of approximately 100 W m^{-2}, which is more than the difference between the modeled and the observed surface fluxes. Since we are able to reproduce the radiosoundings, we assume that the modeled surface heat fluxes are representative for our case.

To conclude, the land-atmosphere model is able to reproduce the most important boundary-layer and surface flux characteristics of the two selected cases, therefore validating the application of the model output data as input for our evapotranspiration analysis framework.

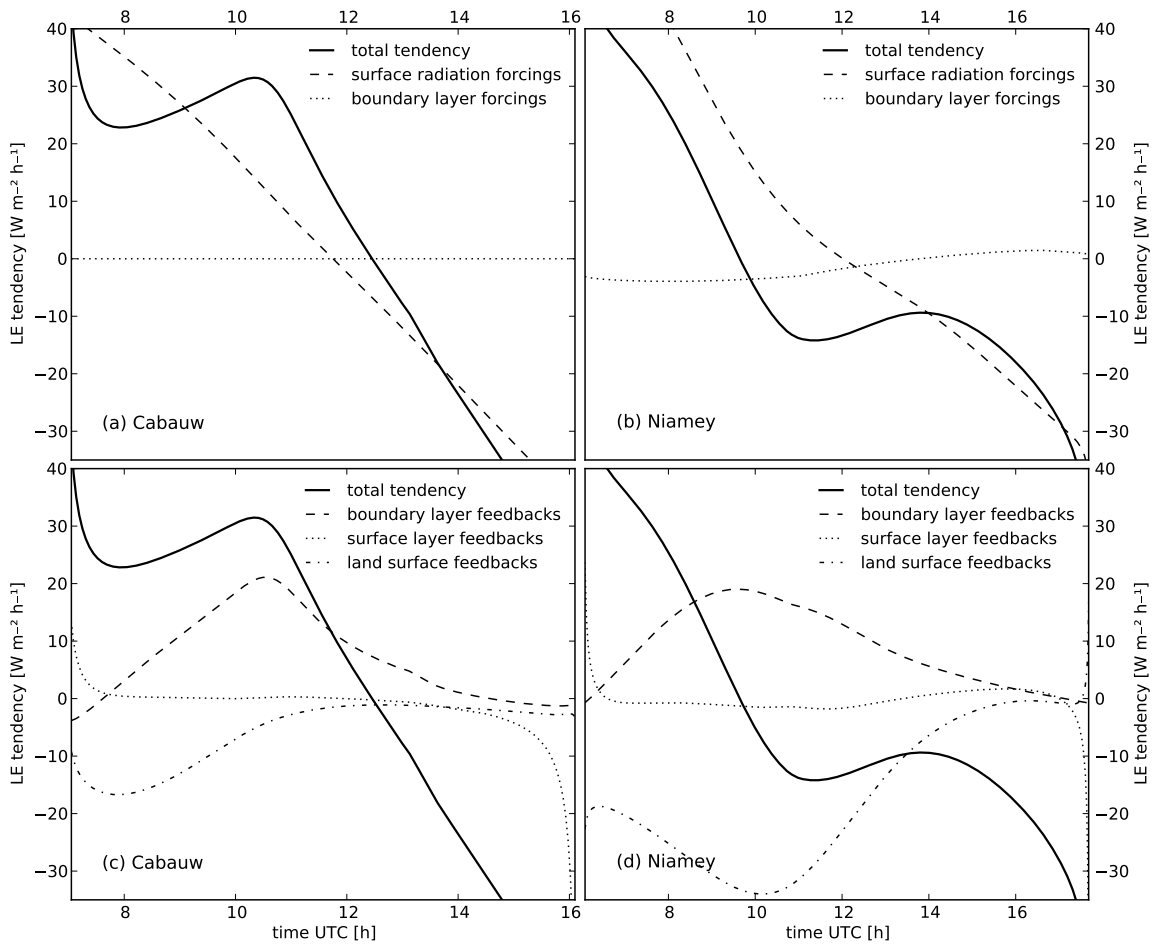

Figure 5.5: Contributions to the tendency of the surface evaporation induced by forcings (Cabauw: top left panel, Niamey: top right panel) and feedbacks (Cabauw: bottom left panel, Niamey: bottom right panel).

5.4.2 Analysis of the daily cycle of evapotranspiration

Overview of forcings and feedbacks

We start the analysis of evapotranspiration by showing in Figure 5.5 an overview of the total tendency of evapotranspiration and the separate contribution of the five categories of forcings and feedbacks defined in Equation 5.1.

According to the figure, there are strong similarities as well as differences between the two cases. In both cases, the surface radiation forcing is the main external driver of the system. It contributes positively in the morning when the sun rises fast, adding more than 30 W m^{-2} h^{-1} to the evapotranspiration. Then, at 11h40 UTC at Cabauw and at 12 h UTC at Niamey it crosses the zero-line, marking the position of the sun closest to the zenith, and during the remainder of the day the contribution becomes more negative as the angle between the sun and the zenith increases again. In Cabauw, the surface radiation forcings decrease linearly over the the majority of the day, whereas in Niamey, the slope of the line representing the forcing is less negative in the afternoon than in the morning, thus radiation is less effective in influencing the surface evapotranspiration later during the day. It is also found that the impact of heat and moisture advection on evapotranspiration is minimal in Niamey. In Section 5.4.2,

we will explain these findings after an in-depth analysis of the forcings.

Despite the similarities in the surface radiation forcings, there is a large difference in the time evolution of the evapotranspiration tendency of the two cases. A first explanation is that in Cabauw the three feedbacks (see Figure 5.5, panel c and d) add up to a positive tendency during the majority of the day, whereas in Niamey they add up to negative values most of the day. The differences in the feedbacks can also be found in the plot showing the forcings (see Figure 5.5, panel a and b). In the case of Cabauw, the total tendency is larger than the tendency induced by the forcings during the period from 9 h UTC to 14 h UTC, which implies that the feedbacks enhance evapotranspiration. The case of Niamey shows the opposite. Here, the total tendency is less than than the tendency induced by the forcings alone until 14 h UTC. Therefore, the impact of the feedbacks must be negative most of the day.

The cause for the large difference between the cases can be found in the land surface feedbacks. In the case of Cabauw, the land surface feedback has only a modest negative impact in the morning with a minimum at -17 W m^{-2} h^{-1} at 8 h UTC. Thereafter, its value quickly rises and after 12 h UTC its contribution is negligible. In Niamey we find a much larger negative impact, reaching -35 W m^{-2} h^{-1} just after 10 h UTC and remaining significantly negative until 16 h UTC. In Section 5.4.2 we elaborate the land surface feedbacks in the two cases and discuss the differences in the driving mechanisms between the two cases, to be able to explain this large difference.

In contrast to the land surface feedbacks, the contribution of the boundary-layer feedbacks is comparable between the two cases. Both have a rising contribution in the morning, with a peak near 10 h UTC of 20 W m^{-2} h^{-1} and are thereafter gradually reducing towards zero. The similarity between the two cases is striking, as there is a large difference in the partitioning of the surface fluxes, and in the related time evolution of the ABL properties (see Figures 5.2 and 5.3). In Section 5.4.2 we discuss the boundary-layer feedbacks in detail.

In both cases, the surface-layer feedback is of low importance throughout the majority of the day. Only in the early morning at the start of convection and in the evening transitions when convection stops, its contribution is large. The weak influence of surface-layer feedbacks is because the relative changes in the aerodynamic resistance are small, because the resistance is strongly buffered in the coupled system. This is caused by the inverse relationship between the drag coefficient and the wind, from which r_a is computed by $r_a = (C_D U)^{-1}$. This relation implies that if wind speed increases, the surface-layer becomes less unstable, thus C_D decreases and vice versa. The irrelevance of the surface-layer feedback confirms the findings of McNaughton and Spriggs (1986), who found that in coupled models, the evapotranspiration is insensitive to the aerodynamic resistance.

To summarize, we have three open questions now, which we will answer by analyzing the boundary-layer feedbacks, land surface feedbacks and forcings in detail using our method. First, we analyze what drives the land surface feedbacks at both locations. Second, we explain why the boundary-layer feedbacks are so similar in both cases, despite the striking differences between the two cases. Third, we explain why the radiation forcing is less efficient in the afternoon in Niamey, while it retains its strength in Cabauw and why the impact of advection is so small in Niamey.

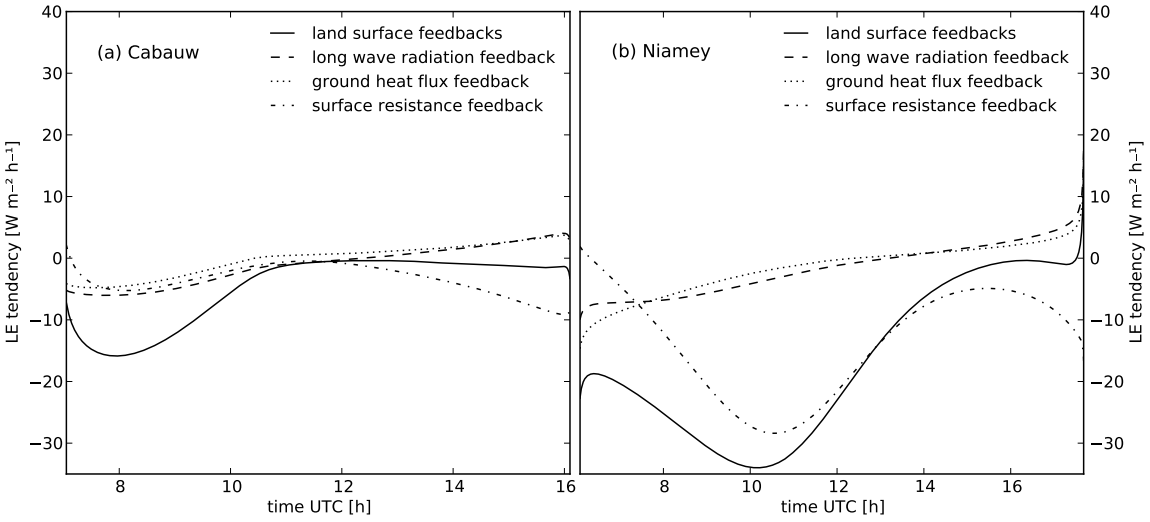

Figure 5.6: Contributions of land surface feedbacks to the tendency of the surface evaporation for Cabauw (left panel) and Niamey (right panel).

Land surface feedbacks

In Figure 5.6 we show the land surface feedbacks, decomposed into the three terms shown in Equation 5.1, which are related to the outgoing long wave radiation, the ground heat flux and the surface resistance. It is the evolution of the surface resistance feedback that makes the large difference between the two cases, having only little dynamics in Cabauw, in contrast to a large diurnal cycle over Niamey. In Cabauw, the contribution is slightly negative throughout the whole day with a minimum of -5 W m^{-2} h^{-1} at 8 h UTC, then rising slightly towards 0 W m^{-2} h^{-1} h near 11 h UTC, and thereafter gradually falling until -10 W m^{-2} h^{-1} in the evening transition when convection stops. In the morning there is dew on the leaves which makes evaporation at the potential rate possible for a limited fraction of the vegetation. The dew water reservoir depletes quickly and the surface resistance consequently rises, thus explaining the modest peak at 8 h UTC. The gradually increasing negative impact in the afternoon is explained by the response of the plants to the fall in shortwave radiation. The time evolution of the surface variables of Cabauw (see Figure 5.7) demonstrates the modest temperature range, and the limited increase of the surface resistance in the morning.

In Niamey, the surface resistance feedback falls to -28 W m^{-2} h^{-1} from the moment that convection starts until 10h30 UTC. Afterwards, the impact of the feedbacks reduces considerably, reaching a maximum of -8 W m^{-2} h^{-1} at 15h20 UTC, but falls thereafter again. Over Niamey, the majority of the evapotranspiration is bare soil evaporation. Since there has been precipitation during the night, the day starts with a moist soil. First, the evapotranspiration is rising (see Figure 5.3), thereby depleting the soil moisture at an increasing rate and progressively increasing the surface resistance. Note that despite the fast increase of the resistance, the evapotranspiration is initially still rising, because the forcings and boundary-layer feedback compensate for it (see Figure 5.5). This phase is pointed out by Brubaker and Entekhabi (1995), who show that anomalies in soil moisture are reinforced by a rise in surface temperature. This rise can be found in Figure 5.7 that shows the time evolution of surface and soil temperature.

After reaching the evapotranspiration peak just before 10 h UTC, the water in the top

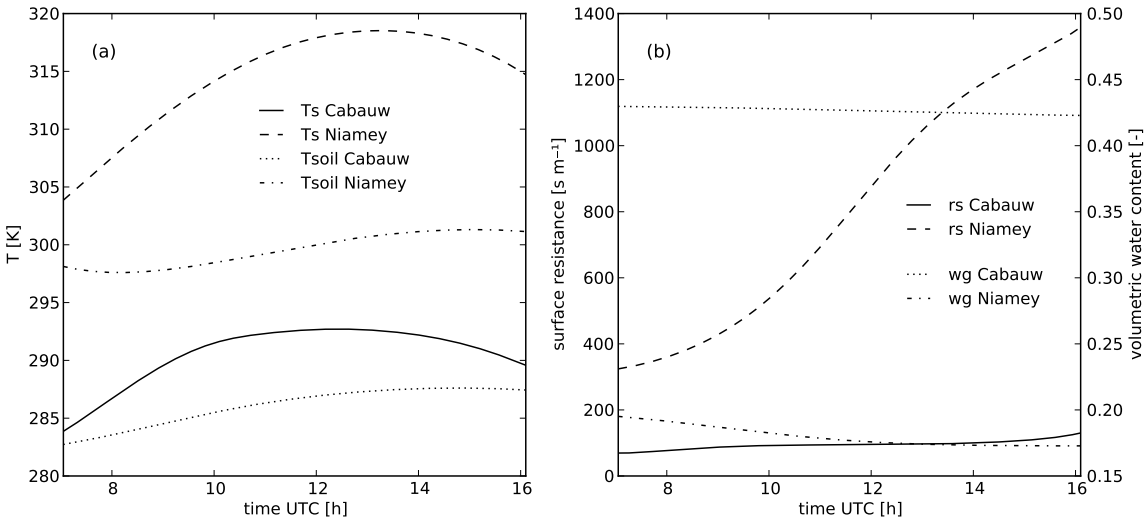

Figure 5.7: Time evolution of surface temperature and soil temperature (left panel) and surface resistance and soil volumetric water content (right panel) for both cases.

soil layer gets depleted. Although the resistance increases at a high pace (see Figure 5.7), the increase of large resistances to even larger resistances only has a limited effect on the evapotranspiration. Therefore, the contribution of the surface resistance to the tendency of evapotranspiration becomes less negative in time.

The contributions of the long wave radiation and the ground heat flux to the land surface feedbacks are similar for the two cases, slightly negative in the morning (-5 W m^{-2} h^{-1} for Cabauw and -10 W m^{-2} h^{-1} for Niamey) and almost linearly increasing throughout the day and is changing to positive sign around noon. Both feedbacks are inversely related to the incoming radiation. If the incoming radiation rises, the surface temperature rises. This means that more energy enters the soil through the ground heat flux and that more of the incoming radiation leaves the surface via the outgoing long wave radiation. Consequently, there is a negative impact on the evapotranspiration. Shortly after the moment that the sun reaches its smallest angle to the zenith, the surface temperature starts decreasing, and both contributions become positive, because the decrease in soil heat flux and outgoing long wave radiation makes more energy available for evapotranspiration. The amplitude of these two contributions is larger in Niamey compared to Cabauw, because the larger diurnal range of surface temperatures.

Boundary-layer feedbacks

Here, we compare in detail the boundary-layer feedbacks of the two cases. To be able to quantify the relevance of each individual boundary-layer process, we calculate the four components of the boundary-layer feedbacks shown in Equation 5.1 (see Figure 5.8).

Although we concluded in the previous analyses that there is a similar total contribution of the boundary-layer feedbacks between the two cases, there is a considerable difference in the magnitude of the four terms that add up to the total. In Cabauw the boundary-layer feedbacks are just as much influenced by the temperature related processes as the moisture related processes. In the morning when the boundary-layer is warming fast, between 9 and 10 h UTC, the increase of the temperature by surface heating has a positive contribution

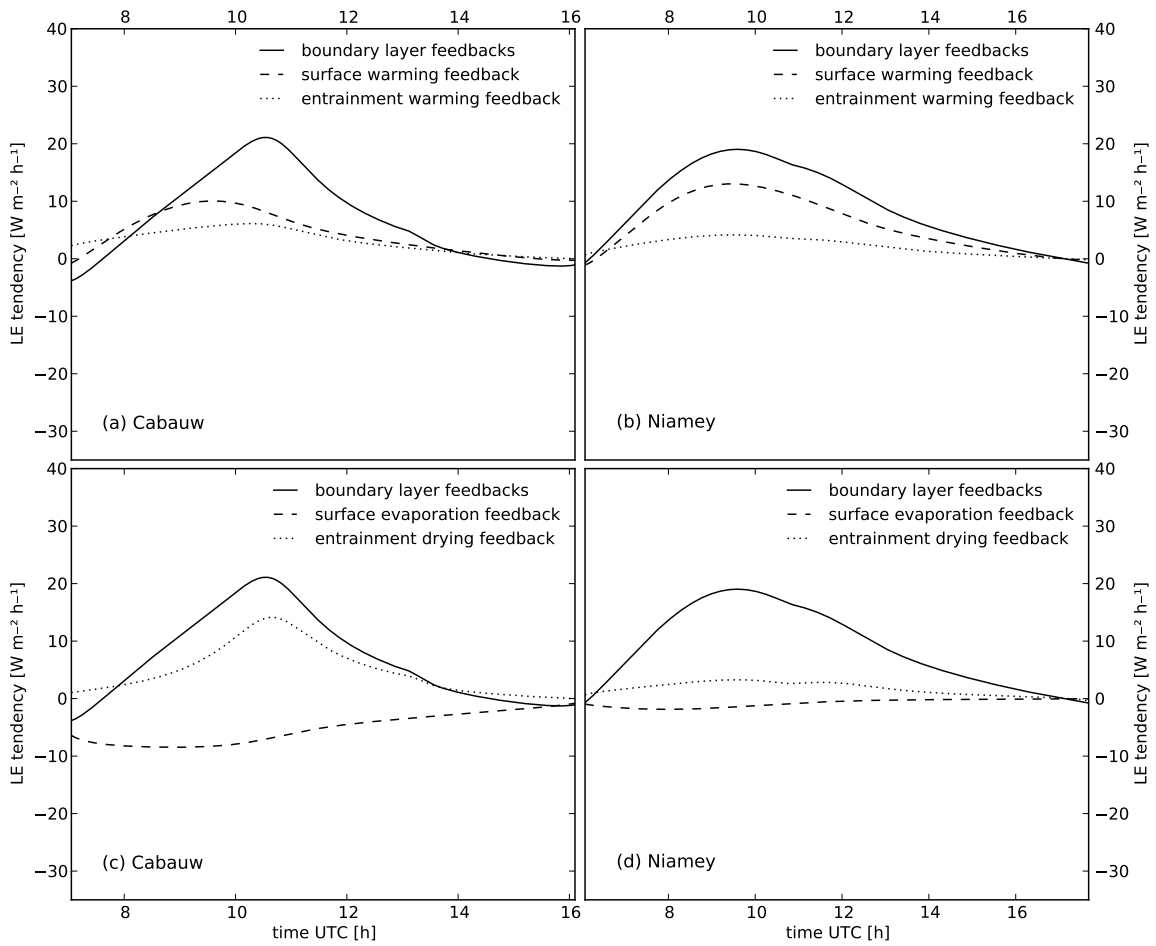

Figure 5.8: Contributions to the tendency of the surface evaporation induced by boundary-layer temperature feedbacks (Cabauw: top left panel, Niamey: top right panel) and boundary-layer humidity feedbacks (Cabauw: bottom left panel, Niamey: bottom right panel).

to the evapotranspiration close to 10 W m^{-2} h^{-1}. This positive enhancement is more than compensated by the decrease of the evapotranspiration caused by the moistening of the air which is close to -10 W m^{-2} h^{-1} until 10 h UTC. Later during the day, the effects of the surface heat fluxes become less, due to boundary-layer growth: now the surface fluxes enter a larger reservoir, the fully developed ABL, and therefore require more time to modify the atmospheric temperature or specific humidity.

The effect of entrainment is well-pronounced. Especially the effect of dry-air entrainment, at 10h40 UTC, has a strong positive contribution to the surface evapotranspiration of 15 W m^{-2} h^{-1}. At this time the boundary-layer grows the fastest and is still relatively moist (see Figure 5.2). The quick drop of specific humidity (from 5.5 to 4.6 g kg^{-1}) occuring then has a strong influence on the moisture deficit and thus on the evapotranspiration. The effect of temperature entrainment contributes also significantly to the surface evapotranspiration. The distinct peak, which we find in moisture is however absent, because temperature entrainment fluctuates less throughout the day than moisture entrainment and is, except for the early morning, in magnitude smaller than the surface sensible heat flux.

In Niamey, the boundary-layer feedbacks are mostly controlled by temperature. The surface warming feedback contributes up to 13 W m^{-2} h^{-1} to the time evolution, whereas the

other three feedbacks have only a limited influence ranging from -2 W m^{-2} h^{-1} for the surface evapotranspiration until approximately 3 W m^{-2} h^{-1} for both entrainment fluxes.

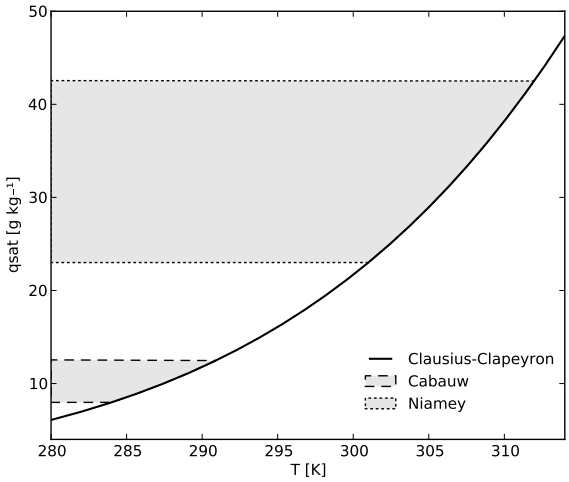

Figure 5.9: Comparison of the daily range of q_{sat} in Cabauw (dashed lines) and Niamey (dotted lines) indicated on the Clausius-Clapeyron relationship between absolute temperature and saturated specific humidity.

The difference between the boundary-layer feedbacks in Cabauw and those in Niamey have two explanations. First, the evapotranspiration flux is smaller in Niamey. Therefore, the opportunity for evapotranspiration to moisten the atmosphere to influence evapotranspiration significantly is limited. Nevertheless, there is a large dry-air entrainment flux in Niamey, thus we need another explanation for the low sensitivity of the evapotranspiration to that. The answer is in the nonlinear relationship between saturated specific humidity and temperature, described by the Clausius-Clapeyron relationship, plotted in Figure 5.9. If the temperature is relatively low, such as in Cabauw, then variations in the moisture deficit $q_{sat} - q$ are just as dependent on variations in temperature as on variations in moisture. In conditions of higher temperatures, however, the saturated specific humidity is much more sensitive to variations in the temperature than at low temperatures. Therefore, variations in the moisture deficit are mainly caused by variations in temperature. To illustrate this: in Cabauw, q_{sat} changes from 10.0 to 12.3 g kg^{-1} from 10 to 15 h UTC (see Figure 5.9), where q changes from 5.6 to 4.9. In Niamey, however, q_{sat} increases from 27.4 to 38.0 g kg^{-1} between 10 and 15 h UTC (see Figure 5.9), whereas q only decreases from 13.5 to 10.9 g kg^{-1}. From this analysis, we can conclude that due to the nonlinear relation between temperature and saturated humidity dry-air entrainment is particularly significant at lower temperatures. These observed cases confirm thus the theoretical experiments of van Heerwaarden et al. (2009), who showed that the impact of dry-air entrainment becomes less at higher temperatures. Our finding also extend previous studies to the effect of dry-air entrainment in the Sahel region (Lothon et al., 2007; Canut et al., 2010), by showing that dry-air only has a minimal impact on the surface heat fluxes, despite its large impact on the specific humidity and thus on cloud formation and convection. In between these two regimes, there is a gradual transition from one regime into the other. This becomes clear in the results of Margulis and Entekhabi (2001), who analyzed a case in which the temperature is significantly higher than in Cabauw, but less than in Niamey, while the Bowen ration resembles that of the Cabauw case. In their results, the sensitivity of

evapotranspiration to the free atmospheric humidity is less than in our Cabauw case, and less than the impact of temperature on evaporation, but it is clearly larger than the impact of free atmospheric humidity in the case of Niamey.

To come back to the question why the boundary-layer feedbacks are so similar between the two cases: this is coincidental as an in-depth analysis shows that there are significant differences between the four contributions of the boundary-layer feedbacks.

Forcings

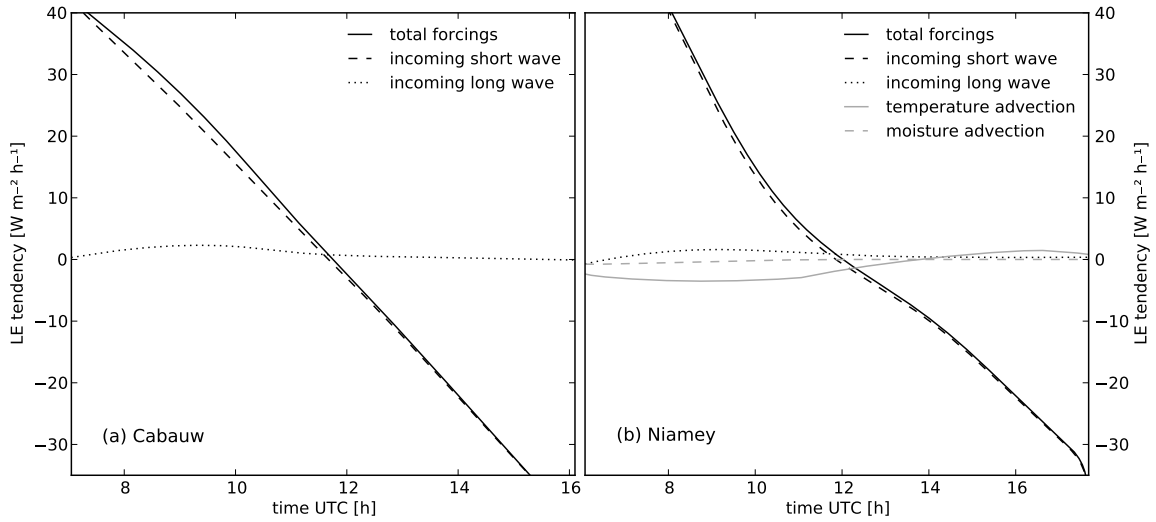

Figure 5.10: Contributions of the forcings to the tendency of the surface evaporation for Cabauw (left panel) and Niamey (right panel).

In Figure 5.10 we give an overview of the forcings of the coupled land-atmosphere system in the two cases. This figure completes the overview of all the terms that were shown in Equation 5.1. In both cases the total forcings are mainly depending on the contribution of incoming shortwave radiation, since both curves in the figure nearly overlap. In the first subsection of Section 5.4b we found that the impact of the forcings reduces in the afternoon in Niamey, while this is not the case in Cabauw. The explanation for this is related to difference in land surface feedbacks discussed in Section 5.4.2. Due to the drying of the soil and the subsequent increase in the surface resistance, the evaporation is strongly limited by the land surface conditions. The response of the evapotranspiration to falling radiation is therefore limited, since at this time the case is fully water-limited and radiation is no longer a limiting factor for evapotranspiration.

Based on this figure, we can argue that our assumption that the incoming long wave radiation is an external forcing is correct. In both situations the daily dynamics of the atmospheric temperature barely influence the impact of the incoming long wave radiation.

There is one extra feature in the forcings of Niamey, which is the large-scale advection of moist and cold air. This gradually decreasing advection has a slight negative impact on the evapotranspiration. Initially, the temperature advection has an impact of -3 W m^{-2} h^{-1}, which gradually increases to 0 W m^{-2} h^{-1}. The moisture advection does not exert any influence at all. The explanation is similar to that of the insensitivity of evapotranspiration to dry-air

entrainment at high temperatures: the moisture deficit is largely determined by temperature variations and only little by variations in specific humidity.

5.5 Conclusion

A method to analyze the daily cycle of surface evapotranspiration has been developed. It reveals novel insights in the driving mechanisms behind surface evapotranspiration during the day. The method shows clearly that surface evapotranspiration is a complex process that can only be understood by considering the land surface and the atmosphere as an interactive system. It quantifies separately variations in the surface evapotranspiration driven by direct forcings, such as radiation, as well as those driven by feedbacks that exist between evapotranspiration and the land surface, the surface-layer and the atmospheric boundary-layer (ABL).

We modeled and validated with data two contrasting observed cases, 25 September 2003 at Cabauw, The Netherlands and 22 June 2006, Niamey, Niger. The first case is a characteristic example of a case in which evapotranspiration is energy-limited, whereas the second is a typical water-limited case. Subsequently, we apply our method to the model output. This reveals insights in the mechanisms that drive evapotranspiration at these locations.

We find that forcings and feedbacks are of equal importance in the control of surface evapotranspiration. The local conditions determine how much the feedbacks enhance or suppress the forcings. In Cabauw, the feedbacks enhance evapotranspiration, because their sum is positive over the majority of the day. In Niamey the opposite is true. Here, the sum of the feedbacks is mostly negative, which indicates that evapotranspiration is suppressed by the land-atmosphere system. In both cases the boundary-layer feedbacks, the effects of changes in the temperature and moisture content of the ABL, have an enhancing effect on evapotranspiration. In the case of Niamey, this effect is offset by the strong negative influence of the land surface feedbacks, induced by the drying of the soil.

Despite the similarity in the sign and magnitude of the boundary-layer feedbacks in both cases, there is a large difference in the processes that drive them. In the case of Cabauw, the variations of moisture and temperature in the atmosphere play an equally important role, and dry-air entrainment has the largest contribution to the boundary-layer feedbacks. In Niamey, however, the effect of temperature fluctuations dominates the feedbacks and moisture fluctuations become irrelevant. In general, it should be true that over cold areas in the world, both the atmospheric moisture and temperature regulate the boundary-layer feedbacks. If we move towards regions with high temperatures, we expect a gradual transition towards a regime where the boundary-layer feedbacks become temperature-controlled.

Although our method shows interesting features of the diurnal cycle of evapotranspiration, we would like to stress that our conclusions are only based on two cases that mainly served as examples of our new method. To acquire a solid understanding of the driving forces behind the daily cycle of evapotranspiration, future studies, which take into account longer time periods and more locations, are necessary. Such studies could enable us to identify for different areas in the world to which changes in the environment the evapotranspiration would be the most sensitive and how this sensitivity varies in space and time. This could for instance be done using output of weather and climate models. Before such studies can be undertaken, our

model needs to be extended to cloudy boundary-layers.

Appendix A: Derivation of evapotranspiration tendency equation

In this appendix we derive the tendency equation for evapotranspiration from the Penman-Monteith equation and the mixed-layer equations that describe the daytime ABL.

$$LE = \frac{\frac{dq_{sat}}{dT}(Q_* - G) + \frac{\rho c_p}{r_a}(q_{sat} - q)}{\frac{dq_{sat}}{dT} + \frac{c_p}{L_v}\left(1 + \frac{r_s}{r_a}\right)} \tag{5.3}$$

The Penman-Monteith equation (equation 5.3) describes the actual evapotranspiration taking into account all processes that create a moisture gradient between the land surface and the atmosphere. These are the available energy, defined as the net radiation Q_* minus the soil heat flux G, and the moisture deficit of the air, which is the saturated specific humidity of the atmosphere q_{sat} minus its specific humidity q. The extent to which moisture can be transported over this gradient is determined by the turbulence near the surface, described by the aerodynamic resistance r_a and the ability of the vegetation and soil to evaporate water, described by the surface resistance r_s. Note that the terms in the equation are in units of specific humidity rather than the more commonly used vapor pressure to facilitate the coupling with our atmospheric model.

If we differentiate this expression in time and group all the terms in the equation per tendency of each of the involved variables and finally replace $Q_* - G - LE$ by H, we obtain equation 5.5.

$$c_0 = \frac{1}{\frac{dq_{sat}}{dT} + \frac{c_p}{L_v}\left(1 + \frac{r_s}{r_a}\right)} \tag{5.4}$$

$$\begin{aligned}
\frac{\partial LE}{\partial t} &= c_0 \frac{dq_{sat}}{dT}\frac{dQ_*}{dt} \\
&- c_0 \frac{dq_{sat}}{dT}\frac{dG}{dt} \\
&+ c_0 \left(H\frac{d^2 q_{sat}}{dT^2} + \frac{\rho c_p}{r_a}\frac{dq_{sat}}{dT}\right)\frac{dT}{dt} \\
&- c_0 \frac{\rho c_p}{r_a}\frac{dq}{dt} \\
&- c_0 \left(\frac{\rho c_p}{r_a^2}(q_{sat} - q) - LE\frac{c_p}{L_v}\frac{r_s}{{r_a}^2}\right)\frac{dr_a}{dt} \\
&- c_0 LE\frac{c_p}{L_v}\frac{1}{r_a}\frac{dr_s}{dt}
\end{aligned} \tag{5.5}$$

With the previous equation, we have decomposed the evolution of evaporation in one term per involved variable. Nevertheless, the tendency of each variable is also the sum of a set of physical processes. We elaborate now some of the terms to improve the physical

interpretation.

First, we split the net radiation tendency into the sum of the tendencies of the net short wave and long wave radiation,

$$\frac{dQ_*}{dt} = (1-\alpha)\frac{dS_{in}}{dt} + \frac{dL_{in}}{dt} - \frac{dL_{out}}{dt} \tag{5.6}$$

where α is the albedo, S_{in} is the incoming short wave radiation at the surface, L_{in} is the incoming long wave radiation at the surface and L_{out} is the outgoing long wave radiation at the surface.

Second, we introduce the essential dynamics of the atmosphere into the temperature and moisture equation. Previous studies (Betts, 1992; Santanello et al., 2009) show that the time evolution of the near-surface temperature and humidity is the effect of both external forcings such as advection and radiation divergence, as well as internal feedbacks such as the surface fluxes of heat and moisture and the entrainment fluxes of heat and moisture, which is the interaction between the turbulent boundary-layer and the free atmosphere above.

During daytime, the effects of the large-scale forcings and feedbacks are rapidly mixed throughout the atmospheric boundary-layer. Therefore, the layer can be considered as well-mixed and one value of the conserved variables specific humidity and potential temperature is representative for that layer. This yields the widely applied mixed-layer model (Lilly, 1968; Tennekes, 1973),

$$w_e = A_{\theta_v}\frac{\frac{H}{\rho c_p} + \theta\left(\frac{R_v}{R_d} - 1\right)\frac{LE}{\rho L_v}}{\Delta\theta_v} \tag{5.7}$$

$$\frac{dh}{dt} = w_e + w_s \tag{5.8}$$

$$\frac{d\theta}{dt} = \frac{1}{h}\left(\frac{H}{\rho c_p} + w_e\Delta\theta\right) + adv_\theta \tag{5.9}$$

$$\frac{dq}{dt} = \frac{1}{h}\left(\frac{LE}{\rho L_v} + w_e\Delta q\right) + adv_q \tag{5.10}$$

$$\frac{d\Delta\theta}{dt} = \gamma_\theta w_e - \frac{d\theta}{dt} \tag{5.11}$$

$$\frac{d\Delta q}{dt} = \gamma_q w_e - \frac{dq}{dt} \tag{5.12}$$

with w_e as the entrainment velocity, A_{θ_v} as the ratio between the entrainment virtual heat flux and the surface virtual heat flux, ρ as the density of air, c_p as the heat capacity of air at constant pressure, R_v as the gas constant of moist air, R_d as the gas constant of dry air, w_s as the large-scale vertical motion.

The most important assumptions that are enclosed in this model are:

- The ABL is well-mixed, therefore one value for the potential temperature and specific humidity is used for the whole layer (see sketch of vertical profiles in Figure 5.1).
- The boundary-layer growth (see Equation 5.8) is driven by the large-scale vertical velocity w_s and the surface virtual potential temperature flux (see Equation 5.7 where this value is written in terms of the heat fluxes). The entrainment parameter A_{θ_v} relates the entrainment flux of virtual potential temperature to the surface flux. The entrainment

zone is assumed to be of infinitesimal thickness (see sketch of vertical profiles in Figure 5.1).

- The prognostic equations for the jumps of potential temperature and specific humidity between the ABL and the free atmosphere (see Equations 5.11 and 5.12) show that the jump is a competition of boundary-layer growth and the time evolution of the mixed-layer values of potential temperature (see Equation 5.9) and specific humidity (see Equation 5.10).

A complete description of all the physical assumptions behind the model can be found in Tennekes (1973).

Equation 5.9 and 5.10 are used to replace the temperature and moisture tendencies in Equation 5.5, thereby assuming that at the land surface the absolute temperature and the potential temperature are equal.

Appendix B: Detailed description of Jarvis-Stewart model

In our model the surface resistance r_s is modeled using a Jarvis-Stewart model with the following specifications:

$$r_s = \frac{r_{s,min}}{LAI} f_1(S_{in})\, f_2(w)\, f_3(VPD)\, f_4(T) \tag{5.13}$$

with $r_{s,min}$ as the minimum surface resistance, LAI as the leaf area index of the vegetated fraction, f_1 as a correction function depending on incoming short wave radiation S_{in}, f_2 as a function depending on soil moisture w, f_3 as a function depending on vapor pressure deficit VPD and f_4 as a function depending on temperature T.

The correction functions, where the first three are taken from the ECMWF IFS and the fourth from Noilhan and Planton (1989), are:

$$\frac{1}{f_1(S_{in})} = \min\left(1, \frac{0.004 S_{in} + 0.05}{0.81\,(0.004 S_{in} + 1)}\right) \tag{5.14}$$

$$\frac{1}{f_2(w)} = \frac{w - w_{wilt}}{w_{fc} - w_{wilt}} \tag{5.15}$$

$$\frac{1}{f_3(VPD)} = \exp\left(g_D VPD\right) \tag{5.16}$$

$$\frac{1}{f_4(T)} = 1.0 - 0.0016(298.0 - T)^2 \tag{5.17}$$

where w_{wilt} is the volumetric soil moisture at wilting point, w_{fc} is the volumetric soil moisture at field capacity and g_D is a correction factor for vapor pressure deficit.

Appendix C: Initial and boundary conditions coupled model

Table 5.1 and Table 5.2 show the initial and boundary conditions of the two cases.

Table 5.1: Initial and boundary conditions for model runs of 25 September 2003, Cabauw, The Netherlands and 22 June 2006, Niamey, Niger, without mixed-layer output, which is in Table 5.2.

variable	description and unit	Cabauw	Niamey
P_0	surface pressure [Pa]	102900.	98500.
w_s	large-scale vertical velocity [m s^{-1}]	0.0	0.0
lat	latitude [deg]	51.97 N	13.48 N
lon	longitude [deg]	4.93 E	2.17 E
doy	day of the year [-]	268.	173.
w_g	volumetric water content top soil layer [m^3 m^{-3}]	0.43	0.198
w_2	volumetric water content deeper soil layer [m^3 m^{-3}]	0.43	0.20
c_{veg}	vegetation fraction [-]	0.9	0.2
T_{soil}	temperature top soil layer [K]	282.	300.
T_2	temperature deeper soil layer [K]	285.	290.
a	Clapp and Hornberger retention curve parameter [-]	0.083	0.219
b	Clapp and Hornberger retention curve parameter [-]	11.4	4.90
p	Clapp and Hornberger retention curve parameter [-]	12.	4.
CG_{sat}	saturated soil conductivity for heat [K m^{-2} J^{-1}]	3.6 x 10^{-6}	3.56 x 10^{-6}
w_{sat}	saturated volumetric water content [m^3 m^{-3}]	0.600	0.472
w_{fc}	volumetric water content field capacity [m^3 m^{-3}]	0.491	0.323
w_{wilt}	volumetric water content wilting point [m^3 m^{-3}]	0.314	0.171
$C1_{sat}$	Coefficient force term moisture [-]	0.342	0.132
$C2_{ref}$	Coefficient restore term moisture [-]	0.3	1.8
LAI	leaf area index of vegetated surface fraction [-]	2.	2.
$r_{c,min}$	minimum resistance transpiration [s m^{-1}]	110.	110.
$r_{s,soil,min}$	minimum resistance soil evaporation [s m^{-1}]	50.	50.
g_D	VPD correction factor for surface resistance [-]	0.	0.
z_{0m}	roughness length for momentum [m]	0.05	0.05
z_{0h}	roughness length for heat and moisture [m]	0.01	0.01
α	surface albedo [-]	0.25	0.21
W_l	equivalent water layer depth for wet vegetation [m]	1.4 x 10^{-4}	0.0

Table 5.2: Mixed-layer initial and boundary conditions of model runs of 25 September 2003, Cabauw, The Netherlands and 22 June 2006, Niamey, Niger.

variable	description and unit	Cabauw	Niamey
h	initial ABL height [m]	175.	400.
θ	initial mixed-layer potential temperature [K]	284.5	301.2
$\Delta\theta$	initial temperature jump at h [K]	4.2	3.6
γ_θ	potential temperature lapse rate [K m^{-1}]	$0.0036_{h\leq 950m}$	$0.010_{h\leq 700m}$
		$0.015_{h>950m}$	$0.0034_{h>700m}$
A_{θ_v}	entrainment ratio virtual potential temperature [-]	0.3	0.18
adv_θ	advection of heat [K s^{-1}]	0.	f_θ(t)
q	initial mixed-layer specific humidity [kg kg^{-1}]	0.0044	0.0138
Δq	initial specific humidity jump at h [kg kg^{-1}]	-8.0 x 10^{-4}	-0.0044
γ_q	specific humidity lapse rate [kg kg^{-1} m^{-1}]	-1.2 x 10^{-6}	-1.4 x 10^{-6}
adv_q	advection of moisture [kg kg^{-1} s^{-1}]	0.	f_q(t)
u	initial mixed-layer wind speed [m s^{-1}]	5.	5.
Δu	initial momentum jump at h [m s^{-1}]	3.	0.
γ_u	free atmosphere wind speed lapse rate [s^{-1}]	0.002	0.001
f_θ(t)	-1.0 x 10^{-4} [K s^{-1}] $_{t\leq 11hUTC}$		
	-1.0 x 10^{-4} *max*(1. - 0.36 (t_{hUTC} - 6), -1) [K s^{-1}] $_{t>11hUTC}$		
f_q(t)	4.17 x 10^{-8} *max*(1. - 0.18 (t_{hUTC} - 6), 0) [kg kg^{-1} s^{-1}] $_{t\leq 11hUTC}$		

6

Land-atmosphere coupling explains the link between pan evaporation and actual evapotranspiration trends in a changing climate

Decreasing trends in pan evaporation are widely observed across the world as a response of the climate system to changes in temperature, precipitation, incoming radiation and wind speed. Nevertheless, we only partially understand how trends in actual evapotranspiration are linked to those trends. Here, we use a model to show that regulation of the near-surface temperature and humidity by land-atmosphere feedbacks results in a strong connection between pan evaporation, actual evapotranspiration and vapor pressure deficit (VPD) depending on the climate forcings. When climate change occurs, the feedbacks direct the system towards a different combination of the three variables. If we know the trends in pan evaporation, VPD and wind speed, we can therefore infer the change in the forcings and estimate the trend in actual evapotranspiration.

6.1 Introduction

A widespread decline in pan evaporation has been observed over the second half of the 20th century (Peterson et al., 1995; Golubev et al., 2001). This was initially regarded as a large controversy—in an environment where temperature is rising, evaporation was expected to increase (Brutsaert and Parlange, 1998). It is, however, only partially understood how pan evaporation is related to the actual evapotranspiration from its surroundings. Only few long term data sets are available for this variable (Teuling et al., 2009; Seneviratne et al., 2010). Therefore, interpreting trends in pan evaporation is key to inferring past and future changes in the terrestrial water cycle. Three hypotheses (Brutsaert and Parlange, 1998; Roderick and Farquhar, 2002; Roderick et al., 2007) with very different implications for the actual evapotranspiration have been put forward to explain decreasing pan evaporation.

This chapter is published as van Heerwaarden et al. (2010b).

The first hypothesis stresses the fact that pan evaporation is a measure of the capacity of the atmosphere to take up water—it does not take into account the supply at the land surface. If global warming accelerates the hydrologic cycle, the increase in actual evapotranspiration reduces the atmospheric capacity to take up water, thus suppressing pan evaporation. This effect is likely strongest in water-limited environments.

A second hypothesis links the decline to global dimming, which is the widely observed decrease in incoming short wave radiation due to increased aerosols and/or cloudiness (Roderick and Farquhar, 2002). In humid climates, where evaporation is limited by the available energy rather than by the water supply at the land surface, this explanation is considered to be the main cause of decreasing trends in both pan evaporation and actual evapotranspiration (Teuling et al., 2009).

The most recent hypothesis is based on the observation that in many areas decreasing trends in pan evaporation coincide with decreasing trends in surface winds (Roderick et al., 2007, 2009a). This phenomenon—stilling—reduces the efficiency of the atmosphere in taking up water. Especially in water-limited regions, the pan evaporation is expected to react strongly to stilling (Roderick et al., 2009a), although the implications for the actual evapotranspiration are yet unsure.

In this paper, we investigate the effects of each of the climate forcings—warming, increasing precipitation, dimming and stilling—separately and provide a method to infer the trend in the actual evapotranspiration by linking trends in forcing with trends in the capacity of the atmosphere to take up water.

6.2 Methodology

The theoretical basis of our study is that the land surface and the atmosphere form a tightly coupled system and should be analysed as such (Lyon et al., 2008; Seneviratne et al., 2010). The lowest part of the atmosphere, the turbulent atmospheric boundary-layer (ABL), regulates the surface evaporation by controlling the temperature and humidity of the near-surface air and thus the capacity of the atmosphere to take up water—a quantity usually expressed in terms of vapor pressure deficit (VPD) (Raupach, 2000; van Heerwaarden et al., 2009). The regulating feedbacks have time scales shorter than one day (Raupach, 2000), whereas the time scale of the trends in the forcings is much longer. Therefore, pan evaporation, actual evapotranspiration and VPD do not respond proportionally to the climate forcings, because they are controlled by land-atmosphere feedbacks. For this reason, understanding how the climate forcings influence the local dynamics of evaporation on a daily time scale is essential in interpreting observed pan evaporation trends.

We investigate the impact of feedbacks by using a coupled land-atmosphere model that features a slab model for the ABL, the Penman-Monteith equation for solving the surface energy balance and a two-layer force-restore soil model (van Heerwaarden et al., 2010a). Canopy resistance is parametrized for grass. We set up the model to reproduce one day that is based on the climate of the Great Plains and compute the daytime sums of actual and pan evaporation and the average VPD at 2 m. To investigate the impact of changes in the climate forcings, we perform sensitivity analyses on the early-morning temperature (warming), soil moisture (increasing precipitation), incoming short wave radiation (dimming) and geostrophic

wind speed (stilling). These variables are all either initial or boundary conditions of our model. In Figure 6.1a we show how the climate forcings enter into the daily dynamics of evaporation. Three of the climate forcings, respectivily temperature, wind speed and the amount of incoming short wave radiation, can be of similar magnitude in other regions, both arid and humid, where decreasing pan evaporation has been observed. Therefore, by taking soil moisture as one of the two free variables in each sensitivity study, our results estimate the impact of the climate forcings from arid to humid conditions, despite being based on the Great Plains climatology.

While our research focuses on local feedbacks according to the recent framework of Shuttleworth et al. (2009), our setup also covers partly nonlocal changes in the atmosphere, as increases in early morning temperature are merely related to global warming, while changes in the geostrophic winds are associated with modifications to the global atmospheric circulation.

6.3 Separate impact of climate forcings

First, we find that both actual and pan evaporation respond positively to warming (Figure 6.1b). The former, however, is more sensitive to the rise than the latter and at high temperatures in arid conditions (low soil moisture), pan evaporation even becomes insensitive to temperature variations, something that has been observed in data sets over Australia (Roderick et al., 2009b). VPD is found to increase strongly with temperature if other conditions are kept constant (moving from bottom to top in Figure 6.1b), whereas pan evaporation becomes relatively insensitive to temperature change at high temperatures. Under such conditions, the atmosphere takes up evaporated water so efficiently, that only the available energy limits the pan evaporation.

Second, if we move from left to right in Figure 6.1b, 6.1c and 6.1d to find the impact of increasing precipitation, it is clear that changes in pan evaporation are not in line with changes in the actual evapotranspiration. Instead, we reproduce the complementary relationship between pan evaporation and actual evapotranspiration that formed the basis of the first hypothesis (Brutsaert and Parlange, 1998). At all temperatures and from arid to humid conditions an increase in soil moisture leads to an increase in the actual evapotranspiration and a reduction in pan evaporation. This confirms the observations of Lawrimore and Peterson (2000), who show that in the USA the complementary relationship between pan evaporation and actual evapotranspiration even holds for the wettest soils. Therefore, evaporation never becomes fully controlled by radiation. Note that in sharp contrast with the effects of temperature rise, increasing precipitation largely reduces the VPD. While Roderick and Farquhar (2002) introduced global dimming as the essential mechanism behind decreasing pan evaporation at constant VPD, we find that VPD could remain constant without dimming, given the right combination of warming and wetting. Nevertheless, we will show in the next section that Roderick and Farquhar (2002) are correct in their interpretation that dimming is essential in linking measured trends in pan evaporation and VPD.

A reduction in short wave radiation (dimming) leads to uniform decreases in both actual and pan evaporation that follow our intuition—less energy, less evaporation (Figure 6.1c). A comparison of actual evapotranspiration between arid and humid places hints at the existence

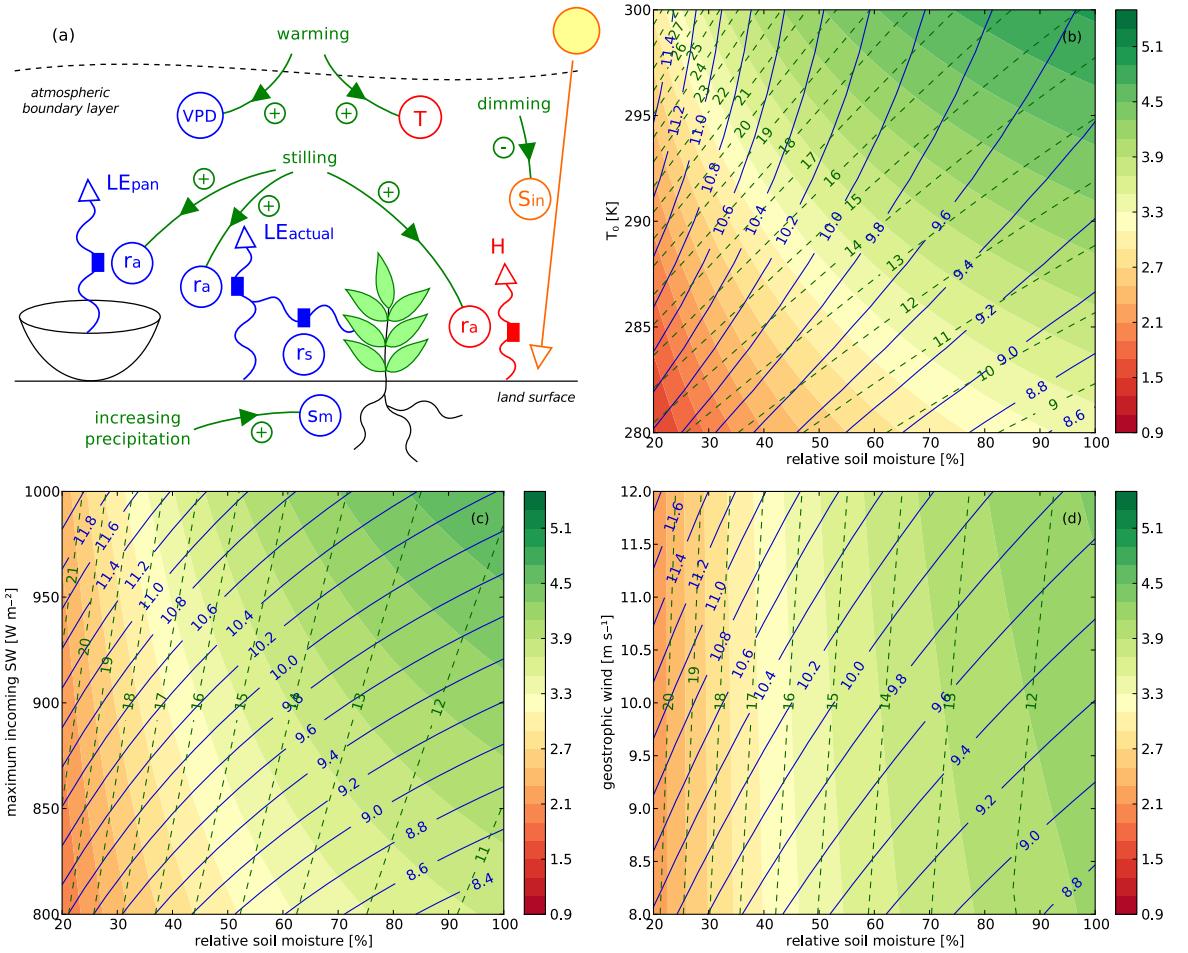

Figure 6.1: ***Impact of climate forcings on pan evaporation and actual evapotranspiration.*** *Panel a shows how climate forcings enter the daily cycle of evapotranspiration. Here, LE_{pan} is the pan evaporation, LE_{actual} is the actual evapotranspiration, VPD is the vapor pressure deficit, T the temperature, S_{in} the incoming short wave radiation, r_a the aerodynamic resistance, r_s the surface resistance and s_m is the soil moisture. The other panels show daytime sums (over 10 h) of actual evapotranspiration in mm (shades), pan evaporation in mm (blue contour lines) and the daytime average in vapor pressure deficit in hPa (green contour lines) as a function of the soil moisture and the early morning temperature (panel b), the incoming short wave radiation (panel c) and the geostrophic wind (panel d). All model runs have T_0 = 290 K, relative soil moisture = 60 %, maximum incoming short wave radiation = 900 W m^{-2} and geostrophic wind = 10 m s^{-1} as a reference, which is inspired on the Great Plains climatology. Panel b, c and d therefore share identical values at their center coordinates.*

of a water-limited regime. In arid places, namely, actual evapotranspiration is barely sensitive to the incoming short wave radiation (Teuling et al., 2009), but responds strongly to an increase in soil moisture. This is not the case for pan evaporation. The sensitivity of this variable to dimming is independent of soil moisture. With this result, we show that decreasing pan evaporation trends in water-limited areas such as India (Roderick et al., 2009a) are strongly influenced by dimming.

Stilling is the last phenomenon that entered the pan evaporation trends discussion (Roderick et al., 2007). This phenomenon is, similar to increasing precipitation, an excellent example to show that pan evaporation trends are not a good proxy for trends in actual evapotranspiration (Figure 6.1d). Pan evaporation is strongly correlated to the wind speed as a 1 m s^{-1} lower

geostrophic forcing can lead up to a 0.4 mm d^{-1} reduction in pan evaporation. The actual evapotranspiration and the VPD, however, show only a very minimal sensitivity to stilling. Despite the fact that our figure confirms the finding that pan evaporation is particularly sensitive to variations in wind speed in arid climates where a large VPD is common (Roderick et al., 2009b), the sensitivity of the actual evapotranspiration to stilling is largest in humid conditions. If there is only little soil moisture, the evaporation is water-limited, and stilling does not feed back on actual evapotranspiration or VPD because the evaporation is insensitive to the atmospheric demand for water and the evaporation flux is too small to influence the VPD. When there is ample soil water, the demand of the atmosphere to take up water becomes relatively more important, which results in an actual evapotranspiration that is sensitive to wind speed.

6.4 Combined impact of climate forcings

With the previous analyses we have demonstrated that each of the climate forcings has a very distinct effect on the relationship between pan evaporation, actual evapotranspiration and VPD. We proceed now by showing that with a set of surface measurements that contain pan evaporation, VPD and wind, we can give a reliable indication of the change in the actual evapotranspiration. We assume that from the four climate forcings we know the temperature rise and the stilling, while we perform a sensitivity analysis on the soil moisture changes and the incoming short wave radiation, since the impacts of these two forcings forms the basis of the debate on the pan evaporation trends. To demonstrate this approach, we apply it to the Great Plains region.

We have taken the forcings for 1950 (Trenberth et al., 2007; Klink, 1999; Hobbins et al., 2004) to run a reference case with our model. Subsequently, we have rerun the model with the temperature (+0.5 K) and wind speed (-0.5 m s^{-1}) characteristic for the year 2000 and a range of soil moisture and incoming radiation values that vary around their magnitudes in the reference case. From these runs, we have subtracted the reference case to get an indication of the trends from past to present as a function of the trend in soil moisture and the trend in incoming radiation (Figure 6.2).

Using the observed changes in temperature and wind speed, but assuming no changes in soil moisture and short wave radiation (center of Figure 6.2a), our model produces increasing trends in pan evaporation (+0.15 mm d^{-1}), actual evapotranspiration (+0.13 mm d^{-1}) and VPD (+0.7 hPa). More importantly, wind and temperature changes alone would have led to an increase in actual evapotranspiration that would resemble the increase in pan evaporation. With dimming and increasing soil moisture, however, that relationship vanishes, emphasizing the importance of taking into account all forcings and feedbacks when interpreting pan evaporation trends. In Figure 6.2b we show the same results as in Figure 6.2a, but here we highlight in colored bands possible combinations of trends in soil moisture and short wave radiation that match trends in measured variables.

The pan evaporation over the Great Plains has decreased in the range of 0.4 to 0.5 mm d^{-1} over 50 years (Golubev et al., 2001). Therefore, there is a large range of combinations of soil moisture and short wave radiation trends that are able to reproduce this decrease. The blue band in Figure 6.2b shows that this trend is possible with a strong dimming of 60 W m^{-2}

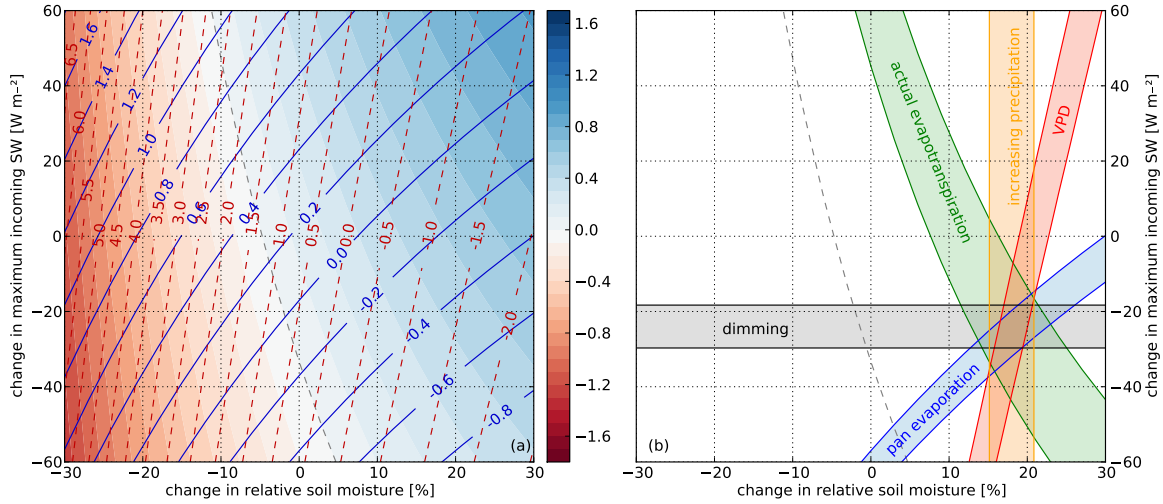

Figure 6.2: ***Impact of changes in climate forcings on changes in pan evaporation and actual evapotranspiration****. Panel a shows long term changes in daytime summed actual evapotranspiration in mm (shades), in daytime summed pan evaporation in mm (blue contours) and daytime mean VPD in hPa (red contours) as a function of the change in soil moisture and the change in maximum incoming short wave radiation over the Great Plains (left panel). The gray dashed line shows the combinations that result in zero trend in actual evapotranspiration. On the left side of the line there is a decreasing trend in actual evapotranspiration, on the right an increasing one. Panel b shows in colored bands combinations of changes in soil moisture and short wave radiation (see panel a) that reproduce the long term change of a specific variable.*

without any soil moisture change, but also with a strong soil moisture increase without any significant dimming. The trend in VPD constrains the possible solutions. Over the Great Plains the VPD has approximately decreased by 1.2 to 1.5 hPa over 50 years (Hobbins et al., 2004). The red band in Figure 6.2b shows the combination of forcings that correspond to the observed VPD trend. By introducing this trend, we limit the possible solutions to a small range of changes in the forcings.

Measurements show that a dimming of approximately 20 W m^{-2} has taken place (Hobbins et al., 2004), while soil moisture increased by nearly 20 per cent (Sheffield and Wood, 2008). The bands of the climate forcings cross almost at the same point as the bands of pan evaporation and VPD, confirming the important role of local feedbacks between the land surface and the ABL in mitigating the impact of changes in forcing and proving the consistency of the measurements. Now, we can make a reliable estimate of the sign and the magnitude of the trend in actual evapotranspiration. Based on the area where the blue and the red band cross, we estimate the trend to be positive with values ranging from 0.3 to 0.45 mm d^{-1} over 50 years. This is in line with water balance studies of the Mississippi basin (Milly and Dunne, 2001).

It should be noted that the crossing of the measurements is located far right of the line that splits the combinations of dimming and increasing precipitation into negative and positive trends. This strengthens the interpretation that the trend in actual evapotranspiration is positive. In addition, the line is nearly vertical. This indicates that despite the large influences that dimming has on pan evaporation, the actual evapotranspiration trend in this region is barely sensitive to it (see Teuling et al., 2009).

6.5 Summary and perspective

In this study we showed using a model how pan evaporation, actual evapotranspiration and VPD are interrelated due to land surface-atmosphere feedbacks. Each climate forcing, such as global warming, increasing precipitation, global dimming or stilling, has a distinct impact on these variables. Therefore, we can interpret which climate forcing drives pan evaporation trends and infer the trend in actual evapotranspiration from data sets containing pan evaporation, VPD and wind speed. This we showed for the Great Plains, USA.

Our findings can help in interpreting whether actual evapotranspiration is increasing or decreasing as an effect of climate change. One of our main conclusions is that an increase in soil moisture leads to more actual evapotranspiration and less pan evaporation under all conditions (Figure 6.1b). If we combine that with our finding that, except over wet soils, the actual evapotranspiration is more sensitive to changes soil moisture than to changes in short wave radiation (Figure 6.1b and 6.1c), we expect the global evaporation to have increased. Nevertheless, Wild et al. (2004) speculate that in the second half of the 20th century an increased moisture advection from the oceans enhanced the precipitation over land, but suppressed the evaporation—opposite to our expectations. In most places where increasing precipitation has been observed, such as in the central part of the USA and Russia, evaporation is water-limited and/or strongly coupled to soil moisture (Koster et al., 2004). Since we showed that under these conditions the atmospheric demand for water barely influences the actual evapotranspiration (Figure 6.1d), it is hard to believe that advection is able to suppress evaporation to such an extent that it can compensate for the enhancing effect of increasing precipitation.

7

Relative humidity as an indicator for cloud formation over heterogeneous land surfaces

The influence of land surface heterogeneity on potential cloud formation is investigated using relative humidity as an indicator. This is done by performing numerical experiments using a large eddy simulation model (LES). The land surface in the model was divided into two patches that had the same sum of latent and sensible heat flux, but different Bowen ratios in order to simulate heterogeneous land surfaces. For heterogeneity in the meso-γ scale (2-20 km) sensitivity analyses were carried out on the heterogeneity amplitude (Bowen ratio difference between contrasting areas) and the inversion strength of potential temperature and specific humidity. The competition between absolute temperature decrease by ABL growth and dry-air entrainment in heterogeneous conditions is analyzed using the LES results. First, it was shown that entrainment is located and enhanced over patches with higher Bowen ratios (warm patches) than their surroundings (cold patches). The heterogeneity-induced strong thermals can further penetrate the inversion at the ABL top, thereby reaching lower absolute temperatures than in homogeneous conditions. Second, due to the heterogeneity induced circulations the moisture is located over the warm patch and higher time averaged RH at the ABL top (RH_{zi}) than over the cold patches are found here, even for dry atmospheres. These RH_{zi} exceed values found over homogeneous land surfaces and are an indication that surface heterogeneity may facilitate cloud formation. In vertical profiles of RH few differences are found between the homogeneous and heterogeneous cases, but the essential heterogeneity induced modifications are in the variability within the domain.

7.1 Introduction

Convective cloud formation over land is a complex phenomenon due to the strong interaction between the land surface and the atmospheric boundary layer (ABL) (Freedman et al., 2001; Kang et al., 2007). Previous studies (e.g. Ek and Mahrt, 1994; Ek and Holtslag, 2004) described the underlying physics of these interactions over homogeneous land surfaces. However, it has

This chapter is published as van Heerwaarden and Vilà-Guerau de Arellano (2008).

been suggested (e.g. Crook, 1997; Pielke, 2001; Kang et al., 2007) that the timing and location of cloud formation are sensitive to heterogeneous forcings at the land surface, which depend on the spatial variability of land use, soil moisture content and topography.

Heterogeneous forcings occur over a wide range of scale levels, but the strongest effects on ABL properties are found when the heterogeneities are in the meso-γ scale (2-20 km) (Mahrt, 2000), since they modify the horizontal and vertical structure of the ABL by inducing circulations. A consequence is that the effects of heterogeneity-induced circulations are difficult to be represented well by mesoscale and large-scale models, as these flows are mostly in the subgrid scales of the models. To date we lack adequate parameterizations, because the effects of circulations on cloud formation in the meso-γ scale are not fully understood.

For scale levels smaller and larger than the meso-γ scale, there is observational and modeling evidence that convective cloud formation and precipitation are enhanced by heterogeneous forcings (e.g. Pielke, 2001; Chagnon et al., 2004; Chagnon and Bras, 2005; Kang et al., 2007). However, these scales differ from the meso-γ scale as the smaller-scale heterogeneities blend in the surface layer and their effects can be introduced by altering the surface parameters, whereas the larger-scale heterogeneities blend above the ABL and induced motions can be resolved well by mesoscale models (Mahrt, 2000).

A key tool for simulating the effects of surface heterogeneity on the ABL is a large-eddy simulation (LES) model, as this can resolve the most relevant scales of turbulent atmospheric flows (e.g. Moeng, 1984). Previous studies (e.g. Hechtel et al., 1990; Hadfield et al., 1991; Avissar and Schmidt, 1998; Letzel and Raasch, 2003; Patton et al., 2005) used the LES technique to investigate the properties of the heterogenously forced ABL. They explained that circulations can be induced by heterogeneous forcings and demonstrated the dependence of these circulations on the length scale and the amplitude of the heterogeneity. There is agreement on the existence of a typical length scale (sequence of one cold and warm patch) at which the ABL is modified the most. According to Avissar and Schmidt (1998) (AV98) this scale is 5-10 km, whereas Patton et al. (2005) (PA05) formulate this range as 5 - 8 times the boundary layer height. The precise effects of amplitude (heat flux difference between different patches at the land surface) are not well understood (Mahrt, 2000). On the basis of these conclusions, we take the heterogeneity length constant in our study and perform a sensitivity analysis on the heterogeneity amplitude. In this study, we define the amplitude as the difference in Bowen ratio between two patches.

Our study focuses on the role of heterogeneous land surfaces in the formation of convective clouds in the meso-γ scale. Avissar and Liu (1996) found an enhancement of clouds and precipitation on this scale with a mesoscale model. However, Mahrt (2000) showed that for these models the surface-layer parameterizations are not valid over heterogeneous landscapes, because induces circulations are not resolved well. Furthermore, PA05 illustrated the failure of free convective scaling laws over a heterogeneous land surface. The computer power we have available today allows for an LES study at high resolution, in which the flow, including the entrainment processes, is dynamically resolved (Sullivan et al., 1998; Pino et al., 2003). In contrast to Avissar and Liu (1996), we did not study cloudy boundary layers, but focus on the use of relative humidity at the ABL top (RH_{zi}) as an indicator for cloud formation (Ek and Mahrt, 1994). On the basis of the general structure changes as shown by Patton et al. (2005) (PA05) and Avissar and Schmidt (1998) (AV98) we study the key elements of the boundary

layer dynamics over a heterogeneous surface that determine RH_{zi}.

A process that merited special attention in the evolution of RH_{zi} is the entrainment of warm and dry air from the free atmosphere into the ABL, since it influences both boundary layer growth and the thermodynamic structure of the ABL. Ek and Mahrt (1994) studied the role of entrainment on RH_{zi} in a bulk model and showed that the evolution of RH_{zi} is a complex competition between the absolute temperature decrease and the drying effect of ABL growth via entrainment and of surface heating and evaporation. They found that the relative magnitudes of the involved processes are largely dependent on the potential temperature and moisture discontinuities in the inversion layer. Here, we extend the previous work to heterogeneous land surfaces. The effects of heterogeneous forcings on entrainment are still under debate, as according to AV98 and Letzel and Raasch (2003) entrainment is enhanced by heterogeneous forcings, while PA05 found no evidence for this. Therefore, we begin our research by investigating entrainment over heterogeneous landscapes, prior to analyzing the heterogeneity induced changes on the moisture structure of the ABL top.

This first part of this paper is devoted to a study of the influence of the heterogeneity amplitude on the entrainment processes and the boundary layer height. Although AV98, Letzel and Raasch (2003) and PA05 have already concluded that ABLs are higher over warm patches than over cold patches, the precise role of heterogeneity amplitude and its influence on entrainment processes remain open. Here, we address these issues by studying the spatial distribution of entrainment and comparing the total entrainment for cases with varying heterogeneity amplitudes and inversion strengths for potential temperature and specific humidity. By applying a statistical decomposition between turbulent and mesoscale components, we investigate the contribution of the heterogeneity-induced circulation to entrainment.

In the second part of this paper, we connect our findings about the ABL height and entrainment processes to the thermodynamic changes in the ABL by studying the specific humidity and the RH. We analyzed the spatial structure of temperature, moisture and RH near the top of the ABL for different heterogeneity amplitudes and inversion strengths of potential temperature and specific humidity. Vertical profiles of the RH and the variances of potential temperature and specific humidity were analyzed in order to study the modification of the horizontally averaged profiles by heterogeneous forcings. Here, we attempt to generalize the results of the different initial conditions to conclude if, and in which conditions, land surface heterogeneity influences the RH and if this is beneficial for cloud formation.

7.2 Methods

7.2.1 Model description

The study is based on numerical experiments performed using the Dutch Atmospheric LES (DALES) model, which was initially developed by Nieuwstadt and Brost (1986), improved by Cuijpers and Duynkerke (1993) and updated to a parallel-processing version by Dosio et al. (2005). DALES solves the filtered Navier-Stokes equations with the Boussinesq approximation applied.

In this study, we introduce a fundamental modification to the DALES code by implementing a third-order Runge-Kutta time integration scheme combined with a 5th-order advection scheme (Wicker and Skamarock, 2002). This scheme resolves more accurately steep gradients

that are characteristic for the ABL top, which allows for an improved simulation of the fine scale entrainment processes.

DALES has periodic boundary conditions in the horizontal plane. At the land surface the surface fluxes for heat $\overline{w'\theta'}$ and moisture $\overline{w'q'}$ and the friction velocity u_* are prescribed. There is a sponge layer in the top of the model, which prevents the reflection of gravity waves back into the model domain.

7.2.2 Experimental setup

For this study we discretized our LES-domain into 256 x 192 x 192 grid cells on the x, y and z axes. The grid length is 25 m in x and y and 12.5 m in z and our domain is thus 6400 x 4800 x 2400 m. According to Bretherton and coauthors (1998) our vertical resolution is sufficient to resolve most of the scales in the entrainment process. All cases are dry convective boundary layers with prescribed surface heat fluxes. There is no background wind ($U_g = V_g = 0$ m s^{-1}) and the friction velocity u_* is fixed at 0 m s^{-1} i.e. free local convection. The initial profiles and surface forcings correspond to the temperature and moisture conditions of a typical early summer day in The Netherlands. All simulations have an initial potential temperature profile that is constant with height for the first 800 m. On top of this layer we prescribe a temperature jump (case dependent) and after this jump the stratified free atmosphere has a temperature lapse rate equal to 0.006 K m^{-1}. The initial specific humidity profile in the mixed layer is constant with height (0.005 kg kg^{-1}), with a jump on top of the mixed layer and a constant value in the free atmosphere (case dependent).

The selected value for the potential temperature jump ($\Delta\theta$) determines the growth rate of the ABL. In case of a small jump, the ABL grows fast and and due to the pressure decrease at the top, the ABL top cools in terms of absolute temperature, which has a positive effect on the RH_{zi}. On the other hand, if the jump is small, a large amount of free atmospheric air enters the ABL. For this air the specific humidity jump (Δq) determines the dryness and thus in what extent the cooling can be compensated by drying. To simulate all combinations, we classified the initial conditions in four regimes (see Table 7.1).

Table 7.1: Four regimes in the relative humidity evolution in the entrainment zone, defined by the initial jump conditions

	$\Delta\theta$ = 2.0 K	$\Delta\theta$ = 0.5 K
Δq = 0 g kg^{-1}	(1) Small cooling rate little dry-air entrainment	(2) Large cooling rate, little dry-air entrainment
Δq = −4 g kg^{-1}	(3) Small cooling rate, modest dry-air entrainment	(4) Large cooling rate, extensive dry-air entrainment

In order to create heterogeneous forcings, the land surface is divided in two parts along the x-axis. All grid cells in the left patch (cells 1 to 128) are characterized by a Bowen ratio below the average Bowen ratio (the cold patch) and the cells in the right patch (grid cell 129 to 256) have an above average Bowen ratio (the warm patch). The length of the heterogeneity (one cycle of a cold and a warm patch) is therefore 6400 m. As the ABL heights vary between 1000 and 1100 m, the ratio between the heterogeneity length and the ABL height is in the range that

AV98 and PA05 specify for the strongest mesoscale contribution to the flow.

For regime 1 (see Table 7.1), we performed a sensitivity analysis on the heterogeneity amplitude, which is defined as the Bowen ratio difference between the cold and the warm patches. In all cases, for every location at the land surface, the sensible H and latent LE heat flux add up to 360 W m^{-2}, but the Bowen ratios for the cold and the warm patch differ among the simulations (see Table 7.3). For the three other regimes we simulated the homogeneous and the largest amplitude case.

Table 7.2: Initial conditions for all LES simulations. θ_{ML} is the initial mixed layer potential temperature, $\Delta\theta$ is the temperature jump at 800 m, Δq is the temperature jump at 800 m, regimes follow from Table 7.1.

simulation	θ_{ML} [K]	$\Delta\theta$ [K]	Δq [kg kg^{-1}]	regime
*Case*1	293.0	2.0	0.000	1
*Case*2	293.0	2.0	0.000	1
*Case*3	293.0	2.0	0.000	1
*Case*4	293.0	2.0	0.000	1
*Case*5	293.0	2.0	0.000	1
*Weak*1	294.5	0.5	0.000	2
*Weak*5	294.5	0.5	0.000	2
*Case*1*dry*	293.0	2.0	-0.004	3
*Case*5*dry*	293.0	2.0	-0.004	3
*Weak*1*dry*	294.5	0.5	-0.004	4
*Weak*5*dry*	294.5	0.5	-0.004	4
*Case*1*large*	293.0	2.0	0.000	1
*Case*5*large*	293.0	2.0	0.000	1

Table 7.3: Surface boundary conditions for all LES simulations. H_L is the sensible heat flux of the cold patch, H_R is the sensible heat flux of the warm patch, LE_L is the latent heat flux of the cold patch, LE_R is the latent heat flux of the warm patch, β_L is the Bowen ratio of the cold patch, β_R is the Bowen ratio of the warm patch.

simulation	H_L [W m^{-2}]	H_R [W m^{-2}]	LE_L [W m^{-2}]	LE_R [W m^{-2}]	β_L [-]	β_R [-]
*Case*1	120	120	240	240	0.50	0.50
*Case*2	105	135	255	225	0.41	0.60
*Case*3	90	150	270	210	0.33	0.71
*Case*4	75	165	285	195	0.26	0.85
*Case*5	60	180	300	180	0.20	1.00
*Weak*1	120	120	240	240	0.50	0.50
*Weak*5	60	180	300	180	0.20	1.00
*Case*1*dry*	120	120	240	240	0.50	0.50
*Case*5*dry*	60	180	300	180	0.20	1.00
*Weak*1*dry*	120	120	240	240	0.50	0.50
*Weak*5*dry*	60	180	300	180	0.20	1.00
*Case*1*large*	120	120	240	240	0.50	0.50
*Case*5*large*	60	180	300	180	0.20	1.00

To verify if our results are sensitive to the model domain, we simulated two additional cases based on *Case*1 and *Case*5 in which the domain is twice as long (512 cells in x, thus 12800 m). In this setup the heterogeneous case consists of four patches (see the *large* cases in Table 7.2 and Table 7.3).

All cases were initially integrated for three hours. After this period a quasi-steady state was reached for all cases. We define a quasi-steady state as a situation in which the ABL-averaged turbulent kinetic energy (TKE) normalized by Deardorff's convective velocity scale w_*^2 is constant in time (PA05). After three hours of spin-up, the three components of the wind, the potential temperature and specific humidity were recorded for each grid cell every five seconds for one hour. The statistics are thus based on 720 time steps.

7.2.3 Statistical methods

To calculate the turbulent statistics of our model runs we used a method based on phase averaging (Hussain and Reynolds, 1970). A similar method was previously employed in the LES study of heterogeneous land surfaces by PA05. Our model forcings are heterogeneous only on the x-axis and thus homogeneous on the y-axis. Therefore, we assume that a local spatial average can be calculated by averaging over y. We decompose an arbitrary space- and time-dependent turbulent variable $\phi_{x,y,z,t}$ in two components.

$$\phi_{x,y,z,t} = \left\langle \phi \right\rangle_{x,z,t} + \phi'_{x,y,z,t} \tag{7.1}$$

We name the first term on the right hand side the local average, which is the spatial average of all values on the y-axis that share the same x, z and t-coordinates. Under homogeneous conditions $\left\langle \phi \right\rangle_{x,z,t}$ equals the slab average as there are no variations in local spatial averages in a horizontal plane. The difference between the local average and the slab average is thus a measure of advection and therefore of the contribution of the heterogeneous surface forcings to the statistics. This contribution we call the mesoscale component from now on. The turbulent fluctuation $\phi'_{x,y,z,t}$ is the second term. In the further analyses we denote spatial averages in the y-direction as $\left\langle \phi \right\rangle$ and in the x-direction as $\left[\phi \right]$. Temporal averages are denoted as $\overline{\phi}$.

7.3 Results

7.3.1 Entrainment processes and ABL growth

Structure of the ABL top and entrainment

Our first objective was to study the influence of the heterogeneity amplitude on entrainment processes and on the evolution of the ABL height. Figure 7.1 shows the 1-h averaged ABL height as a function of space along the x-axis. The heights are derived using the maximum potential temperature gradient following the procedure in Sullivan et al. (1998). For every x, y-coordinate the ABL height is calculated for each time step and these values are averaged over y and time. The values in the figure are scaled by the horizontally averaged ABL height.

Figure 7.1 shows that the presence of horizontal variability in the surface forcings results in a spatial variability of the ABL height z_i along the heterogeneity. The homogeneous case (*Case*1) has an ABL height that is $z/z_i = 1.0$ with small fluctuations around this value, whereas

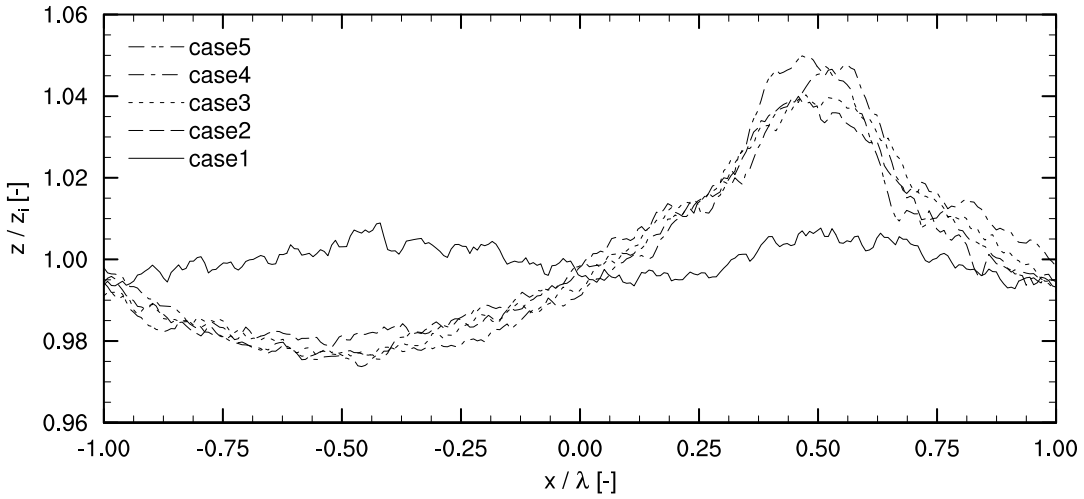

Figure 7.1: Averaged ABL height along the x-coordinate during 1 h. Horizontal coordinates are scaled by the patch size λ, vertical coordinates are scaled by the time- and area-averaged ABL height $\left[\overline{\langle z_i \rangle}\right]$.

in all heterogeneous cases a clear spatial pattern is visible, with a deeper boundary layer over the warm patch. Therefore, we corroborate the earlier findings of AV98 and PA05 who showed ABL height variations for different heterogeneity lengths.

Slight variations in this pattern are visible, caused by differences in the heterogeneity amplitude. For instance, above the warm patch ($x/\lambda = 0.5$), there is an increase in ABL height related to the larger heterogeneity amplitude. *Case*2 has a height that is 4 per cent larger than the average ABL height ($z/z_i = 1.04$), whereas *Case*5 attains values up to 5 per cent larger ($z/z_i = 1.05$) than the average. Over the cold patch, the opposite effect is visible, with a decreasing ABL height for increasing heterogeneity amplitude. In spite of the small variations caused by the heterogeneity amplitude, the main variations in ABL height are due solely to the presence of a heterogeneity-induced circulation. For cases with weak inversions (not shown), we found for *Case*5*dry* the same relative increase over the warm patch ($z/z_i = 1.05$).

Figure 7.2 shows the spatial distribution of entrainment and contains the cross sections of the 1-h averaged values of the normalized turbulent heat flux $\overline{\langle w'\theta_v' \rangle} / \left[\overline{\langle w'\theta_v' \rangle}_0\right]$ for *Case*2 and *Case*5. The overlying vector plot shows the wind that is driven by the differential heating of the domain. Before analyzing the figure, it is worth mentioning that the average subgrid scale contribution to the heat flux at $z/z_i = 0.95$ is 5.6 % for *Case*5 (subgrid flux 0.0011 K m s^{-1}, resolved 0.0183 K m s^{-1}), which indicates that the resolved part largely exceeds the subgrid part, thus that the flow is resolved accurately.

A stronger heterogeneity amplitude results in stronger surface winds towards the center of the warm patch where thermals are merged. *Case*2 has, for instance, a wind of approximately 1 m s^{-1} at $x/\lambda = 0.3$ and $z/z_i = 0.05$, whereas *Case*5 has more than 2 m s^{-1} at the same location. The strongly buoyant thermals that are the product of the merging can penetrate the entrainment zone more vigorously, thereby locally enhancing entrainment, for instance at $x/\lambda = 0.5$ and $z/z_i = 1.0$. The normalized entrainment minima found for *Case*2 are -0.4 and -0.6 times the surface flux, while in *Case*5 the values have a range from -0.8 to -1.0 times the surface flux. These local values largely exceed the ratio of -0.2 times the surface flux that is widely used in parameterizations of the entrainment flux. Although the ABL heights over the

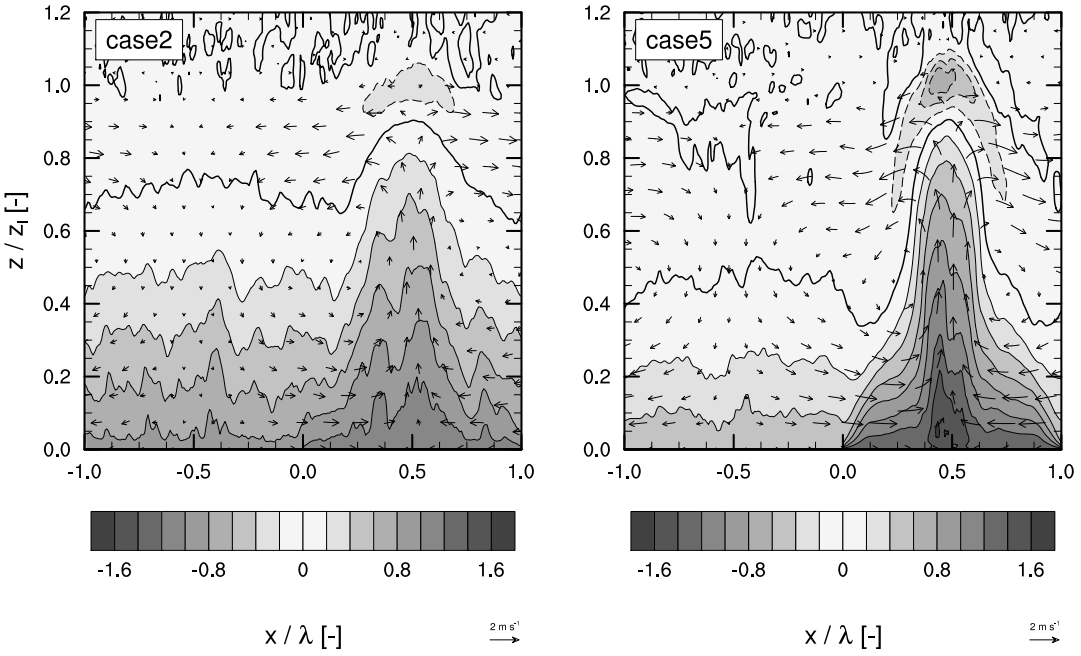

Figure 7.2: Cross-section of the 1-h-averaged normalized turbulent heat transport $\overline{\langle w'\theta_v'\rangle}/\left[\overline{\langle w'\theta_v'\rangle}_0\right]$ *for Case*2 *(left) and Case*5 *(right). Vectors indicate the wind direction and magnitude. The horizontal coordinates are scaled by the patch size* λ *and the vertical coordinates are scaled by the ABL height* $\left[\overline{\langle z_i\rangle}\right]$.

warm patch are only slightly sensitive to heterogeneity amplitude, the entrainment minima increase greatly with increasing amplitude. In the next section we discuss the effects of this local entrainment enhancement on the total area averaged entrainment over the heterogeneous land surfaces.

In contrast to the warm patch, over the cold patch thermals are surpressed by the downward wind of the induced mesoscale circulation (downward motions x/λ = -1.0 to 0.0). At the top of the ABL winds are directed towards the cold patch (x/λ = 0.2 and 0.8). Convergence of air occurs here and the warm air is advected downwards towards the land surface. This downward-moving warm air does not allow thermals generated over the cold patch to reach the ABL top and thereby prevents entrainment over the cold patch. The line at which the turbulent flux becomes zero is located at z/z_i = 0.7 for *Case*2 and at z/z_i = 0.5 for *Case*5. The surpression of upward moving thermals is thus enhanced as heterogeneity amplitude increases. Above the warm patch we find strong upward motions (more than 3 m s^{-1} for *Case*5) over a small area, while the cold patch has gentle downward motions (less than 1 m s^{-1}) over the whole cold patch. We discuss now how the temperature at the ABL top is influenced by the modified entrainment.

Figure 7.3 shows the 1-h averaged space-dependent values for the potential temperature and the absolute temperature near the top of the ABL. The potential temperature is nearly uniform in *Case*1 as expected, although there are some fluctuations which are the result of the domain size. For all heterogeneous cases, the potential temperature at x/λ = 0.5 (core of the thermals) has a range of values approximating 295.1 K. These values are colder than their surroundings, as the thermals have become negatively buoyant in the temperature inversion.

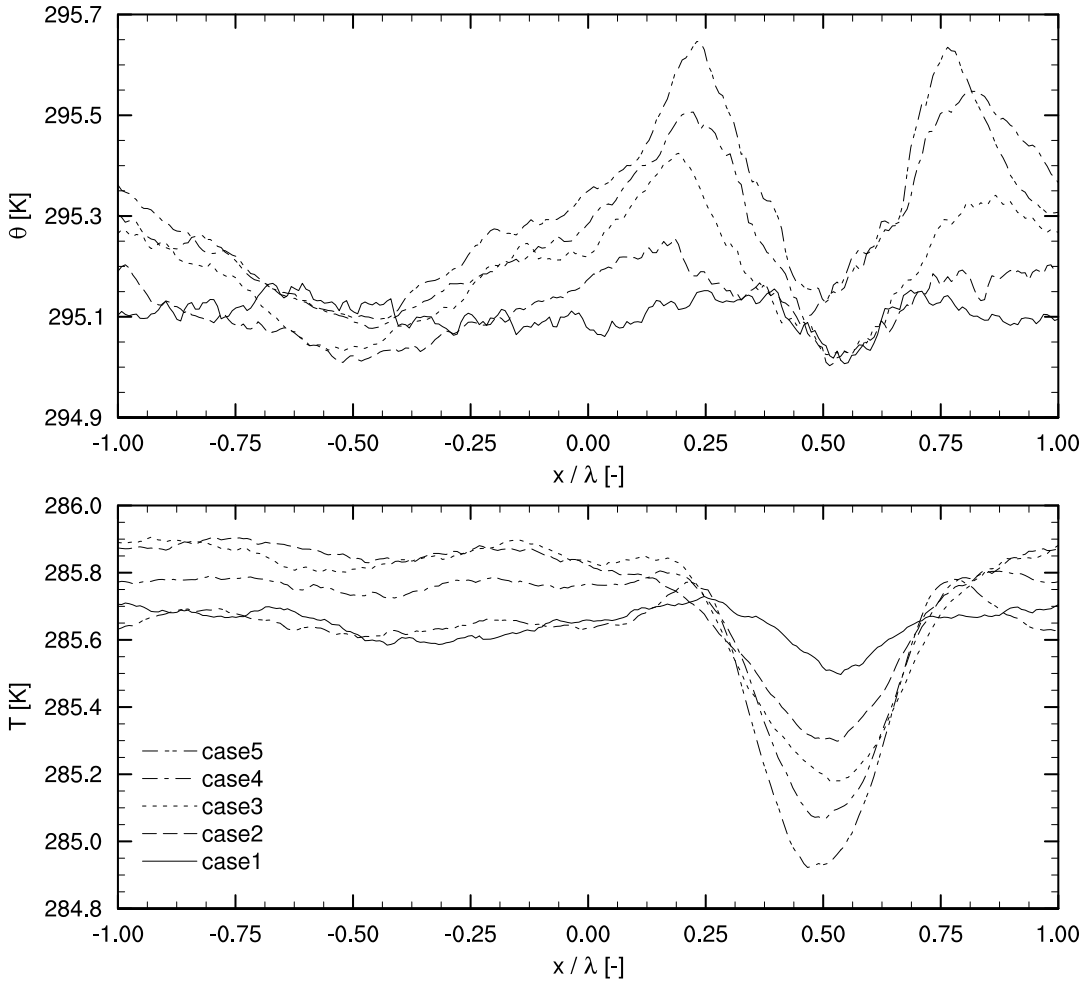

Figure 7.3: 1-h-averaged potential (top panel) and absolute (bottom panel) temperature along the x-axis at $z/z_i = 0.95$. Horizontal coordinates are scaled by the patch size λ.

As shown in Figure 7.2, at the top of the ABL the entrained air is horizontally advected to the cold patch. The entrainment events are very well visible in *Case*5, with the two temperature peaks of 295.7 K at $x/\lambda = 0.25$ and $x/\lambda = 0.75$, caused by the warm free tropospheric air that is engulfing into the ABL.

The absolute temperature at the top of the ABL shows more variation than the potential temperature, because of the variation in boundary layer height over the patches (see Figure 7.1). Although the rising thermals for the heterogeneous cases at $x/\lambda = 0.5$ have comparable potential temperatures at the ABL top, their absolute temperatures decrease if the heterogeneity amplitude increases. The homogeneous *Case*1 has an absolute temperature of 285.5 K, whereas the temperature here gradually decreases, as heterogeneity amplitude becomes larger. For the strongest amplitude case (*Case*5), we find an absolute temperature of 284.9 K. In consequence, under the assumption of equal moisture conditions, the relative humidity will increase for larger heterogeneity amplitudes. In cases characterized by weaker inversions (smaller temperature jump at the ABL top) we found identical variation in the ABL height within the domain (not shown) and therefore the entrainment zone has a similar absolute temperature variability. The fact that weaker inversions do not yield a larger variability in ABL height and temperature may be explained by the nature of the motions in the entrainment zone

in these conditions. If the inversion is weak, folding of the interface between the ABL and the free atmosphere occurs and these type of motions are associated with larger horizontal spatial scales, than entrainment events in strong inversion cases (Sullivan et al., 1998). Therefore, additional ABL height variation in heterogeneous cases with weak inversions may not exists as the effects are spread out in the horizontal.

Area averaged ABL growth and entrainment

Here, we further discuss the effects of surface variability on the thermodynamic vertical profiles. To address these effects, the vertical profiles of the homogeneous *Case*1 are compared with the four heterogeneous cases. Just as a reminder, notice that all cases have the same area-averaged sensible and latent heat flux and initial thermodynamic profiles. Consequently, differences among the simulations must be induced by the heterogeneous forcings and by the subsequent local effects on entrainment.

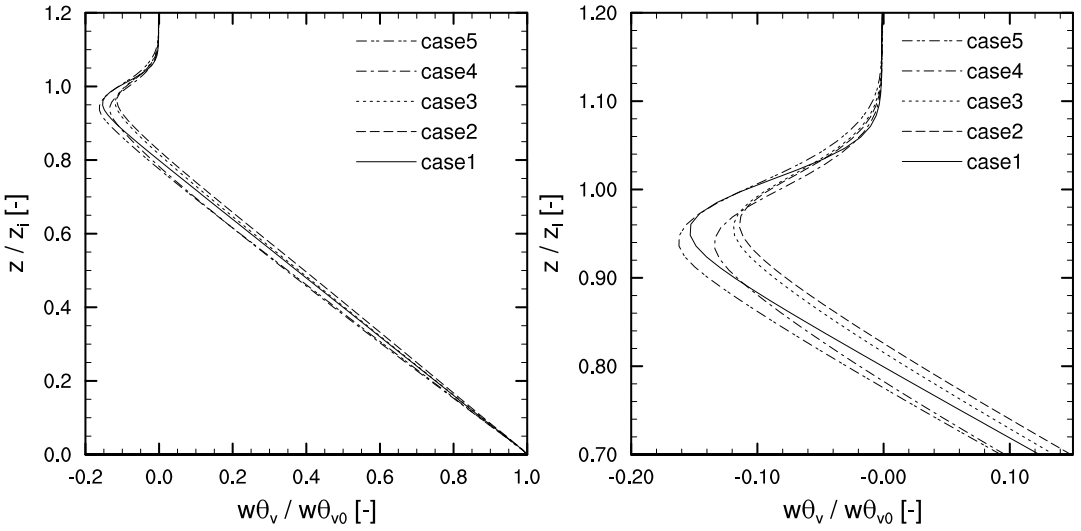

Figure 7.4: Vertical profiles of the 1-h-averaged total heat transport $\left[\overline{w\theta_v}\right]$. *Right-hand panel is a zoom of the left-hand panel. Horizontal coordinates are scaled by the surface sensible heat flux* $\left[\overline{\langle w'\theta'_v\rangle_0}\right]$, *vertical coordinates are scaled by the ABL height* $\left[\overline{\langle z_i\rangle}\right]$.

Figure 7.4 shows the 1-h area averaged heat flux profiles for all the simulations. In spite of the large structural changes that heterogeneity induces, there are only small differences between the homogeneous and heterogeneous cases, although as we show later, the distribution between mesoscale and turbulent contributions to the heat flux varies considerably. All cases show a linear heat flux profile in the ABL (z/z_i = 0 - 0.8) and an area of negative heat flux at the top of the ABL which is characterizing the entrainment zone (z/z_i = 0.8 - 1.1). The curved profiles of the heat flux that AV98 found for heterogeneous cases are not present in our cases. We found linear profiles similar to those in PA05. Therefore, we assume that heterogeneous cases should yield linear profiles and that AV98 results are the effect of the low resolution of their model runs.

The region with negative heat flux is a measure of the contribution of entrainment (vanZanten et al., 1999) to the heating of the ABL. This implies that the depth of the entrainment zone

δ and the magnitude of the minimum flux both correlate positively with the total entrainment. Compared to the homogeneous case, the two smallest amplitude cases (*Case*2 and *Case*3) have a shallower entrainment zone (δ/z_i = 0.85 - 1.1) with a lower minimum flux ($\overline{\langle w'\theta_v'\rangle}/\overline{\langle w'\theta_v'\rangle}_0$ = -0.12). The total entraiment of heat for these two cases thus appears to be less than in the homogeneous *Case*1 (δ/z_i = 0.3, $\overline{\langle w'\theta_v'\rangle}/\overline{\langle w'\theta_v'\rangle}_0$ = -0.16). In the two largest amplitude cases, the entrainment zone have become larger (both δ/z_i = 0.35) than the homogeneous case, characterized by a larger minimum for *Case*5 ($\overline{\langle w'\theta_v'\rangle}/\overline{\langle w'\theta_v'\rangle}_0$ = -0.16), which suggests that more heat is entrained in these cases.

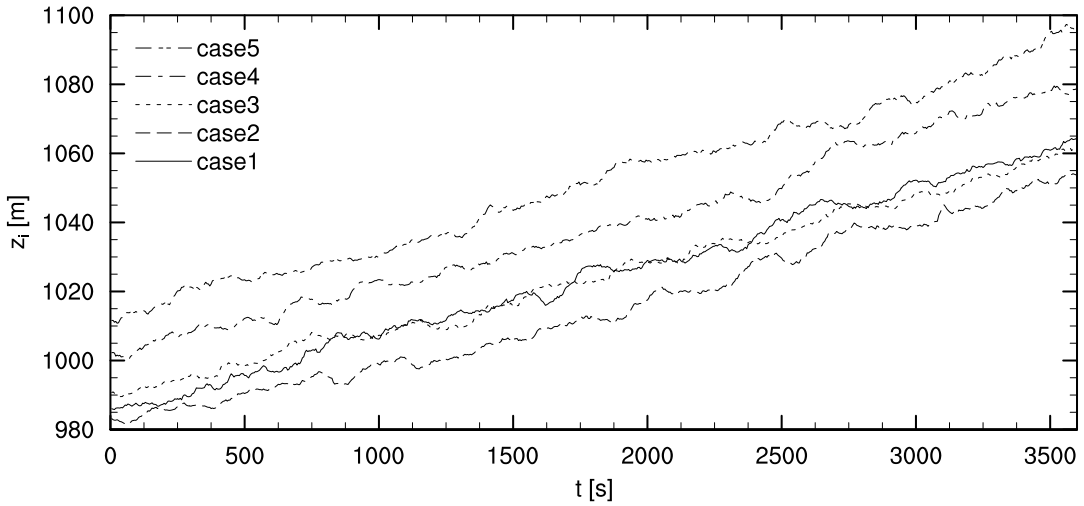

Figure 7.5: Domain-averaged ABL height [$\langle z_i \rangle$] *during the hour of data recording.*

Figure 7.5 shows the temporal evolution of the area-averaged ABL height for all five cases computed following the maximum temperature gradient method (Sullivan et al., 1998). After three hours of spin-up, the ABL heights of *Case*4 (1000 m) and *Case*5 (1010 m) are the largest, but the growth rate of all five cases, which is the entrainment velocity, has a similar magnitude (approximately 70 m h^{-1}). If all cases have the same entrainment velocity, the entrainment differences found in the previous section can not exist. Therefore, the suggested enhancement found in Figure 7.4 may be the result of the horizontal averaging, where the strongest amplitude cases have a deeper negative area due to the greater variability in ABL height over the domain. This connects with the findings of Lilly (2002) who suggest that the smooth heat flux profiles in the entrainment zone found in LES are mostly an effect of horizontal averaging and the that link to the entrainment rate should be made carefuly. PA05 found no significant enhancement of entrainment when they performed a sensitivity analysis of the effect of the heterogeneity length, but they did not vary the heterogeneity amplitude. We showed by varying the amplitude that the results of PA05 are correct and we thus disagree on previous suggestions of AV98 and Letzel and Raasch (2003) that the area averaged entrainment is enhanced. Changes in ABL height are the result of the model spin up, and once the model is in quasi-stationary state, the entrainment rate is constant for all heterogeneity amplitudes. Therefore, only the spatial changes will influence the structure of the RH, but the spatially averaged ABL growth is not affected.

Mesoscale contributions to entrainment

We discussed previously that Figure 7.4 showed similar linear heat flux profiles in the ABL for both homogeneous and heterogeneneous cases. Nevertheless, there is a fundamental difference between the cases. In the homogeneous case all the heat transport is driven by small scale turbulence, but in the heterogeneous cases the total heat flux is the sum of the the mesoscale and turbulent part that add up to the linear profile. The left panel of Figure 7.6 shows the decomposition for *Case*5.

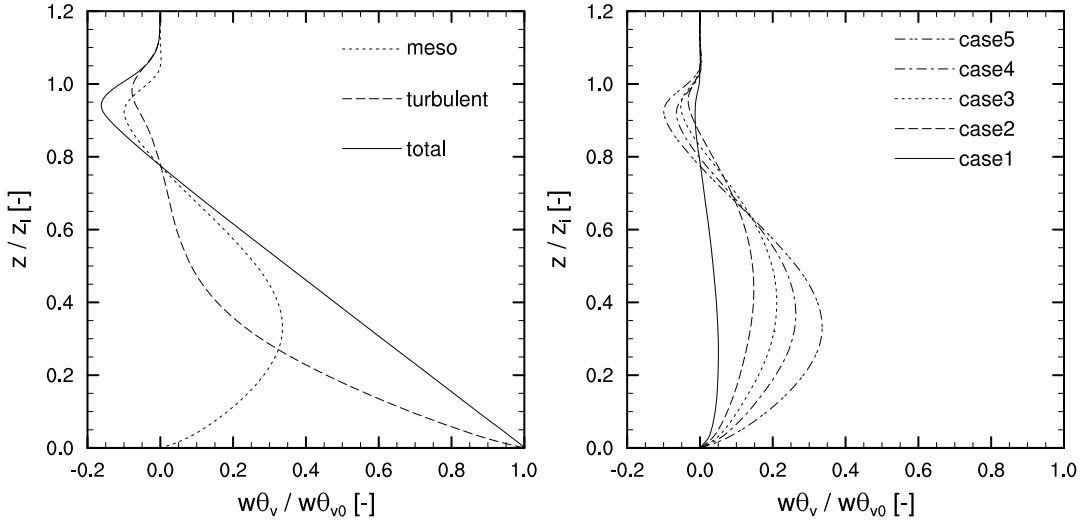

*Figure 7.6: Left panel shows the horizontally-averaged vertical profile of the 1-h-averaged heat transport for Case*5 $\left[\overline{w\theta_v}\right]$ *decomposed in a mesoscale* $\left[\overline{\langle w\rangle\langle\theta_v\rangle}\right]$ *and turbulent contribution* $\left[\overline{\langle w'\theta_v'\rangle}\right]$*. The right panel shows the mesoscale* $\left[\overline{\langle w\rangle\langle\theta_v\rangle}\right]$ *contributions for five cases. Horizonal coordinates are scaled by the surface flux* $\left[\overline{w\theta_{v0}}\right]$ *and the vertical coordinates are scaled by the ABL height* $\left[\overline{\langle z_i\rangle}\right]$*.*

The mesoscale component for the flux is present throughout the whole ABL, but the strongest contributions are found at $z/z_i = 0.3$ for the heat transport, which was also obtained by PA05. The division between mesoscale and turbulent contributions in the entrainment zone shows that the lower region of the entrainment zone ($z/z_i = 0.8$ - 0.95) is mostly driven by mesoscale motions, whereas in the top ($z/z_i = 0.95$ - 1.1) of the entrainment zone the turbulent contribution is the dominant one. The reason is that only the strongest engulfing motions reach the lower half of the entrainment zone. Due to the induced circulation, these events are always at the same location (see the peaks in Figure 7.3) and are therefore enclosed in the mesoscale contribution. They are associated with large pockets of warm tropospheric air that enter the ABL at the edges of the strong thermals that are pushing the inversion layer. In contrast, the small-scale mixing, quantified by the turbulent part, occurs only at the top of the warm patch, but not at a fixed location. For increasing heterogeneity amplitude, the mesoscale contribution to entrainment increases (see right panel in Figure 7.6) as the induced circulation becomes stronger (see wind vectors in Figure 7.2).

*Case*2 has only $\left[\overline{\langle w\rangle\langle\theta_v\rangle}\right] / \left[\overline{w\theta_{v0}}\right]$ = -0.03, while *Case*5 may even reach $\left[\overline{\langle w\rangle\langle\theta_v\rangle}\right] / \left[\overline{w\theta_{v0}}\right]$ = -0.12. We showed in Figure 7.6 that these contributions are caused by large-scale entrainment events, which have a fixed location.

7.3.2 Relative and specific humidity in the ABL

Structure of the specific humidity

In the previous section we focused on the heterogeneity amplitude to study how the strength of the mesoscale circulation influenced entrainment and ABL growth. Now, we discuss the effect of these structure changes on the spatial distribution of specific humidity in the ABL top.

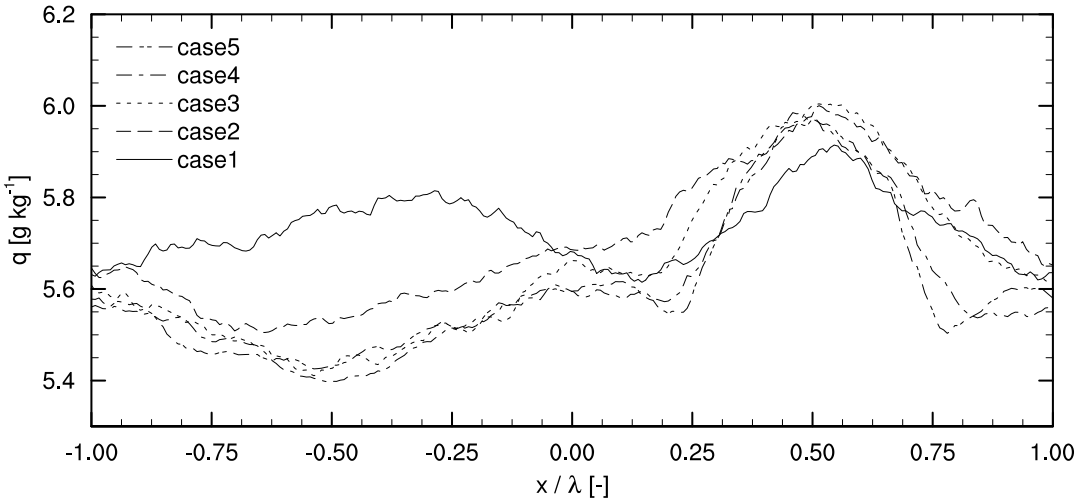

Figure 7.7: 1-h averaged specific humidities q along the x-axis. Horizontal coordinates are scaled by the patch size λ.

Figure 7.7 is a 1-h spatially-dependent cross-section of the specific humidity at $z/z_i = 0.95$. We find that the largest values of the specific humidity are found over the center of the warm patch (6.0 g kg^{-1}). Just as for the potential temperature at z_i, the specific humidity near the ABL top is only slightly dependent on heterogeneity amplitude, as the concentration of specific humidity is nearly the same in the rising thermals (6.0 g kg^{-1}) for all heterogeneous cases. The increasing ABL height (see Figure 7.1) over the warm patch with increasing amplitude does not influence the specific humidity of the thermals, as it is a conservative variable, like potential temperature. The homogeneous case exhibits a large fluctuation, which is a result of the domain size (see Appendix A) and of the fact that the scale of moisture fluctuations has a tendency to increase in time (Jonker et al., 1999; De Roode et al., 2004). Therefore, a larger domain in the y-axis should yield smaller fluctuations as the mean then consists of multiple cycles of the largest spatial scales.

The low specific humidity at the top of the ABL near the center of the cold patch (5.4 g kg^{-1}) is caused by the entrainment of relatively dry air that is horizontally advected by the mesoscale flow, shown in Figure 7.2. The downward transport dries the cold patch from the top, which explains the pocket of dry air that Avissar and Liu (1996) and AV98 found over the cold patch. Thus, the atmosphere over the warm patch is moist, despite the low surface evaporation that characterizes this patch, and the cold patch with the high rate of evaporation is dry. Therefore, the location of the largest moisture content in the ABL top coincide with the location of the lowest absolute temperatures (see Figure 7.3) and a situation is created that should result in larger values of RH_{zi} over the warm patch.

The beneficial effect of the heterogeneity induced moisture transport towards the thermals

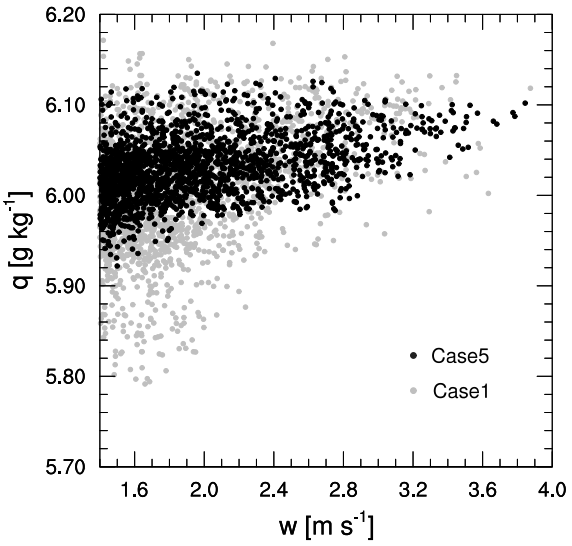

*Figure 7.8: Scatter plot of vertical wind speeds w larger than 1.4 m s^{-1} versus the specific humidity q at z/z_i = 0.95 for Case*1*large and Case*5*large during the first time step of data recording.*

over the warm patch becomes obvious in a scatter plot of vertical wind speed and specific humidity for *Case*1*large* and *Case*5*large* (see Figure 7.8). This figure contains data from an instantaneous horizontal field taken in the entrainment zone at z/z_i = 0.95 during the first time step of the sampling hour. We have conditionally sampled the vertical wind and the specific humidity for the thermals by taking the area where the vertical velocity exceeds 1.4 m s^{-1}. The plot shows that the thermals for the homogeneous case *Case*1*large* are on average drier, as there are significantly more points in the range from 5.8 to 6.0 g kg^{-1}, than for the heterogeneous case *Case*5*large* for which the values of most of the points are slightly larger than 6.0 g kg^{-1}. If we assume that the largest vertical wind speeds are associated with the core of the thermals, then both cases have the same specific humidity in the core (6.05 g kg^{-1} if the wind exceeds 3.0 m s^{-1}). Under the assumption that lower wind speeds occur at the edges of the thermals, we can argue that for this region the heterogeneous case is more efficient in transporting moisture. Due to the merging of thermals by the circulation, the thermals in the heterogeneous case may have a larger ratio of volume to surface and suffer less from drying by detrainment at the side of the thermals. Therefore, in heterogeneous conditions more moisture reaches the entrainment zone and thus the RH_{zi} may increase.

Spatial distribution of relative humidity

Relative humidity is the indicator that links the results of the boundary layer growth and temperature analyses with the findings on the moisture structure. Here, we include the simulations that are performed for the regimes with weaker temperature inversions and a drier upper atmosphere to investigate the importance of the thermodynamic structure of the entrainment zone. Figure 7.9 shows the 1-h-averaged cross-section of $\overline{\langle RH \rangle}$ for *Case*5 and *Case*5*dry*.

For *Case*5, the ABL top over the warm patch reaches values up to RH = 62.5 % (x/λ = 0.5, z/z_i = 0.95), while the cold patch does not exceed RH = 55 %. At the center of the cold patch, there is a dry area at x/λ = -0.5, z/z_i = 0.9 caused by the entrained dry air that is transported

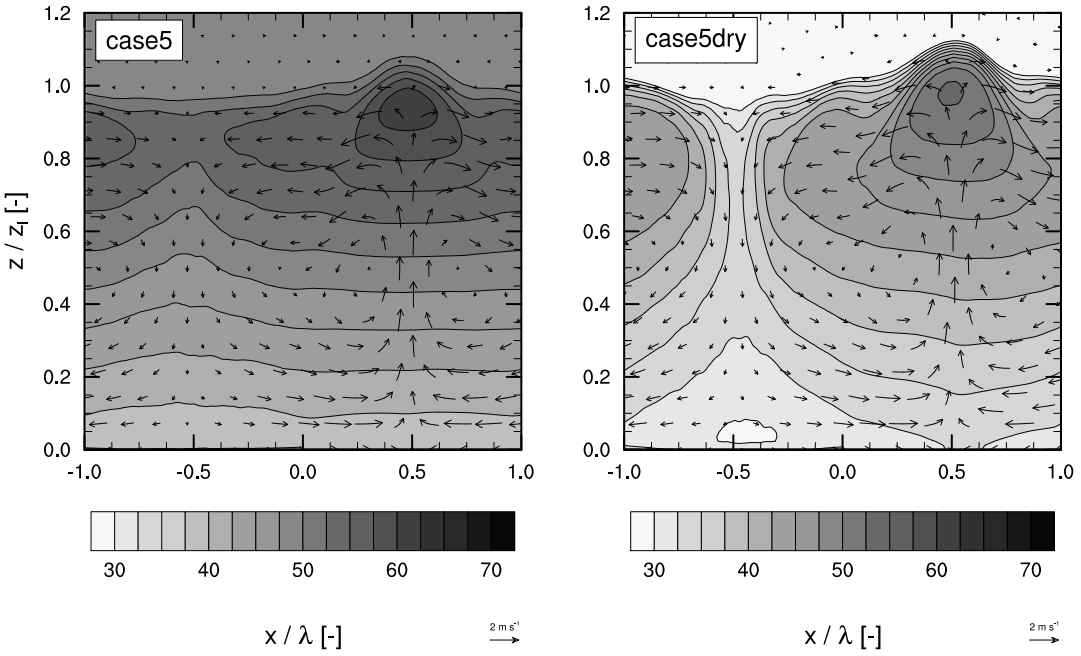

Figure 7.9: Cross section of the 1-h-averaged relative humidity $\overline{\langle RH \rangle}$ for Case5 (left) and Case5dry (right). The horizontal coordinates are scaled by the patch size λ and the vertical coordinates are scaled by the ABL height z_i. Vectors indicate the wind direction and magnitude.

downwards here (see vectors in Figure 7.9). The structure of *Case5dry* is similar to *Case5* over the warm patch. Despite the dry upper air, there is still an enhanced RH over the center of the warm patch (RH = 55 %), but over the cold patch the effect of dry-air entrainment is much more profound, with an RH of 30 % at the ABL top. Above the center of the cold patch (x/λ = 0.5), the RH is the minimum for that height. The effects of dry-air entrainment extend down to the land surface, as the surface RH at x/λ = -0.5 is less than 30 per cent, while over the warm patch at x/λ = 0.5, the RH exceeds 35 per cent. A comparison of *Weak5* and *Weak5dry* yielded similar structures (not shown).

The maximum RH over the warm patch (RH = 62.5 %) of *Case5* exceeds the value found over a homogeneous land surface sharing the same area-averaged fluxes (RH = 59 %, see Figure 7.10). In the cases characterized by a drier upper atmosphere, the RH-enhancement effect is still important, despite the intense dry-air entrainment, since this air is horizontally advected towards the cold patch and does not directly influence the RH over the center of the warm patch (see Figure 7.9). As RH is our chosen indicator for cloud formation (Ek and Mahrt, 1994), we therefore expect that in free convective conditions cloud formation may occur earlier over heterogeneous land, independent of temperature and moisture inversion strengths. This finding provides a thorough explanation for the finding of previous observational and modeling studies (Avissar and Liu, 1996; Chagnon et al., 2004) that found that cloud formation is enhanced over areas that are warmer and drier than their environment.

Variability of area averaged relative humidity

Figure 7.11 shows the 1-h-averaged vertical profiles of the relative humidity. In the left figure, the shaded area is the range of the 1-h-average relative humidities found in *Case5*, the hatched

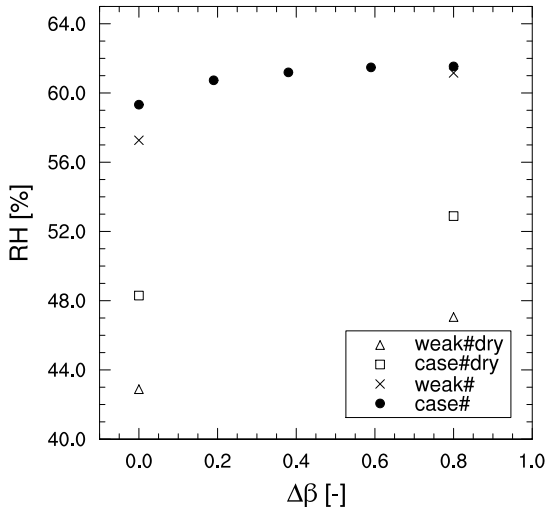

Figure 7.10: Relation between the maximum time averaged relative humidity $\overline{\langle RH \rangle}_{max}$ per domain versus the heterogeneity amplitude, $\Delta\beta$ for all regimes.

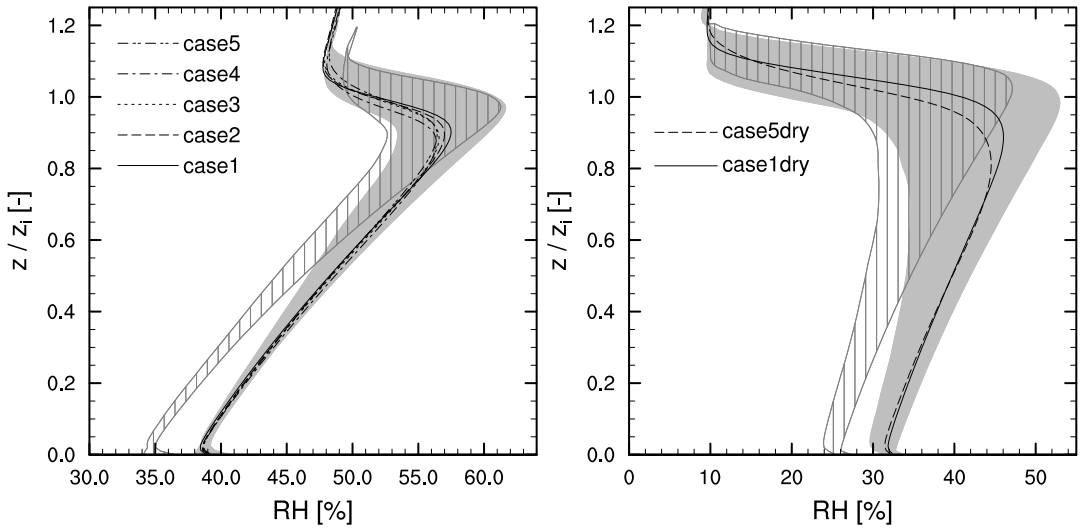

Figure 7.11: Vertical profile of the spatial- and time-averaged value of the relative humidity $\left[\overline{\langle RH \rangle}\right]$ for all cases (left). The gray shading shows the range of time-averaged values of relative humidity $\overline{\langle RH \rangle}$ within the domain of Case5. The gray hatched area shows the same range but for Weak5. The right figure shows the $\left[\overline{\langle RH \rangle}\right]$ for Case1dry and Case5dry with the variability of Case5dry shaded in gray and of Weak5dry hatched.

area is the range of temporal averaged RHs in *Weak*5. This figure shows that the mean profiles of RH are nearly identical, with the maximum RH at $z/z_i = 0.95$. The large-amplitude cases are characterized by a deeper entrainment zone (see Figure 7.4), which tend to distribute the moisture over a larger region. The RH peak in the homogeneous case is thus slightly higher (RH = 57 %) than in the heterogeneous cases (RH = 55 %). Notice that the area averaged RH is not enhanced by heterogeneity, which is supported by the fact that we have identical surface fluxes and entrainment velocities for all amplitudes (see Figure 7.5).

The large RH-variability of *Case*5 (grey shaded area) indicates the importance of variability

on possible cloud formation. The mean profiles of *Case*1 and *Case*5 are very similar, but in *Case*1 there is hardly any variability within the domain (not shown). In *Case*5 we find a range of 7 % (RH = 54 - 61 %) within the domain. This variability range is even larger (9 %, RH = 52 - 61 %) if the temperature inversion strength becomes weaker, caused by the extra dry-air entrainment that sinks over the cold patch.

The cases with a dry upper atmosphere (right panel in Figure 7.11) have a larger range of RH-values in the ABL (as we found in Figure 7.9), and again have similar mean profiles. *Case*5*dry* has at z/z_i = 0.95 a range of 25 % (RH = 25 - 50 %), whereas the range of *Weak*5*dry* is 20 % (RH = 26 - 46 %). By comparing the left and the right panel it becomes clear that the dry upper atmosphere decreases the RH for the whole ABL, but according to the shaded and hatched areas, the effects are mostly noticable in the RH-decrease over the cold patch. For instance, *Case*5*dry* has a maximum RH over the warm patch that is approximately 10 % lower than *Case*5 (50 % versus 61 %), whereas the minimum over the cold patch is approximately 30 % less (25 % versus 54 %) due to the advection of the very dry entrained air to here. An important consequence therefore is that, even with dry upper atmosphere conditions, the RH over the warm patch is enhanced compared to the homogeneous case sharing the same conditions.

Figure 7.10 shows the maximum time-averaged $\overline{\langle RH \rangle}$ found in the entrainment zone for all cases. The maximum value of RH increases with heterogeneity amplitude for the four defined regimes of potential temperature and specific humidity inversion strengths. For the numerical experiments with a strong inversion, the values range from 59.4 % (*Case*1) to 61.8 % (*Case*5) for a moist upper atmosphere and from 48.5 % (*Case*1*dry*) to 51.0 % (*Case*5*dry*) in the dry case. The weak inversion cases show a slightly stronger correlation between the maximum RH and the heterogeneity amplitude (*Weak*1 = 57.4 %, *Weak*5 = 61.3 %, *Weak*1*dry* = 43.0 %, *Weak*5*dry* = 47.0 %), which is in agreement with our previous finding that in weak inversions the ABL height variability is relatively larger compared to the strong inversion cases. Although a difference of 3 - 4 % between the homogeneous and strongest heterogeneous case is small, Ek and Mahrt (1994) found that in the afternoon the typical RH_{zi} tendency per hour has similar values. Therefore, there might be a difference in cloud onset between the homogeneous and heterogeneous cases in the order of an hour, if we would take initial conditions for the LES simulations closer to saturation.

Vertical profiles of variances

We conclude this study with an analysis of the variances of the potential temperature and specific humidity in the entrainment zone to show that these variables are influenced by the non-uniform forcings at the land surface (see Figure 7.12). The first finding we discuss, is the creation of mesoscale variance. The figure shows that for potential temperature one third (0.06 K^2) of the total variance of 0.18 K^2 is in the mesoscale contribution at z/z_i = 1.0. Specific humidity has at this height a significantly larger part of the variance in the mesoscale (see bottom right panel in Figure 7.12), as this contribution is approximately two third of the total (0.08 / 0.12 $\mathrm{g}^2\ \mathrm{kg}^{-2}$). An explanation for the shift is that in the heterogeneous case, thermals are organized over the center of the warm patch in a line on the y-axis. Therefore, if we apply our statistical procedure over the warm patch, there are only marginal turbulent fluctuations as most of the y-axis is covered by thermals. Also over the cold patch there is a reduction of the

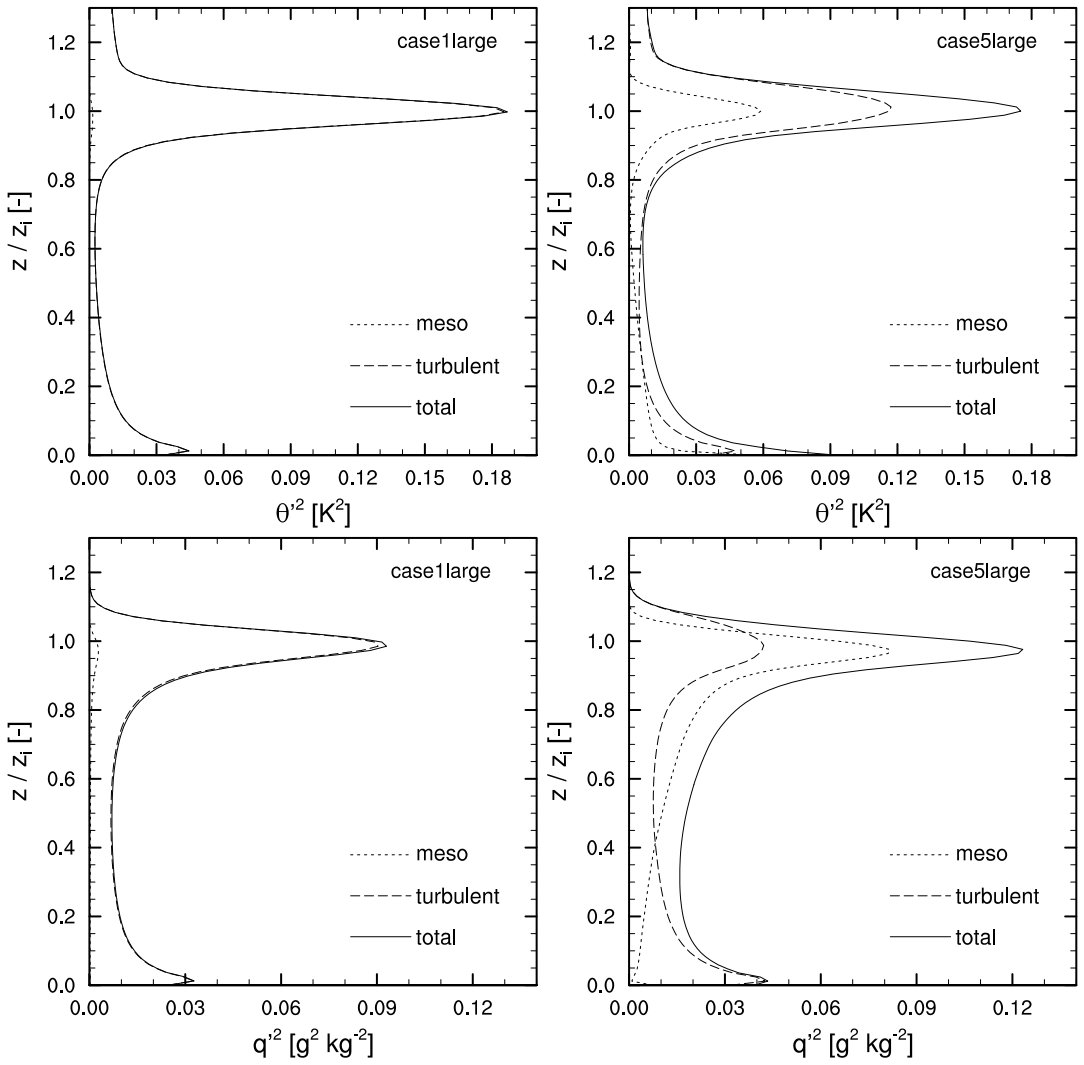

Figure 7.12: Vertical profiles of the potential temperature variance for Case1large and Case5large (top panels) decomposed in mesoscale $\left[\overline{\langle\theta\rangle^2}\right] - \left[\overline{\langle\theta\rangle}\right]^2$ *and turbulent parts* $\left[\overline{\langle\theta'^2\rangle}\right]$*. The bottom panels show decomposed variances of specific humidity for the same cases.*

turbulence as here there are no thermals, but only a mean sinking motion that is enclosed in the mesoscale contribution (see Figure 7.2) instead of the turbulent one. An explanation why there is more mesoscale contribution in the specific humidity variance than in the temperature variance connects with the findings in the next paragraph.

Our second finding is that the total potential temperature variance peaks in the entrainment zone for *Case1large* and *Case5large* (see top panels in Figure 7.12) at a value of approximately 0.18 K^2, while the variance of specific humidity is largely enhanced from 0.09 $g^2\ kg^{-2}$ to 0.12 $g^2\ kg^{-2}$ due to the presence of heterogeneity. This finding could be explained by the opposing entrainment ratios of potential temperature and specific humidity. The specific humidity has in both cases a positive entrainment ratio (approximately 0.3), thus moisture leaves the ABL and free atmospheric dry air enters. We have then a circulation in which moist air is transported upwards over the warm patch and very dry air is advected downwards over the cold patch (see Figure 7.9). Therefore, we have, in addition to the shift from the turbulent to

the mesoscale because of the fixed thermal location, an extra enhancement of the mesoscale variance in the entrainment zone, caused by a large horizontal fluctuation of specific humidity. Consequently, also the total variance increases. In this situation the induced heterogeneous circulation contributes significantly to the variance and a stronger heterogeneity amplitude yields a larger mesoscale variance if the circulation enhances. Many boundary layer cloud parameterizations in large scale models assume a relation between specific humidity variance and cloud cover (Teixeira and Hogan, 2002), thus heterogeneity may play a role here.

On the other hand, potential temperature has a negative entrainment ratio (-0.2), thus air colder than the free atmosphere leaves the ABL and is replaced by warmer air. In consequence, the circulation is characterized by rising warm thermals over the warm patch and sinking warm air over the cold patch. Therefore, the mesoscale contribution is independent of the heterogeneity amplitude, as stronger thermals are compensated by faster downward motions (see the difference between the wind vectors in *Case*2 and *Case*5 in Figure 7.2) and the total variance will not exceed the homogeneous case.

These results can be related to the studies of Jonker et al. (1999) and De Roode et al. (2004), who show that the maximum spatial scales in the variances of heat, moisture and scalars that can develop in the homogeneous ABL are determined by the entrainment ratio. They also found that for the typical -0.2 ratio of the surface and entrainment potential temperature flux, the variability is bounded and large scale can not develop. On the other hand, for scalars with a positive ratio, as specific humidity in our case, larger scale fluctuations can develop and increase the variance. Although this is only a qualitative connection, a future study should address the development of scale levels in the heterogeneously forced ABL.

7.4 Summary and conclusions

We investigated the effect of heterogeneous forcings on the potential formation of convective clouds using relative humidity as an indicator. This was done by analyzing numerical experiments using a large eddy simulation model. A sensitivity analysis was performed on the heterogeneity amplitude and the inversion strengths of potential temperature and specific humidity for a land surface that is heterogeneous in the meso-γ scale (2 - 20 km). The cases are integrated for four hours of which the last hour was used to record statistics. We analyzed the height of the ABL, the specific and relative humidity structure near the ABL top for a free convective boundary layer that was forced by a sensible and latent heat flux that added up to 360 W m^{-2} for all simulations. The land surface was divided in 2 patches, one with a low Bowen ratio (cold patch) and one with a high Bowen ratio (warm patch). Different heterogeneity amplitudes were simulated by varying the difference between the Bowen ratios of the two patches.

An analysis of entrainment and ABL growth of the heterogeneously forced ABL indicated that under heterogeneous conditions the ABL increases over the warm patch, and decreases over the cold patch. The greater ABL heights over the warm patch lead to lower absolute temperatures over the center of the warm patch. Due to the mesoscale circulation that is induced by the heterogeneous forcings, moisture is advected to the center of the warm patch. Low absolute temperatures in combination with high specific humidity over the warm patch lead to a situation which has a relative humidity that is higher under heterogeneous condititions

than under homogeneous forcings. These are the first indications in this study that cloud formation may be favorable over the warm patches of a heterogeneous landscape.

The comparison of vertical heat flux profiles of homogeneous and heterogeneous cases sharing the same area-averaged forcings revealed that entrainment in low-amplitude heterogeneous cases appears to be less than in homogeneous cases, whereas the entrainment of large amplitude cases exceeds the entrainment of homogeneous cases. Nevertheless, this finding is rejected by the analysis of the time evolution of the ABL height, as identical entrainment velocities for all cases are found here.

The analysis of the scale levels involved in the heat transport showed us that the entrainment heat flux consists of a mesoscale and a turbulent part. This is explained by the fact that strong entrainment events are closely linked to the mesoscale motion and always at the same location. A larger heterogeneity amplitude leads to an increased contribution of the meso scale motions to entrainment.

Mean vertical profiles of relative humidity are very similar in all cases, but the variability in the time-averaged RH near the top of the ABL (RH_{zi}) is largely enhanced by the presence of heterogeneity. This finding is proven to be true for all cases with strong and weak potential temperature inversions and with moist and dry upper atmospheres. In all situations the RH_{zi} over the warm patch is larger than over the cold patch and than in homogeneous conditions. By conditionally sampling the data, we show that thermals over heterogeneous surface conditions are more effective in transporting moisture upwards, due to their larger volume to surface ratio. In addition, the RH cross sections show that dry air that is entrained is transported downwards mostly over the cold patch and low values of RH are found over this patch. In cases with a drier free atmospheres, these effects can be more pronounced and dry entrainment events extend to the land surface. Therefore, we conclude that the mean RH profile shows incomplete information with regard to RH modifications by heterogeneity. It is highly relevant to calculate the variability of RH as a function of the amplitude of the heterogeneity, as this variable contains the influence of heterogeneity on the maximum RH that occurs in the domain. The variances of potential temperature and specific humidity also contain the spatial variability and show a shift of the variances from the turbulent to the meso scale. Heterogeneous forcings enhance the total variance of specific humidity, while the total variance of potential temperature does not increase, which is explained by the entrainment ratio.

All of the above findings suggest that land surface heterogeneity plays a significant role in the stucture and value of the RH_{zi}. Cloud formation may be enhanced over heterogeneous landscapes as the maximum RH and the specific humidity variance in the entrainment zone are larger than in homogeneous conditions.

Appendix A: Sensitivity to domain size

This appendix shows the sensitivity of our results to the size of our domain. For the homogeneous case we analyzed if the horizontal fluctuations that we found in the time averaged potential temperature and specific humidity are the result of the limited size of the y-axis, thus that our local average is not accurate enough. For the heterogeneous case we tested for the same variables the sensitiviy to the number of patches in our domain. We carried out the

analysis on *Case*1 and *Case*5 for a domain that has 512 cells in the x-axis instead of 256, thereby creating *Case*1*large* and *Case*5*large*. Consequently, the domain on the x-axis is 12800 m instead of 6400 m and *Case*5*large* has 4 patches instead of 2. We use the same statistical procedures to create statistics for 256 cells on the x-axis, but the local average (see Section 7.2.3) is now computed using the average of all cells on the y-axis for that specific location and all values on the y-axis for the cell at the same height, but shifted 256 grid cells in positive x-direction. For instance, a local mean calculated at grid cell $x = 1, z = 1$ is the mean of all cells in the y-direction for $x = 1, z = 1$ and $x = 257, z = 1$. All of these cells have exactly the same surface forcings.

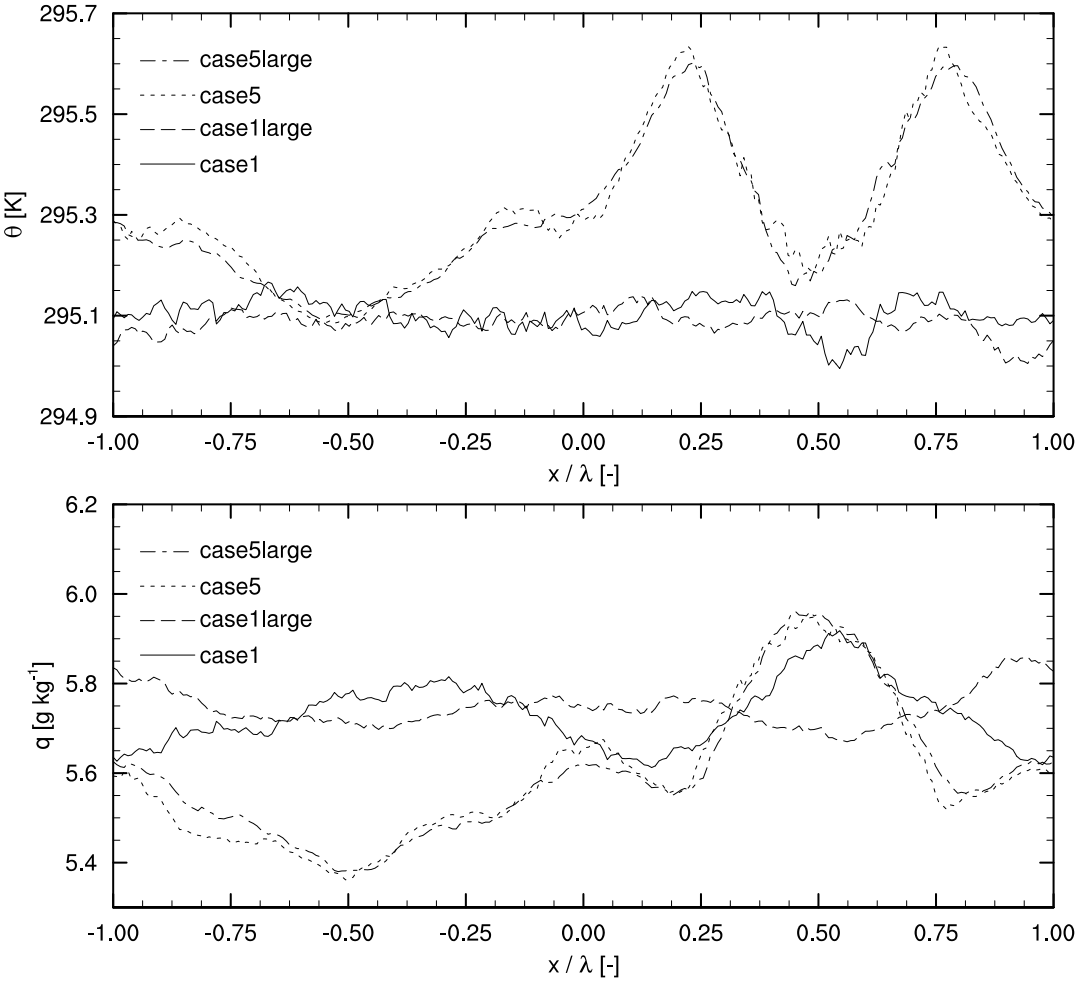

*Figure 7.13: 1-h time-averaged potential temperatures (top) and specific humidities (bottom) along the x-axis for Case*1*large and Case*5*large. Horizontal coordinates are scaled by the patch size* λ.

Figure 7.13 shows the time averaged potential temperature and specific humidity during the hour of recording for the four cases. *Case*5 and *Case*5*large* yield identical profiles for both variables, with minima of 295.1 K at x/λ = -0.5 and 0.5 and two maxima of 295.6 K at x/λ = 0.25 and 0.75. Therefore, our chosen domain setup of two patches resolves the heterogeneous cases correctly. On the other hand, the homogeneous case improves considerably when the local average is based on a greater number of points, as the profile converges to a straight line (295.1 K for potential temperature and 5.75 g kg^{-1} for specific humidity), which we would expect for a case with identical surface forcings over the whole domain.

8

On land-surface modeling in large-eddy simulations of convective boundary layers

In this study it is investigated to which extent the results of LES simulations with a coupled land surface are sensitive to the numerical formulation of the land surface model (LSM). This is done for a convective boundary layer (CBL) over a grass-covered land surface. LES simulations designed based on observations taken on 25 September 2003 in Cabauw (The Netherlands) show that the surface energy balance and the turbulence statistics are remarkably insensitive to the formulation of the LSM. The heat capacity of the vegetation layer, the spatial scale at which the surface model is applied and the subgrid model formulation near the land surface also have minimal influences on the results. There are two main explanations for these findings. First, due to the very fast response of the surface temperature to radiation and the atmospheric conditions, the incoming radiation, rather than the turbulence, controls the surface fluxes. Second, under convective conditions the self-organization of rising thermals is so strong, that any small scale heterogeneity in surface temperature is quickly reorganized in the flow. A relevant implication of our findings is that the land surface models currently used in NWP models can be applied in LES simulations of a CBL over a vegetated land surface.

8.1 Background

Large-Eddy simulation models (LES) have been serving as a virtual laboratory for atmospheric turbulent flows (e.g Moeng, 1984; Sullivan et al., 1998) for about three decades, but only since recent years the increasing computer power is allowing for simulations of large domains and diurnal cycles. Therefore, the coupling of the LES with the land surface gained interest among the modeling community striving towards "real-world" LES simulations. To be able to perform these type of studies, there is a need for a better understanding of the impact that land surface interactions have on the turbulent fields and vice versa (e.g. Albertson and Parlange, 1999; Patton et al., 2005; Huang and Margulis, 2008).

Submitted to *Mon. Wea. Rev.* in collaboration with Jordi Vilà-Guerau de Arellano and Elie Bou-Zeid.

In several LES studies that take into account the interactive land surface (Patton et al., 2005; Huang and Margulis, 2010) an existing land surface model (LSM) used in weather or climate models was coupled to the LES to resolve the energy and water balance of the land surface and the underlying soil. Nevertheless, coupling such a LSM to a LES is not straightforward. The common LSMs are optimized for the use in models which integrate the Reynolds-Averaged Navier-Stokes (RANS) equations and that have fully parameterized turbulence. Contrastingly, LES models resolve the largest and most energetic scales of the turbulent motions and only parametrize the smallest ones. Therefore, it is unclear whether the assumptions that are enclosed in the land surface and surface layer descriptions in the LSM, are valid in LES. In this study, we thoroughly evaluate these assumptions.

A typical LSM, for instance NOAH (Ek et al., 2003), ISBA (Noilhan and Mahfouf, 1996) or TESSEL (developed at ECMWF), consists of two parts, often modeled separately. First, there is the component that solves the surface energy balance (SEB) and that forms the interface between the land surface and the atmosphere. Second, there is the component solving the vertical transport of heat and moisture in the soil.

In this paper, we focus on the surface energy balance, which we consider an important aspect of coupling a LSM to LES, because the surface temperature and the surface fluxes of momentum and heat respond instantaneously to the actual atmospheric conditions and therefore are expected to have the strongest link with turbulence. Our focus is only on the daytime convective boundary layer over a grass covered land surface. Although we do not focus on the dynamical behavior of the soil temperature, there are indications that fast fluctuations in soil temperature have an impact on the turbulent flow (Gentine et al., 2010, 2011).

We analyze four aspects of the SEB formulation in the LSM that we consider the most likely to produce differences between RANS and LES. The first one is the method chosen to calculate the surface temperature. There are two common methods to do this. In the first method, the surface temperature is implictly resolved as a function of the atmospheric conditions and the radiation balance (Ek et al., 2003; Best et al., 2004). Under such conditions, the surface temperature adjusts instantaneously to its forcings. In the other method a heat capacity is attached to the skin layer (Noilhan and Planton, 1989; Duynkerke, 1991). Therefore, fluctuations in surface temperature can never be faster than the characteristic time scale of the skin layer. Here, we investigate whether fluctuations in surface temperature influence the SEB and how they feed back on the atmospheric flow.

The second aspect that we study is the application of Monin-Obukhov similarity theory (MOST) in LES. Due to the large Reynolds numbers of atmospheric flow, the interaction with the surfaces needs to be parameterized as the resolution requirements for resolving a viscous sublayer and imposing a no-slip boundary condition are far beyond the computational possibilities (Piomelli and Balaras, 2002). Therefore, both in LES and RANS, MOST-based surface models are used for computing either the near-surface gradients or the surface fluxes of wind, temperature and humidity depending on the chosen boundary conditions. However, the application of MOST in LES models is questionable as it requires averaged turbulent fields as input (Piomelli and Balaras, 2002). Since a universal locally applicable theory is lacking, MOST is still the most widely used theory for surface models in LES (Moeng, 1984; Sullivan et al., 1994; Piomelli and Balaras, 2002). Huang and Margulis (2010) already point out the

potential errors introduced by local application of MOST, but do not investigate their impacts.

The third aspect is related to the fact that in the zone where the parameterized turbulence of the MOST-based surface model and the (partially) resolved fields in the LES blend, LES models are often not able to produce proper logarithmic wind and scalar profiles (e.g. Andren et al., 1994; Sullivan et al., 1994; Porté-Agel et al., 2000; Chow et al., 2005; Brasseur and Wei, 2010). In short, these errors are related to the fact that close to wall the integral length scale of turbulence converges to zero, which violates the assumptions that are enclosed in subgrid models in LES such as Smagorinsky and TKE. The errors can as well be related to the numerics of the model (Brasseur and Wei, 2010) and to the differences in the mixing lengths implied by the LSM and the SGS models. The use of a scale-dependent dynamic subgrid model (Porté-Agel et al., 2000; Bou-Zeid et al., 2005) or wall damping (Mason and Thomson, 1992; Sullivan et al., 1994) can largely correct these errors. If no correction is applied, the result is an overprediction of the gradients near the surface in comparison to the theoretical gradients predicted by MOST. We investigate in this study if and how such errors propagate into the solution of the SEB.

The fourth and last aspect that needs to be considered when coupling a LSM to LES is the behavior of the LSM in free convective conditions, thus without background wind. This is a flow that has been extensively studied using LES (e.g. Moeng, 1984; Sullivan et al., 1998; Jonker et al., 1999). In situations of free convection without background wind, the wind speed is locally larger than zero, while its horizontally-averaged value approaches zero at the same time. Under such conditions, the functions for predicting the gradients near the wall are no longer applicable. Weather and climate models prevent this behavior using two different approaches. Either the convective velocity scale w_* is added to the wind speed (Beljaars, 1994) to take the effect of convection on the wind at the surface into account, or a lower limit is set on the wind speed. The first method is an undesirable one in LES, as the horizontal motions induced by convection that w_* parameterizes are partially resolved by the model and therefore enclosed in the local horizontal wind speeds.

We use the Dutch Atmospheric Large-Eddy Simulation model (DALES) (Heus et al., 2010) to address the above-mentioned aspects. We base our study on an idealized case based on observations taken in Cabauw, The Netherlands, 25 September 2003 (Casso-Torralba et al., 2008; van Heerwaarden et al., 2010a). In this case we reproduce the transition from the onset of convection after sunrise until the mid-afternoon. During this time of the day, land-atmosphere interactions have the strongest impact on the evolution of the convective boundary layer (CBL) (van Heerwaarden et al., 2010a), which makes this case very suitable for evaluating the assumptions behind the coupled LES-LSM.

The setup of this paper is the following. In the Section 8.2 we discuss each of the four aspects in detail and describe how they enter into the model formulation. We also present here how the sensitivity of the LES results to each of the aspects can be analyzed. In Section 8.3 we explain the model setup and give an overview of all simulations. In Section 8.4 we discuss the results with respect to the evaluated assumptions, followed by the conclusions in Section 8.5.

8.2 Essential aspects of land surface modeling in LES

Here, we explain in detail the four previously defined essential aspects in coupling a LSM to a LES model. We introduce their mathematical formulations and the enclosed assumptions and discuss briefly their hypothesized impacts on the LES results. Before introducing the aspects in detail, we would like to stress that we model the surface using a roughness length, and that we do not consider individual surface objects in this study.

8.2.1 Calculation of the surface temperature

In Section 8.1 we sketched an outline of the two methods for computing the surface temperature. Before discussing the methods, we show how the surface temperature enters into multiple components of the surface energy balance:

- Sensible heat flux H

$$H = \frac{\rho c_p}{r_a} (\theta_s - \theta_1) \tag{8.1}$$

  where ρ is the density of air, c_p the heat capacity of air at constant pressure, r_a the aerodynamic resistance computed using MOST and θ_1 and θ_s the filtered values of potential temperature at respectivily the first model level and the land surface. At the surface we assume the potential and absolute surface temperatures to be equal ($\theta_s = T_s$).

- Latent heat flux LE

$$LE = \frac{\rho L_v}{r_a + r_s} (q_{sat}(T_s) - q_1) \tag{8.2}$$

  where L_v is the latent heat of vaporization, r_s the surface resistance, $q_{sat}(T_s)$ the saturated specific humidity evaluated at the filtered surface temperature and q_1 the filtered specific humidity at the first model level.

- Ground heat flux G

$$G = \Lambda (T_s - T_{soil}) \tag{8.3}$$

  where Λ is the conductivity of the skin layer per unit of area and T_{soil} is the soil temperature immediately below the skin layer.

- Outgoing long wave radiation L_{out}

$$L_{out} = \epsilon_s \sigma T_s^4 \tag{8.4}$$

  where ϵ_s is the emissivity of the surface and σ the Stefan-Boltzmann constant.

The skin layer of a vegetated land surface has a very small heat capacity compared to the soil, which implies that the temperature of the vegetation layer can adjust very quickly to changes in incoming radiation, atmospheric temperature and wind speed. As explained in the introduction, two methods of computing the surface temperature are commonly used: solving it implicitly, or solving it prognostically by attaching a small heat capacity to it that is significantly lower than that of the soil. In this study we evaluate the impact of both.

In the first approach the skin temperature is solved diagnostically. The SEB is defined as:

$$Q_* = S_{in} - S_{out} + L_{in} - L_{out} = H + LE + G \tag{8.5}$$

in which Q_* is the net radiation, S_{in} and S_{out} are incoming and outgoing short wave radiation and L_{in} is the incoming long wave radiation. As S_{in}, S_{out} and L_{in} are provided by the radiation scheme, and the other terms can be substituted by Equations 8.1 - 8.4, an implicit equation for the surface temperature can be derived. If we take the resistances and the values at the first model level from the previous time step, surface temperature can be resolved by iteration, or directly through linearization of Equation 8.2.

In the second method, the surface temperature is solved using the following prognostic equation:

$$C_{skin}\frac{dT_s}{dt} = Q_* - G - H - LE \tag{8.6}$$

in which C_{skin} is the heat capacity per unit of area for the skin layer. In this method, the vegetation layer has a heat capacity and therefore the surface temperature has an associated response time scale. As such, equation 8.5 is a special case of equation 8.6, where either the heat capacity or the rate of change of surface temperature is so small, that the left hand side of equation 8.6 can be neglected.

8.2.2 The impact of the surface model on the surface energy balance

As described in the introduction, connecting a MOST-based surface model to LES raises several potential problems as MOST assumes Reynolds-averaged turbulent fields, whereas LES delivers only resolved instantaneous ones. MOST enters the land surface model through the aerodynamic resistance r_a (see Equations 8.1 and 8.2). This variable is defined as:

$$r_a = \frac{1}{C_\phi U_1} \tag{8.7}$$

with C_ϕ as the drag coefficient for scalars and U_1 as the filtered total wind speed at the first model level. The drag coefficient contains information about the atmospheric stability and is calculated as:

$$C_\phi = \frac{\kappa^2}{\left[\ln\left(\frac{z_1}{z_{0m}}\right) - \Psi_M\left(\frac{z_1}{L}\right) + \Psi_M\left(\frac{z_{0m}}{L}\right)\right]\left[\ln\left(\frac{z_1}{z_{0h}}\right) - \Psi_H\left(\frac{z_1}{L}\right) + \Psi_H\left(\frac{z_{0h}}{L}\right)\right]} \tag{8.8}$$

where κ is the Von Karman constant of 0.4, z_{0m} and z_{0h} are the roughness lengths for momentum and heat, z_1 is the height of the first model level, L is the Monin-Obukhov length and Ψ_M and Ψ_H are the integrated stability functions for momentum and heat (Paulson, 1970).

The Monin-Obukhov length is acquired by equating the bulk Richardson number Ri_B to the integrated stability functions using Equation 8.9 and solving the equality using a Newton-Raphson method.

$$Ri_B = \frac{g}{\theta_{vs}}\frac{z_1\left(\theta_{v1} - \theta_{vs}\right)}{U_1^2} = \frac{z_1}{L}\frac{\left[\ln\left(\frac{z_1}{z_{0h}}\right) - \Psi_H\left(\frac{z_1}{L}\right) + \Psi_H\left(\frac{z_{0h}}{L}\right)\right]}{\left[\ln\left(\frac{z_1}{z_{0m}}\right) - \Psi_M\left(\frac{z_1}{L}\right) + \Psi_M\left(\frac{z_{0m}}{L}\right)\right]^2} \tag{8.9}$$

Here, g is the gravity acceleration, θ_{vs} is the filtered virtual potential temperature at the surface, θ_{v1} is the filtered virtual potential temperature at the first model level. Note that by using

virtual potential temperature, we take into account the effects of moisture on buoyancy.

In LES, the Richardson number used in Equation 8.9 needs to be calculated using Reynolds-averaged fields to be consistent with MOST. An important consequence is that the land-atmosphere interactions cannot be calculated locally, which makes the application of MOST over heterogenous land surfaces questionable. To do cases with heterogeneous surface forcings, Bou-Zeid et al. (2004); Huang and Margulis (2010), among others, implemented MOST locally. A reason why this can work is related to the large Reynolds number of atmospheric flows (Piomelli and Balaras, 2002). Therefore, close to the surface, where the characteristic spatial scales of turbulence quickly decreases, the horizontal grid spacing is large in comparison to the largest eddies at that height, since the integral length scale of the turbulence is on the order of the height above the surface (Meneveau and Katz, 2000). Consequently, most of the turbulent kinetic energy in these regions is in the subfilter scale range of the model and therefore represents an ensemble of eddies that have sizes smaller than the filter. In that limit LES approaches Reynold-averaged numerical simulations, for which the surface models are designed.

To address this issue, we compare three methods of applying MOST in this paper: horizontally averaged, local and filtered over a limited area. Over homogeneous terrain, horizontally averaged values are consistent with MOST and serve as a reference for the other two approaches. We investigate to which extent averaging-related variations in the gradients influence the solutions of the surface energy balance.

8.2.3 Wall damping: turbulence near the surface

The third aspect that could have an impact on the solution of the SEB is the behavior of the subgrid model close to the surface. Close to a solid wall, the integral length scale of turbulence quickly decreases, because the presence of a surface restricts the possibilities of movements in the direction normal to the surface. As the standard subgrid schemes, such as Smagorinsky-Lilly or some forms of the 1.5-order TKE, assume isotropic turbulence and filtering in the inertial subrange, corrections need to be made close to the wall, in order to make sure the implied mixing length converges to zero at the surface. In our model, we introduce this effect by applying the wall-damping method of Mason and Thomson (1992). In short, in case of a Smagorinsky scheme, the mixing length λ is defined as

$$\lambda = c_S \Delta, \tag{8.10}$$

where c_S is the Smagorinsky constant and Δ the filter size. Following the method of Mason and Thomson (1992), the mixing length is dampened close to the surface, resulting in a lower Smagorinsky constant close to the surface as the filter size remains constant. The mixing length correction is calculated as:

$$\frac{1}{\lambda^n} = \frac{1}{\lambda_0^n} + \frac{1}{[\kappa\,(z + z_{0m})]^n} \tag{8.11}$$

where λ_0 is the mixing length in the limit of isotropic turbulence and κ is the Von Karman constant, z the height above the surface, and z_{0m} the roughness length for momentum. Variable n is a tunable parameter that is in our case set to 2, following Bou-Zeid et al. (2005).

We study the influence of wall damping on the solution of the SEB. Disabling wall damping

leads to excessive dissipation near the surface and results in decoupling of the surface and the atmospheric flow. Therefore, wind, temperature and moisture gradients are generally overestimated in the vicinity of the wall (Andren et al., 1994; Chow et al., 2005).

8.2.4 Convection at low wind speeds

The last aspect of coupling a LSM to a LES under investigation is the solution of the SEB in a turbulent field under free convective conditions. Equation 8.7 shows that the aerodynamic resistance is a function of wind speed. In a situation of free convection without any background wind, the horizontally-averaged wind equals zero. Under such conditions, the stability functions used (Businger et al., 1971) are not valid anymore. Nevertheless, if a local form of MOST (see Section 8.2.2) is applied, the winds generated by convection still produce local friction. This results in a discrepancy with the global method, where the selected value for the minimum wind speed determines the aerodynamic resistance, as the mean wind speed converges to zero.

Since a solid theory linking local friction to the mean properties of the flow in free convection is lacking, we can only investigate whether the sensitivity of the surface energy balance to the model formulation increases for decreasing wind speed. Here, we compare locally and globally evaluated MOST. Furthermore, we investigate whether wall damping has a stronger impact on the SEB with or without a geostrophic forcing.

8.3 Methods

8.3.1 Case overview

To investigate the previously described essential aspects in coupling a land surface model to LES, we have used DALES (Heus et al., 2010) for simulating an appropriate case. As explained in the introduction, the case is based on observations taken in Cabauw, The Netherlands, 25 September 2003 (Casso-Torralba et al., 2008; van Heerwaarden et al., 2010a).

8.3.2 Model setup

DALES is initialized at 6.5 h UTC with an initial mixed-layer of 150 m having a potential temperature of 285 K and a specific humidity of 4.5 g kg^{-1}. At the top of that layer, there is a jump of 5 K in the potential temperature, and one of -1.0 g kg^{-1} in the specific humidity. The free atmosphere has a lapse rate of 0.005 K m^{-1} for potential temperature and 0 g kg^{-1} km^{-1} for specific humidity. The horizontal wind is initialized with u and v components of respectivily 3 and 2.5 m s^{-1} in the mixed-layer and 5 and 0 m s^{-1} above, where the latter two are the geostrophic forcing. There is no large-scale forcing for temperature and humidity.

The land surface is covered for 90% with grass (LAI of 2 and a minimum resistance of 110 s m^{-1}) and the residual 10% is bare soil. Soil moisture is initialized uniform with depth, with a volume fraction of 0.27 m^3 m^{-3}. For simplicity we do not consider dew water. The initial soil temperature is 287 K over the first 0.07 m, 286 K over the next 0.21 m, 285 K the next 0.72 m and 283 K the last 1.89 m. At the bottom boundary, the soil temperature is fixed at 283 K. The roughness length for momentum is 0.1 m and for scalars 0.02 m. The surface pressure is $1.0 \cdot 10^5$ Pa.

Table 8.1: Overview of numerical experiments. Label name is the name of the run, C_{skin} is the heat capacity of the skin layer, uniform indicates whether heat fluxes are spatially averaged over de whole domain, before being provided to the atmospheric component, surface shows if MOST is evaluated globally or locally, filter shows whether a 9-points top-hat filter is applied to data before local MOST is applied and mixing length indicates whether a mixing length reduction is applied near the surface.

name	C_{skin}	uniform	surface	filter	wall damping
ref	0	*false*	global	n/a	*true*
cskin	20.000	*false*	global	n/a	*true*
smooth	0	*true*	global	n/a	*true*
mostlocal	0	*false*	local	*false*	*true*
mlfilter	0	*false*	local	*true*	*true*
nomason	0	*false*	global	*true*	*false*

To avoid the use of a complex radiation scheme, the model is forced with a very basic radiation scheme. The incoming long wave radiation is calculated following a simple model that evaluates the radiation at the first temperature level (5 m) using the Stefan-Boltzmann law using an emissivity of 0.8 for the atmosphere. The outgoing long wave radiation is evaluated using the surface temperature. Here, an emissivity of 1 is attached to the land surface. For the calculation of the incoming short wave radiation we take 51.96 N and 4.95 E as the latitude and longitude for Cabauw and assume a cloud free day. The day of the year is 268 (25 September 2003). The outgoing shortwave calculation is calculated as the product of the incoming short wave radiation and the albedo, which is 0.25 in this case.

The initial TKE is 1 m^2 s^{-2} over the whole profile. Potential temperature perturbations of 0.1 K and specific humidity perturbations of $2.5{\cdot}10^{-5}$ kg kg^{-1} are applied over the initial mixed layer.

The model domain consists of 192 levels in the vertical at a grid size of 10 m and 128 cells in both horizontal directions with a grid size of 25 m. This results in a domain of 4800 m x 4800 m x 1920 m. The lateral boundary conditions are periodic.

8.3.3 Numerical experiments

To address all of the aspects in land surface modeling defined in Section 8.2, we have defined an experiment of which the associated runs are shown in Table 8.1.

Run *ref* describes the reference case, which is a run with a skin layer without heat capacity, where MOST is evaluated globally and the length scale correction as proposed by Mason and Thomson (1992) is used near the surface. The two runs *cskin* and *smooth* are used to address the first issue (see Section 8.2.1), which is the impact of the surface temperature calculation. Here, we have chosen for two perturbations of the reference run. By introducing a heat capacity at the surface (*cskin*) we introduce an extra reservoir of heat which dampens out fluctuations in the surface fluxes and introduces a time lag compared to the reference case *ref*. To be able to evaluate the impact of the damping of the surface heat flux fluctuations without introducing a time lag, we perform *smooth*. In this run no heat capacity is used, but the heat fluxes are spatially averaged after the evaluation of the fluxes, to enforce that all grid points have identical heat and moisture fluxes.

The runs *mostlocal* and *mlfilter* provide the necessary information to address the issue of

the application of MOST (see Section 8.2.2). In *mostlocal* in each cell the Obukhov length and the surface fluxes for momentum and heat are evaluated using local values, compared to the global evaluation in the reference case *ref*. In *mlfilter* we also evaluate the Obukhov length and the surface fluxes locally, but construct Ri_B (Equation 3.23) from data that is filtered using a 9-point top-hat filter.

Run *nomason* shows the impact of the length scale corrections on the surface energy balance, by disabling this correction (see Section 8.2.3). This leads to excessive dissipation, resulting in too high subgrid-TKE values near the surface.

To investigate the impact of free convection all runs are repeated without initial and geostrophic wind (see Section 8.2.4). In the results, these runs are labeled by the same names as the runs in Table 8.1 including a suffix fc.

8.4 Results

8.4.1 General case evaluation

Before studying the numerical aspects of land surface modeling in detail, we start with an overview of the general characteristics of the LES runs of our selected case in Cabauw, The Netherlands, 25 September 2003.

Figure 8.1, which contains all runs, shows the diurnal cycle of the surface energy balance, the mean vertical profiles of heat and moisture and the CBL height. Based on the boundary layer growth rate, the day can be divided into three periods. First, there is the early morning phase before the period of fast boundary-layer growth, lasting until 9 h UTC. In this simulation this coincides with the spin up of turbulence in our model, visible in the wiggle in the time series of sensible heat flux. During this period, the specific humidity increases to values close to 5.5 g kg^{-1}. After the initial jump in potential temperature has nearly vanished, a phase of fast boundary-layer growth starts, during which large amounts of dry air are being entrained into the boundary layer. Therefore, the specific humidity in the mixed layer drops to approximately 5.1 g kg^{-1}. As shown in van Heerwaarden et al. (2010a), the entrainment of dry air leads to a significant boost in evapotranspiration during this period. In the final phase, the latent heat flux at the surface and the dry-air entrainment balance, resulting in a nearly constant specific humidity in time until the end of our simulation, and a gradually increasing potential temperature and CBL height.

Striking in Figure 8.1 are the minimal differences in the model results among the separate runs. Despite the range of choices of the heat capacity of the vegetation layer, the surface model and the subgrid model, the time evolution of the surface fluxes and the CBL properties are very similar. In the coming sections, we investigate each part of the formulation in detail, explain why the surface heat fluxes and mean profiles are similar and compare differences in the turbulence statistics among all runs.

8.4.2 Calculation of the surface temperature

The first aspect of the numerics of the LES-LSM under discussion is the method of computing the surface temperature (see Section 8.2.1). First, in Figure 8.2 we compare in the top two panels the spatial structure of the surface temperature of run *ref* and that of *cskin*, which correspond

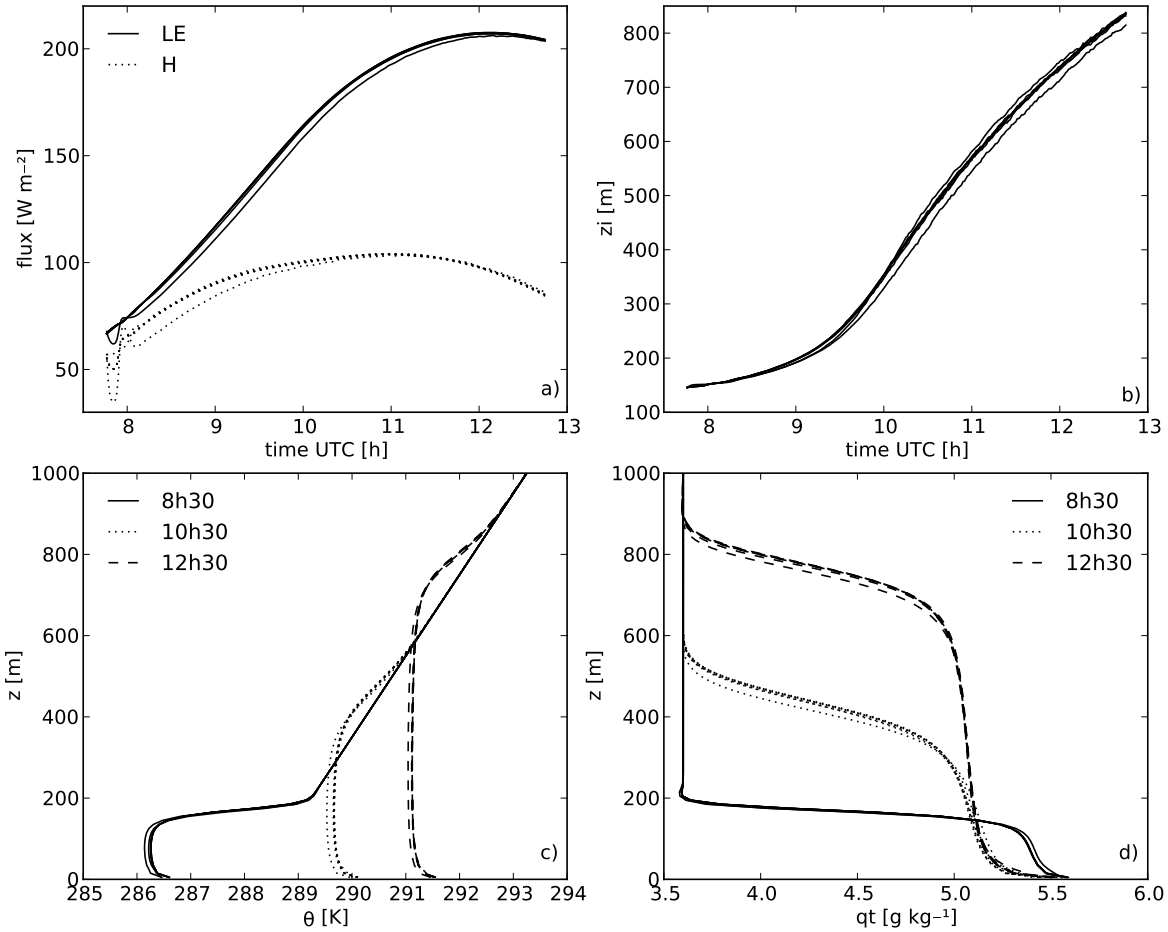

Figure 8.1: General case overview containing lines for all performed cases. Panel a shows the sensible and latent heat flux, panel b the time evolution of the boundary-layer height and panel c and d the 30 min averaged vertical profiles of temperature and specific humidity before (8h30 UTC), during (10h30 UTC) and after (12h30 UTC) the period of fast CBL growth in the morning. Note that the only line that is distinguishable from the other lines belongs to experiment cskin.

to the runs without and with a heat capacity attached to the vegetation layer. Run *ref* shows structures that resemble the typical hexagonal patterns that are associated with turbulent convection (see Figure 8.2a), whereas *cskin* shows larger structures that resemble the streaks that are associated with wind-driven turbulence (see Figure 8.2b). The heat capacity of the skin layer acts as a low pass filter on the surface temperature. Since the shortest time scales near the surface are associated with the convection that is being generated in small thermals, which will organize themselves at higher levels, their footprint is found in the surface temperature cross section of run *ref*, but not in that of *cskin*. Despite the differences in the structure of the surface temperature, cross sections of the horizontal and vertical wind speed at the first model level are similar for both *ref*, *cskin* and *smooth* (not shown). In Figure 8.2c and 8.2d, we show the cross section of horizontal and vertical wind speed at the 4th model level (35 m), thus in the middle of the surface layer, for *ref*. Herein, the similarities between the vertical wind speed (Figure 8.2c) and the surface temperature of *ref* are obvious. It can also be found that the patterns in *cskin* (Figure 8.2d) have a similar size as the structures in the horizontal wind and that they are aligned with these structures.

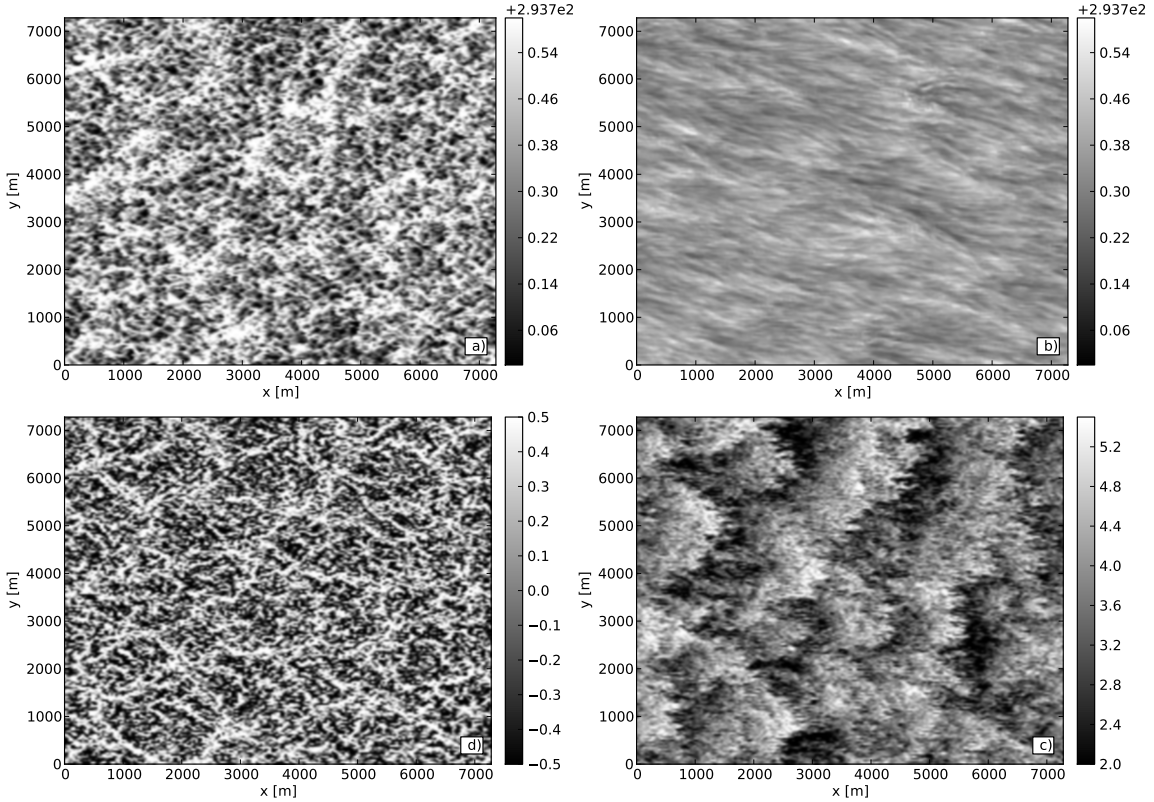

Figure 8.2: Horizontal crossection of surface temperature in cases ref (panel a) and cskin (panel b), horizontal wind speed of case ref (panel c) and vertical wind speed (panel d) at the 4th model level (35 m) for case ref. All values are taken at 12h30 UTC and represent instantaneous values.

In Figure 8.3, we show the impact of these rather different surface temperature structures on the surface energy balance, the friction velocity and the u and w variances. The surface heat flux time evolution clearly shows the time lag that is being introduced by the heat capacity of the skin layer, which is in the order of ten minutes. Despite the time lag, the magnitude and time evolution of the friction velocity are very similar in *ref*, *cskin* and as well in *smooth*, reaching a dip of 0.3 m s^{-1} at 9h UTC after the model spinup, thereafter gradually increasing to 0.35 m s^{-1} at 12h30 UTC. The similarity in u_* between *ref* and *smooth* backs up the previous finding that all three runs lead to similar cross sections of horizontal and vertical wind close to the land surface. The turbulence can therefore be seen as the mechanism that drives the structure in surface temperature, but apparently there is no significant feedback from the pattern in surface temperature back to the flow. This finding can be connected to the results of Huang and Margulis (2008), who studied the impact of land surface heterogeneity on the turbulent structure of the CBL. The insensitivity of the results to the pattern in surface temperature at the land surface is confirmed by the variance profiles of the three runs, which are hardly distinguishable for *ref*, *cskin* and *smooth* (see Figures 8.3c and 8.3d).

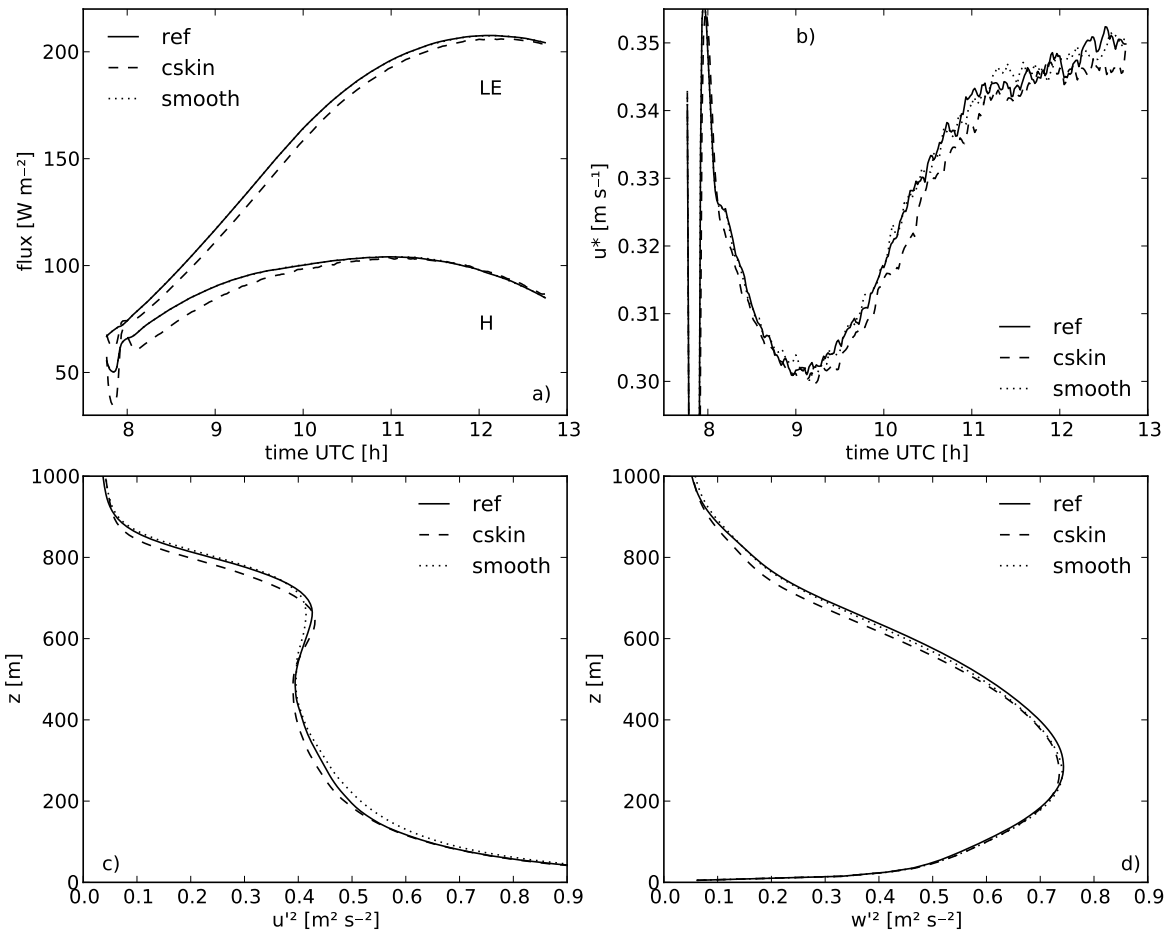

Figure 8.3: The impact of the treatment of the skin layer for runs ref, cskin and smooth. Panel a shows the sensible and latent heat flux, panel b the time evolution of the friction velocity u_* and panel c and d the horizontal and vertical velocity variance at 12h30 UTC.

8.4.3 Surface model

A comparison of global and local implementations of surface layer similarity theory reveals that, despite changes in the friction velocity (see Figure 8.4a), the surface energy balance is not affected by the choice of surface layer formulations (see Figure 8.1, where the lines exactly overlap). This is striking at first sight as MOST predicts a linear dependence of the flux on u_* ($\overline{w'\phi'} = -u_*\phi_*$, with $\overline{w'\phi'}$ as the vertical turbulent flux of an arbitrary scalar ϕ and ϕ_* as the characteristic scale of that scalar). The insensitivity can be understood by considering the role of the net radiation in the surface energy balance. Over a vegetated land surface, the net radiation is distributed over the sensible, latent and ground heat fluxes and storage in the vegetation layer. Under conditions of a vegetated land surface, approximately ten per cent of the net radiation is stored in the soil through the ground heat flux (De Bruin and Holtslag, 1982). This implies that the other ninety per cent reenters the atmosphere, or is stored in the vegetation layer. A decrease in near-surface wind speeds results in a fast (if C_{skin} in Equation 8.5 is larger than zero) or an instantaneous (if C_{skin} is zero) adjustment of the surface temperature to the new wind speed conditions, which is necessary for closing the surface energy balance. Therefore, a decrease in u_* results in a compensating increase in

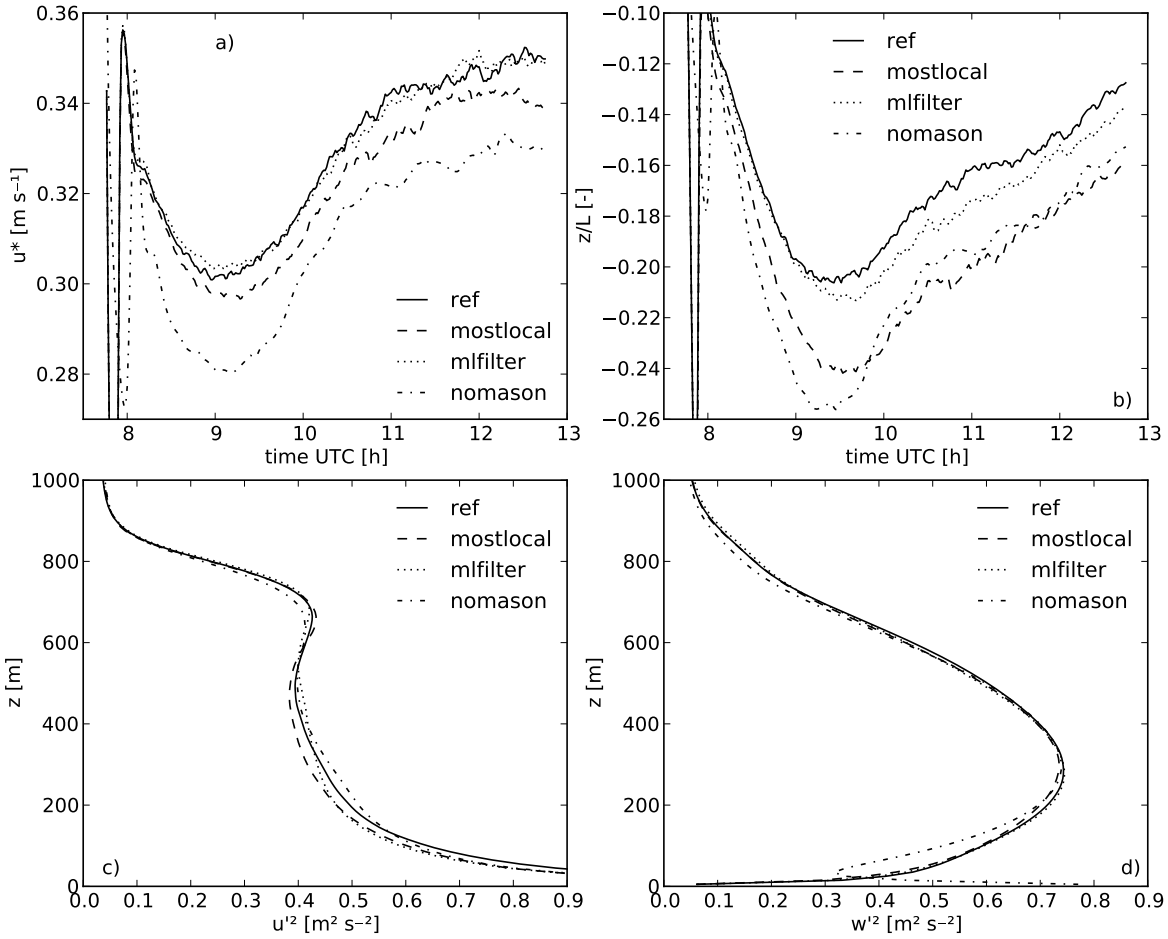

Figure 8.4: The impact of the surface model and wall damping for runs ref, mostlocal, mlfilter and nomason. Panel a shows the time evolution of the friction velocity, panel b the time evolution of the stability expressed in z/L and panel c and d the horizontal and vertical velocity variance at 12h30 UTC.

the gradient of moisture and temperature (enclosed in ϕ_* in MOST) and therefore the flux is maintained. An additional important mechanism in maintaining similar area-averaged fluxes in situations where the incoming radiation is the same but where the value of u_* differs, is the similar sign of the response of the sensible and latent heat flux to turbulent fluctuations: a decrease in the wind speed lowers both fluxes (both Equation 8.1 and 8.2 are inversely related to r_a) and an increase in surface temperature increases both fluxes (θ_s in Equation 8.1 and q_{sat} (T_s) in Equation 8.2). Therefore, also the ratio between the fluxes is largely maintained during turbulent fluctuations.

Due to the lower friction velocity and the larger temperature and moisture gradients between surface and atmosphere, an increase in the stability parameter z/L is observed (see Figure 8.4b). In the case of local application of MOST (run *mostlocal*) a lower friction velocity, ranging from 0.30 m s^{-1} at 9h UTC to approximately 0.34 m s^{-1} after 12h UTC is found, whereas *ref* and *mlfilter* produce similar values for u_*, ranging from 0.31 to 0.35 m s^{-1} from morning until afternoon. Our results confirm the hypothesis of Bou-Zeid et al. (2005), who suggest that using a nine-point local filter (run *mlfilter*) is sufficient to let a local method produce the same domain-averaged results as the area-averaged method (run *ref*). They, however, found

a higher u_* for runs applying the surface model locally. In our model, the wind profiles show that a local application of the surface model results in lower wind speeds at the first model level (see Figure 8.5). Where Bou-Zeid et al. (2005) found overpredicted wind speed gradients near the surface, we find lower gradients that coincide with an oscillating wind profile. Although it is hard to trace down the exact cause, it is most likely that the cause is found in the different SGS model and the different numerical discretization schemes in Bou-Zeid et al. (2005). Despite the differences in u_*, stability and wind speed, minimal differences in the horizontal and vertical wind speed variances are found in the bulk of the CBL (see Figures 8.4c and 8.4d).

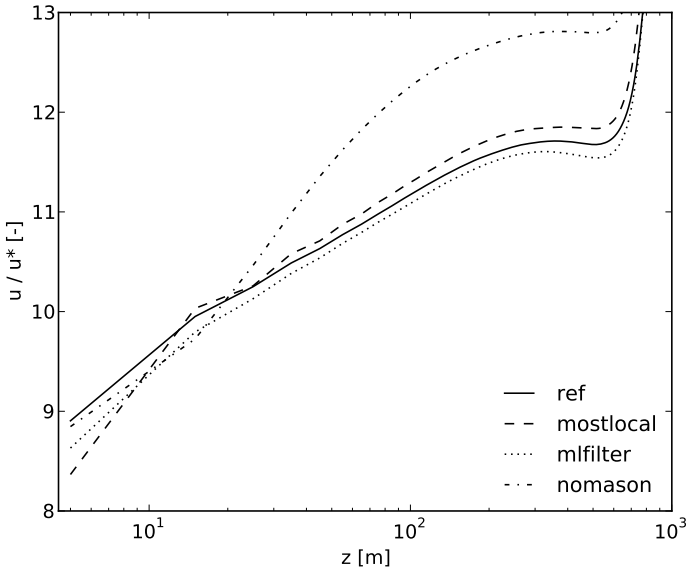

Figure 8.5: 30-min averaged wind profiles at 12h30 UTC for runs ref, mostlocal, mlfilter and nomason.

8.4.4 Wall damping

As described in Section 8.1, one of the main shortcomings of LES models is their failure in producing logarithmic wind and scalar profiles that are consistent with MOST. Here, we investigate the impact of such errors on the solution of the SEB in the LSM. Figure 8.1 shows that the time evolution of the SEB is identical for the runs with (*ref*) and without (*nomason*) wall damping, as the only line that deviates from the others is that of *cskin*.

The differences between *ref* and *nomason* are found in the momentum related variables. Figure 8.4 contains, in addition to the surface model related runs, also the results of *nomason*. The latter shows that disabling the wall damping results in a significantly lower u_*, with 0.28 m s^{-1} at 9 h UTC and 0.33 m s^{-1} at 12h30 UTC. The reduced mixing close to the wall allows for larger temperature and moisture gradients. Therefore, run *nomason* produces a value of z/L of -0.26 shortly after 9 h UTC, which is more unstable than *ref*. The reduced mixing in *nomason* is the effect of excessive dissipation by the subgrid scheme. Due to the isotropy and homogeneity assumptions that are enclosed in the use of a constant coefficient in the common subgrid schemes, which is not valid close to the wall, too much energy is transferred from the resolved to the subgrid scale and consequently excessive dissipation occurs. This can be observed in the profile of vertical variance of *nomason* (Figure 8.4d) which

does not approach zero at the wall. Although these type of errors do not feed back on the solution of the surface energy balance, their impact on the wind profile is evident (see Figure 8.5). Due to the excessive dissipation, there is insufficient mixing of the slower air that resides close to the surface and the faster moving air of the mixed layer.

The question that arises from these findings is why the surface heat fluxes do not respond to the wall damping, while the momentum flux and the wind profile show a strong response. The reason is that in the case of the surface heat fluxes, the energy is bounded by the net radiation (see Equation 8.5), as already explained in Section 8.4.3. In the absense of wall damping the local temperature and moisture gradients are enhanced. Therefore, both the sensible and latent heat flux tend to increase, but they cannot due to the radiation constraint. In turn, the interaction of the wind with the surface is not limited by available energy and the momentum fluxes can therefore respond freely to the flow.

8.4.5 Convection at low wind speeds

The last subject under investigation is the impact of the method of applying MOST in the surface model and the wall damping at low wind speeds. Figure 8.6 shows the impact of both on the surface energy balance, the friction velocity and the variance profiles of the horizontal and vertical wind components. Albeit small, in conditions of free convection, there is a sensitivity of the surface energy balance to the model formulation, with approximately the same energy balance evolution for $reffc$ and $nomasonfc$, and the same for $mostlocalfc$, and $mlfilterfc$.

In contrast to the cases that include wind, the method of applying MOST has more relevant consequences under free convective conditions. When there is no geostrophic forcing, the area averaged wind speed is zero. The local wind speeds, however, are non-zero, since they are associated with thermals, which are local phenomena. Consequently, $mostlocalfc$ gives the largest value of u_* (0.16 m s^{-1}) as it has the smallest averaging window, namely one cell. The application of a nine-point filter in $mlfilterfc$ results in a reduced u_* (0.13 m s^{-1} at 12h30 UTC), but since the characteristic horizontal size of a thermal is on the order of the CBL height (Jonker et al., 1999), it largely exceeds the size of the nine-point filter (here 75 x 75 m), thus the largest part of the friction velocity remains. In $reffc$ and $nomasonfc$, where u_* is computed based on area-averaged values, u_* does not exceed 0.04 m s^{-1}.

Despite a factor of four higher values of the locally computed u_* compared to the area-averaged computed value, the difference in the variance profiles is limited. The only exception is the reduced horizontal velocity and increased vertical velocity variance that is found in the middle of the CBL in case $nomasonfc$. In the case of free convection wall damping has a significant impact on the organization of convective turbulence. A cross section of vertical wind speed at the 4th model level (35 m) for $reffc$ and $nomasonfc$ shows this impact in greater detail (see Figure 8.7). The impact of the wall damping on the structures in vertical velocity is evident. Wall damping reduces the subgrid diffusion near the surface. Therefore, since the smallest structures are dissipated the fastest, more fine scale structures are found in the case with wall damping. In the case without wall damping these fine scale structures are absent and turbulence organizes more efficiently into larger structures. This could explain why the vertical velocity variance is larger in the case without wall damping.

Nonetheless, despite the larger sensitivity of the model results to the LSM formulation in

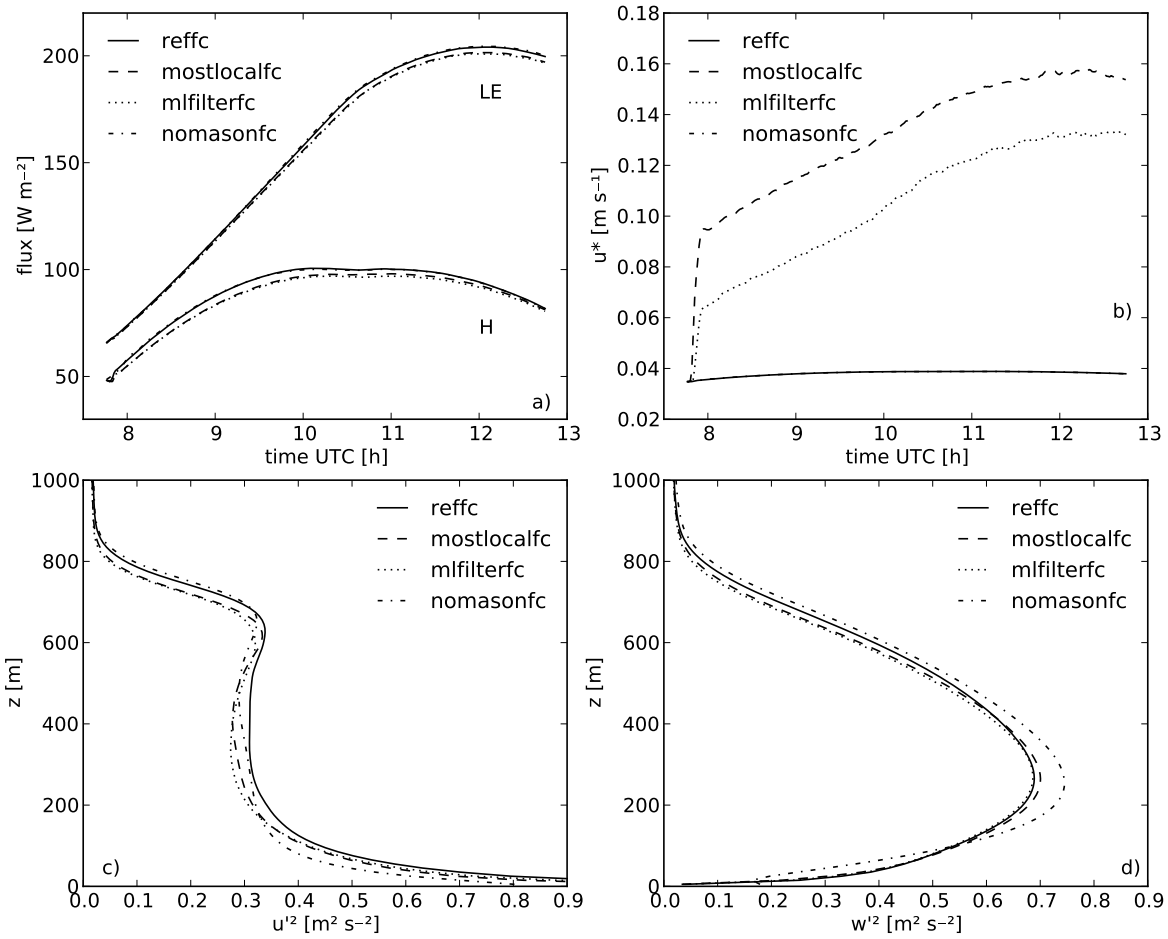

Figure 8.6: The impact of the treatment of surface-layer similarity and wall damping under free convective conditions for runs ref_{fc}, $mostlocal_{fc}$, $mlfilter_{fc}$ and $nomason_{fc}$. Panel a shows the sensible and latent heat flux, panel b the time evolution of the friction velocity u_* and panel c and d the horizontal and vertical velocity variance at 12h30 UTC.

free convective conditions than in conditions with a geostrophic forcing, under free convective conditions the general sensitivity remains low.

8.5 Conclusion

We have analyzed four turbulence-related aspects of the land surface model (LSM) formulation on the simulation of a convective boundary layer (CBL) using a coupled LES-LSM. A case based on 25 September 2003 in Cabauw (The Netherlands) showed that both the surface energy balance and the statistics of the turbulent fields in the CBL show remarkably little sensitivity to the formulation of the surface energy balance.

The main findings of the analysis of the LSM formulation of a grass-covered surface under convective conditions are:

- The pattern in the surface temperature resembles the turbulent flow above the surface. This pattern is closely related to the heat capacity of the vegetation layer, but it does not feed back to the flow: the results show that the statistics of the turbulence are similar for

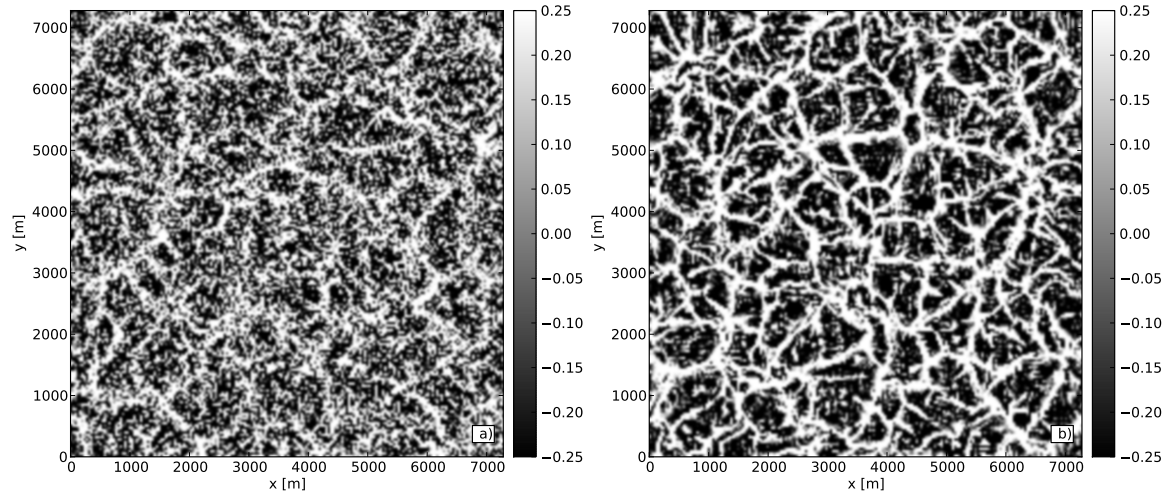

Figure 8.7: Horizontal instantaneous cross section of vertical wind speed at the 4th model level (35 m) in runs ref_{fc} and $nomason_{fc}$ at 12h30 UTC.

a run with zero heat capacity, a run including a heat capacity and a run in which zero heat capacity is used, but where horizontal averaging is applied on the surface fluxes.

- The surface energy balance is insensitive to whether Monin-Obukhov Similarity Theory (MOST)-based surface models are applied locally or on area-averaged fields. The intensity and stability of the turbulence near the surface, measured in u_* and z/L, are slightly influenced by the method of applying MOST, but this has limited impact on the turbulence statistics in the mixed-layer and the entrainment zone of the CBL.

- If wall damping is not applied to take into account the reduction in the SGS mixing length near the land surface, too much turbulent kinetic energy dissipates near the land surface. This results in a lower u_* and larger temperature and moisture gradients between the surface and the atmosphere, but the surface energy balance remains insensitive.

- In free convective conditions, the surface energy balance is more sensitive to the method of applying MOST than in conditions with a geostrophic forcing. Nevertheless, the sensitivity remains low. Under these conditions, using wall damping or not has a significant influence on the vertical velocity variance as disabling wall damping allows the turbulence to organize faster into vertically oriented structures.

These findings can be explained by two physical mechanisms that exist in the coupled land-atmosphere system. First, in a CBL the self-organization of the turbulence is so strong that a field of surface fluxes containing small scale spatial variability leads to the same turbulence statistics as a field having spatially homogeneous surface fluxes as long as both have the same area-averaged heat fluxes. Second, the surface heat fluxes are constrained by the net radiation rather than by the amount of turbulence, because the surface temperature adjusts very fast to changes in radiation and atmospheric variables induced by turbulence.

Our results contain an interesting message for LES and numerical weather prediction (NWP) modelers. The land surface formulations as commonly used in NWP and climate models still perform well if resolution is increased towards the resolutions typically used

in LES, despite the fact that some of the assumptions that form the basis of RANS models gradually break down while moving towards higher resolutions. These results apply to the convective boundary layer: we expect the sensitivity of the coupled LES-LSM model to be higher under neutral and stable conditions.

9 Summary and perspectives

This section contains an overview of the most relevant findings of this PhD research. It is discussed here to which extent the objectives of this thesis have been met and how future research can build upon the results presented in the thesis. This section does therefore not discuss all results in detail, as this is already done in Chapters 4 to 8.

9.1 Summary of most relevant findings

9.1.1 Interactions between surface evaporation and the convective boundary layer

The first objective in this thesis is to improve the understanding of surface evaporation and transport of water vapor in the convective boundary layer (CBL). The results show that the amount of water that evaporates at the land surface is tightly connected to the processes in the CBL. This research confirms and quantifies the large impact of entrainment processes on the surface energy balance and the related time evolution of the CBL. The mathematical analysis and the model results in Chapter 4 show that the entrainment of dry air into the CBL is able to enhance evaporation in all conditions: in cold and warm atmospheres, and over wet and dry soils. The strongest effects are found in a cold atmosphere over a wet soil. As long as there are no clouds, the feedbacks in the coupled system direct the system to an equilibrium state in which the temperature and humidity profile of the CBL determine the fraction of the available energy that is used for evaporating water.

This equilibrium evaporation rate can be related to the equilibrium of Priestley and Taylor (1972). They show that over a well-watered land surface the evaporative fraction becomes 1.26 (the value of their famous constant α) times their equilibruim evaporative fraction. The ratio of our derived equilibrium evaporative fraction and that of Priestley and Taylor (1972) also approaches 1.26 under a wide range of conditions. This proves that the derived equilibrium in this thesis, rather than that of Priestley and Taylor (1972), is the correct state of equilibrium evaporation beneath a growing CBL.

In Chapter 5 a tendency equation for surface evaporation is derived that can be used to quantify the influence of all feedbacks and forcings in the coupled land-atmosphere system that act on evaporation. Based on two observed cases, one in the midlatitudes (Cabauw, The Netherlands) and the other in a semi-arid region (Niamey, Niger), most of the qualitative findings of Chapter 4 are confirmed. The coupled mixed-layer model (see Chapter 2), on which output the analysis in Chapter 5 is based, is, despite its simplicity, able to reproduce the measurements well. The entrainment of dry air is found to be very important in the midlatitudes, where an enhancement of evaporation of up to 20 W m^{-2} h^{-1} was found in the data of Cabauw. The feedbacks between the CBL and the land surface are of similar importance in both the midlatitudes and the semi-arid regions, but the relative importance of temperature and moisture related processes varies greatly. The daily variations in the aerodynamic part of the evaporation (related to the specific humidity deficit of the air $q_{sat} - q$) depend in the midlatitudes as much on variations in q_{sat}, thus on temperature, as on variations in q, the water processes. Under conditions of high temperatures, such as in Niamey, the daily variations in q_{sat} are so large compared to those in q, that the impact of moist processes is relatively small.

The set of negative feedback mechanisms that govern the coupled land surface-CBL system (see Chapter 4) imposes a tight coupling between temperature, vapor pressure deficit (VPD) and surface evaporation. This coupling can serve as guide in interpreting long term climate data, which we demonstrate in Chapter 6, where we show that the coupling allows for the interpretation of the controversial negative trends in pan evaporation under conditions of global warming. As climate forcings, such as global warming, dimming, changes in precipitation and decreasing wind speed, have their unique footprint in the measurements of pan evaporation, temperature and VPD, it is possible to deduce the most important climate forcings from these measurements. Furthermore, we are also able to infer the trend in the actual evaporation from the measurements. This is useful, as actual evaporation is hard to measure directly.

9.1.2 Surface evaporation and water vapor transport over heterogeneous terrain

The second objective of this thesis is to understand surface evaporation and water transport in the CBL over a land surface with spatially varying surface conditions. Here, a large-eddy simulation (LES) model (see Chapter 3) served as the main tool. The study of water transport over heterogeneous terrain without taking into account land-atmosphere interactions (see Chapter 7) shows that heterogeneity has a strong influence on the atmospheric flow. In situations with low geostrophic wind speeds, thermal heterogeneity introduces mesoscale circulations that are able to transport heat and moisture in large turbulent structures. These circulations transport moisture from locations with high evaporation rates and low sensible heat fluxes to locations with low evaporation rates and high sensible heat fluxes. Therefore, the atmospheric moisture is mostly located over the areas with the lowest evaporation rates. Despite the strong modification of the atmospheric flow, the horizontally averaged vertical profiles of moisture and heat and their associated vertical fluxes are remarkably similar between homogeneous and heterogeneous land surfaces as long as the horizontally averaged energy input is the same. Nevertheless, the redistribution of moisture and heat due to the heterogeneity-induced circulations influences the relative humidity in the CBL top: under heterogeneous conditions peaks in the relative humidity at the CBL top are significantly higher than under conditions of homogeneous surface forcings. Therefore, cloud formation is more likely to occur over

heterogeneous land surfaces.

A thorough evaluation of the assumptions behind land surface models (see Chapter 8) reveals that the surface energy balance as produced by a typical land surface model is insensitive to the most important formulations in the scheme. The heat capacity of the skin layer slightly influences the reaction time of the system, but has little impact on the turbulent structure of the atmosphere. The model results show also little sensitivity to whether Monin-Obukhov similarity theory is applied locally, or on area averaged fields.

There are two main explanations why the results of the LES simulations of a CBL with a coupled land surface are insensitive to the formulation of the land surface model. The first is related to the constraint that radiation puts on the system. As the heat capacity of the vegetation layer is small, the incoming energy is quickly distributed over the latent, sensible and ground heat flux. Consequently, in cases where turbulence influences the speed at which the atmosphere can take up heat and moisture, the surface temperature adapts rapidly to the flow, thereby acting as a negative feedback mechanism by maintaining the heat fluxes at a constant rate. An important element of this mechanism is that both the flux of moisture and temperature respond in the same direction to turbulent fluctuations: a decrease in the wind speed lowers both fluxes and an increase in surface temperature increases both fluxes. Therefore, turbulent fluctuations hardly influence the ratio between the fluxes.

The second explanation is related to the strong self-organization in turbulent flow. The structures that are found in the surface temperature of a vegetated surface without heat capacity resemble the turbulent flow. By increasing the heat capacity of the vegetation larger structures are being smoothed out at the surface. This, however, has no effect on the variances of wind, temperature and moisture close to the surface. This proves that turbulent flow is so effective in organizing itself that it can impose a structure in surface temperature on the vegetation layer, without experiencing any feedback from this structure. Therefore, small scale heterogeneity in surface temperature at the surface leads to exactly the same variances in the CBL as a fully homogeneous surface energy input with the same area averaged value.

9.2 Perspectives

9.2.1 Extending the view of the coupled land-atmosphere system

In this thesis a complete view of the coupled land-atmosphere system has been acquired that has been validated over short vegetation (grass) during daytime on a cloudless day. The obvious extensions of this research are the incorporation of boundary-layer clouds and their associated processes and of more advanced types of vegetation. Furthermore, extending the time frame to longer periods (multiple days or weeks) opens many new possible studies. Figure 9.1 shows three new variants of the feedback diagram introduced in Chapter 4 (Figure 4.1).

Boundary-layer clouds introduce additional processes that can largely influence the daily dynamics (see Figure 9.1b). Clouds influence the system in two ways. First, cloud formation restricts the growth of the well-mixed layer (the layer below cloud base), as thermals that condensate transfer mass from the CBL into the cloud layer. This would weaken the link between the sensible heat flux (H) and the CBL height (h). In addition, as the mass that leaves the CBL is relatively moist, drying of the subcloud layer occurs. Second, cloud formation has

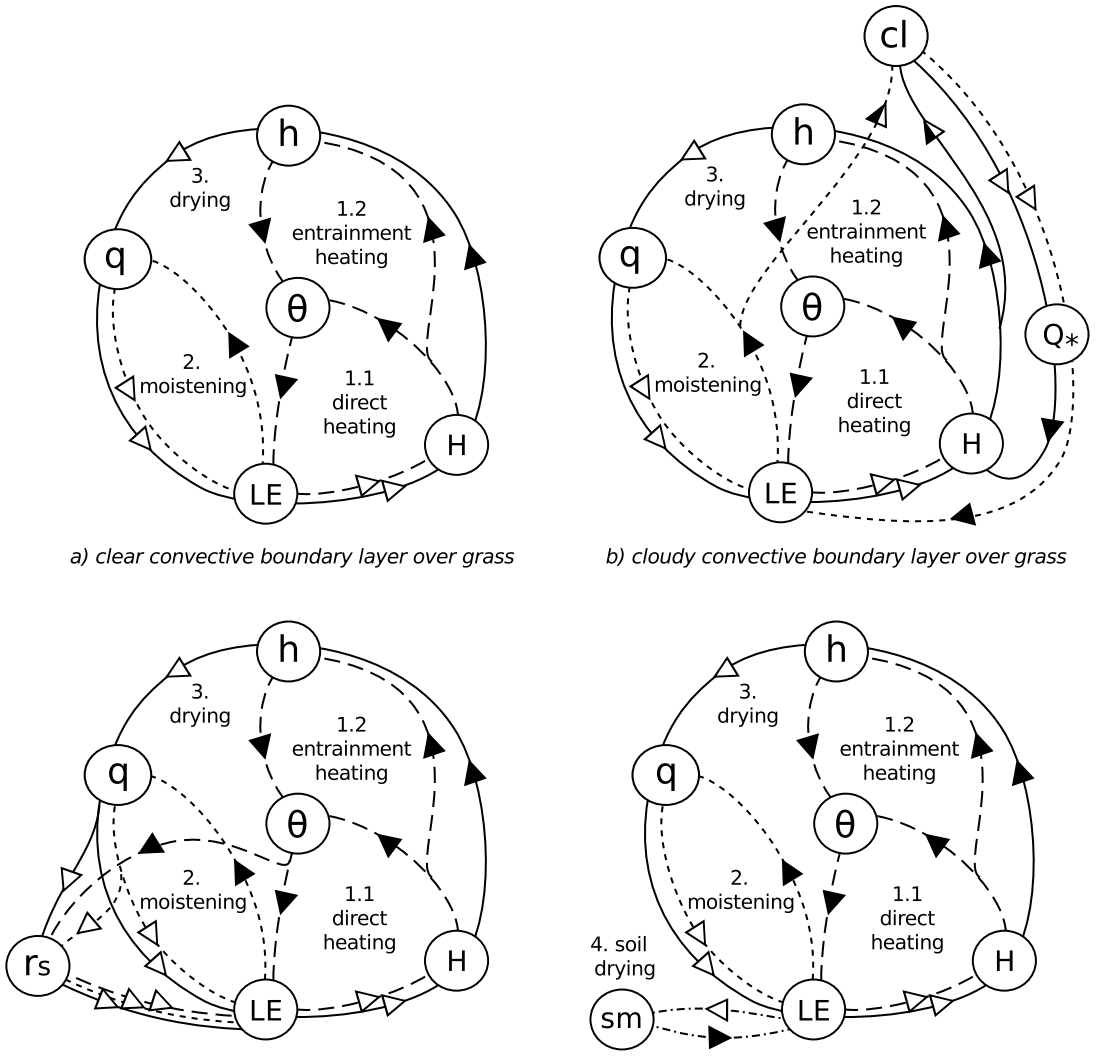

Figure 9.1: Feedbacks in four conceptual setups of the coupled land-atmosphere system. Closed arrows represent positive relationships, open arrow negative relationships. The arrows which are half open, half closed can be both positive and negative. Each of the three feedbacks has a distinct line style. LE is the latent heat flux, H is the sensible heat flux, θ is the bulk potential temperature of the CBL, q is the bulk specific humidity of the CBL, h is the CBL height, r_s is the stomatal resistance, cl is the cloud fraction and Q_* is the net radiation.

a strong impact on the radiation balance. Fair-weather cumulus clouds, which would be the most natural extension of the research in this thesis, reflect short wave radiation that would otherwise reach the land surface. The most complex part in understanding this system is the link between the surface fluxes H and LE and the actual formation of clouds, which can be either positive or negative (Ek and Holtslag, 2004).

The daily dynamics of the coupled system over a forest introduces a bifurcation point in the system as the drying feedback can turn from a negative into a positive feedback (Figure 4.1c). As forests strongly reduce their evaporation rate in the presence of dry air, the entrainment of dry air does not only enhance the atmospheric demand for water (through θ and q), but at the same time it also decreases the capacity of the land surface to provide it (increasing r_s). Therefore, in conditions that the latter effect is stronger than the former, the system no longer converges to the equilibrium evaporation as defined in Chapter 4. Instead, it will shift to a

lower evaporation rate *LE*. This rate will become either zero, or the point where the increase in atmospheric demand for water is balanced by the capacity of the land surface to provide it. However, it remains to be determined how the feedback mechanisms are acting exactly.

The next step would be to move from the daily time scale towards the weekly or monthly time scale. Except for the analysis of the data of Niamey (Niger) (see Chapter 5), the soil moisture dynamics only played a role as a forcing in the system. On longer time scales, however, in many situations soil moisture is the key variable in the most important feedback mechanisms of the system (see Seneviratne et al. (2010)) as it determines the amount of water that can be evaporated over a longer time span when there is no recharge via precipitation or ground water. This link introduces a fourth feedback loop in the system: *soil drying*. Evaporation results in less soil moisture (*sm*) and a reduction in soil moisture results in a decrease in evaporation (*LE*). This feedback can introduce complex interactions between multiple time scales. For instance, the water-limiting feedback in forests explained in the previous paragraph, can have an evaporation enhancing effect over a longer time span (see for instance Teuling et al. (2010)). The exact interactions between short and longer time scales are poorly understood.

9.2.2 LES simulations of land surface interactions over heterogeneous land surfaces

This thesis contains a LES-study to water transport over a heterogeneous land surface (see Chapter 7) and contains a thorough evaluation of a land surface model performed for a homogeneous land surface (see Chapter 8). The next step, which joins both previous chapters, is modeling heterogeneous land surfaces which can freely interact with the flow.

The most relevant open question is to which extent land-atmosphere interactions enhance or suppress the effects of heterogeneity. If, for instance, we consider the surface heterogeneity pattern of Chapter 7, where the heterogeneity consist of a warm and dry patch adjecent to a cold and wet patch, the land-atmosphere interactions might enhance the heterogeneity because the entrainment of dry air over the cold and wet patch might boost the evaporation, resulting in a patch that is even colder and moister. On the other hand, it is not unlikely that the opposite effects happen, where the generation of wind by the heterogeneity might result in a smoother transition between the two patches than in the case with the forced fluxes, thereby dampening the effect of the heterogeneity.

The extension towards clouds also poses interesting challenges where the LES-LSM could be an appropriate tool. Interesting here is the question whether the response of the land surface to the shading induced by individual clouds has an impact on the turbulent structure of the CBL. In Chapter 8 it was shown that radiation is a leading variable of the system. If, in this case, strong patterns in radiation are imposed at the land surface, the turbulence is expected to respond, but only if the clouds are large and sufficiently persistent. How large, that remains the question.

In the last place, we should ask ourselves whether the cases that are generally studied under the topic of heterogeneity are not too idealized. In Chapter 7, but also in many other studies (e.g. Avissar and Schmidt, 1998; Letzel and Raasch, 2003; Patton et al., 2005) a case of free convection without background wind is studied. Avissar and Schmidt (1998) showed that with minimal wind the majority of the effects of heterogeneity on the turbulent flow vanish. If

the effects of land surface heterogeneity on turbulence are small in most daytime conditions, then it makes more sense to aim future heterogeneity related research on cloudy boundary layers as the results in Chapters 7 and 8 indicate that the strongest effects might be found there.

References

Albertson, J. D. and M. B. Parlange, 1999: Natural integration of scalar fluxes from complex terrain. *Adv. Water Res.*, **23**, 239–252.

Andren, A., A. R. Brown, J. Graf, P. J. Mason, C.-H. Moeng, F. T. M. Nieuwstadt, and U. Schumann, 1994: Large-eddy simulation of a neutrally stratified boundary layer: A comparison of four computer codes. *Quart. J. Roy. Meteor. Soc.*, **120**, 1457–1484.

Avissar, R. and Y. Liu, 1996: Three-dimensional numerical study of shallow convective clouds and precipitation induced by land surface forcing. *J. Geophys. Res.*, **101**, 7499–7518.

Avissar, R. and T. Schmidt, 1998: An evaluation of the scale at which ground-surface heat patchiness affects the convective boundary layer using large-eddy simulations. *J. Atmos. Sci.*, **55**, 2666–2689.

Beljaars, A. C. M., 1991: Numerical schemes for parametrizations. *Proceedings of the ECMWF Seminar on Numerical Methods in Atmospheric Models*, ECMWF, 1–42.

Beljaars, A. C. M., 1994: The parametrization of surface fluxes in large-scale models under free convection. *Quart. J. Roy. Meteor. Soc.*, **121**, 255–270.

Best, M. J., A. Beljaars, J. Polcher, and P. Viterbo, 2004: A proposed structure for coupling tiled surfaces with the planetary boundary layer. *J. Hydrometeor.*, **5**, 1271–1278.

Betts, A. K., 1992: FIFE atmospheric boundary layer budget methods. *J. Geophys. Res.*, **97**, 18 525–18 531.

Betts, A. K., 1994: Relation between equilibrium evaporation and the saturation pressure budget. *Bound.-Layer Meteor.*, **71**, 235–245.

Betts, A. K., 2004: Understanding hydrometeorology using global models. *Bull. Amer. Meteor. Soc.*, **85**, 1673–1688, doi:10.1175/BAMS-85-11-1673.

Betts, A. K., J. H. Ball, A. C. M. Beljaars, M. J. Miller, and P. A. Viterbo, 1996: The land surface-atmosphere interaction: A review based on observational and global modeling perspectives. *J. Geophys. Res.*, **101**, 7209–7225.

Bou-Zeid, E., C. Meneveau, and M. Parlange, 2005: A scale-dependent lagrangian dynamic model for large eddy simulation of complex turbulent flows. *Phys. of Fluids*, **17**, 025 105, doi:10.1063/1.1839152.

Bou-Zeid, E., C. Meneveau, and M. B. Parlange, 2004: Large-eddy simulation of neutral atmospheric boundary layers flow over heterogeneous surfaces: Blending height and effective surface roughness. *Water Resour. Res.*, **40**, W02 505, doi:10.1029/2003WR002475.

Bou-Zeid, E., M. B. Parlange, and C. Meneveau, 2007: On the parameterization of surface roughness at regional scales. *J. Atmos. Sci.*, **64**, 216–227, doi:10.1175/JAS3826.1.

Brasseur, J. G. and T. Wei, 2010: Designing large-eddy simulation of the turbulent boundary layer to capture law-of-the-wall scaling. *Phys. of Fluids*, **22**, 021 303, doi:10.1063/1.3319073.

Bretherton, C. S. and coauthors, 1998: An intercomparison of radiately-driven entrainment and turbulence in a smoke cloud, as simulated by different numerical models. *Quart. J. Roy. Meteor. Soc.*, **125**, 391–423.

Brotzge, J. A. and K. C. Crawford, 2003: Examination of the surface energy budget: a comparison of eddy correlation and bowen ratio measurement systems. *J. Hydrometeor.*, **4**, 160–178, doi:10.1175/1525-7541(2003)4<160:EOTSEB>2.0.CO;2.

Brubaker, K. L. and D. Entekhabi, 1995: An analytic approach to land-atmosphere interaction, 1, Model construct and equilibrium results. *Water Resour. Res.*, **31**, 619–632.

Brubaker, K. L. and D. Entekhabi, 1996: Analysis of feedback mechanisms in land-atmosphere interaction. *Water Resour. Res.*, **32**, 1343–1357.

Brutsaert, W. and M. B. Parlange, 1998: Hydrologic cycle explains the evaporation paradox. *Nature*, **396**, 30.

Businger, J. A., J. C. Wyngaard, Y. Izumi, and E. F. Bradley, 1971: Flux-profile relationships in the atmospheric surface layer. *J. Atmos. Sci.*, **28**, 181–189.

Canut, G., M. Lothon, F. Saïd, and F. Lohou, 2010: Observations of entrainment at the interface between monsoon flow and the Saharan air layer. *Quart. J. Roy. Meteor. Soc.*, **136**, 34–46, doi:10.1002/qj.471.

Casso-Torralba, P., J. Vilà-Guerau de Arellano, F. Bosveld, M. R. Soler, A. Vermeulen, C. Werner, and E. Moors, 2008: Diurnal and vertical variability of the sensible heat and carbon dioxide budgets in the atmospheric surface layer. *J. Geophys. Res.*, **113**, D12 119, doi:10.1029/2007JD009583.

Chagnon, F. J. F. and R. L. Bras, 2005: Contemporary climate change in the Amazon. *Geophys. Res. Lett.*, **32**.

Chagnon, F. J. F., R. L. Bras, and J. Wang, 2004: Climatic shift in patterns of shallow clouds over the Amazon. *Geophys. Res. Lett.*, **31**.

Chow, F. K., R. L. Street, M. Xue, and J. H. Ferziger, 2005: Explicit filtering and reconstruction turbulence modeling for large-eddy simulation of neutral boundary layer flow. *J. Atmos. Sci.*, **62**, 2058–2077.

Clapp, R. B. and G. M. Hornberger, 1978: Empirical equations for some soil hydraulic properties. *Water Resour. Res.*, **14**, 601–604.

Conzemius, R. J. and E. Fedorovich, 2006: Dynamics of sheared convective boundary layer entrainment. Part I: methodological background and large-eddy simulations. *J. Atmos. Sci.*, **63**, 1151–1178.

Crook, N. A., 1997: Sensitivity of moist convection forced by boundary layer processes to low-level thermodynamic fields. *Mon. Wea. Rev.*, **124**, 1767–1785.

Cuijpers, J. W. M. and P. G. Duynkerke, 1993: Large-eddy simulation of trade-wind cumulus clouds. *J. Atmos. Sci.*, **50**, 3894–3908.

Culf, A., 1994: Equilibrium evaporation beneath a growing convective boundary layer. *Bound.-Layer Meteor.*, **70**, 37–49.

De Bruin, H. A. R., 1983: A model for the Priestley-Taylor parameter α. *J. Applied Met.*, **32**, 572–578, doi:10.1175/1520-0450(1983)022<0572:AMFTPT>2.0.CO;2.

De Bruin, H. A. R. and A. A. M. Holtslag, 1982: A simple parameterization of the surface fluxes of sensible and latent heat during daytime compared with the Penman-Monteith concept. *J. Applied Met.*, **21**, 1610–1621.

De Roode, S. R., P. G. Duynkerke, and H. J. J. Jonker, 2004: Large-eddy simulation: how large is large enough? *J. Atmos. Sci.*, **61**, 403–421.

Deardorff, J. W., 1973: Three-dimensional numerical modeling of the planetary boundary layer. *Workshop on Meteorology*, D. A. Haugen, Ed., American Meteorological Society, 271–311.

Deardorff, J. W., 1980: Stratocumulus-capped mixed layers derived from a three-dimensional model. *Bound.-Layer Meteor.*, **18**, 495–527.

Dosio, A., J. Vilà-Guerau de Arellano, A. A. M. Holtslag, and P. J. H. Builtjes, 2005: Dispersion of a passive tracer in buoyancy- and shear-driven boundary layers. *J. Atmos. Sci.*, **42**, 1116–1130.

Duynkerke, P. G., 1991: Radiation fog: A comparison of model simulation with detailed observations. *Mon. Wea. Rev.*, **119 (2)**, 324–341.

Duynkerke, P. G., 1999: Turbulence, radiation and fog in Dutch stable boundary layers. *Bound.-Layer Meteor.*, **90**, 447–477, doi:10.1023/A:1026441904734.

Eichinger, W. E., M. B. Parlange, and H. Stricker, 1996: On the concept of equilibrium evaporation and the value of the Priestley-Taylor coefficient. *Water Resour. Res.*, **32**, 161–164.

Ek, M. B. and A. A. M. Holtslag, 2004: Influence of soil moisture on boundary layer cloud development. *J. Hydrometeor.*, **5**, 86–99.

Ek, M. B. and L. Mahrt, 1994: Daytime evolution of relative humidity at the boundary layer top. *Mon. Wea. Rev.*, **122**, 2709–2721.

Ek, M. B., K. E. Mitchell, Y. Lin, E. Rogers, P. Grunmann, V. Koren, G. Gayno, and J. D. Tarpley, 2003: Implementation of NOAH land surface model advances in the National Centers for Environmental Prediction operational mesoscale ETA model. *J. Geophys. Res.*, **108**, D22, 8851, doi:10.1029/2002JD003296.

Emanuel, K. A., 1994: *Atmospheric Convection*. Oxford University Press, New York.

Freedman, J. M., Fitzjarrald, D. R., K. E. Moore, and R. K. Sakai, 2001: Boundary layer clouds and vegetation-atmosphere feedbacks. *J. Climate*, **14**, 180–197.

Gentine, P., D. Entekhabi, and J. Polcher, 2010: Spectral behaviour of a coupled land-surface and boundary-layer system. *Bound.-Layer Meteor.*, **134**, 157–180, doi:10.1007/s10546-009-9433-z.

Gentine, P., J. Polcher, and D. Entekhabi, 2011: Harmonic propagation of variability in surface energy balance within a coupled soil-atmosphere system. *Water Resour. Res.*, **In press**, doi:10.1029/2010WR009268.

Golubev, V. S., J. H. Lawrimore, P. Y. Groisman, N. A. Speranskaya, S. A. Zhuravin, M. J. Menne, T. C. Peterson, and R. W. Malone, 2001: Evaporation changes over the contiguous United States and the former USSR: a reassessment. *Geophys. Res. Lett.*, **28**, 2665–2668.

Hadfield, M. G., W. R. Cotton, and R. A. Pielke, 1991: Large-eddy simulations of thermally forced circulation in the convective boundary layer. Part I: A small scale circulation with zero wind. *Bound.-Layer Meteor.*, **57**, 79–114.

Hechtel, L. M., C. H. Moeng, and R. B. Stull, 1990: The effects of nonhomogeneous surface fluxes on the convective boundary layer: A case study using large-eddy simulations. *J. Atmos. Sci.*, **47**, 1721–1741.

Heus, T., et al., 2010: Formulation of the Dutch Atmospheric Large-Eddy Simulation (DALES) and an overview of its applications. *Geosci. Model. Dev. Discuss.*, **3**, 99–180.

Hobbins, M. T., J. A. Ramirez, and T. C. Brown, 2004: Trends in pan evaporation and actual evapotranspiration across the conterminous U.S.: paradoxical or complementary? *Geophys. Res. Lett.*, **31**, L13 503, doi:10.1029/2004GL019846.

Huang, H.-Y. and S. A. Margulis, 2008: On the impact of surface heterogeneity on a realistic convective boundary layer. *Water Resour. Res.*, **45**, W04 425, doi:10.1029/2008WR007175.

Huang, H.-Y. and S. A. Margulis, 2009: On the impact of surface heterogeneity on a realistic convective boundary layer. *Water Resour. Res.*, **45**, W04 425, doi:10.1029/2008WR007175.

Huang, H.-Y. and S. A. Margulis, 2010: Evaluation of a fully coupled large-eddy simulation-land surface model and its diagnosis of land-atmosphere feedbacks. *Water Resour. Res.*, **46**, W06 512, doi:10.1029/2009WR008232.

Hundsdorfer, W., B. Koren, M. Vanloon, and J. G. Verwer, 1995: A positive finite-difference advection scheme. *J. Comput. Phys.*, **117**, 35–46, doi:10.1006/jcph.1995.1042.

Hussain, A. K. M. F. and W. C. Reynolds, 1970: The mechanics of an organized wave in turbulent shear flows. *J. Fluid Mech.*, **41**, 241–258.

Jacobs, C. J. M. and H. A. R. De Bruin, 1992: The sensitivity of regional transpiration to land-surface characteristics: significance of feedback. *J. Climate*, **5**, 683–698, doi:10.1175/1520-0442(1992)005<0683:TSORTT>2.0.CO;2.

Jarvis, P. G., 1976: The interpretation of the variations in leaf water potential and stomatal conductance found in canopies in the field. *Philos. Trans. Roy. Soc. London*, **273B**, 593–610.

Jonker, H. J. J., P. G. Duynkerke, and J. W. M. Cuijpers, 1999: Mesoscale fluctuations in scalars generated by boundary layer convection. *J. Atmos. Sci.*, **56**, 801–811.

Juang, J.-Y., A. Porporato, P. C. Stoy, M. S. Siquera, A. C. Oishi, M. Detto, H.-S. Kim, and G. Katul, 2007: Hydrologic and atmospheric controls on initiation of convective precipitation events. *Water Resour. Res.*, **43**, doi:10.1029/2006WR004954.

Kang, S.-L., K. J. Davis, and M. LeMone, 2007: Observations of the ABL structures over a heterogeneous land surface during IHOP2002. *J. Hydrometeor.*, **8**, 221–244.

Klink, K., 1999: Climatological mean and interannual variance of United States surface wind speed, direction and velocity. *Int. J. Climatol.*, **19**, 471–488.

Koster, R. D., et al., 2004: Regions of strong coupling between soil moisture and precipitation. *Science*, **305**, 1138–1140, doi:10.1126/science.1100217.

Lawrimore, J. H. and T. C. Peterson, 2000: Pan evaporation trends in dry and humid regions of the United States. *J. Hydrometeor.*, **1**, 543–546.

Letzel, M. O. and R. Raasch, 2003: Large eddy simulation of thermally induced oscillations in the convective boundary layer. *J. Atmos. Sci.*, **60**, 2328–2341.

Lilly, D. K., 1968: Models of cloud-topped mixed layers under a strong inversion. *Quart. J. Roy. Meteor. Soc.*, **94**, 292–309.

Lilly, D. K., 2002: Entrainment into mixed layers. Part I: Sharp-edged and smoothed tops. *J. Atmos. Sci.*, **59**, 3340–3352.

Lothon, M., F. Couvreux, S. Donier, F. Guichard, P. Lacarrère, D. H. Lenschow, J. Noilhan, and F. Saïd, 2007: Impact of coherent eddies on airborne measurements of vertical turbulent fluxes. *Bound.-Layer Meteor.*, **124**, 425–447, doi:10.1007/s10546-007-9182-9.

Louis, J. F., 1979: A parametric model of vertical fluxes in the atmosphere. *Bound.-Layer Meteor.*, **17**, 187–202, doi:10.1007/BF00117978.

Lyon, S. W., et al., 2008: Coupling terrestrial and atmospheric water dynamics to improve prediction in a changing environment. *Bull. Amer. Meteor. Soc.*, **89**, doi:10.1175/2008BAMS25.

Mahrt, L., 2000: Surface heterogeneity and vertical structure of the boundary layer. *Bound.-Layer Meteor.*, **96**, 33–62.

Margulis, S. A. and D. Entekhabi, 2001: Feedback between the land surface energy balance and atmospheric boundary layer diagnosed through a model and its adjoint. *J. Hydrometeor.*, **2**, 599–620.

Mason, P. J. and D. J. Thomson, 1992: Stochastic backscatter in large-eddy simulation of boundary layers. *J. Fluid Mech.*, **242**, 51–78.

McNaughton, K. G. and T. W. Spriggs, 1986: A mixed-layer model for regional evaporation. *Bound.-Layer Meteor.*, **34**, 243–262.

Meneveau, C. and J. Katz, 2000: Scale-invariance and turbulence models for large-eddy simulation. *Annu. Rev. Fluid Mech.*, **32**, 1–32.

Miller, M. A. and A. Slingo, 2007: The ARM mobile facility and its first international deployment: measuring radiative flux divergence in West Africa. *Bull. Amer. Meteor. Soc.*, **88**, 1229–1244, doi:10.1175/BAMS-88-8-1229.

Milly, P. C. D. and K. A. Dunne, 2001: Trends in evaporation and surface cooling in the Mississippi River basin. *Geophys. Res. Lett.*, **28**, 1219–1222.

Moeng, C. H., 1984: A large-eddy simulation for the study of planetary boundary layer turbulence. *J. Atmos. Sci.*, **41**, 2052–2062.

Monteith, J. L., 1965: Evaporation and environment. *Symp. Soc. Exp. Biol.*, **XIX**.

Nieuwstadt, F. T. M. and R. A. Brost, 1986: The decay of convective turbulence. *J. Atmos. Sci.*, **43**, 532–546.

Noilhan, J. and J.-F. Mahfouf, 1996: The ISBA land surface parameterisation scheme. *Glob. Plan. Change*, **13**, 145–159.

Noilhan, J. and S. Planton, 1989: A simple parameterization of land surface processes for meteorological models. *Mon. Wea. Rev.*, **117**, 536–549.

Patton, E. G., P. P. Sullivan, and C. H. Moeng, 2005: The influence of idealized heterogeneity on wet and dry planetary boundary layers coupled to the land surface. *J. Atmos. Sci.*, **62**, 2078–2097.

Paulson, C. A., 1970: The mathematical representation of wind speed and temperature profiles in the unstable atmospheric surface layer. *J. Applied Met.*, **9**, 857–861.

Peterson, T. C., V. S. Golubev, and P. Y. Groisman, 1995: Evaporation losing its strength. *Nature*, **377**, 687–688.

Pielke, R. A., 2001: Influence of the spatial distribution of vegetation and soils on the prediction of cumulus convective rainfall. *Rev. Geophys.*, **39**, 151–178.

Pino, D., J. Vilà-Guerau de Arellano, and P. G. Duynkerke, 2003: Formulation of turbulent fluxes in the stable boundary layer. *J. Atmos. Sci.*, **60**, 2538–2548.

Pino, D., J. Vilà-Guerau de Arellano, and S.-W. Kim, 2006: Representing sheared convective boundary layer by zeroth- and first-order-jump mixed-layer models: large-eddy simulation verification. *J. Applied Met.*, **45**, 1224–1243.

Piomelli, U. and E. Balaras, 2002: Wall-layer models for large-eddy simulations. *Annu. Rev. Fluid. Mech.*, **34**, 349–374.

Porté-Agel, F., C. Meneveau, and M. B. Parlange, 2000: A scale-dependent dynamic model for large-eddy simulation: application to a neutral atmospheric boundary layer. *J. Fluid Mech.*, **415**, 261–284.

Priestley, C. H. B. and R. J. Taylor, 1972: On the assessment of surface heat flux and evaporation using large-scale parameters. *Mon. Wea. Rev.*, **100**, 81–92.

Ramier, D., et al., 2009: Towards an understanding of coupled physical and biological processes in the cultivated Sahel - 1. Energy and water. *J. Hydrology*, **375**, 204 – 216.

Raupach, M. R., 1991: Vegetation-atmosphere interaction in homogeneous and heterogeneous terrain: some implications of mixed-layer dynamics. *Plant Ecology*, **91**, 105–120, doi:10.1007/BF00036051.

Raupach, M. R., 2000: Equilibrium evaporation and the convective boundary layer. *Bound.-Layer Meteor.*, **96**, 107–141.

Raupach, M. R., 2001: Combination theory and equilibrium evaporation. *Quart. J. Roy. Meteor. Soc.*, **127**, 1149–1181.

Redelsperger, J. L., C. D. Thorncroft, A. Diedhiou, T. Lebel, D. J. Parker, and J. Polcher, 2006: African Monsoon Multidisciplinary Analysis: An international research project and field campaign. *Bull. Amer. Meteor. Soc.*, **87 (12)**, 1739–1746.

Roderick, M. L. and G. D. Farquhar, 2002: The cause of decreased pan evaporation over the past 50 years. *Science*, **298**, 1410–1411.

Roderick, M. L., M. T. Hobbins, and G. D. Farquhar, 2009a: Pan evaporation trends and the terrestrial water balance. II. Energy balance and interpretation. *Geography Compass*, **3**, 761–780, doi:10.1111/j.1749-8198.2008.00214.x.

Roderick, M. L., M. T. Hobbins, and G. D. Farquhar, 2009b: Pan evaporation trends and the terrestrial water balance. I. Principles and observations. *Geography Compass*, **3**, 746–760, doi:10.1111/j.1749-8198.2008.00213.x.

Roderick, M. L., L. D. Rotstayn, G. D. Farquhar, and M. T. Hobbins, 2007: On the attribution of changing pan evaporation. *Geophys. Res. Lett.*, **34**, L17 403, doi:10.1029/2007GL031166.

Santanello, J. A., M. A. Friedl, and M. B. Ek, 2007: Convective planetary boundary layer interactions with the land surface at diurnal time scales: diagnostics and feedbacks. *J. Hydrometeor.*, **8**, 1082–1097.

Santanello, J. A., C. D. Peters-Lidard, S. V. Kumar, C. Alonge, and W.-K. Tao, 2009: A modeling and observational framework for diagnosing local land-atmosphere coupling on diurnal time scales. *J. Hydrometeor.*, **10**, 577–599, doi:10.1175/2009JHM1066.1.

Sellers, P. J., F. G. Hall, G. Asrar, D. E. Strebel, and R. E. Murphy, 1992: An overview of the First International Satellite Land Surface Climatology Project (ISLSCP) Field Experiment (FIFE). *J. Geophys. Res.*, **97**, 18 345–18 371.

Seneviratne, S. I., T. Corti, E. Davin, M. Hirschi, E. B. Jaeger, I. Lehner, B. Orlowsky, and A. Teuling, 2010: Investigating soil moisture-climate interactions in a changing climate: A review. *Earth-Sci. Rev.*, **99**, 125–161, doi:10.1016/j.earscirev.2010.02.004.

Sheffield, J. and E. F. Wood, 2008: Global trends and variability in soil moisture and drought characteristics, 1950-2000, from observation-driven simulations of the terrestrial hydrologic cycle. *J. Climate*, **21**, 432–458, doi:10.1175/2007JCLI1822.1.

Shuttleworth, J. W., A. Serrat-Capdevila, M. L. Roderick, and R. L. Scott, 2009: On the theory relating changes in area-average and pan evaporation. *Quart. J. Roy. Meteor. Soc.*, **135**, 1230–1247, doi:10.1002/qj.

Siqueira, M., G. Katul, and A. Porporato, 2009: Soil moisture feedbacks on convection triggers: the role of soil-plant hydrodynamics. *J. Hydrometeor.*, **10**, 96–112, doi:10.1175/2008JHM1027.1.

Steeneveld, G. J., B. J. H. van de Wiel, and A. A. M. Holtslag, 2007: Diagnostic equations for the stable boundary layer height: evaluation and dimensional analysis. *J. App. Meteor. Clim.*, **46**, 212–225, doi:10.1175/JAM2454.1.

Sullivan, P. P., J. C. McWilliams, and C.-H. Moeng, 1994: A subgrid-scale model for large-eddy simulation of planetary boundary-layer flows. *Bound.-Layer Meteor.*, **71**, 247–276.

Sullivan, P. P., C. H. Moeng, B. Stevens, D. Lenschow, and S. D. Mayor, 1998: Structure of the entrainment zone capping the convective atmospheric boundary layer. *J. Atmos. Sci.*, **55**, 3042–3064.

Teixeira, J. and T. F. Hogan, 2002: Boundary layer clouds in a global atmospheric model: Simple cloud cover parameterizations. *J. Climate*, **15**, 1261–1276.

Tennekes, H., 1973: A model for the dynamics of the inversion above a convective boundary layer. *J. Atmos. Sci.*, **30**, 558–567.

Tennekes, H., 1981: Basic entrainment equations for the atmospheric boundary layer. *Bound.-Layer Meteor.*, **20**, 515–531.

Teuling, A. J., et al., 2009: A regional perspective on trends in continental evaporation. *Geophys. Res. Lett.*, **36**, L02 404, doi:10.1029/2008GL036584.

Teuling, A. J., et al., 2010: Contrasting response of European forest and grassland energy exchange to heatwaves. *Nature Geoscience*, doi:10.1038/NGEO950.

Trenberth, K. E., et al., 2007: Observations: Surface and atmospheric climate change. *Climate Change 2007: The Physical Science Basis. Contribution of Working Group I to the Fourth Assessment Report of the Intergovernmental Panel on Climate Change*, S. Solomon, D. Qin, M. Manning, Z. Chen, M. Marquis, K. B. Averyt, M. Tignor, and H. L. Miller., Eds., Cambridge University Press, Cambridge, United Kingdom and New York, NY, USA.

Trier, S. B., F. Chen, K. W. Manning, M. A. LeMone, and C. A. Davis, 2008: Sensitivity of the PBL and precipitation in 12-day simulations of warm-season convection using different land surface models and soil wetness conditions. *Mon. Wea. Rev.*, **136**, 2321–2343, doi:10.1175/2007MWR2289.1.

van Heerwaarden, C. C. and J. Vilà-Guerau de Arellano, 2008: Relative humidity as an indicator for cloud formation over heterogeneous landscapes. *J. Atmos. Sci.*, **65**, 32633277, doi:10.1175/2008JAS2591.1.

van Heerwaarden, C. C., J. Vilà-Guerau de Arellano, A. Gounou, F. Guichard, and F. Couvreux, 2010a: Understanding the daily cycle of evapotranspiration: a method to quantify the influence of forcings and feedbacks. *J. Hydrometeor.*, **11**, 1405–1422, doi:10.1175/2010JHM1272.1.

van Heerwaarden, C. C., J. Vilà-Guerau de Arellano, A. F. Moene, and A. A. M. Holtslag, 2009: Interactions between dry-air entrainment, surface evaporation and convective boundary layer development. *Quart. J. Roy. Meteor. Soc.*, **135**, 1277–1291, doi:10.1002/qj.431.

van Heerwaarden, C. C., J. Vilà-Guerau de Arellano, and A. J. Teuling, 2010b: Land-atmosphere coupling explains the link between pan evaporation and actual evapotranspiration trends in a changing climate. *Geophys. Res. Lett.*, **37**, L21 401, doi:10.1029/2010GL045374.

vanZanten, M. C., P. G. Duynkerke, and J. W. M. Cuijpers, 1999: Entrainment parameterization in convective boundary layers. *J. Atmos. Sci.*, **56**, 813–828.

Vilà-Guerau de Arellano, J., 2007: Role of nocturnal turbulence and advection in the formation of shallow cumulus over land. *Quart. J. Roy. Meteor. Soc.*, **133**, 1615–1627.

Viterbo, P. and A. C. M. Beljaars, 1995: An improved land surface parameterization scheme in the ECMWF model and its validation. *J. Climate*, **8**, 2716–2748.

Wesseling, P., 1996: Von Neumann stability conditions for the convection-diffusion equation. *IMA Journal of Numerical Analysis*, **16**, 583–598, doi:10.1093/imanum/16.4.583.

Wicker, L. J. and W. C. Skamarock, 2002: Time-splitting methods for elastic models using forward time schemes. *Mon. Wea. Rev.*, **130**, 2088–2097.

Wild, M., A. Ohmura, H. Gilgen, and D. Rosenfeld, 2004: On the consistency of trends in radiation and temperature records and implications for the global hydrological cycle. *Geophys. Res. Lett.*, **31**, L11 201, doi:10.1029/2003GL019188.

Wyngaard, J. C., 2004: Toward numerical modeling in the terra incognita. *J. Atmos. Sci.*, **61**, 1816–1826, doi:10.1175/1520-0469(2004)061<1816:TNMITT>2.0.CO;2.

Yaglom, A. M., 1977: Comments on wind and temperature flux-profile relationships. *Bound.-Layer Meteor.*, **11**, 89–102, doi:10.1007/BF00221826.

Samenvatting

Dit proefschrift heeft twee doelen. Het eerste doel is het begrijpen van de verdamping van water vanaf het landoppervlak en hoe dit water getransporteerd wordt in de convectieve grenslaag (CBL). De resultaten in hoofdstukken 4, 5 en 6 laten zien dat dat de hoeveelheid water die verdampt aan het landoppervlak sterk bepaald wordt door processen in de CBL. Dit proefschrift bevestigt en kwantificeert de invloed van entrainment van droge lucht op de energiebalans van het landoppervlak en de gerelateerde invloed op de ontwikkeling van de CBL. De mathematische analyse en de modelresultaten in hoofdstuk 4 laten zien dat entrainment van droge lucht de verdamping kan verhogen boven zowel droge als natte bodems en onder een droge en vochtige atmosfeer. De sterkste effecten worden gevonden in een koude atmosfeer boven een vochtige bodem. In afwezigheid van wolken begeeft het systeem zich door de terugkoppelingsmechanismes naar een staat van evenwicht waarin de fractie van de beschikbare energie die wordt gebruikt voor verdamping bepaald wordt door de temperatuur- en vochtprofielen van de atmosfeer.

De hoeveelheid verdamping in de evenwichtstoestand kan gerelateerd worden aan de evenwichtsverdamping zoals deze bepaald is door Priestley and Taylor (1972). Zij laten zien dat boven een vochtig landoppervlak de fractie van de beschikbare energie die besteed wordt aan verdamping gelijk is aan 1.26 (de waarde van hun befaamde constante α) maal hun evenwichtsfractie. De ratio tussen onze afgeleide evenwichtsfractie en die van Priestley and Taylor (1972) benadert ook 1.26 onder een groot bereik van toestanden van de atmosfeer. Dit toont aan dat de evenwichtsfractie zoals afgeleid in dit proefschrift de juiste is voor een groeiende grenslaag, omdat deze, in tegenstelling tot de fractie van Priestley and Taylor (1972), wel de effecten van entrainment mee neemt.

In hoofdstuk 5 wordt een vergelijking voor de tijdsevolutie van verdamping afgeleid. Hiermee kunnen de effecten van alle forceringen en terugkoppelingsmechanismen die van invloed zijn op verdamping worden gekwantificeerd. Een analyse van twee waargenomen situaties, waarvan een in de gematigde streken (Cabauw, Nederland) en een in de semi-aride streken (Niamey, Niger) bevestigt de kwalitatieve bevindingen van hoofdstuk 4. Het gekoppelde landoppervlak-menglaagmodel (zie hoofdstuk 2), waarvan de uitvoer gebruikt is voor de analyse in hoofdstuk 5, laat zien dat het in staat is om de metingen te reproduceren. Met name in de gematigde streken blijkt de invloed van drogeluchtentrainment erg belangrijk: de data van Cabauw laten een verhoging van 20 W m^{-2} h^{-1} zien door dit proces. De invloed van terugkoppelingsmechanismen tussen de CBL en het landoppervlak op verdamping is van gelijke orde in de gematigde streken en in de semi-aride streken, maar er is een sterk verschil in het relatieve belang van temperatuur- en vochtgerelateerde processen tussen de streken. De dagelijkse variatie in het aerodynamische deel van de verdamping (gerelateerd aan het specifieke vochtigheidsdeficiet van de lucht $q_{sat} - q$) hangt in de gematigde streken evenveel af van

variaties in q_{sat}, dus van temperatuurgerelateerde processen, als van variaties in q, ofwel de watergerelateerde processen. Wanneer de temperatuur hoog is, zoals in Niamey, is de dagelijkse variatie in q_{sat} zo groot in vergelijking tot die in q, dat de impact van vochtgerelateerde processen relatief klein is.

De set van negatieve terugkoppelingsmechanismen die het gekoppelde landoppervlak-CBL systeem reguleert (zie hoofdstuk 4) veroorzaakt een sterke koppeling tussen de temperatuur, het deficiet van de waterdampdruk en de verdamping aan het landoppervlak. Kennis van deze koppeling kan helpen bij het interpreteren van langetermijnklimaatdata (zie hoofdstuk 6). Klimaatforceringen zoals opwarming, veranderingen in inkomende straling, veranderingen in neerslag en afnemende windsnelheden laten een uniek spoor na in meetreeksen van panverdamping, temperatuur en het deficiet van de waterdampdruk. Het is daarom mogelijk om uit meetdata van deze drie variabelen de belangrijkste veranderingen in de klimaatforceringen te vinden en bovendien om de trend in de actuele verdamping af te leiden. Het laatste is van belang, omdat actuele verdamping moeilijk te meten is.

Het tweede doel van dit proefschrift is het begrijpen van verdamping vanaf het landoppervlak en watertransport in de CBL boven een landschap met een ruimtelijk variërend patroon van landgebruik (zie hoofdstuk 7). Voor dit doel is een zogenaamd Large-Eddy Simulatiemodel (LES) gebruikt (zie hoofdstuk 3). Een studie naar watertransport boven thermisch heterogeen landgebruik laat zien dat heterogeniteit een sterke invloed heeft op de atmosferische stroming. Wanneer de geostrofische windsnelheid laag is, leidt thermische heterogeniteit tot mesoschaalcirculaties die in staat zijn om warmte en vocht in grote structuren te transporteren. Deze circulaties transporteren vocht naar locaties met een grote voelbare warmteflux. Dit heeft tot gevolg dat vocht veelal geconcentreerd raakt boven gebieden met weinig verdamping. Ondanks de sterke modificatie van de stroming in de CBL door heterogeniteit zijn de horizontaal gemiddelde profielen van vocht en warmte en hun verticale fluxen opvallend gelijk in de CBL voor homogene en heterogene landoppervlakken, onder de voorwaarde dat hun horizontaal gemiddelde oppervlaktefluxen hetzelfde zijn. Desondanks zorgt de redistributie van vocht door circulatie ervoor dat er boven heterogene landschappen pieken in de relatieve vochtheid dichtbij de grenslaagtop voorkomen die hoger zijn dan de pieken boven een homogeen landoppervlak. Hierdoor lijkt de kans op wolkenvorming groter boven een heterogeen landoppervlak.

Een grondige evaluatie van de aannames in de formulering van de energiebalans in een landoppervlakmodel (LSM) (zie hoofdstuk 8) laat zien dat de oplossing van de energiebalans van het landoppervlak ongevoelig is voor veel van de formuleringen. De warmtecapaciteit van de vegetatielaag introduceert een kleine vertraging in het systeem, maar heeft nauwelijks invloed op de structuur van de turbulentie in de atmosfeer. De modelresultaten laten ook weinig gevoeligheid zien voor de ruimtelijke schaal waarop Monin-Obukhov similarity theory wordt toegepast: zowel een lokale toepassing als de toepassing op horizontaal gemiddelde velden laten nagenoeg dezelfde resultaten zien.

Er zijn twee belangrijke verklaringen voor het feit dat de resultaten van LES-simulaties van een CBL met een gekoppeld landoppervlak zo ongevoelig zijn voor de formulering van het landoppervlakmodel. De eerste verklaring is gerelateerd aan de limitatie die straling oplegt aan het systeem: vanwege de beperkte warmtecapaciteit van de vegetatielaag wordt de

inkomende energie snel verdeeld over de latente warmteflux, de voelbare warmteflux en de bodemwarmteflux. De oppervlaktetemperatuur past zich daarom snel aan aan de hoeveelheid straling en de turbulente toestand van de atmosfeer. Hierbij treedt het aanpassingsvermogen van de oppervlaktetemperatuur op als een negatief terugkoppelingsmechanisme, omdat het fluctuaties in fluxen door turbulentie teniet tracht te doen. Een belangrijk element van dit mechanisme is dat de fluxen van vocht en temperatuur in dezelfde richting reageren op turbulente fluctuaties: een verlaging van de windsnelheid verlaagt beide fluxen, terwijl de bijbehorende verhoging van de oppervlaktetemperatuur beide fluxen zal verhogen. Daarom hebben turbulente fluctuaties slechts een beperkte invloed op de ratio tussen de fluxen van vocht en temperatuur.

De tweede verklaring is gerelateerd aan de sterke zelforganisatie in turbulente stroming. De structuren die gevonden worden in de oppervlaktetemperatuur van een met vegetatie bedekt landoppervlak lijken op de structuren die gevonden worden in een turbulente stroming. Wanneer de warmtecapaciteit van de vegetatielaag groot is, zijn kleinere structuren, in tegenstelling tot een geval waarin de warmtecapaciteit klein is, niet langer zichtbaar in de oppervlaktetemperatuur. Dit heeft echter geen effect op de varianties van wind, temperatuur en vocht dichtbij het landoppervlak. Deze bevinding bewijst dat de turbulente stroming zo effectief is in het organiseren van zichzelf dat ze wel een structuur achterlaat in de oppervlaktetemperatuur, maar dat er geen terugkoppeling is van de structuur in de oppervlaktetemperatuur naar die van de atmosferische temperatuur. Daaruit kan geconcludeerd worden dat kleinschalige heterogeniteit in oppervlaktetemperatuur zal leiden tot dezelfde karakteristieken van de turbulentie in de CBL als een landoppervlak waarvan de oppervlaktetemperatuur volledig homogeen is, wanneer deze dezelfde gemiddelde oppervlaktetemperatuur heeft als het landoppervlak met kleinschalige heterogeniteit.

Dankwoord / Acknowledgments

Behalve dat dit proefschrift vier jaar aan werk bevat, zitten er ook vier jaar herinneringen aan vast. Deze herinneringen zijn onlosmakelijk verbonden met de mensen met wie ik de laatste vier jaar heb opgetrokken. Er is een aantal mensen dat een woord van dank verdient, omdat de kwaliteit van dit proefschrift gecorreleerd is met hun aanwezigheid in mijn leven.

I shall switch to English now, as the person to whom I am most grateful, is not particularly known for his Dutch languague skills. Jordi, thank you for everything! We have been working together for five years and I cannot think of a single moment that I have regretted this as you gave me an excellent introduction in the world of science. It was great to experience your never-ending dedication as a teacher, a supervisor, a colleague and, I hope you don't mind after all these years, as a friend.

Bert, ik wil jou graag bedanken voor het bieden van de mogelijkheid te werken in onze groep en voor de adviezen gedurende de weg. Ik heb vier jaar in volledige vrijheid kunnen werken aan de dingen die ik leuk vond en ik hoop dat dit proefschrift laat zien dat het het waard is geweest.

Mijn twee paranimfen, Ruud en Joel, zijn de volgende op de lijst. Knakkers, ik kan mij niet voorstellen hoe het hele traject zou zijn geweest zonder jullie. We hebben vele uren gevuld met het zwetsen over werk, muziek, boeken, Duitsers, politiek en de leuke en minder leuke dingen uit het leven en ik kan slechts concluderen dat jullie er altijd waren wanneer ik jullie nodig had en ik hoop dat dit ook andersom het geval is. Ik ben de eerste van ons drieën die een paar jaar geknutsel in een boekje mag stoppen en ik hoop van harte dat het jullie ook gaat lukken en dat wij ons over een paar jaar alle drie stakkerig wijs mogen noemen.

Tijdens de afgelopen jaren heb ik met twee mensen aan twee erg leuke projecten gewerkt. Thijs, ik begin bij jou. Ik ben zelden aan iets begonnen dat zo uit de hand is gelopen als het geknutsel aan ons LES model. Bovendien kan ik mij niet aan de indruk onttrekken dat mijn nieuwe baan in Hamburg als jouw collega er nooit zou zijn gekomen zonder onze samenwerking! Mijn dank is groot en ik beloof Jessica plechtig om niet te veel van je tijd op te eisen voor ons nieuwste uit-de-hand-aan-het-lopende project en voor de legendarische serie papers die we nu eindelijk maar eens moeten produceren!

Bart, ook jou wil ik graag bedanken voor de toffe samenwerking in de laatste jaren. Samen met Jordi en Kees hebben we een mooi model met bijbehorende interface gebouwd dat het erg goed lijkt te doen en waar we volgens mij best trots op mogen zijn!

Dan wil ik graag alle studenten bedanken die ik (deels) begeleid heb tijdens hun BSc- of MSc-thesis. Jan, Dirk, Daphne, Natalie, Bart, Maarten en Esther, jullie hebben me regelmatig gedwongen om zorgvuldig na te denken over jullie en over mijn eigen onderzoek en daarom hebben jullie bijgedragen aan de kwaliteit van dit proefschrift.

I would also like to thank the all the coauthors of my papers. Fleur, Françoise and Amanda,

thank you for the great visit at Metéo-France and for your contribution to our paper! Elie, thanks for sharing your knowledge on LES and turbulence. Arnold, bedankt voor je scherpe oog voor detail. Ryan, bedankt voor de hulp in het verbinden van mijn theoretische geneuzel met de echte wereld en voor het demonstreren van je skills in paperlengtereductie.

Mijn collega's hebben hebben er voor gezorgd dat ik (bijna) elke dag met plezier naar mijn werk ben gegaan. Ik wil mijn kamergenoten Joel, Joost, Daniëlle, Bram, Bart en Monica bedanken voor de gezelligheid gedurende de afgelopen vier jaar. Met enige regelmaat liepen de (wetenschappelijke) discussies uit de hand, maar jullie hebben me enorm geholpen bij het begrijpen van complexe problemen die soms mijn voorstellingsvermogen te boven gingen (maar nooit die van Joost).

Kees, ook jij verdient een woord van dank voor het oplossen van alle praktische problemen die opgelost dienden te worden. Of het nu op de vakgroep was, in de Alpen of op Cyprus, alles kwam altijd goed. Gerrie, bedankt voor het verwerken van mijn niet ingevulde uren en mijn dubieuze reisdeclaraties.

Ook buiten werktijd was het goed toeven met de vakgroep. Ik denk met plezier terug aan onze avonden in de kroeg, aan een hoop etentjes en feestjes en aan onze sportsessies. Gert-Jan, het waren goede roddelsessies. Bert, bedankt voor het demonstreren hoe levensmoeheid eruit ziet op een racefiets. Miranda, tof dat je je werkschema om mijn promotie heengevouwen hebt. Natalie, bedankt voor de mentale ondersteuning. Huug, Denica, Michal en Anneke bedankt voor de gezelligheid. Ivar, Eduardo en Marina, ik heb veel plezier beleefd aan onze muzieksessies tijdens de laatste maanden en de resultaten vallen zeker niet tegen!

Om te voorkomen dat deze toch al lange opsomming nog langer wordt (en dat ik mensen vergeet), wil ik graag in één keer mijn overige collega's in Wageningen bedanken. Ook wil ik graag iedereen van de BBOS meetings bedanken voor de uiterst leerzame, maar ook gezellige sessies. En niet te vergeten Henk de Bruin voor de mooie verhalen en de goede suggesties.

En dan zijn er nog mijn vrienden die niets met dit hele proefschrift te maken hebben, maar die het leven wel leuk maken. Meinie, ik wil je graag bedanken voor alles. En alles is in jouw geval heel veel. De rest van mijn vrienden wil ik ook maar in één keer bedanken (om nogmaals te vermijden dat ik mensen vergeet): tof dat jullie me regelmatig bij mijn werk vandaan hebben gehouden!

Tenslotte vond ik het fijn om me op momenten waarop dit nodig was te kunnen realiseren dat ik ontzettend geluk heb met mijn ouders. Pap en mam, bedankt voor alle steun!

List of journal publications

1. van Heerwaarden, C. C. and J. Vilà-Guerau de Arellano, 2008: Relative humidity as an indicator for cloud formation over heterogeneous landscapes. *J. Atmos. Sci.*, **65**, 32633277, doi:10.1175/2008JAS2591.1.

2. Gorska, M., J. Vilà-Guerau de Arellano, M. A. LeMone and C. C. van Heerwaarden, 2008: Mean and flux horizontal variability of virtual potential temperature, moisture and carbon dioxide: aircraft observations and LES study. *Mon. Wea. Rev.*, **136**, 4435-4451, doi:10.1175/2008MWR2230.1

3. van Heerwaarden, C. C., J. Vilà-Guerau de Arellano, A. F. Moene, and A. A. M. Holtslag, 2009: Interactions between dry-air entrainment, surface evaporation and convective boundary layer development. *Quart. J. Roy. Meteor. Soc.*, **135**, 1277–1291, doi:10.1002/qj.431.

4. Lenaerts, J. T. M., C. C. van Heerwaarden and J. Vilà-Guerau de Arellano, 2009: Shallow convection over land: a mesoscale modelling study based on idealized WRF experiments. *Tethys*, **6**, 51-66, doi:10.3369/tethys.2009.6.04.

5. van Heerwaarden, C. C., J. Vilà-Guerau de Arellano, A. Gounou, F. Guichard, and F. Couvreux, 2010: Understanding the daily cycle of evapotranspiration: a method to quantify the influence of forcings and feedbacks. *J. Hydrometeor.*, **11**, 1405–1422, doi:10.1175/2010JHM1272.1.

6. Heus, T., C. C. van Heerwaarden et al., 2010: Formulation of the Dutch Atmospheric Large-Eddy Simulation (DALES) and an overview of its applications. *Geosci. Model. Dev. Discuss.*, **3**, 99–180, doi:10.5194/gmd-3-415-2010.

7. van Heerwaarden, C. C., J. Vilà-Guerau de Arellano, and A. J. Teuling, 2010: Land-atmosphere coupling explains the link between pan evaporation and actual evapotranspiration trends in a changing climate. *Geophys. Res. Lett.*, **37**, L21401, doi:10.1029/2010GL045374.

8. Wolters, D., C. C. van Heerwaarden, J. Vilà-Guerau de Arellano, B. Cappelaere and D. Ramier, 2010: Effects of soil moisture gradients on the path and the intensity of a West-African squall line. *Quart. J. Roy. Meteor. Soc.*, **136**, 2162-2175, doi:10.1002/qj.712.

9. van Stratum, B. J. M., J. Vilà-Guerau de Arellano, and C. C. van Heerwaarden, 2011. Sub-cloud heat and moisture budgets in a transient cloud-topped convective boundary layer. *J. Atmos. Sci.*, submitted.

10. van Heerwaarden, C. C., J. Vilà-Guerau de Arellano, and E. Bou-Zeid, 2011. On land-surface modeling in large-eddy simulations of convective boundary layers. *Mon. Wea. Rev.*, submitted.

The research in this thesis was financially supported by NWO TopTalent (2007) and the National Computing Facilities Foundation (NCF project SH-060-10).

Financial support from Wageningen University for printing this thesis is gratefully acknowledged.

Netherlands Research School for the
Socio-Economic and Natural Sciences of the Environment

C E R T I F I C A T E

The Netherlands Research School for the
Socio-Economic and Natural Sciences of the Environment (SENSE),
declares that

Chiel Constantijn van Heerwaarden

born on 26 April 1982 in Apeldoorn, The Netherlands

has successfully fulfilled all requirements of the
Educational Programme of SENSE.

Wageningen, 8 June 2011

the Chairman of the SENSE board	the SENSE Director of Education
Prof. dr. Rik Leemans	Dr. Ad van Dommelen

The SENSE Research School has been accredited by the Royal Netherlands Academy of Arts and Sciences (KNAW)

KONINKLIJKE NEDERLANDSE
AKADEMIE VAN WETENSCHAPPEN

The SENSE Research School declares that **Mr. Chiel Constantijn van Heerwaarden** has successfully fulfilled all requirements of the Educational PhD Programme of SENSE with a work load of 67 ECTS, including the following activities:

SENSE PhD courses

- Environmental Research in Context
- Research Context Activity: Co-organizing WIMEK Water Cycle Symposium (Wageningen, 29 January 2009)
- Understanding Global Environmental Change: Processes, compartments and Interaction
- Summer school on Atmospheric Boundary Layers
- Autumn School: Biogeochemistry and -physics of the lower atmosphere

Other Phd and MSc courses

- PhD Scientific Writing

Management Skills

- Core maintainer of the Dutch Atmospheric Large-Eddy Simulation (DALES)
- Software development of interactive model to be used in several courses in the Meteorology and Air Quality section

Didactic Skills

- Teaching assistant Boundary-Layer Processes (MAQ -32206)
- Supervision and co-supervision of eight BSc and MSc students

Oral Presentations

- Cloud formation over heterogeneous land surfaces, Conference AMS Boundary layer and turbulence, 10 June 2008, Stockholm, Sweden
- Trends in pan and actual evaporation, WIMEK Water Cycle Symposium, 29 January 2009, Wageningen, The Netherlands
- Interactions between the free troposphere, surface evaporation and convective boundary layer development, SIAM Conference on Mathematical & Computational Issues in the Geosciences, 16 June 2009, Leipzig, Germany
- A framework to quantify the role of land-atmosphere feedbacks on surface evaporation, EMS Conference, 23 September 2009, Toulouse, France
- A framework to quantify the role of land-atmosphere feedbacks on surface evaporation, AGU Fall Meeting 2009, 17 December 2009, San Francisco, USA
- An explanation for decreasing trends in pan evaporation based on research on interactions between surface evaporation and the atmospheric boundary layer, AGU Fall Meeting 2009, 19 December 2009, San Francisco, USA
- On land surface modelling in large-eddy simulations of atmospheric boundary layers, AGU Fall Meeting 2010, 14 December 2010, San Francisco, USA

SENSE Coordinator PhD Education and Research

Mr. Johan Feenstra